



Review Article



Atomic wires on substrates: Physics between one and two dimensions

H. Pfnür^{a,*}, C. Tegenkamp^{a,b,**}, S. Sanna^{c,***}, E. Jeckelmann^d, M. Horn-von Hoegen^e,
U. Bovensiepen^e, N. Esser^f, W.G. Schmidt^g, M. Dähne^h, S. Wippermannⁱ, F. Bechstedt^j,
M. Bode^k, R. Claessen^k, R. Ernstorfer^l, C. Hogan^{m,n}, M. Ligges^e, A. Pucci^o, J. Schäfer^k,
E. Speiser^f, M. Wolf^l, J. Wollschläger^p

^a Institut für Festkörperphysik, Leibniz Universität Hannover, Appelstr. 2, D-30167, Hannover, Germany

^b Institut für Physik, Technische Universität Chemnitz, Reichenhainer Str. 70, D-09126 Chemnitz, Germany

^c Institut für Theoretische Physik and Center for Materials Research (LaMa/ZfM), Justus-Liebig-Universität Gießen, Heinrich-Buff-Ring 16, D-35392, Gießen, Germany

^d Institut für Theoretische Physik, Leibniz Universität Hannover, Appelstr. 2, D-30167, Hannover, Germany

^e Fakultät für Physik, Universität Duisburg-Essen, Lotharstr. 1-21, D-47057, Duisburg, Germany

^f Leibniz-Institut für Analytische Wissenschaften (ISAS), Schwarzschildstr. 8, D-12489, Berlin, Germany

^g Theoretische Materialphysik, Universität Paderborn, D-33095, Paderborn, Germany

^h Institut für Festkörperphysik, Technische Universität Berlin, Hardenbergstr. 36, D-10623, Berlin, Germany

ⁱ Interface Chemistry and Surface Engineering Department, Max-Planck-Institut für Eisenforschung, Düsseldorf, Germany

^j Institut für Festkörpertheorie und -optik, Universität Jena, Fröbelstieg 1, D-07743, Jena, Germany

^k Physikalisches Institut, Universität Würzburg and Würzburg-Dresden Cluster of Excellence "ct.qmat", Am Hubland, D-97074, Würzburg, Germany

^l Physikalisches Institut, Fritz-Haber-Institut der MPG, Faradayweg 4-6, D-14195, Berlin, Germany

^m Istituto di Struttura della Materia, Consiglio Nazionale delle Ricerche (ISM-CNR), Via del Fosso del Cavaliere 100, 00133, Rome, Italy

ⁿ Dipartimento di Fisica, Università di Roma "Tor Vergata", Via della Ricerca Scientifica 1, I-00133, Rome, Italy

^o Kirchhoff Institut, Fakultät für Physik und Astronomie, Ruprecht-Karls-Universität Heidelberg, Germany

^p Fachbereich Physik, Universität Osnabrück, Barbarastr. 7, D-49076, Osnabrück, Germany

A B S T R A C T

Wires having a width of one or two atoms are the smallest possible physical objects that may exhibit one-dimensional properties. In order to be experimentally accessible at finite temperatures, such wires must be stabilized by interactions in two and even three dimensions. These interactions modify and partly destroy their one-dimensional properties, but introduce new phenomena of coupling and correlation that entangle both charge and spin. We explore this fascinating field by first giving an overview of the present status of theoretical knowledge on 1D physics, including coupling between chains and to the substrate, before we set out for experimental results on ordered arrays of atomic wires on both flat and vicinal Si(111) surfaces comprising Si(111)-In, Si(hhk)-Au, Si(557)-Pb, Si(557)-Ag, on Ge(001)-Au and of rare earth silicide wires. While for these systems structural, spectroscopic and (magneto-)conductive properties are in the focus, including temperature- and concentration-induced phase transitions, explicit dynamics on the femto- and picosecond time scales were explored for the modified Peierls transition in indium chains on Si(111). All these systems are characterized by strong correlations, including spin, that are extended over whole terraces and partly beyond, so that small geometric changes lead to large modifications of their electronic properties. Thus this coupling in one (1D), two (2D) (and even three) dimensions results in a wealth of phase transitions and transient quasi-1D conductance. As extremes, modified quasi-1D properties survive, as in the Si(111)-In system, whereas strong Fermi nesting results in entanglement of spin and charge between terraces for Si(557)-Pb, so that spin orbit density waves across the steps are formed.

* Corresponding author.

** Corresponding author.

*** Corresponding author.

E-mail addresses: herbert.pfnuer@fkp.uni-hannover.de (H. Pfnür), christoph.tegenkamp@physik.tu-chemnitz.de (C. Tegenkamp), simone.sanna@theo.physik.uni-giessen.de (S. Sanna).

<https://doi.org/10.1016/j.surfrep.2024.100629>

Received 3 January 2024; Received in revised form 4 April 2024; Accepted 4 April 2024

Available online 7 May 2024

0167-5729/© 2024 The Authors. Published by Elsevier B.V. This is an open access article under the CC BY-NC license (<http://creativecommons.org/licenses/by-nc/4.0/>).

1. One-dimensional systems and the real world¹

1.1. Introduction

One-dimensional systems have fascinated solid-state physicists for more than 60 years [1–9]. Theory predicts that one-dimensional (1D) electron systems feature unusual properties which set them apart from ordinary materials. Well-known examples are the Peierls instability [10], the Luttinger liquid theory of 1D conductors [11], and the absence of thermodynamic phase transitions [12,13].

The main motivation for studying one-dimensional systems of solids was originally their (apparent) simplicity compared to more realistic three-dimensional (3D) systems. Indeed, a very common mathematical approach is to reduce complex high-dimensional problems to independent one-dimensional problems using transformation and separation of variables. A textbook example is the solution of the Schrödinger equation for the hydrogen atom using spherical coordinates. It has turned out, however, that 1D models of solids may have markedly different properties than their 3D counterparts. What could be seen as a drawback has actually spurred intensive research efforts in condensed matter physics over more than six decades to find materials exhibiting this 1D physics.

These efforts have led to the discovery of numerous materials that can be regarded in first approximation as being *quasi-1D* electron systems over a finite energy and temperature scale. In this context, the adjective *quasi* is chosen to distinguish real-world structures from true 1D objects. While the latter are mathematical idealizations, curves with no width and no interactions with the ambient space in which they are embedded, real-world examples always have a finite width and an arbitrary small but non-zero coupling with their environment. The atomic chains formed on various surfaces [8,14–16] are very promising realizations of quasi-1D systems and will be the main subject of this review. Other prominent quasi-1D materials are highly anisotropic crystalline solids such as Bechgaard salts [3,5,8,17] and π -conjugated polymers [2,9,18]. More recent realizations of quasi-1D electron systems are carbon nanotubes [19] and quantum wires in semiconductor heterostructures [20,21]. Additionally, 1D physics can be observed in other condensed-matter systems such as in edge channels of quantum Hall fluids [22,23] and of quantum spin Hall insulators [24,25], as well as in ultracold atomic or molecular gases in optical lattices [26,27]. However, they are quite different both experimentally and theoretically from atomic wires on surfaces and they are not further discussed in the following.

Many of the peculiar features predicted by the theory of 1D electron systems have been observed experimentally in quasi-1D materials. Mostly they are long-range-ordered symmetry-breaking phases induced by the perfect nesting of the 1D electron gas, e.g. Peierls insulators, charge-density waves (CDW), and spin-density waves (SDW) [1–5,9,17,28]. Other features have proven to be more elusive, for instance the dynamical separation of spin and charge excitations and the Luttinger liquid behavior of 1D conductors [6,28–30].

From a theoretical point of view, strictly 1D electron systems are very well understood. This knowledge is mostly based on minimal effective models [31] representing only the low-energy degrees of freedom and interactions that are relevant for the particular phenomenon to be described (e.g. a Peierls transition) [4–7,28,29,32–34]. Although these effective models do not provide us with a realistic description of any material, they are “simple” enough to be solved (analytically or numerically). Thus they allow us to investigate and understand the peculiar properties of 1D systems. The theoretical discussion in this chapter is almost entirely based on results obtained from effective models with some input from first-principles simulations and experiments.

In real systems, however, even in the most anisotropic ones, 3D fluctuations and interactions play a significant role [1,4–7,33]. Consequently, the coupling to the 3D environment must be taken into account when theoretical predictions are used to interpret experiments. In the case of atomic wires on surfaces both the two-dimensional (2D) coupling between wires (interchain coupling) and the coupling between wires and substrate could play a substantial role [8,35]. For instance, thermal fluctuations prevent any long-range order at finite temperature in one dimension [13] and mean-field approximations break down. Couplings of 1D systems to their environment make possible the experimental observation of the ordered phases and transitions characterizing 1D physics at finite temperatures but they also reduce the anisotropy of these systems. Thus an important issue in the field of quasi-1D materials is the question as to whether these systems possess experimental and theoretical properties that are different from more ordinary (i.e. anisotropic 3D) materials when the coupling to the real world is taken into account.

The first aim of this chapter is to introduce some basic theoretical concepts about 1D systems that are relevant for atomic wire systems. Thus we will review the theory of strictly 1D electron systems and our understanding of the 3D coupling in quasi-1D crystalline materials. The second goal is to discuss the question of the coupling of atomic wires to the real world. In particular, we will examine the effects of the 2D coupling between wires and the role of the substrate on the 1D physics in atomic wires on semiconducting surfaces. The focus is on two phenomena that are often invoked to explain experimental observations in atomic wires, namely Peierls-CDW transitions and the Luttinger liquid behavior of 1D conductors. We will summarize some results obtained in the last decade including a grand-canonical theory of the Peierls-like transition in Indium on the Si(111) surface, the stability of Luttinger liquids and electronic CDW on a 3D substrate, substrate-mediated interactions between wires, and a comparison of a 2D array of Luttinger liquids with an anisotropic 2D Fermi liquid with a view to gold chains on the Ge(100) surface.

1.1.1. Outline

The structure of this chapter is as follows. In the next section we will summarize some general information about quasi-1D materials and their theoretical description. Basic theoretical results about strictly 1D electron systems are reviewed in the third section. Then we will discuss four topics in more detail. Section 1.4 is devoted to the effect of the interchain coupling. The role of the substrate is analyzed in sec. 1.5. Peierls-CDW transitions and quasi-1D metallic states in atomic wires are discussed in sec. 1.6 and 1.7, respectively. First conclusions are presented in the last section.

1.2. Quasi-one-dimensional systems: materials and theoretical approach

This section summarizes some information about quasi-1D systems that is necessary to understand the theoretical discussion in the next sections. It includes a brief presentation of atomic wire systems as quasi-1D electron systems (section 1.2.1), an overview of some well-established quasi-1D crystalline materials (section 1.2.2), a discussion of dimensional confinement (section 1.2.3), and an overview of some models and methods used to study specific phenomena in low-dimensional solids (section 1.2.4).

1.2.1. Atomic wires on surfaces

Self-assembled atomic wires on the surface of semiconducting substrates appear to be an ideal realization of 1D electron systems [8,15,16]. They are the thinnest possible solid-state structures and they can be studied experimentally with surface spectroscopy methods, such as angle-resolved photoemission spectroscopy (ARPES) and scanning tunneling spectroscopy (STS), as well as with imaging techniques such as scanning tunneling microscopy (STM). Advances in atomic-scale manipulation could also enable the creation of *ad hoc* artificial

¹ Author mainly responsible for this section: E. Jeckelmann

low-dimensional atomic structures that realize selected quasi-1D phases of matter [36]. Thus atomic wire on surfaces provide us with unprecedented opportunities to observe real quasi-1D electron systems.

From a theoretical point of view, the degrees of freedom responsible for the low-energy electronic properties of atomic wires on semi-conducting substrates are confined spatially around the surface. Thus they build an effectively 2D electron system. Moreover, the adatoms build parallel wires on the surfaces. These anisotropic atomic structures typically result in electronic properties that differ markedly in the wire direction and in the perpendicular direction. The observed effects are usually ascribed to the internal degrees of freedom of the atomic wires or their immediate surrounding in the substrate. Thus atomic wires on surfaces can be regarded in first approximation as 2D arrays of (more or less weakly) coupled chains that are embedded in a 3D environment (the underlying substrate). Consequently, concepts from the physics of 1D electron systems are often invoked to explain some experimental observations in these atomic wire systems but these interpretations remain often controversial.

As a first example, there is a controversy about the dimensionality of the metallic state in the system made of gold chains on Ge(100) surfaces and the relevance of the Luttinger liquid theory to describe its low-energy properties [15,37–44]. Theoretically, the question is whether the Luttinger liquid behavior found in strictly 1D conductors survives in atomic wires on surfaces despite the interchain coupling and the coupling to the substrate, or whether the system is better described as an anisotropic Fermi liquid [28,30,45]. This issue is discussed in the following sections, in particular in sec. 1.7. Experimental properties of Au/Ge(100) are discussed in sec. 2.5.

As another example, the relevance and mechanism of the (second-order) Peierls-CDW transition are intensively debated for the structural and metal-insulator transition observed at 120 K in indium nanowires on the Si(111) surface [16,46–56]. There is clear evidence that the original Peierls theory does not apply to these systems. First, experimental evidence shows that the transition is first order. Second, the substrate may act as a charge reservoir for the wire subsystem and thus its band filling is not fixed. This raises questions about the occurrence of a Peierls instability, and, more generally, of the $2k_F$ instability of the 1D electron gas due to the Fermi surface nesting. Last, the suppression of fluctuations by the 3D interchain coupling explains the occurrence of Peierls or CDW transitions at finite temperature in quasi-1D crystalline materials, but the weak 2D interchain coupling between atomic wires may not be enough to explain the observed critical temperature in In/Si(111). This issue is also discussed in the following sections, in particular in sec. 1.6. Experimental and first-principles simulation results for In/Si(111) are discussed in detail in sec. 2.3 and 3.

One reason for these controversies is often the lack of a proper theory for the 1D physics to be found in atomic wire systems and, consequently, the unwarranted adoption of theoretical concepts and predictions for strictly 1D electron systems, which are summarized in section 1.3. The influence of the 3D world must be taken into account when experimental results are compared to theoretical predictions for quasi-1D electron systems. The above examples show that the influence of the substrate and the interaction between the wires cannot be disregarded a priori for atomic wire systems.

Theoretical studies of atomic wire systems have been mostly based on the concepts and methods of surface physics so far [57]. Couplings between atomic wires and with the substrate are usually taken into account in these studies. As for experimental results, however, when seemingly 1D features are found, their interpretation is often based on the theory for strictly 1D electron systems. In contrast, the theory of 1D systems is mostly based on effective models for the relevant degrees of freedom. It was successfully extended over several decades to explain the properties of numerous real quasi-1D materials in the 3D world, in particular strongly anisotropic crystals. Although intensive research on self-assembled atomic wires on surfaces started more than twenty years ago, the extension of this theoretical approach to atomic wire systems in

the real world is still in its infancy. In sections 1.5 to 1.7 we will review some results obtained in the last decade.

1.2.2. Quasi-1D crystalline materials

Much of our knowledge about quasi-1D systems in the 3D world come from theoretical and experimental investigations of strongly anisotropic crystalline materials. Thus it is helpful to recapitulate some basic facts about these systems. The crystal anisotropy leads to a dynamical dimensional confinement of the electronic degrees of freedom and, consequently, to anisotropic electronic properties. Various phases and phenomena that characterize 1D electron systems have been observed in these materials but they also clearly demonstrate the role of the 3D environment, in particular the interchain coupling.

The most prominent example of these quasi-1D bulk materials is the family of organic charge-transfer complexes known as Bechgaard and Fabre salts [3–5,8,17,58]. They are made of weakly-coupled linear stacks of an organic planar molecule, tetramethyl-tetrathiofulvalene (TMTTF) or tetramethyl-tetraselenafulvalene (TMTSF), with inorganic anions ($X = \text{PF}_6, \text{ClO}_4, \dots$). The strength of the 3D interchain coupling differs in the various salts and can also be varied using external pressure. Taken together the phase diagram of the materials $(\text{TMTTF})_2X$ and $(\text{TMTSF})_2X$ covers the dimensional crossover from quasi-1D to anisotropic 3D systems as illustrated in Fig. 1. Thus Bechgaard and Fabre salts are the paradigm for the effects of the 3D interchain coupling on 1D electron systems. They can be quasi-1D Mott or spin-Peierls insulators, commensurate or incommensurate antiferromagnetic SDW, or anisotropic 3D organic superconductors at low temperature. The Luttinger liquid behavior is observed in the metallic state at higher temperature. In particular, a power-law predicted for 1D correlated metals was observed in the optical conductivity of the $(\text{TMTSF})_2X$ salts [6,59].

For instance, the $(\text{TMTTF})_2\text{PF}_6$ compound is strongly anisotropic and corresponds to the left-hand side of the phase diagram in Fig. 1 [58]. At high temperature this material is a quasi-1D conductor that behaves like a Luttinger liquid. Below a critical temperature $T_c = 250\text{K}$ this compound becomes a paramagnetic Mott insulator: the resistivity increases by several orders of magnitude while the spin susceptibility remains unchanged. This phase does not break any symmetry (see sec. 1.3.3). A symmetry-breaking charge ordering transition (electronic CDW) occurs at $T_c = 70\text{K}$ (not shown in Fig. 1). Finally, the spin degrees of freedom undergo a transition to a spin-Peierls state with spin gap and lattice distortion (dimerization) below $T_c = 19\text{K}$ (see sec. 1.3.2).

Numerous phases and phenomena predicted by the theory of 1D electron systems have been found in other quasi-1D bulk materials. One important family of materials is formed by π -conjugated polymers, such as polyacetylene $(\text{CH})_x$, in thin films [2,8,9,18,60]. They are insulators

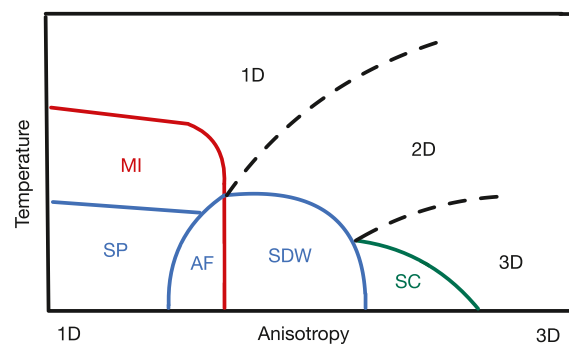


Fig. 1. Sketch of the combined phase diagram of Bechgaard and Fabre salts: Paramagnetic Mott-Hubbard or CDW insulator (MI), commensurate antiferromagnetic insulator (AF), spin-Peierls insulator (SP), incommensurate spin-density wave (SDW), superconductor (SC), Luttinger liquid (1D), quasi two-dimensional (2D) and normal (3D) Fermi liquid. The anisotropy diminishes from left to right due to applied pressure or substitution of inorganic anions. See Fig. 56 in Ref. [17], 8.14 in Ref. [6], or 4.31 in Ref. [58] for more details.

because electronic correlations and electron-phonon coupling work together to generate a Mott-Peierls gap. Some π -conjugated polymers undergo a transition from insulators to quasi-1D conductors upon doping. These doped polymers are unusual metals with a conductivity as high as copper at room temperature but with vanishing Pauli susceptibility. Some unusual properties can be explained by a fractionalization of low-energy excitations (i.e. the existence of charge and neutral solitons that are domain walls in the long-range Peierls-CDW order [61, 62]), which is related to a hallmark of 1D electron systems, the dynamical separation of spin and charge excitations. The metal-insulator transition upon doping can be explained by a generalization of the Peierls theory [63,64]. Luttinger liquid behavior has not been reported, however. One possible explanation is that dopant ions intercalated between polymer chains create bridges between them. Thus the doping induces a transition from an insulating quasi-1D system to an anisotropic 3D metallic system.

Yet another important group is made of various quasi-1D bulk materials that undergo Peierls-CDW transitions at finite temperature. As a first example, the charge transfer salt TTF-TCNQ is made of weakly-coupled linear stacks of two types of molecules, tetrathiafulvalene (TTF) and tetracyanoquinodimethane (TCNQ) [1,8]. It is a realization of an incommensurate Peierls insulator at low temperature and of a Luttinger liquid above the critical Peierls temperature $T_c = 59\text{K}$. The separation of spinon and holon excitations was demonstrated by ARPES experiments [65,66]. The transition metal trichalcogenides (MX_3), for instance NbSe_3 and TaS_3 , are examples of incommensurate Peierls-CDW systems [1,4,8] with critical temperatures that are reduced by fluctuations from the values expected from mean-field theory (see section 1.4). They exhibit collective excitation modes (sliding CDW), which are pinned by defects and interchain couplings, and, consequently, nonlinear dynamical properties due to the depinning of sliding modes at strong electric fields [4,67]. Lastly, mixed-valence platinum complex compounds such as $\text{K}_2\text{Pt}(\text{CN})_4\text{-Br}_{0.3} \cdot 3.2\text{H}_2\text{O}$ (potassium-tetracyanoplatinate, KCP), also called Krogmann salts, exhibit highly anisotropic electrical conductivity [1,4,8]. They are made of stacks of planar tetracyanoplatinate $[\text{Pt}(\text{CN})_4]^-$ anions and can be regarded as 3D arrays of weakly-coupled chains of platinum atoms. The $2k_F$ instability of metals driving the Peierls-CDW transition, in particular a giant Kohn anomaly, was first observed in these materials.

Strongly correlated copper oxide compounds constitute the last family of quasi-1D systems to be discussed here. The crystal structure of some transition metal oxides contains chains or ladders of Cu atoms surrounded by O atoms [8,68]. GeCuO_3 , SrCuO_2 , and Sr_2CuO_3 are examples of spin chain systems while spin-ladders are realized in SrCu_2O_3 (two-leg ladder) and $\text{Sr}_2\text{Cu}_3\text{O}_5$ (three-leg ladder). These materials are Mott or charge transfer insulators with strongly anisotropic magnetic properties. Theoretical descriptions are based on generalizations of the Heisenberg model for quantum magnets when electron spins are the only degrees of freedom taken into account. Indeed, various theoretical predictions of 1D magnetism are realized in these materials [6,69,70]. For instance, a spin-Peierls transition has been observed in the spin-chain compound GeCuO_3 at $T_c = 14\text{K}$ with a quasi-long-range SDW order above T_c [71,72]. Additionally, the magnetic excitation spectra measured in SrCuO_2 [73] and Sr_2CuO_3 [74] are well described by the 1D spin-1/2 antiferromagnetic Heisenberg model. However, measured critical temperatures T_c for the 3D antiferromagnetic ordering are orders of magnitude smaller than the intrachain spin exchange couplings J determined from excitation spectra (e.g. $k_B T_c = 5\text{K}$ and $J = 250\text{meV}$ for Sr_2CuO_3 [74]). Thus these systems illustrate the suppression of the 1D antiferromagnetic order by fluctuations at the temperature scale of the intrachain coupling and the stabilization of the 3D antiferromagnetic long-range order at a lower temperature scale set by the 3D interchain coupling (see section 1.4).

1.2.3. Dimensional confinement

There are various definitions for systems of reduced dimensions in

condensed matter physics. The most relevant concepts for the electronic properties of atomic wires on semiconducting substrates are the spatial and dynamical confinements. They are introduced below as they have different consequences for phase transitions as explained in sec. 1.4.

1.2.3.1. Spatial confinement. The most intuitive of these definitions is the spatial confinement of some degrees of freedom [75]. A quasi-1D system can be realized in a solid that is much longer than wide such as isolated carbon nanotubes [19] and quantum wires in semiconductor heterostructures [20,21]. Consider a 3D solid in which all relevant degrees of freedom (e.g., electrons, phonons, ...) are spatially confined in two directions within a region of linear sizes L_y and L_z but at least one (electronic) degree of freedom can propagate over a distance $L_x \gg L_{y,z}$ in the third direction (wire direction). If we look at this system with a resolution λ fulfilling $L_{y,z} \ll \lambda \ll L_x$, we effectively observe a 1D geometric object.

This geometry affects the electronic structure drastically. Consider an electron gas confined in this quasi-1D solid (i.e. a system of noninteracting electrons in an homogeneous background of positive charges). The eigenenergies of single-particle eigenstates are given by

$$\epsilon(k_x, n_y, n_z) = \frac{\hbar^2}{2m} \left[k_x^2 + \left(\frac{\pi n_y}{L_y} \right)^2 + \left(\frac{\pi n_z}{L_z} \right)^2 \right], \quad (1)$$

where m is the electron mass. The dispersion is continuous in the wire direction as a function of the wave number $k_x \in \mathbb{R}$ but discrete in the perpendicular directions (with quantum numbers $n_y, n_z \in \mathbb{N}^*$). In a strictly 1D system ($L_{y,z}/L_x \rightarrow 0$) the electronic spectrum reduces to a single 1D band

$$\epsilon(k_x) = \frac{\hbar^2}{2m} k_x^2 \quad (2)$$

(up to a constant), shown in Fig. 2. However, real systems such as carbon nanotubes and semiconductor quantum wires have a finite length to width ratio and thus the condition $L_{y,z}/L_x \rightarrow 0$ is never fully satisfied. Moreover, they must be embedded in or deposited on a 3D substrate to be stable when $L_x \gg L_{y,z}$.

1.2.3.2. Dynamical confinement. Alternatively electrons can be confined dynamically (or energetically) in strongly anisotropic 3D crystalline solids. Such a solid extends in three dimensions but is so anisotropic that electrons are much more delocalized or mobile in one direction than in the other two directions. Thus they can be seen as a 3D array of 1D

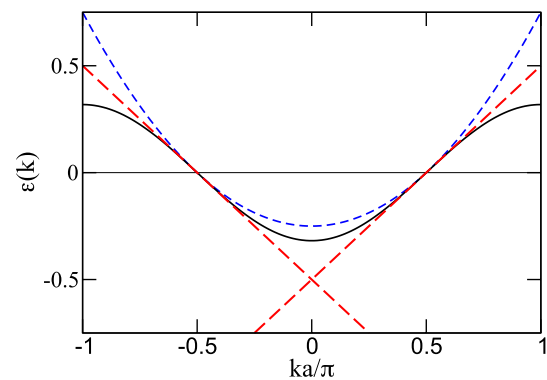


Fig. 2. Dispersions of single-particle eigenenergies in strictly 1D systems. Continuum model, Eq. (2), (blue dashed line), tight-binding model, Eq. (4), (black solid line), and Tomonaga-Luttinger model (see sec. 1.3.5) (red dashed line). The dispersions are shifted and rescaled to have the same Fermi energy $\epsilon_F = 0$ and Fermi points $k_F = \pi/(2a)$. (For interpretation of the references to color in this figure legend, the reader is referred to the Web version of this article.)

chains. They are numerous realizations of such quasi-1D systems as discussed in section 1.2.2.

The basic electronic structure of these materials is better understood using a tight-binding approach. In a tight-binding model for a (orthorhombic) lattice with constants a , b , and c the dispersion of single-electron states has the form

$$\epsilon(\vec{k}) = -2t_x \cos(k_x a) - 2t_y \cos(k_y b) - 2t_z \cos(k_z c) \quad (3)$$

with the wave vector $\vec{k} = (k_x, k_y, k_z) \in \mathbb{R}^3$. The hopping parameters t_x , t_y , and t_z determine the bandwidth (or dispersion width) in each direction. In a continuum model the anisotropic electronic structure would be described by an anisotropic effective mass tensor with effective masses $m_\alpha \sim 1/t_\alpha$ for $\alpha = x, y, z$.

This dispersion of the electron gas is the starting point for the discussion of electronic properties in quasi-1D crystalline materials. For a strongly anisotropic lattice the (intra-) chain hopping parameter $|t_x|$ is much larger than the interchain hopping parameters $|t_y|$, $|t_z|$, resulting in a much larger bandwidth or broader dispersion in the chain direction than in the perpendicular directions. For instance, the band structure of Bechgaard and Fabre salts is represented by the above tight-binding model with hopping parameters that may differ by an order of magnitude, i.e. $t_x/t_y \approx 10$ and $t_y/t_z \approx 10$. Thus the system properties are strongly anisotropic if probed at a temperature T or an excitation energy E fulfilling $|t_y|$, $|t_z| \ll k_B T$, $E \ll |t_x|$. A strictly 1D electronic system is obtained for $t_{y,z}/t_x \rightarrow 0$. The resulting electronic spectrum is dispersionless in the directions perpendicular to the chains and can also be seen as a 1D band

$$\epsilon(k_x) = -2t_x \cos(k_x a) \quad (4)$$

localized in each chain (see Fig. 2) but one should keep in mind that the system is made of (infinitely) many equivalent parallel chains with this band structure.

For a given anisotropic crystalline material the main question is whether it should be considered as an array of (more or less) independent 1D chains or as an anisotropic 3D system. For most materials it is not possible to give a clear answer to this question as the boundary between these two points of view is not sharp. In particular, the answer does not only depend on the crystal and electronic structure but also on the current system state (e.g., its temperature) and the measured properties (e.g. excitation energy). This issue is discussed in detail in section 1.4.

1.2.3.3. Wires on surfaces. The low-energy electronic properties of atomic wires on semiconducting substrates are typically determined by a few electronic bands that are confined spatially close to the substrate surfaces. Thus we will assume that atomic wire systems are strictly 2D electronic systems, which corresponds to setting $L_z/L_{x,y} \rightarrow 0$ in Eq. (1) or $t_z/t_{x,y} \rightarrow 0$ in Eq. (3). Note that it does not matter whether the surface is flat or stepped, or whether the relevant electronic bands are built from adatom orbitals or from substrate surface bands. In our approach it is sufficient that the electronic wave functions are spatially confined in the direction perpendicular to the surface on a length scale L_z much smaller than their typical extension in (at least) one direction parallel to the surface. This assumption does not exclude that the wire bands could be strongly hybridized with surface bands. For instance, such a hybridization is discussed for Luttinger liquids and electronic CDW in section 1.5.

The atomic wire systems that are possible realizations of quasi-1D electronic systems build clearly anisotropic atomic structures on the substrate surfaces and can be seen as 2D arrays of chains. In addition, some systems exhibit strongly anisotropic electronic properties, e.g. a much broader dispersion in the chain direction than in the perpendicular direction (parallel to the surface). Thus dynamical confinement is expected to play a role for the directions parallel to the surface.

Assuming a strictly 2D tight-binding model for a rectangular lattice with constants a and b , the corresponding dispersion of single-electron Bloch states has the form

$$\epsilon(\vec{k}) = -2t_x \cos(k_x a) - 2t_y \cos(k_y b) \quad (5)$$

with the wave vector $\vec{k} = (k_x, k_y) \in \mathbb{R}^2$. This dispersion interpolates smoothly between strictly 1D electron gas with the dispersion (4), which is recovered for $t_y/t_x \rightarrow 0$, and a 2D isotropic electron gas, which is obtained for $t_y = t_x$ and $a = b$. Therefore, this dispersion will be the starting point for the discussion of electronic properties in atomic wires on surfaces. In summary, the relevant electronic degrees of freedom in atomic wires on semiconducting substrates are confined spatially at the surface and dynamically in the anisotropic 2D array of wires.

1.2.4. Models and methods

Textbook models of solids describe electrons in Bloch states moving in a crystalline atomic structure and coupled to adiabatically slow lattice vibrations, while interacting weakly with one another due to their Coulomb repulsion. These simplified models suffice to explain the common properties of normal metals, semiconductors, insulators and superconductors [76,77]. In addition magnetic insulators can be described with models including localized electron spins as the only relevant degrees of freedom. Many existing materials are not covered by these basic models, however.

A difficulty for the theory of 1D solids is that common theoretical methods and approximations break down. For instance, mean-field approximations often predict the existence of symmetry-breaking long-range-ordered phases that contradict the Mermin-Wagner theorem [13] or exact solutions of low-dimensional models. As a second example, perturbation expansions often diverge because of the instability of 1D systems. These issues are explained in detail in section 1.3. Consequently, the validity of theories relying on these methods is questionable in low dimensions, for instance, Landau's theory of the Fermi liquid in metals [28,30,45]. Thus the theoretical description of quasi-1D materials require concepts, models and methods taking into account strong correlations as well as (quantum and thermal) fluctuations, which goes beyond the content of most solid-state textbooks [6,7,28,30].

In principle, most properties of solids are determined by the quantum Hamiltonian for electrons and nuclei coupled by the Coulomb interaction. As this many-body problem is not tractable for more than a couple of atoms and nuclei, solid properties have to be calculated using various approximations. A widely used and very successful approach is the numerical computation of these properties from the full Hamiltonian using various numerical schemes (*ab initio* or first-principles methods), most often based on the density functional theory (DFT) [78,79].

A different approach is to reduce the full Hamiltonian problem to a more "simple" effective model or theory including the most relevant degrees of freedom and interactions for a selected question while neglecting the less relevant ones [31]. The goal of this approach is to understand some generic physical phenomena within the simplified model rather than to achieve a full description of a material. Various effective models and theories have become de facto standards for specific aspects of the theory of quasi-1D electron systems. In this section some aspects of the two most important approaches are reviewed: lattice models and field-theoretical approaches. See Ref. [80] for a review of the connections between *ab initio* calculations and effective model studies.

1.2.4.1. Lattice models. Effective lattice models are usually extensions of the tight-binding model. They can describe quasi-1D electron systems with a dynamical confinement, i.e. with an electronic structure similar to Eq. (3), but strictly 1D models are often investigated. A well-known example is the Su-Schrieffer-Heeger (SSH) model [61,62] introduced to describe the Peierls insulating state of π -conjugated polymers [2,9,18,

34]. Other well-known models were originally developed to study properties of 3D solids, but are also routinely investigated in other dimensions. They include the Hubbard model [81] for locally interacting electrons, which describe correlated phases of matter such as Luttinger liquids, Mott insulators, and antiferromagnetic SDW [28], the Holstein molecular crystal model [82] and the Fröhlich model [83,84], which describe the role of the electron-phonon coupling in Peierls-CDW states, and the Heisenberg model [85] for localized spin systems, which plays an important role in the theory of quantum magnetism, including 1D magnetism and SDW [4,69,70]. Finally, the Ising model [12] is a cardinal model in statistical mechanics, in particular for phase transitions in reduced dimensions [7].

A systematic method for deriving effective lattice models does not exist. In principle, these models can be deduced from first-principles Hamiltonians using cornerstones of solid-state physics such as the Born-Oppenheimer approximation, the frozen-core approximation, the tight-binding approximation, etc. Extensive justifications of the most important models can be found in the literature, e.g. the SSH model [34, 60] and the Hubbard model [34,86]. In practice, effective models are often based on phenomenological considerations and handwaving arguments. Model parameters are usually inferred from experimental data. In some cases they can be determined from first-principles simulations, as done for the extended 1D (two-band) Hubbard model representing metallic TTF-TCNQ [87] and for a generalization of the 1D SSH model for In/Si(111) [52].

As explained in the introduction, a major motivation for studying low-dimensional systems is that they are “simpler” than their 3D counterparts. In fact, several low-dimensional lattice models are exactly solvable. For instance, the properties of the 1D spin-1/2 Heisenberg model can be determined with the Bethe Ansatz [88] and this method has been extended to obtain the eigensystem of the 1D Hubbard model [89,90], the occurrence of Peierls-CDW ground states has been proven exactly for a generalization of the SSH model [91,92], and the thermodynamics of Ising model is exactly solvable in one dimension [12] and on a square lattice [93]. These exact results provide us with some of the best paradigms for the unusual properties of low-dimensional systems.

As most models are not exactly solvable, numerous approximate analytical and numerical methods have been used to study lattice models. In particular, two types of numerical methods have proven to be reliable and versatile tools for investigating effective lattice models for quasi-1D systems: classical and quantum Monte Carlo (QMC) simulations [94–96] and the density-matrix renormalization group (DMRG) [97–101]. Together they allow us to calculate almost any quantities of interest in finite-size 1D lattice models. When applied to quasi-1D electron models, QMC simulations are mostly limited by statistical errors, which are most significant close to phase transitions, while DMRG computations are limited by the system long-range entanglement, which grow rapidly when the system is not strictly 1D. Naturally, both methods can also be used in higher dimensions but the computational cost increases rapidly. Thus only relatively small systems can be simulated and finite-size effects often hinder the interpretation of the numerical data. In particular, no reliable method is available to treat large strongly-correlated 2D electron systems. Nevertheless, these numerical methods have been successfully adapted to study quantum lattice models representing atomic wires on surfaces. For instance, the DMRG method can be used to study the effects of the substrate and the inter-chain coupling on Luttinger liquids and electronic CDW, as discussed in sections 1.5 and 1.7.

1.2.4.2. Field-theoretical approaches. Field theory is commonly used to investigate the low-energy long-wavelength limit (i.e., the continuum limit in real space) of 1D electron systems. In contrast to lattice models this approach does not suffer from finite-size effects but it is not applicable to the short-length physics (i.e., of the order of the lattice

constants). Thus theoretical studies based on effective lattice models and field-theoretical approaches are often complementary.

The most well-known example of quantum field theory in one dimension is the Luttinger-liquid theory for 1D conductors [11] based on the Tomonaga-Luttinger model [102,103]. A generalization (called *g*-ology) describes the generic low-energy long-wavelength physics of interacting electrons in one dimension including symmetry-breaking phases [33]. The derivation of quantum field-theoretical models (i.e. Tomonaga-Luttinger model and its extensions) from the weak-coupling limit of effective lattice models is explained in detail in many publications [6,33,104]. It is very difficult to determine parameters for field-theoretical models from first-principles Hamiltonians. For instance, this has been done for the Luttinger liquid parameters describing single-channel quantum wires using quantum Monte Carlo simulations [105,106]. As for effective lattice models, reasonable parameter ranges for field-theoretical models are usually inferred from experimental data.

Like for lattice models, 1D field-theoretical models are often “simpler” than their counterpart in higher dimensions. For instance, the Tomonaga-Luttinger model [102,103] is exactly solvable using bosonization and provides us with the paradigm for the Luttinger liquid behavior of 1D metals [11]. Field-theoretical methods such as bosonization and renormalization group are often used to analyze the low-energy properties of more general strongly-correlated 1D systems [6,33]. They provide us with accurate results for the phase diagram as well as information about the low-energy excitations. Most of the “universal” properties of 1D systems, such as the power law in the single-particle density of states of a Luttinger liquid, have been obtained using these approaches. For 1D systems with several potentially gapless modes (e.g., ladder and nanotube systems) and for systems in higher dimensions (e.g. coupled wire systems), bosonization and renormalization group become sophisticated and demanding techniques that usually requires additional approximations to obtain physical results [6,107]. Thus the predictions of these field-theoretical studies are less conclusive than in one dimension (Basic results are discussed in sections 1.3 and 1.4.).

Another type of field-theoretical approach is the Ginzburg-Landau theory of broken-symmetry phases found in quasi-1D materials [4,5, 28,108,109]. Generalizations of the Ginzburg-Landau theory of superconductivity [110,111] have been used to model a wide variety of physical systems [112]. They can be seen as simple applications of the more sophisticated statistical field theory [113–116]. In the context of quasi-1D materials this classical field theory allows us to study thermal and spatial fluctuations as well as the nonequilibrium dynamics in long-range ordered CDW and SDW phases in the continuum limit. In practice, generalized Ginzburg-Landau equations describe the long-wavelength variations of the order parameters. Model parameters can often be determined from mean-field solutions of the effective lattice models mentioned above. This approach provides theoretical interpretations for numerous experimental observations in the quasi-1D crystalline materials discussed previously.

As with the other theoretical approaches discussed above, 1D versions of the Ginzburg-Landau equations are simpler than their 3D counterparts and numerous analytical results have been obtained. Renormalization group [113–115,117] and numerical methods such as Monte Carlo simulations [118] are used for more complicated cases, e.g., to describe fluctuation effects quantitatively. For instance, the Ginzburg-Landau formalism can be used to investigate the effects of thermal fluctuations on Peierls-CDW transitions. As the time-evolution of order parameters can be described within the Ginzburg-Landau formalism, this approach has been extensively used to study collective excitations of electronic and phononic degrees of freedom as well as the electrodynamics of CDW and SDW in quasi-1D materials [4]. Basics of the nonequilibrium Ginzburg-Landau theory are introduced in sec. 1.6.3.

1.3. Theory of strictly one-dimensional electron systems

In this section we will review basic theoretical concepts and results about strictly 1D electron systems. This includes the instability of the 1D electron gas (section 1.3.1), various broken-symmetry phases occurring in 1D electron systems (section 1.3.2), a couple of non-metallic homogeneous phases (section 1.3.3), the suppression of spontaneous symmetry breaking by fluctuations (section 1.3.4), and the theory of 1D metals (section 1.3.5).

A system is said to be strictly one-dimensional if its 3D environment is nonreactive. Thus the degrees of freedom of a strictly 1D system may be confined by an atomic structure, be under the influence of external fields such as an electromagnetic field, and be in equilibrium with a heat bath or particle reservoirs. However, the 3D world does not react to the states of the 1D degrees of freedom. In particular, interactions between wires or chains are not taken into account. This theoretical idealization paves the way toward understanding the special physics that is found in quasi-1D materials.

1.3.1. $2k_F$ instability of the 1D electron gas

Consider an electron gas under the influence of a static but spatially oscillating electric field. If we neglect the Coulomb interaction between electrons and any coupling between electrons and lattice degrees of freedom, its linear response is characterized by the charge susceptibility

$$\chi(\vec{Q}, T) = -\frac{2}{N} \sum_{\vec{k}} \frac{f(\epsilon(\vec{k} + \vec{Q})) - f(\epsilon(\vec{k}))}{\epsilon(\vec{k} + \vec{Q}) - \epsilon(\vec{k})} \quad (6)$$

where \vec{Q} is the wave vector of the electric field, $f(\epsilon)$ is the Fermi-Dirac distribution at temperature T , $\epsilon(\vec{k})$ is the single-electron eigenenergy dispersion, the sum runs over all wave vectors \vec{k} in the first Brillouin zone, and N is the number of these vectors.

In one dimension [1,3,4,6,58] we can show that this susceptibility diverges logarithmically at zero temperature for $|Q| \rightarrow 2k_F$

$$\chi(Q, T=0) \sim \ln \left| \frac{Q + 2k_F}{Q - 2k_F} \right| \quad (7)$$

where $k_F = \frac{\pi n}{2a}$ is the Fermi wave number of the 1D electron gas. The electronic density n corresponds to the number of electrons per site in a 1D tight-binding model. Moreover, one can show that the susceptibility diverges logarithmically at $Q = \pm 2k_F$ for $T \rightarrow 0$

$$\chi(Q = 2k_F, T) \sim \ln \left(\frac{W}{k_B T} \right) \quad (8)$$

where W is proportional to the 1D bandwidth, e.g. $W = 4t_x$ if one assumes the dispersion (4).

Thus any small perturbation of the 1D electron gas by an electric field generates a large charge density distortion. This is a manifestation of the $2k_F$ instability of the 1D electron gas. This instability occurs for other observables such as the magnetic susceptibility and for integer multiples of $2k_F$. It is responsible for many of the unusual properties of 1D electron systems, which are discussed below, such as the occurrence of various non-metallic phases as well as the failure of perturbation expansions and the breakdown of the Fermi liquid theory.

The $2k_F$ instability is due to the perfect nesting of the Fermi “surface” in a 1D one-band electron gas. The analysis is more complicated if the system has more than one band with different Fermi wave numbers but an instability is always present. For instance, if the system has two bands with Fermi wave numbers k_F and k'_F , there is perfect nesting for $|Q| = |k_F \pm k'_F|$. Similarly, for a 2D system with weak interchain dispersions, e.g. $|t_x| \gg |t_y|$ in Eq. (5), the instability occurs for $\vec{Q} = (\pm 2k_F, \pi/b)$.

1.3.2. Long-range ordered phases

The $2k_F$ instability leads to numerous competing phases in 1D electron systems when the Coulomb interaction between electrons or the coupling between electrons and lattice degrees of freedom are taken into account [1,3,4,6,28,33,58]. Some of these phases are characterized by the spontaneous appearance of a long-range order that breaks a symmetry of the system Hamiltonian. We summarize in this section some basic results about prominent 1D long-range ordered phases, namely CDW and SDW, which are relevant for the quasi-1D crystalline materials or for atomic wires on surfaces. Some non-metallic phases without long-range order are presented in the next section.

Our theoretical knowledge of the competing 1D phases is mostly based on the effective models and methods discussed in section 1.2.4. The possible long-range ordered phases are easily revealed using mean-field approximations although this approach does not allow us to determine the dominant phase and its properties reliably. This is due to the importance of thermal and quantum fluctuations in low-dimensional systems. In a strictly 1D theory, fluctuations completely destabilize long-range-ordered states for any temperature $T > 0$. In quasi-1D crystalline materials, however, the 3D interchain coupling may stabilize the long-range order at low temperatures. Here we discuss the unusual properties of 1D long-range-ordered phases assuming that they are stable. The effects of fluctuations and the coupling to the 3D environment are discussed in detail in later sections and will justify this approach.

1.3.2.1. Charge density waves. The 1D electron gas is unstable against the formation of a charge density wave (CDW) [4,5,17,108].

$$\rho(x) = \rho_0 + \delta\rho \cos(Qx + \varphi) \quad (9)$$

with the wave number $Q = 2k_F$ (or integer multiples thereof), an amplitude $\delta\rho$, and a phase φ . A long-range-ordered CDW is sketched in Fig. 3. Typically, the order parameter is written as a complex number $\Delta \exp(i\varphi)$ with an amplitude Δ proportional to the charge modulation amplitude $\delta\rho$. Spatial and temporal variations of the order parameter can be induced by thermal fluctuations in equilibrium or by external perturbations such as in transport and spectroscopy experiments. Fluctuations and dynamics are often described by variations of the amplitude Δ and the phase φ with position and time within the Ginzburg-Landau approach [4,108].

A CDW is said to be commensurate if the ratio between the wave number Q and the reciprocal lattice “vector” G is a rational number. In that case, the phase φ can take only a finite number of different values and the ground state degeneracy is finite. Consequently, the order parameter is discrete. Commensurate CDW are usually studied in lattice models with particular band fillings, e.g. for half filling $2k_F = \pi/a = G/2$. A CDW is incommensurate if G/Q is irrational or in any continuum model. In that case, φ can take any real value and the ground state is infinitely degenerate. Commensurate CDW are usually stronger than

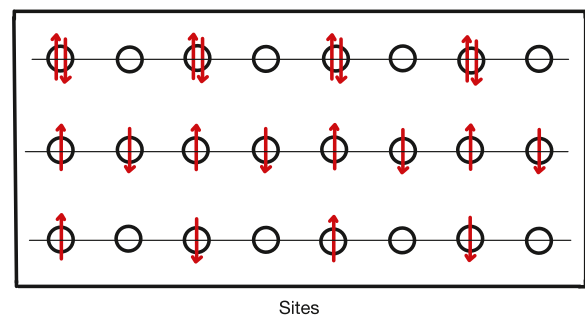


Fig. 3. Sketch of a $2k_F$ -CDW in a half-filled lattice (top), an antiferromagnetic $2k_F$ -SDW in a half-filled lattice (middle), and a $4k_F$ -CDW with $2k_F$ -SDW in a quarter-filled lattice (bottom). Each circle represents one site while each arrow represents one electron (with up or down spin).

incommensurate ones. The first reason is that an incommensurate CDW often means breaking a continuous symmetry, which is suppressed by fluctuations in strictly 1D systems. The second reason is that commensurate CDW often involve Umklapp scattering processes that enhance interaction effects (i.e., $2k_F = G$ or $4k_F = G$ in a half-filled or quarter-filled lattice model, respectively). For instance, the SSH model and its generalizations undergo a transition from a commensurate to an incommensurate Peierls-CDW ground state upon varying the electronic density away from half filling [18,63,64]. This weakening of the CDW is believed to play a role in the metal-insulator transition observed in polyacetylene. Undoped π -conjugated polymers are well-known examples of commensurate CDW in real materials while incommensurate CDW are realized, among others, in the MX_3 family of quasi-1D crystalline materials.

A CDW state may be driven by the electron-electron interaction [119, 120]. We will call these states electronic CDW. (They are sometimes called charge ordering). This CDW type is found in the spinless fermion model [6], the extended Hubbard model [121], and the interacting electron gas (g-ology) [5,6,33]. A very strong electronic CDW can be seen as a 1D Wigner crystal [122,123]. CDW may also be driven by the electron-phonon interaction [1,4,5]. In that case the CDW is accompanied by a lattice distortion with the same wave number Q as the density modulation and thus a softening of the corresponding phonon mode (or at least a significant Kohn anomaly) [1,5]. If the wave number is $Q = 2k_F$, this is completely equivalent to Peierls instability [10] and thus we will call this CDW type a Peierls-CDW. Peierls-CDW are found in the Holstein model [124,125] and the SSH model [18,34,91,92]. Note that the term CDW is sometimes reserved for ionic density modulations as found in the Holstein molecular crystal model [82] while the designation bond order wave (BOW) is used for covalent bond density modulations as found in the SSH model [61,62].

In real materials both electron-electron and electron-phonon interactions play a significant role. Their combined effects can be studied with generalized 1D effective models (See ref. [126] for a recent study using *ab initio* simulations.). In particular, one finds that both mechanisms can cooperate to build a CDW state [63] or compete to build different ground states [127]. In the Peierls-Hubbard model one even observes that the interplay of these interactions changes with the band filling, from cooperating at half filling to competing away from half filling [63,64].

Typically systems with a CDW ground state undergo a transition from the CDW phase (order parameter $\Delta \neq 0$) at low temperature to a uniform metallic phase at high temperature ($\Delta = 0$). They exhibit unusual excited-state properties in the low temperature phase although they have a gap in their single-electron excitation spectrum, which corresponds to the gap seen in STS or ARPES experiments. The gap width is proportional to the amplitude of the order parameter Δ . Thus it is a soft gap that varies with temperature and vanishes above the critical temperature for the CDW phase. The dispersion of single-particle excitations (electrons and holes) has the typical form

$$\epsilon(k) = \pm \sqrt{\Delta^2 + (\hbar v_F k)^2} \quad (10)$$

in the long-wavelength limit $k \rightarrow 0$ with the Fermi velocity in the metallic phase v_F .

However, the low-energy physics of CDW states is determined by collective excitations combining many electrons (and the lattice degrees of freedom for Peierls-CDW) rather than single-electron excitations. In commensurate CDW the low-energy excitations can be visualized as mobile domain walls in the charge ordering where the phase φ jumps between two allowed discrete values. This domain walls are known as solitons in the theory of π -conjugated polymers [18,34,61,62]. These collective excitations can display the separation of elementary spin and charge excitations that characterized 1D metals, e.g. in the form of charged and neutral solitons in the SSH model and its generalizations. Incommensurate CDW states exhibit gapless collective sliding modes

corresponding to a continuous change of their phase φ (phason) [1,4, 108]. Their dispersion has the form of “sound” waves $E(k) = \hbar u |k|$ with a velocity u . In principle, a sliding mode could transport charge without dissipation and this was proposed as a possible mechanism for 1D superconductivity [128]. In real CDW materials, however, sliding modes are pinned by the interchain coupling and disorder. Nevertheless they are responsible for non-linear effects in the charge dynamics of CDW “conductors” below the energy threshold set by the single-electron gap (e.g., the transport at finite electric field in the MX_3 compound NbSe_3) [1,4,8,67,108]. Finally, variations of the Peierls-CDW amplitude Δ also correspond to collective excitations, which are visible as vibrational modes in Raman spectroscopy [4,118,129,130].

The theory of 1D CDW is often invoked when discussing the properties of atomic wires on surfaces. For instance, a Peierls-CDW has been proposed to explain the insulating state observed below 120 K in indium wires on the Si(111) surface [16,46,52]. The occurrence of topological solitons in this system has also been discussed [131–137] based on the SSH theory which was originally developed to explain the properties of conjugated polymers [18,34,61,62].

1.3.2.2. Spin density waves. The 1D electron gas is also unstable against the formation of spin density waves (SDW) [4,28]. The simplest SDW is given by

$$S(x) = \mathcal{S} \cos(Qx + \varphi) \quad (11)$$

where $S(x)$ is the magnetization (expectation value of the electron spin operator) along a given axis. Alternatively, as 1D SDW are typically antiferromagnetically ordered, $S(x)$ can represent the staggered magnetization. A long-range-ordered antiferromagnetic SDW is sketched in Fig. 3. As the theory of SDW is very similar to the theory of CDW, only a couple of specific features are summarized here.

Commensurate and incommensurate SDW-ordered states play an important role in quasi-1D crystalline materials, in particular in Bechgaard and Fabre salts (see the phase diagram in Fig. 1), and their properties have been extensively investigated in that context [3–5,17, 109]. In atomic wire systems, experiments have shown that a large spin-orbit coupling and strong electronic correlations lead to the formation of a spin-ordered phase in Pb wires grown on Si(557) surfaces [138,139], but it is not clear whether this material can be seen as a quasi-1D system. This material is discussed in sec. 2.4.

The designation SDW is usually reserved for magnetic order driven by the electron-electron interaction or the resulting exchange interaction. In a system of localized electrons with gapped charge excitations but at least one gapless spin mode (e.g., a Mott or CDW insulator), a magnetoelastic coupling can lead to a magnetic ordered phase called a spin-Peierls phase [17,58]. This is analogous to the Peierls state but it involves the electron spin instead of its charge. This state is characterized by a spin density modulation (typically a dimerization as pairs of nearest-neighbor spins build singlets) and it is accompanied by a lattice distortion as well as a soft phonon mode (or a Kohn anomaly). The spin-Peierls phase is probably the most convincing realization of 1D physics in real materials. For instance, the existence of this phase is clearly established in the most anisotropic molecular salts of the TMTTF family [58,140,141] (the lower left corner of the phase diagram in Fig. 1) and in the copper oxide compound GeCuO_3 [71,72].

Finally, we note that CDW and SDW orders can coexist in electron systems, either as true long-range order or as quasi-long-range order [4, 6,120]. A well-known theoretical example is the coexistence of CDW with $Q_C = 4k_F$ and SDW with $Q_S = 2k_F$ in quarter-filled lattice models [142,143], which is illustrated in Fig. 3. Moreover, this coexistence is invoked to explain experimental observations in some quasi-1D crystalline materials [58]. Interestingly, unpaired electron spins can become spontaneously localized at silicon step edges and antiferromagnetically ordered according to first-principles simulations of gold chains on the Si(557) surface [144]. These charge and magnetization modulations can

be seen as the combination of a $4k_F$ -CDW and an antiferromagnetic $2k_F$ -SDW. STM and STS experiments for Au/Si(553) have confirmed the CDW-like localization of charges at the step edges, but the magnetic order has not been observed directly yet [145,146]. This material is discussed in sec. 2.2.

1.3.3. Disordered non-metallic phases

The instability of the 1D electron gas can lead to the formation of non-metallic phases without long-range order or broken symmetry. Two important phases of this type are briefly discussed here: the Mott-Hubbard insulator and the Luther-Emery liquid.

In a Mott insulator electrons are localized without breaking any symmetry by their mutual Coulomb repulsion in a partially filled band [86,147–149]. Thus all charge excitation modes are gapped with the dispersion of eq. (10). This so-called Mott gap exists at all temperatures and thus is a hard gap contrary to the soft gaps found in 1D CDW and SDW phases. A paramagnetic Mott insulator is found in the exactly solvable half-filled 1D Hubbard model with the non-interacting dispersion of eq. (4) for any strength of the on-site Coulomb repulsion $U > 0$ because of Umklapp scattering [89,90]. Without Umklapp scattering (e.g. with long-range hopping terms) a Mott-Hubbard metal insulator occurs at finite coupling U equal to the bandwidth W [150]. Spin excitations remain gapless as in the isotropic 1D Heisenberg model [6,69,70]. Thus the spin degrees of freedom can be seen as a Luttinger liquid with a quasi-long-range antiferromagnetic order as explained below. This phase is usually called a Mott-Hubbard insulator. The concept of Mott insulators has been used to explain the properties of various quasi-1D crystalline materials such as Bechgaard salts [6], π -conjugated polymers [34], and copper oxide compounds [149]. A Mott insulator state has also been realized in ultracold Bose gases in 1D optical lattices [26,27].

The Luther-Emery phase of a 1D electron system is characterized by gapless charge excitations and gapped spin excitations with the dispersion of eq. (10) [6,151]. It exhibits a quasi-long-range pairing order in the charge sector. For instance, it is realized in the 1D half-filled Hubbard model with attractive interaction. A Luther-Emery phase has not been observed in any real materials but it is nonetheless important from a theoretical point of view. First, it competes directly with other phases such as Luttinger liquids and Peierls-CDW in strictly 1D electron-phonon models, e.g. in the Holstein model and its generalizations [152,153]. Thus it may be relevant when discussing the occurrence of Luttinger liquids and Peierls-CDW in quasi-1D crystalline materials and atomic wire systems. Second, the Luther-Emery state can be regarded as the 1D precursor for superconducting phases in higher dimensions. A superconducting phase is a state with gapped spin excitations and at least one gapless charge excitation mode but also with a long-range off-diagonal pairing order corresponding to a broken $U(1)$ gauge symmetry. Thus a true superconducting phase cannot exist in a 1D electron systems, even at zero temperature, as explained in the next section. Nevertheless, a few quasi-1D crystalline materials are known to become anisotropic superconductors under pressure, in particular some Bechgaard salts [3,58] and cuprate ladder compounds [154]. This is understood as a crossover from 1D to higher dimensions as illustrated in the phase diagram in Fig. 1. Therefore, theorists search for Luther-Emery phases in 1D models of superconductors as a possible signature of superconductivity in the higher-dimensional counterparts, e.g. for the superconducting cuprates [155].

Finally, it should be kept in mind that many other principles of 3D solid-state physics that are not discussed here may require adaptation when apply to 1D electron systems. For instance, it is well known that spin and charge transport properties depend sensitively on disorder (impurities and lattice imperfections) in any dimension, but strictly 1D systems can become (Mott-)Anderson insulators in the presence of any weak disorder due to the so-called Anderson localization [156,157].

1.3.4. Absence of long-range order

As discussed above, a purely 1D electron gas is unstable with respect to states with a $2k_F$ modulation. Within mean-field approximations various phases with spontaneous symmetry-breaking long-range orders, such as CDW, SDW, spin-Peierls, or superconducting phases, can appear in the ground state and at low temperatures. However, mean-field approximations break down in one dimension. Indeed, exact results and more reliable approximations show that mean-field phases are unstable with respect to thermal fluctuations in strictly 1D systems.

Besides the system dimension, the nature (discrete or continuous) of a broken symmetry influences the phase stability at finite temperature. A symmetry can be continuous (e.g. a rotation symmetry) or discrete (e.g. a reflection symmetry). For instance, a SDW would break the continuous $SU(2)$ symmetry in the 1D Hubbard model [81,90] while a Peierls-CDW/BOW only breaks discrete symmetries of the electron and lattice degrees of freedom in the SSH model [18,34,61,62].

The Mermin-Wagner theorem [13,158] is probably the best-known mathematically exact result in the theory of phase transitions in reduced dimensions. It forbids ordered phases that break continuous symmetries at finite temperature in less than three dimensions, by showing that they are destabilized by long-wavelength fluctuations. Strictly speaking Mermin and Wagner only showed that “*at any nonzero temperature, a one- or two-dimensional isotropic spin-S Heisenberg model with finite-range exchange interaction can be neither ferromagnetic nor antiferromagnetic*”. However, their method of proof, which is based on the Bogoliubov inequality, has been successfully applied to many models. Thus it is generally accepted that the lower critical dimension is 2 for ordered phases with broken continuous symmetries [113–116].

The Mermin-Wagner theorem does not apply to phases breaking only discrete symmetries. Nevertheless, it is generally accepted that long-range-ordered phases with broken discrete symmetries do not occur at finite temperature in strictly 1D systems with finite-range interactions. First, according to statistical field theory (treating thermal fluctuations within the framework of the Ginzburg-Landau theory) the lower critical dimension is 1 for spontaneously broken discrete symmetries [113–116]. Second, exact solutions of strictly 1D models do not reveal any ordered phases with discrete symmetry breaking for $T > 0$. For instance, the exact solution of the 1D Ising model is paramagnetic for all non-zero temperatures [12].

Therefore, thermal fluctuations prevent the existence of spontaneous long-range order at any finite temperature in one dimension in all realistic models. Magnetic moments do not align ferromagnetically, electrons do not superconduct, Bose-Einstein condensation does not occur, and liquids do not freeze in one dimension [7]. The peculiar phases that we discussed in sec. 1.2.2 and 1.3.2 do not exist in strictly 1D systems at $T > 0$. It is the coupling of 1D electron systems to the 3D environment that makes possible the experimental observation of symmetry-breaking Peierls, CDW or SDW phases in quasi-1D materials at finite temperature. This will be discussed in detail in later sections.

Additionally, it should be noted that the Mermin-Wagner theorem and statistical field theory only disallow symmetry-breaking ordered phases in equilibrium in the thermodynamic limit. They do not necessarily exclude the existence of metastable symmetry-breaking orders in finite-size samples or over a finite time span. The relevant size and time scales can be macroscopically large for real physical systems [159]. For instance, in the 1D Ising model with ferromagnetic exchange coupling $J > 0$, correlations between two spins decrease exponentially with the distance. The correlation length $\xi = 1/\ln(\coth(J/k_B T))$ diverges for $T \rightarrow 0$. Thus a segment of finite length L can appear to be ferromagnetically ordered when the temperature T is low enough, i.e. for $L \ll \xi \Rightarrow k_B T \ll 2J/\ln(2L)$. As an experimental example, 1D superconductivity can be observed in carbon nanotubes although the superconducting phase breaks the continuous electromagnetic gauge symmetry [160,161]. Thus one should always evaluate the relevant size and time scales to determine whether a symmetry-breaking order can be observed in finite-size regions of a material over the time scale of a given

experiment.

As neither the electron gas nor long-range-ordered phases are stable, the question arises as to which kind of states occurs in strictly 1D models. Typically, the (mean-field predicted) long-range order is replaced by a quasi-long-range order. A state with a quasi-long-range order (or long-range fluctuations) exhibits a slow (power-law) decay of correlation functions at long distance and a divergent response function (susceptibility) for the operators characterizing the order. In strictly 1D systems this gapless state is usually a Luttinger liquid, which is discussed in the next section. For instance, the ground-state spin correlation function of the antiferromagnetic spin-1/2 Heisenberg chain has been determined using field-theoretical methods [162,163]. It behaves for asymptotically large distance m as

$$\langle \vec{S}_n \vec{S}_{n+m} \rangle \sim \frac{(-1)^m}{m} \ln(\text{const.} \cdot m). \quad (12)$$

the slowest decaying correlation functions or the strongest diverging response function defines the so-called dominant correlations (or fluctuations).

1.3.5. Theory of 1D metals

Another essential feature of 1D physics is the breakdown of the Fermi liquid theory in 1D metals and the importance of the Luttinger liquid phenomenology for all 1D gapless excitation modes. Numerous introductions to the Luttinger theory have been published [28–30,32,104,164,165]. More detailed presentations can be found in Refs. [6,33,45,166].

1.3.5.1. Breakdown of the Fermi liquid theory. Landau's theory of the Fermi liquid is a cornerstone for our understanding of ordinary (3D) metals [28,30,45,165]. It explains why many properties of the strongly interacting conduction electrons can be explained using models of weakly-interacting fermions. More precisely, the Fermi liquid theory assumes that the low-energy excitations of an interacting electron system can be mapped onto the low-energy excitations of a fermionic quasiparticle system with weak residual interactions. The residual interactions can be treated with perturbative methods such as the random-phase approximation (RPA). One finds that the low-energy excitation spectrum of 3D and 2D metals is dominated by a continuum of single-fermion excitations called Landau quasiparticles, in agreement with the initial assumptions. (Strictly speaking the Fermi liquid is unstable at sufficiently low temperature but this is not relevant experimentally for ordinary metals [167].) Collective excitations of the charge and spin degrees of freedom (called plasmons and magnons, respectively) are also present.

This approach breaks down in one dimension because scattering processes transferring finite momenta cause the Fermi liquid to be unstable for any weak residual interactions [28,30,45,166]. (Similar scattering processes cause the $2k_F$ instability of the electron gas.) For instance, the calculation of dynamical response functions within the RPA framework shows that for low energies and long wavelengths quasiparticles are unstable, which contradicts the initial assumptions of the Fermi liquid theory. Instead, plasmons and magnons are the stable elementary excitations. Note that they have dispersions $E(k) \propto |k|$, which turns out to be qualitatively correct (see below) even though the overall result is inconsistent with the initial assumption.

1.3.5.2. Luttinger liquid theory. Forty years ago Haldane conjectured that gapless excitation modes in strictly 1D fermion systems always follow the phenomenology of the Tomonaga-Luttinger model (TLM) at low energy and named this “universality” class Luttinger liquids [11]. The TLM [102,103] describes a system of interacting fermionic charges in one dimension. (Spin degrees of freedom are neglected in this first step.) It is obtained through linearization of the fermion dispersion, Eq. (2) or (4), around its two Fermi points, $\epsilon(k) = \epsilon_F \pm \hbar v_F(k \mp k_F)$, see Fig. 2.

Moreover, the Coulomb interaction between charges is represented by a subset of the scattering processes only (forward/backward scattering).

Thanks to these simplifications the TLM is exactly solvable because it can be mapped onto a system of noninteracting bosons using a field-theoretical technique called bosonization [168]. The excitation spectrum is characterized by gapless collective bosonic excitations describing density waves of the original fermionic degrees of freedom. Their dispersion is linear

$$E(k) = \hbar u |k| \quad (13)$$

with a renormalized velocity u . This is completely similar to acoustic phonons, which are bosonic degrees of freedom representing the low-energy long-wavelength excitations of atom nuclei in a crystal (sound waves). For this reason the elementary excitations of a Luttinger liquid are also called “sound” waves. As the displacement of a single atom nucleus corresponds to a superposition of coherent and squeezed acoustic phonon states, a quasiparticle excitation corresponds to an (unstable) superposition of coherent and squeezed bosonic excitations in a Luttinger liquid.

Besides the eigenenergy spectrum, static and dynamical correlation functions can also be calculated from the solution of the TLM. One finds that the physics of the Luttinger liquid is fully described by two parameters: the renormalized velocity $u > 0$ and a Luttinger parameter $0 < K < \infty$. Well-known examples of Luttinger liquid properties are the power-law behavior of the density of states at the Fermi energy

$$D(\epsilon) \propto |\epsilon - \epsilon_F|^\alpha \quad (14)$$

with an exponent $\alpha = (K + K^{-1} - 2)/2$ [6,29,32] and the renormalization of the conductance quantization $G = Kq^2/h$ with the charge q carried by one fermionic particle [169–171]. The vanishing of the density of states at the Fermi energy reflects the instability of single-particle excitations in the interacting system (i.e. for $K \neq 1$). Both features can be observed in the spinless fermion model [172,173].

The Tomonaga-Luttinger approach can be generalized to include several excitation modes, spin degrees of freedom, and more general interactions [33]. Although the generalized models are no longer exactly solvable by bosonization alone, field-theoretical methods, in particular renormalization group studies, confirm that their gapless modes are Luttinger liquids [6,33,166]. Note that the parameters u and K can be different for each excitation mode.

Similarly, the Hamiltonians of strictly 1D lattice models for interacting fermions (see sec. 1.2.4) can be mapped onto these generalized TL models using the linearization of the fermion spectrum around the Fermi energy and the renormalization group. (Technically, the TLM is a fixed point of the renormalization flow for a large class of Hamiltonians.) Once the mapping is achieved, one obtains an asymptotically exact description of the low-energy long-wavelength gapless excitations of the original Hamiltonians. This description is said to be universal because it does not depend on the Hamiltonian details but only on the parameters u and K for each gapless mode. A priori, the linearization (and thus the mapping) is only valid for weak Coulomb interactions that only scatter fermions close to the Fermi points. However, field-theoretical calculations and exact solutions of 1D models confirm that the Luttinger liquid phenomenology applies to gapless modes regardless of the interaction strength. Moreover, Haldane's conjecture is supported by all known exact solutions of strictly 1D fermion models with gapless excitation modes such as the Hubbard chain away from half-filling [6,90].

Therefore, it is well accepted that the Luttinger liquid theory describes the universal low-energy long-wavelength behavior of any gapless excitation mode in a strictly 1D many-fermion system. As any 1D conductor must possess at least one gapless charge excitation mode, it is a Luttinger liquid according to Haldane's conjecture. Experimental observations of Luttinger liquid signatures have been reported for numerous quasi-1D conductors, in particular for the quasi-1D crystalline materials [17] (discussed in sec. 1.2.2) and in atomic wires on

semiconducting surfaces [15] such as Au/Ge(100) [37], Bi/InSb(001) [174] and Pt/Ge(001) [175].

Moreover, decades of research suggest that the Luttinger liquid phenomenology applies to all gapless excitation modes in strictly 1D quantum many-body systems. Thus the term Luttinger liquid is also used for systems with other degrees of freedom than fermions. For instance, the Luttinger liquid theory describes the low-energy gapless excitations in spin chains such as the Heisenberg model [6,69]. As a second example, the Luttinger phenomenology has been observed experimentally in 1D ultracold atomic Bose gases by probing density profiles and sound propagation [176].

1.3.5.3. Properties of electronic Luttinger liquids. A 1D metal must possess (at least) one gapless charge mode and one gapless spin mode. According to Haldane's conjecture it is a multicomponent Luttinger liquid. Its bosonic elementary excitations are called holons and spinons. A holon is a charge excitation and can be regarded as an electronic CDW fluctuation. A spinon is a magnetic (spin) excitation and can be regarded as a SDW fluctuation. An (unstable) electronic quasiparticle excitation is built as a superposition of coherent states of holons and spinons.

Assuming that the 1D metal has exactly one holon and one spinon excitation mode, its low-energy long-wavelength properties are determined by four parameters only: a charge velocity u_c , a charge Luttinger parameter K_c , a spin velocity u_s , and a spin Luttinger parameter K_s . (Note that the 1D electron gas corresponds to a Luttinger liquid with $u_c = u_s = v_F$ and $K_c = K_s = 1$.) This two-component Luttinger liquid exhibits properties that differ markedly from those of ordinary metals. As already discussed above for the TLM model, the density of states vanishes as a power law at the Fermi energy, see (14). However, the exponent is now $\alpha = (K_c + K_c^{-1} - 2)/4$ for an interacting but spin rotation invariant system like the Hubbard model without magnetic field ($\Rightarrow K_c < 1$ and $K_s = 1$) [6,177]. This vanishing of the density of states in a 1D conductor is in stark contrast with an ordinary metal, where the conductivity is proportional to the density of states at the Fermi energy. As mentioned above, the vanishing of the density of states reflects the instability of quasiparticle excitations in the interacting strictly-1D electron system. The conductance quantum is also slightly different, $G = 2K_c e^2/h$ [171], where the factor 2 comes from the spin degrees of freedom. Only for a noninteracting wire ($K_c = 1$) the 1D electron gas result is recovered.

Unfortunately, it is difficult to observe these features in numerical investigations of 1D lattice models such as the Hubbard model because they involve very small energy scales [178–181]. Experimentally, the vanishing of the density of states has been observed with photoemission spectroscopy or STS in various quasi-1D crystalline materials such as TTF-TCNQ [66], Bechgaard salts [182], and the purple bronze $\text{Li}_{0.9}\text{Mo}_6\text{O}_{17}$ [183,184] as well as in carbon nanotubes [185] and in atomic wire systems [37,174]. In contrast, the renormalization of the conductance quantum does not occur in the standard experimental setup (a quantum wire between two ordinary metallic leads) [186–188].

Another significant difference between Fermi and Luttinger liquids is their spectral functions. The single-particle Green's function $G(\vec{k}, \omega)$ of a Fermi liquid has poles for $\hbar\omega = E(\vec{k})$, where $E(\vec{k})$ is the excitation energy of the Landau quasiparticle with momentum $\hbar\vec{k}$. In a Luttinger liquid, however, $G(\vec{k}, \omega)$ has no poles but the spectral function $A(\vec{k}, \omega) = -\frac{1}{\pi} \text{Im} G(\vec{k}, \omega)$ exhibits a continuum with power-law singularities (divergence or cusp) on the holon branches $\hbar\omega = u_c|k|$ and the spinon branches $\hbar\omega = u_s|k|$ [177,189]. We speak of a dynamical separation of spin and charge when the elementary excitations split into independent spin and charge modes. This hallmark of 1D physics can be observed in lattice models for strictly 1D electron systems. For instance, Fig. 4 shows a spectral function of the 1D Hubbard model away from half filling calculated with the numerical DMRG method [190,191]. The distinct spinon and holon branches are clearly visible over finite energy

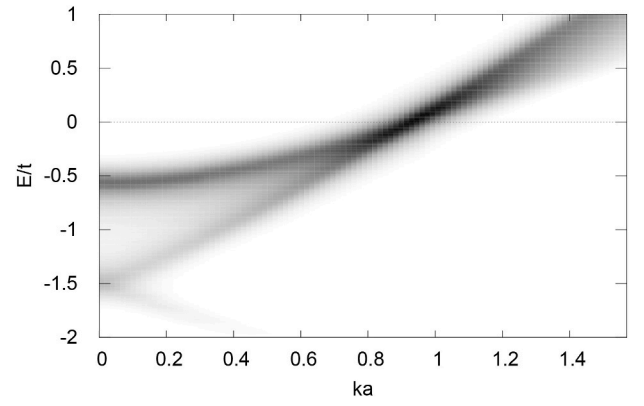


Fig. 4. Spectral function $A(k, E = \hbar\omega)$ of the 1D Hubbard model with $U = 4.9t$ and a density $n = 0.59$. The chemical potential $\mu = -0.2399t$ is chosen so that the Fermi energy is $E = \epsilon_F = 0$. The spinon and holon branches start from the Fermi points at $k_F a = n\pi/2 \approx 0.93$ but below the Fermi energy they clearly split away as momentum is lowered. The spinon branch is the upper intense feature reaching $E \approx -0.5t$ for $k = 0$ while the holon is the lower weaker feature reaching $E \approx -1.5t$ for $k = 0$.

and momentum ranges. In first approximation one can consider that ARPES experiments measure the spectral function $A(\vec{k}, \omega)$. Indeed, one can observe the signature of spin-charge separation in the ARPES spectrum of quasi-1D materials such as TTF-TCNQ [65,66].

Finally, we note that the Luttinger liquid theory has been extended to describe numerous physical quantities (e.g., optical absorption, charge and spin dynamical structure factors, thermodynamic quantities) and to address impurity, boundary, and disorder effects [6,107].

1.3.6. Summary: 1D theory

To conclude this overview of the physics in strictly 1D electron systems, we point out that three very different theoretical approaches predict that gapless excitation modes are collective excitations with linear dispersion in the low-energy long-wavelength limit, although the nature of the collective excitations is quite different in each case. These are (I) the phasons of incommensurate CDW and SDW in the Ginzburg-Landau theory (see sec. 1.3.2), (II) plasmons and magnons in the Fermi liquid theory, and (III) holons and spinons in the Luttinger liquid theory. Consequently, holons and spinons are often seen as the counterpart of plasmons and magnons [30] and are often pictured as CDW and SDW. This agreement reveals the “universal” nature of the physics in strictly 1D systems, i.e., the low-energy long-wavelength properties do not depend qualitatively on the details of the models.

Similarly, the spin-charge separation is often associated with Luttinger liquids, but actually it is a feature of 1D physics that can be observed in various phases. For instance, this fractionalization of elementary excitations is found in the doped SSH model and its generalizations in the form of charged and neutral solitons [18,34,61,62]. This type of spin-charge separation is observed experimentally in quasi-1D doped π -conjugated polymers.

The theory of 1D quantum systems is a very broad and active research field. Obviously this short overview cannot cover all important aspects. In particular, finite-temperature transport [192] and non-equilibrium dynamics [193–195] are current hot topics that are not discussed here.

1.4. Systems of coupled chains

Obviously, even the most anisotropic quasi-1D materials are 3D electron systems in reality. From a theoretical point of view, a quasi-1D material can be seen as a system of linear chains, which (I) act upon one another directly and (II) interact with their 3D environment.

Interactions with the 3D environment (e.g. a heat bath or a substrate) will be addressed in the next section (1.5). In this section we discuss the role of the direct interchain coupling. A fundamental question is how this interchain coupling influences the 1D physics discussed in the previous section. First, the stabilization of long-range-ordered phases is discussed in sec. 1.4.1. Then the nature of strongly anisotropic metals is addressed in sec. 1.4.2. Finally, the concept of dimensional crossover is presented in sec. 1.4.3.

Until recently, the best realizations of quasi-1D electronic systems have been the strongly anisotropic crystalline materials discussed in sec. 1.2.2. They can be regarded as 3D arrays of weakly-interacting chains. Consequently, the role of the 3D interchain coupling has been extensively investigated and is well understood [1,4–7,33,34,45,58,107,149,166]. For these reasons, we will first summarize the most important results for 3D arrays of chains. Atomic wire systems on substrates are regarded as 2D arrays of chains, however (see sec. 1.2.3). Therefore, we will also point out some significant theoretical differences between both cases.

Naturally, the most basic effect of the 3D interchain coupling in quasi-1D crystalline materials is the stabilization of their anisotropic atomic structure. Without this coupling these materials would not be solid. However, this problem is not considered here because the focus lies on electronic properties and related lattice distortions (Peierls transition, e.g.).

Obviously, the direct interaction between chains should become weaker when the distance between chains becomes larger. Experimentally, the interchain distance can be modified by applying pressure as well as by substitution of atoms or molecules between the chains. This is how the anisotropy is varied in the phase diagram of the Bechgaard and Fabre salts in Fig. 1. From the theoretical point of view, the interchain coupling strength is a model parameter and we will assume that we can vary it at will.

1.4.1. Ordered phases

1.4.1.1. 3D arrays of chains. We are accustomed to the spontaneous appearance of symmetry-breaking order in the 3D world when the temperature is lowered. For instance, liquids condense to form solids below their crystallization points while in some solids magnetic moments align to form permanent magnets below their Curie temperatures. Thus it not surprising that symmetry-breaking long-range-ordered phases are stable at sufficiently low temperatures in quasi-1D crystalline materials as well as in 3D models of coupled chains. Theoretically, as soon as there is an infinitesimal coupling between chains, long-range order is possible,

Numerous theoretical studies have revealed the dual role of the interchain coupling [1,4,5,7,34,149]. On the one hand, it reduces thermal (and quantum) fluctuations and thus enables the appearance of long-range ordered phases at finite temperature. If this effect is dominant, a stronger interchain coupling increases the phase stability and thus the critical temperature above which the ordered phase becomes thermodynamically unstable. Typically, the critical temperature remains lower than the value predicted by mean-field theory or expected from the strength of the intrachain interactions. Transition metal trichalcogenides such as NbSe₃ and TaS₃ are examples of quasi-1D materials with a Peierls-CDW phase at finite temperature thanks to the interchain coupling but with a critical temperature that is reduced by fluctuations from the mean-field prediction [1,4,8].

On the other hand, an increase of the interchain hopping [i.e., the ratio between t_y , t_z and t_x in the tight-binding dispersion (3)] increases the total bandwidth and thus reduces the relative strength of the intrachain interactions responsible for the 1D symmetry-breaking phase. Moreover, it warps the Fermi surface and can destroy the perfect nesting responsible for the ordered phase. If these effects are dominant, a stronger interchain coupling can result in a lower critical temperature. Moreover,

the reduced anisotropy can do away with the 1D nature of the long-range-ordered phase. However, the critical temperature can also increase with increasing interchain two-body interactions, such as the Coulomb repulsion between electrons in different chains or the exchange coupling between spins in different chains.

Thus the critical temperature can be non-monotonic as a function of the interchain coupling for a phase that is essentially an anisotropic ordering, such as a Peierls-CDW. For instance, the evolution of the Peierls critical temperature is summarized in Fig. 5 as a function of the interchain hopping in a 3D array of chains (See Fig. 35 in Ref. [149] for more details.). First, the critical temperature is zero in the strictly-1D limit ($t_{y,z} = 0$), then it increases as fluctuations are reduced by the increasing interchain coupling. A further increase progressively destroys the $2k_F$ nesting of the Fermi surface that is responsible for the Peierls instability and thus the critical temperature decreases. The critical temperature can also drop to zero if the Peierls instability vanishes for a too small anisotropy of the electron dispersion (3) [196]. In that case the system undergoes a quantum phase transition (i.e. at $T = 0$) from the Peierls insulating state to a metallic state at a critical value of $t_{y,z}$. We note that the nature of the metallic phase above the critical Peierls temperature is also affected by the interchain coupling. This will be discussed in the following sections.

Other types of long-range order, e.g. CDW and SDW, can occur in isotropic 3D systems as well as quasi-1D ones. If the nesting of the Fermi surface is preserved when the interchain coupling increases, only the reduction of thermal fluctuations occurs and the critical temperature can increase monotonically. In such a case, it may be difficult or even impossible to define a clear boundary between a quasi-1D CDW/SDW phase and an anisotropic 3D CDW/SDW phase as the interchain coupling increases from zero to the isotropic limit.

In these examples we have assumed that only one type of long-range order can occur. In reality, various phases compete in real materials as well as in realistic models. This competition leads to a high sensitivity to external influences such as temperature and pressure. Consequently, a model consisting of a 3D array of chains typically undergoes one or more transitions between different ordered phases as the interchain coupling increases. Experimentally, this complexity is illustrated by the rich phase diagram of the Bechgaard and Fabre salts in Fig. 1.

1.4.1.2. 2D arrays of chains. The physics of 2D arrays of chains is more complicated than the 3D case. As discussed in section 1.3.4, the nature of the spontaneously broken symmetry (discrete or continuous) plays a crucial role for the possible long-range ordered phases because the lower critical dimension is one for discrete symmetries but two for continuous ones.

This prediction of statistical field theory [113–116] (or the Mermin-Wagner theorem [13,158]) is a consequence of

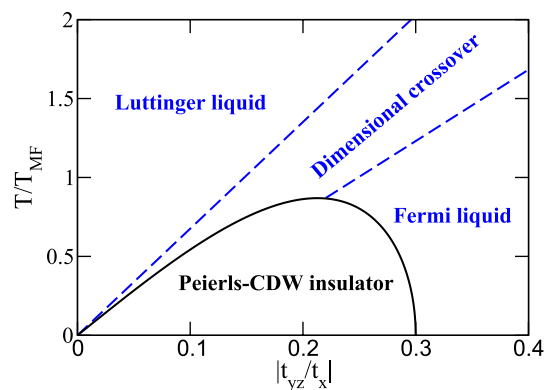


Fig. 5. Sketch of the phase diagram for a 3D array of Peierls chains as a function of temperature T and interchain hopping $|t_{y,z}|$. The scales are set by the mean-field temperature T_{MF} at $t_{y,z} = 0$ and the intrachain chain hopping t_x .

long-wavelength fluctuations in the thermodynamic limit. Contrary to the dynamical confinement, a spatial confinement (see sec. 1.2.3) necessarily imposes a finite length cutoff (i.e. L_y or L_z). Thus long-wavelength fluctuations are not possible in the direction of confinement. It follows that atomic wires on a substrate constitute a strictly 2D system from the point of view of statistical field theory and the Mermin-Wagner theorem.

Therefore, we can expect to observe long-range ordered phases that spontaneously break discrete symmetries in atomic wire systems at finite temperature. For instance, this includes a Peierls-CDW that doubles the lattice periodicity in the chain direction (and possibly in the interchain direction) as observed in indium wires on the Si(111) surface [16,46]. A second example is the quasi-1D CDW with a threefold periodicity predicted by first-principles simulations on the step edges of Au/Si(553) [144] and confirmed by STM and STS experiments [145, 146].

By contrast, long-range ordered phases that spontaneously break continuous symmetries should not occur in atomic wire systems at finite temperature. This usually includes incommensurate CDW and SDW phases as well as magnetic ordering because of the electron spin SU(2) symmetry. But as spin-orbit interactions generally do not preserve the spin rotation symmetry [197], magnetic ordering is allowed in atomic wire systems with a strong spin-orbit coupling. For instance, a spin-ordered phase has been found experimentally in Pb/Si(557) [138, 139], which is interpreted as a spin-orbit density wave (SODW) [198].

However, it should be kept in mind that the Mermin-Wagner theorem does not prohibit metastable 2D ordered phases at finite temperature in finite size samples [159]. As discussed in sec. 1.3.4 the relevant size and time scales can be macroscopically large. Thus the experimental observation of a broken continuous symmetry in an atomic wire material would not necessarily contradict the theory. Finally, note that the Mermin-Wagner theorem does not apply to topological ordering of the Kosterlitz-Thouless type [199].

Unfortunately, there are few exactly solvable models describing the thermodynamics of long-range ordered phases in anisotropic 2D or 3D systems. An illustrative example is the 2D Ising model on a square lattice with ferromagnetic couplings $J_x > 0$ in the x-direction and $J_y \geq 0$ in the y-direction [12]. For $J_y < J_x$ it can be viewed as a 2D system of coupled chains in the x-direction with the interchain coupling J_y . This model is exactly solvable [93]. It undergoes a transition from a paramagnetic phase to a ferromagnetic phase when the temperature is lowered below a critical value T_c given by

$$\sinh(2J_x / k_B T_c) \sinh(2J_y / k_B T_c) = 1. \quad (15)$$

the magnetization only breaks the discrete spin flip symmetry so that the

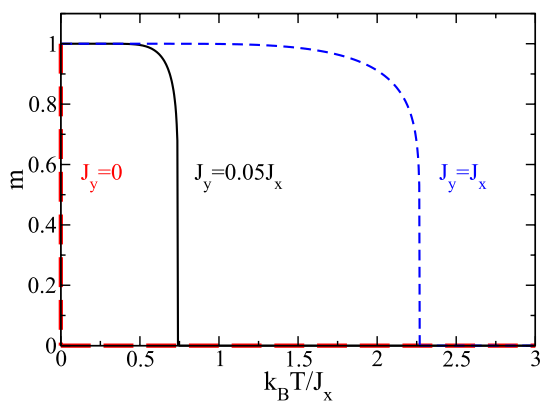


Fig. 6. Average absolute magnetization of the anisotropic 2D Ising model as a function of the temperature for various coupling anisotropies J_y/J_x . The fully polarized ferromagnetic phase corresponds to $m = 1$ and the paramagnetic phase to $m = 0$.

Mermin-Wagner theorem does not apply. The average magnetization is shown in Fig. 6 as a function of temperature for several ratios J_y/J_x . We see that T_c is lower in the anisotropic case ($J_y < J_x$) than in the isotropic case ($J_y = J_x$). Only for a system of strictly independent 1D chains ($J_y = 0$) we recover the generic absence of long-range order discussed in sec. 1.3.4. The critical temperature increases monotonically with J_y in that system because the interchain interaction only strengthens the overall ferromagnetic coupling and thus reduces thermal fluctuations. Finally, we note that the critical temperature is not an analytical function of J_y around $J_y = 0$. This precludes a perturbative expansion in the interchain coupling starting from the solution for the strictly 1D system. This non-analyticity as a function of the interchain coupling is a general issue with quasi-1D systems and reflects the singularity of strictly-1D models.

Although the Ising model does not describe any real magnetic materials accurately, its properties explain qualitatively experimental observations in quasi-1D materials. For instance, the excitation spectrum of Sr_2CuO_3 is well described by the spin-1/2 antiferromagnetic Heisenberg model [74]. However, the measured critical temperature for the antiferromagnetic ordering ($k_B T_c = 5\text{K}$) is orders of magnitude smaller than the intrachain spin exchange coupling ($J = 250\text{meV}$). On the basis of the Ising model thermodynamics, we understand that fluctuations destroy the antiferromagnetic order at the temperature scale set by the intrachain coupling J but the long-range order is stabilized at the lower temperature scale T_c set by the 3D interchain coupling.

1.4.2. Anisotropic metals

An interesting question is the nature of metallic phases in quasi-1D electron systems. Consider a 3D array of chains with a tunable interchain coupling. If one starts from the Luttinger liquid phase in strictly-1D chains and progressively increases the interchain coupling, we recover a Fermi liquid at the latest when the system becomes isotropic. In particular, we can ask where is the boundary between coupled Luttinger liquids and an anisotropic Fermi liquid. Answering this question is a difficult theoretical problem that is far from being solved because we lack exact solutions for models describing a 2D or 3D array of interacting electron chains as well as reliable numerical or analytical methods to study such models. Thus this problem has prompted many studies using various approximations [6,29,33,45,107,149,166]. A common approach starts from the Luttinger liquid solutions for single chains and assumes that the interchain coupling is a weak perturbation. Another approach starts from the electron gas in anisotropic 3D systems and assumes that the electron-electron interaction is a weak perturbation. A third approach consists in studying systems made of a finite number of coupled chains and extrapolating the results to the limit of a bulk material (i.e., an infinite number of chains). We will summarize the main theoretical results in this section and discuss some consequences for experimental observations in sec. 1.4.3.

The stability of coupled Luttinger liquids depends on the two types of interactions between chains. The first type describes the electron motion from a chain to another one (hopping or tunnelling), which is responsible for the t_y and t_z terms in the 3D dispersion (3). The second type is any two-body scattering process such as the Coulomb interaction between electrons in different atomic chains.

Most studies have reached the conclusion that an infinitesimally small interchain hopping is relevant and destroys the Luttinger liquid within a renormalization group approach [6,33,45,107,166,200–203]. Generally, Luttinger liquids in strictly-1D chains exhibit some quasi-long-range orders. As soon as the interchain hopping is finite, one of them becomes a stable long-range order with broken symmetry in a 3D array of chains [33]. The thermodynamics of these phases have been discussed in the previous section 1.4.1. Thus one expects to observe the Luttinger liquid phase only at temperatures above the critical temperature of the ordered phase. This scenario is seen in the Peierls phase diagram in Fig. 5 for $0 < |t_{y,z}/t_x| \lesssim 0.2$ as well as in the left part of the phase diagram of Bechgaard and Fabre salts in Fig. 1. If one assumes that the system remains metallic despite the interchain hopping, however,

one finds that the asymptotically low-energy and low-temperature properties correspond to a Fermi liquid [6,58,107,149,203].

The effects of two-body interactions between chains are less plain than those of the interchain hopping. These interactions can also destabilize Luttinger liquids but in some cases low-energy excitations of coupled chains still obey the Luttinger liquid phenomenology [6,204,205]. If the Luttinger liquid is destabilized, two-body interchain interactions do not always stabilize a quasi-long-range order of the strictly-1D chain but often favor the appearance of a symmetry-breaking long-range ordering that can also occur in higher dimensions such as CDW and SDW [33].

The above discussion deals mostly with 3D arrays of coupled chains, which is relevant for quasi-1D crystalline materials. The possibility of non-Fermi liquids has been extensively investigated in 2D systems but mostly with a view to layered materials, in particular the metallic phase of the high-temperature superconducting cuprates [149,206,207]. Few studies have focused on the peculiarities that could be relevant for Luttinger liquids or other non-Fermi liquids in atomic wire systems. Therefore, theoretical predictions for metallic states in 2D arrays of chains are rare and not so clearcut as in 3D. We will address the question of anisotropic 2D metals in sec. 1.7.

1.4.3. Dimensional crossover

A key concept of solid-state physics in reduced dimensions is the dimensional crossover observed in thermodynamical quantities and dynamical response functions as a function of temperature or excitation energy [7,29,107,149]. Summarily, we speak of dimensional crossover when the (experimental) properties of quasi-1D materials display the usual characteristics of (anisotropic) 3D solids at low temperature and low excitation energy but the signatures of strictly-1D physics are found at higher temperature or excitation energy. The typical energy or temperature scale of this crossover depends on the nature and the strength of the interchain coupling. Naturally, a double dimensional crossover can also take place from 3D to 2D and then from 2D to 1D physics (or a single crossover from 3D to 2D in layered materials). Moreover, the crossover can occur as a function of other control parameters than temperature and excitation energy, such as pressure.

The simplest example of a dimensional crossover is given by a system of noninteracting electrons in the quasi-1D tight-binding model with the dispersion of eq. (3) and hopping terms $|t_{y,z}| \ll |t_x|$. The system response to an external perturbation of frequency ω at temperature T corresponds to an anisotropic 3D metal for $kT, \hbar\omega \ll |t_{y,z}|$ but becomes similar to the response of a strictly 1D system for $|t_{y,z}| \ll kT, \hbar\omega \ll |t_x|$. In particular, the system behaves as an anisotropic 3D conductor for $kT \ll |t_{y,z}|$ but as a 1D conductor for $|t_{y,z}| \ll kT \ll |t_x|$ because the charge transport between chains becomes incoherent. Thus in this non-interacting model the bare interchain coupling $|t_{y,z}|$ sets the characteristic scale for the crossover between the 1D and 3D regime.

For long-range-ordered phases, we can also understand the dimensional crossover in terms of length scales. At high enough temperatures, the correlation length is shorter than the distance between chains. Thus the chains are independent and exhibit quasi-long or short range order like strictly-1D systems. When the temperature is lowered, the correlation length becomes longer than the interchain distance and a phase transition to an anisotropic 3D ordered phase is allowed to take place. Theoretically, this behavior is seen in the exact solution of the anisotropic 2D Ising model discussed previously [93]. Experimentally, various dimensional crossovers are visible in the Bechgaard and Fabre salts [17,208], e.g. see Fig. 1.

The above discussion of the dimensional crossover in a noninteracting electron system remains qualitatively correct for interacting systems. A first significant difference is that not only the effective dimension is modified but also the physics is changed qualitatively. For instance, the properties of a metallic system can undergo a crossover from a Luttinger-liquid to a Fermi-liquid behavior. Such crossovers are shown in the phase diagram of Bechgaard and Fabre salts in Fig. 1 and in

the Peierls phase diagram in Fig. 5. Another significant difference is that interactions strongly renormalize the energy and temperature scales at which the crossover takes place [6,29,166]. Usually, the scale becomes smaller when interactions become stronger. For instance, stronger Coulomb interactions reduce the scale over which a quasi-1D metal obeys the 3D Fermi liquid phenomenology.

The dimensional crossover can be observed experimentally if the energy or temperature scale is within an accessible range. For instance, the crossover between Luttinger-liquid and Fermi-liquid behavior has been thoroughly studied for the spectral function $A(\vec{k}, \omega)$ [6,29,58,107,149,203]. In the physically relevant case of finite but small interchain hoppings the quasiparticle pole does not vanish and a narrow coherent peak with a featureless incoherent background is visible at low energy and temperature, as expected for a Fermi liquid. However, $A(\vec{k}, \omega)$ exhibits the signature of a Luttinger liquid at higher energy or temperature: a continuum with two peaks or cusps (power-law singularities) on the holon and spinon branches (and thus the separation of spin and charge excitations).

Thus the dimensional crossover can be observed in ARPES experiments. For instance, the photoemission spectrum of a quasi-1D organic conductor with strong interchain coupling, (DMe-DCNQI)₂Cu, exhibits such a behavior [209]. The spectrum displays features predicted by the Luttinger liquid theory at high excitation energy or at high temperature, while characteristics of a 3D Fermi liquid are observed at the Fermi energy at low temperatures. The crossover occurs around $T \approx 300\text{K}$ or $\hbar\omega \approx 30\text{meV}$.

Finally, a dimensional crossover could also play a role in the controversy about the dimensionality of the metallic state of Au/Ge(100) and the relevance of the Luttinger liquid theory to describe its low-energy properties [15,37–44]. However, as this material is a 2D array of coupled chains and the nature of the metallic state in such a 2D system is also controversial, we cannot draw a conclusion at this point. We will discuss this issue in sec. 1.7.

1.4.4. Summary: Interchain coupling

In summary, the direct interchain coupling plays a complex role in quasi-1D materials. First, a too strong coupling between 1D chains can obviously lead to higher dimensional physics. Second, a finite but weak interchain coupling stabilizes long-range ordering with a broken symmetry at finite temperature and thus makes possible the experimental observation of these phases. Third, a finite but weak interchain coupling destabilizes Luttinger liquids in most cases. Nevertheless, Luttinger liquid phenomenology can still be observed at a high energy or temperature scale (if this scale remains in the experimentally accessible range). The same applies to the signature of 1D physics in long-range-ordered phases.

An important advantage of strictly 1D systems is that their properties are often “universal”, i.e. they are qualitatively identical for large classes of models. In contrast, the combined effects of interchain coupling and fluctuations depend sensitively on the models. Consequently, one expects that they also depend sensitively on the materials considered and it is much more difficult to make theoretical predictions about experiments. Thus one has to keep in mind the limited applicability of the theory of strictly-1D systems when discussing the properties of real materials and investigate how interchain interactions modify the properties of quasi-1D systems.

1.5. The role of the substrate

Self-assembled atom chains on substrate surfaces seem to be an ideal realization of 1D electron systems. However, an important and unsolved theoretical issue is the influence of the substrate on the quasi-1D physics presented in previous sections. As discussed there, most of the theory for 1D systems is based on effective models and theories including only a

few relevant degrees of freedom and interactions that are required to answer a specific question while neglecting the less relevant ones. However, this theoretical approach was rarely used to study the role of the substrate until 10 years ago.

A few prior studies indicated that the coupling between wires and substrate could play a substantial role although they were often inconclusive. For instance, an early theoretical model for an atomic wire on a surface is made of two chains: one chain represents the wire, which is coupled to another chain representing the surface. This approach was used to show that a Peierls insulating state may become unstable when coupled to a substrate depending on the interaction strength [8] and that some aspects of the Luttinger liquid behavior survive the coupling to a surface but the question whether the system is a Luttinger liquid or a Fermi liquid could not be answered [210]. Additionally, the Peierls-CDW in wires was studied in the presence of surface phonons using scaling theory [211] while another investigation showed that the conductance depends strongly on the electronic states in the substrate when electron flows through a quantum wire in the presence of leakage to the substrate [212]. Moreover, the role of the substrate was studied in the context of quasi-1D magnetism in atomic spin chains on semi-conducting, metallic or superconducting surfaces [35].

Therefore, during the last decade we have purposefully investigated how the substrate affects 1D systems using the theoretical approach described in sec. 1.2.4. In this section we will first summarize some theoretical expectations and questions about the substrate influence (sec. 1.5.1). Then we will review our approach and results for 1D correlated electron systems on a substrate, such as Luttinger liquids (sec. 1.5.2). Finally, we will discuss a simple example showing how a substrate-mediated coupling can stabilize a quasi-1D long-range ordered phase at finite temperature (sec. 1.5.3).

1.5.1. General considerations

Here we discuss qualitatively some general theoretical expectations and questions about the role of the substrate in atomic wire systems and its influence on the physics predicted by the theory of quasi-1D systems in sec. 1.3 and 1.4.

1.5.1.1. Structural stability. Naturally, the most basic effect of the substrate is to maintain a stable ordered atomic structure with parallel atomic wires on its surface. Without the substrate the atomic wires would be disordered or even unstable. From a purely theoretical point of view, a strictly 2D array of wires without substrate breaks the continuous translation symmetry and thus this ordering is prohibited by the Mermin-Wagner theorem at any temperature greater than zero [13, 158]. This is similar to the role of the interchain coupling in stabilizing quasi-1D crystalline materials (see sec. 1.4) and will not be discussed further.

1.5.1.2. Charge reservoir. The substrate can act as a charge reservoir for the atomic wires deposited on its surface. For instance, electrons flowing through a quantum wire can leak to a metallic substrate [212]. However, even a semiconducting or insulating substrate can act as a charge reservoir for atomic wires on its surface because changing the average number of charges in the 2D wire system corresponds to an infinitesimal fluctuation of the average charge or polarization in the 3D substrate. Thus the theory of 1D systems, which is largely based on the canonical ensemble with a fixed number of electrons, must be generalized to the grand-canonical ensemble with a chemical potential set by the substrate. We do not expect theoretical results to be significantly modified for metallic systems and insulators with a hard gap (e.g. Mott insulators). However, we have found drastic consequences for phases with a soft gap (e.g. CDW and SDW) because a band edge can cross the chemical potential as the gap varies with the temperature. The grand-canonical theory of the Peierls-CDW phase and its role for the In/Si(111) material are discussed in more detail in sec. 1.6.

1.5.1.3. Heat reservoir. Just as infinitesimal charge fluctuations in the substrate can modify the electronic density in the wires, infinitesimal energy fluctuations can modify the average energy of the wire subsystem. Nevertheless, we can see the substrate as a heat bath for the 2D wire subsystem in first approximation. Thus the substrate just fixes the wire subsystem temperature. This is not different from the usual theory for 1D systems, which often assumes a fixed temperature set by some external heat bath.

1.5.1.4. Renormalization of interaction parameters. Clearly, the presence of the substrate can modify the strength and the range of interactions within and between atomic wires. An obvious example is the screening of the interchain Coulomb interaction by the electronic degrees of freedom in the substrate. Within our theoretical approach these effects can usually be interpreted as a renormalization of the model parameters. For instance, we will see in sec. 1.5.2 that the renormalization of nearest-neighbor repulsion and hopping shifts the phase transition between a Luttinger liquid and an electronic CDW.

1.5.1.5. Interchain coupling. We have seen in sec. 1.4 that the interchain coupling plays a decisive role in real quasi-1D materials. In particular, the interchain coupling is required to stabilize long-range ordered phases with broken symmetries and critical temperatures depend sensitively on its strength. Various CDW phases and magnetic orders have been observed in atomic wire materials such as In/Si(111) [16,46], Au/Si(553) [145,146], or Pb/Si(557) [138,139]. A priori, the direct interchain coupling appears to be too weak to explain the observed critical temperatures because of the distance between wires. Thus a very important question is whether the substrate can generate an indirect interchain coupling or significantly amplify an existing one. We will discuss two examples to show that substrate-mediated interchain couplings can destabilize a Luttinger liquid (sec. 1.5.2) but can stabilize a long-range ordered quasi-1D phases at finite temperature (sec. 1.5.3).

1.5.1.6. Substrate field. As their low-energy degrees of freedom are confined spatially close to the surface, atomic wire materials can be seen in first approximation as strictly 2D systems. However, the atoms forming the substrate surface generate a periodic potential that is felt as an external field by the electronic degrees of freedom in the wires. Theoretically, this spatially varying field can influence the thermodynamics of the 2D wire system in opposing ways.

On the one hand, we expect that the various phases found in strictly 1D systems will be modified by the interplay of the surface lattice periodicity with the Fermi surface nesting wavevector, which is set by the band filling of the 1D subsystem (i.e., the $2k_F$ instability). Experimentally, the periodicity of CDW phases observed in atomic wire materials seems to be determined by the substrate rather than the electronic band filling [16]. This raises questions about the role of the $2k_F$ instability in the formation of long-range ordered phases in these materials. Note that recent DFT calculations have shown that the CDW instability can be suppressed by the substrate in a quasi-2D material [monolayer 1H-TaS₂ on Au(111)] [213].

On the other hand, the periodic surface potential can also pin CDW and SDW spatial fluctuations (e.g., phasons or domain walls). Similarly to the confinement of fluctuations by the interchain coupling (discussed in sec. 1.4.1), this pinning reduces thermal and quantum fluctuations and thus could stabilize long-range ordered phase in the ground state and at finite temperature. For instance, the example discussed below in sec. 1.5.3 can be interpreted as the suppression of fluctuations in the antiferromagnetic wires by the magnetic field of the surface. Moreover, in a strictly 2D system no long-range ordered phase can exist at finite temperature if it spontaneously breaks a continuous symmetry according to statistical field theory and the Mermin-Wagner theorem [13,158]. However, if the surface field breaks this symmetry, the long-range ordered phase becomes stable at finite temperature.

In summary, the thermodynamics of atomic wires on a surface could be quite different from the theoretical predictions for strictly 2D systems because of the surface potential acting on the wire degrees of freedom as an external field. Therefore, this issue should be investigated in the future to understand the stability of quasi-1D phases in atomic wire materials.

1.5.1.7. Dimensional crossover. A practical issue is to identify the signature of 1D physics in experiments for atomic wires on substrates. As discussed in sec. 1.4.3, the dimensional crossover is a key concept in our understanding of the experimentally observable 1D physics in quasi-1D crystalline materials. However, the influence of a substrate on the dimensional crossover is not well known. Actually, we have found an “inverse” dimensional crossover from 1D to higher dimensional physics with increasing excitation energies in simple models of correlated wires on semiconducting substrates as explained in sec. 1.5.2. Therefore, further investigations are required to determine the observable 1D physics in atomic wire materials.

1.5.2. Correlated wires

An important question is the effect of the substrate on the correlated phases predicted by the theory of strictly 1D electron systems, e.g. Luttinger liquids, electronic CDW, or Mott insulators. As there are no well-established models describing correlated atomic wires on substrates in the scientific literature yet, we have first explored the modeling of these systems. Additionally, we have developed a practical procedure for studying the effects of electronic correlations in these models using well-established methods for 1D systems. This approach has allowed us to obtain clear results about the stability of some 1D correlated states. These results are reviewed here.

1.5.2.1. Asymmetric two-leg ladders. Previous studies of the substrate impact on atomic wires introduced asymmetric ladder models with one chain representing the wire and one making up the substrate [8,210]. However, this approach was not pursued systematically. Therefore, we have first investigated an asymmetric Hubbard ladder with two inequivalent legs, a Hubbard chain and a tight-binding chain, coupled by an interchain hopping t_{\perp} [214,215]. Ground-state properties, gaps, and spectral functions, have been determined using analytical approximations, the numerical DMRG method, and QMC simulations. We have found that the physics of this asymmetric ladder is very rich and includes various 1D phases. In particular, it exhibits a Luttinger liquid phase with a spatial separation of elementary spin and charge excitations [215]. The results also confirm that 1D correlated systems are extremely sensitive to their environment and that their properties can be drastically modified by varying the strength of the (wire-substrate) hybridization t_{\perp} . Thus the study of asymmetric ladders is a useful approach for exploring the physics of 1D systems coupled to an environment. However, it is not realistic to represent a substrate by a single chain because the wire interaction can dominate the full system. Instead, the substrate should include many more degrees of freedom than the wire. This can be realized with wider ladders made of several legs as discussed below.

1.5.2.2. Mapping to narrow ladder models. To define basic quantum lattice models for correlated wires deposited on a substrate, we have combined models that are routinely used to study strictly 1D correlated electrons (see sec. 1.2.4) with a 3D tight-binding model representing the non-interacting substrate [216]. The 1D model sites correspond to atomic orbitals of the wire and are represented by gray balls in Fig. 7(a). The bands of the substrate have dispersions of the form (3) with $t_x = t_y = t_z = t_s$. A two-band tight-binding model is used to represent a gapped (i.e., insulating or semiconducting) substrate while a single band suffices for a metallic substrate. Wires and substrates are coupled by a hopping term t_{ws} .

As investigations of the full interacting 3D wire-substrate system are

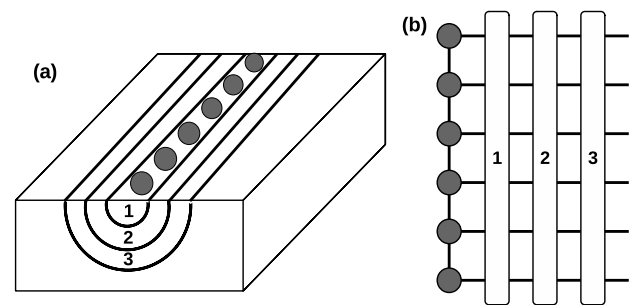


Fig. 7. Illustration of the mapping for a single wire on a metallic (i.e. one-band) substrate. (a) Sketch of the atomic wire (gray balls) with three numbered shells in the substrate. (b) Ladder representation of the same system with the left-most leg corresponding to the atomic wire and the other legs representing shells one to three. For a gapped (i.e. two-band) substrate there would be two legs per shell.

extremely difficult, the modeling by 1D ladder-like models seems to be a more feasible approach. Thus we have developed a systematic procedure to construct such models from the basic 3D wire-substrate models [216]. Our method generalizes the idea used to map multi-orbital, multi-site quantum impurity problems onto ladder systems [217,218], which is a generalization of Wilson’s method for solving the Kondo problem [219]. In a second step [220] we have generalized the procedure to map multiple wires onto a system of coupled ladders (one ladder per wire). The mapping of the 3D wire-substrate system onto a ladder-like system is illustrated in Fig. 7(b) for a single wire. The first leg of the ladder represents the atomic wire while successive legs represent cylindrical shells of the substrate with increasing diameter around the atomic wire.

In principle, this mapping is exact but, in general, the number of legs is infinite. If the substrate is gapped, however, the influence of outer shells on the wire decreases fast with increasing leg index. Thus we can obtain an approximate ladder representation of finite width [216,220]. If the number of ladder legs is small enough, the model can be investigated with well-established methods for 1D correlated systems such as DMRG and field-theoretical methods. If we consider a single wire and use only one leg to represent the substrate, we recover the asymmetric ladder models discussed above [8,210,214,215].

We have first tested this approximation of 3D wire-substrate systems by narrow effective ladders on noninteracting wires as we can separately solve the full 3D problem in that case [216,220]. We have found that the approximation is valid for a gapped substrate but not for a metallic one. Thus we will discuss only our findings for gapped substrates in the remainder. Moreover, one has to use the same number of legs to represent the substrate conduction and valence bands. Consequently, the total number of legs must be odd to represent a system made of a single wire on a gapped substrate and the minimal width is three legs.

We have successfully applied this method to various systems representing interacting wires. Our results are discussed below. They shed some light on the effects of a gapped substrate on correlated 1D systems, in particular on the fate of Luttinger liquids. In addition, they demonstrate that the mapping of 3D wire-substrate systems onto effective narrow ladder models enables a systematic study of correlated phases in atomic wires deposited on semiconducting substrates.

1.5.2.3. Hubbard chain. First, we have considered the case of a single Hubbard chain coupled to the substrate [221]. The 1D Hubbard model is exactly solvable without the substrate (i.e., for $t_{ws} = 0$): it exhibits a Mott insulating phase at half filling but an electronic Luttinger liquid away from half filling [89,90]. We have determined ground-state properties, gaps, and spectral functions of the coupled wire-substrate system using DMRG and QMC simulations. We have found that both phases subsist for a wide range of parameters when the chain is coupled to the substrate. Low-energy excitations are localized on or around the chain in these

quasi-1D phases. Moreover, we have found that charge and spin velocities are different and thus a clear signature of 1D physics, spin-charge separation, is confirmed.

However, the nature of the excitation changes for high enough energy. They become quasi-particles (electrons and holes) delocalized in the substrate. Thus we observe an “inverse” dimensional crossover from 1D physics at low energy to 3D physics at higher energy. Moreover, quantum phase transitions occur from the 1D correlated phases (Mott insulator or Luttinger liquid) to uncorrelated phases (band insulator or metal, respectively) upon increasing the local Hubbard interaction U between electrons or decreasing the wire-substrate hybridization t_{ws} . In the uncorrelated phases low-energy excitations are quasi-particles delocalized in the substrate like the high-energy excitations in the 1D phases. Both the transitions and the dimensional crossover occur when the intrawire interaction energies become comparable to the substrate band gap.

Interestingly, a very strong wire-substrate coupling has no detrimental effect on the 1D physics. In that regime, the wire orbitals and the surrounding substrate shells become strongly hybridized and form a 1D subsystem that is only weakly hybridized with the rest of the substrate. In a real material, this implies that the quasi-1D electronic subsystem would not be localized in the wires only but mostly in the substrate region close to the wires.

1.5.2.4. Spinless fermion chain. Due to the high computational cost of DMRG for electronic ladder systems, we are not always able to study the properties of electronic Luttinger liquids with sufficient accuracy. However, the effects of the substrate on the Luttinger liquid phenomenology is an important issue for atomic wire materials. Indeed, experimental observations of Luttinger liquid signatures have been reported for various materials [15] such as Au/Ge(100) [37], Bi/InSb(001) [174], or Pt/Ge(001) [175]. Hence, we have turned to the spinless fermion model, which is another well-established but simpler model for 1D correlated systems, in particular for Luttinger liquids and CDW [6]. Using spinless fermions as degrees of freedom essentially amounts to focusing on the charge excitations and neglecting spin excitations.

We have first considered the case of a single spinless fermion chain with nearest-neighbor repulsion V and intrachain hopping t_w [222]. Without coupling to the 3D substrate this model is exactly solvable using the Bethe ansatz method and its properties are well known [6,223,224]. In particular, it exhibits a quantum phase transition from a Luttinger liquid phase for $V \leq 2t_w$ to an “electronic” CDW phase for $V > 2t_w$ at half filling. Using DMRG we have computed properties of the ground state (including CDW order parameters and correlation functions) and the lowest excitations. DMRG allows us to compute broader ladder systems for spinless fermions than for electronic models and we have simulated ladders with up to 15 legs.

Three ground-state phases are observed: a one-component Luttinger liquid at weak couplings $V < V_c$, a quasi-1D CDW insulator at intermediate couplings $V > V_c$, and a band insulator at large couplings V . The critical nearest-neighbor interaction V_c increases with the wire-substrate coupling t_{ws} and is larger than the value $2t_w$ for a strictly 1D chain. The reason is that the substrate causes a renormalization of the interaction V to a smaller effective value while the intrachain hopping t_w is renormalized to a stronger value. Thus a strong wire-substrate hybridization t_{ws} stabilizes the Luttinger liquid in that model too. In the first two phases, low-energy excitations are localized on or close to the wire for a wide range of model parameters and exhibit the usual features of Luttinger liquids or quasi-1D CDW insulators. As for the Hubbard chain, we observe a quantum phase transition to a 3D band insulator phase as well as a dimensional crossover from 1D to 3D low-energy excitations when the intrawire interaction energies become comparable to the substrate band gap.

1.5.2.5. Coupled chains. As discussed in sec. 1.4 interchain hopping

destabilizes Luttinger liquids. If the distance between atomic wires is relatively large, the direct interchain hopping could be negligible. However, wire orbitals are indirectly coupled through their hybridization with the substrate bands, which can generate an indirect hopping process between wires. Thus in the absence of a direct wire-wire hopping the substrate-mediated indirect coupling could have a decisive influence on the atomic wire properties. For spinless fermions the instability of the Luttinger liquid phase is already observable in a system of two coupled chains (without substrate). This system was thoroughly investigated a few decades ago using field theoretical methods [6, 225–227]. At half filling it becomes a CDW insulator for arbitrarily weak nearest-neighbor repulsion V and interchain hopping. This sensitivity provides us with a simple approach for testing whether the substrate-mediated coupling between wires is detrimental to Luttinger liquids.

We have investigated a system made of two spinless fermion chains without any direct interchain coupling but on a gapped substrate using the mapping to narrow ladders [220]. The main result is the non-universal influence of the substrate on the two-chain system. We have found in some cases that the substrate can mediate an effective coupling that destabilizes the Luttinger liquid phase in favor of the CDW insulating phase for any $V > 0$ as in a system of two directly coupled chains. In other cases, however, the two chains remain effectively uncoupled even for strong wire-substrate hybridizations t_{ws} , leading to two independent Luttinger liquids at weak nearest-neighbor repulsion V . More precisely, the substrate-mediated coupling depends on the relative positions of both chains on the substrate bipartite lattice. Therefore, it may be difficult to determine under which conditions the physics of correlated 1D phases such as Luttinger liquids can be realized in atomic wires on semiconducting substrates because they seem to depend on the model particulars.

1.5.2.6. Summary. In summary, all our results show that 1D correlated phases can survive the coupling to a substrate. Explicitly, we have found Luttinger liquids, “electronic” CDW, and Mott insulators in models describing interacting wires on gapped substrates. Their low-energy excitations are localized along the wires and exhibit characteristics of 1D electron systems such as the dynamical separation of spin and charge excitations. Therefore, our results confirm that quasi-1D correlated phases could occur in the low-energy properties of atomic wires deposited on semiconducting substrates. However, they also show that the existence and properties of these quasi-1D correlated phases depend significantly on the model parameters and details of the coupling to the substrate. Thus we cannot draw generic conclusions about the properties of quasi-1D phases in real materials. Nevertheless, we have found two counterintuitive features in all studied correlated wire-substrate models. First, strong wire-substrate hybridization is not detrimental to 1D physics but strong interactions in the wires may cause a transition to a 3D phase. Second, 1D phases exhibit an “inverse” dimensional crossover from 1D low-energy excitations to 3D high-energy excitations.

1.5.3. Surface-mediated quasi-1D long-range order

The above discussion shows that a substrate-mediated coupling can play a significant role in the ground-state and excited state properties of atomic wire models. Another important question is whether such a coupling can stabilize a strongly anisotropic symmetry-breaking long-range order when the direct coupling is a priori too weak to allow for the observation of quasi-1D ordered phases in atomic wire systems at finite temperature.

To demonstrate this effect we have devised and studied a simple generalization of the Ising model [12]. Our model is a bi-layer Ising model on a square lattice with couplings between nearest-neighbor spins $s_{x,y,z} = \pm 1$. Within one layer ($z = 1$) the spins interact ferromagnetically in both x and y directions with the exchange coupling strength $J_s > 0$. This layer represents the substrate surface. The other layer ($z = 2$)

represents the atomic wires. Here the spins are coupled antiferromagnetically in the x -directions with an exchange constant $J_w > 0$ to mimic the intrachain interactions but do not interact directly in the y -direction (i.e., there is no direct interchain interaction). The layers are coupled ferromagnetically with an exchange constant $J_{ws} \geq 0$ that represents the wire-substrate coupling. The energy of a spin configuration $s = \{s_{x,y,z}; x = 1, \dots, L_x, y = 1, \dots, L_y, z = 1, 2\}$ is given by

$$E(s) = -J_s \sum_{x,y} (s_{x,y,1} s_{x,y+1,1} + s_{x,y,1} s_{x+1,y,1}) + J_w \sum_{x,y} s_{x,y,2} s_{x+1,y,2} - J_{ws} \sum_{x,y} s_{x,y,1} s_{x,y,2}. \quad (16)$$

Note that quasi-1D magnetism can be realized in atomic spin chains on semiconducting, metallic or superconducting surfaces [35]. The role of the substrate and the effect of strong coupling between spin chains and the substrate electron bath were investigated previously in that context.

The bi-layer Ising model cannot be solved exactly in the general case but interesting conclusions can be drawn in limiting cases. First, the system is exactly solvable when both layers become decoupled ($J_{ws} \rightarrow 0$). The substrate layer is just the isotropic 2D ferromagnetic Ising model, which undergoes a transition from a long-range ordered ferromagnetic phase to a disordered paramagnetic phase at a finite critical temperature given by (15) with $J_x = J_y = J_s$ [93], as discussed in sec. 1.4.1. The substrate magnetization m is shown as a function of temperature in Fig. 8 for this case. The wire layer is made of L_y independent 1D antiferromagnetic Ising chains, which are disordered for any temperature $T > 0$. Thus there is no quasi-1D order at finite temperatures and the staggered magnetization is $m_{AF} = 0$. Second, the system is exactly solvable in the strong-coupling limit $J_{ws} \rightarrow \infty$ because each spin pair $s_{x,y,1}$ and $s_{x,y,2}$ must be ferromagnetically ordered and thus can be treated as a single spin. Therefore, the model of eq. (16) reduces to an anisotropic 2D Ising model with couplings $J_x = J_s - J_{ws}$ and $J_y = J_s$. For $J_{ws} > J_s$ and low temperatures the system is antiferromagnetically ordered in the x -direction (and ferromagnetically ordered in the y -direction). It undergoes a transition to a disordered paramagnetic phase above a critical temperature given by eq. (15) with $|J_s - J_{ws}|$ substituted for J_x . The wire staggered magnetization m_{AF} is shown in Fig. 8 as a function of temperature for the case $J_w > 2J_s$ ($\Leftrightarrow |J_x| > J_y$). Thus the quasi-1D antiferromagnetic order favored by the wires is stabilized by the coupling with the substrate. Thirdly, one can easily determine the ground-state phase diagram. The quasi-1D antiferromagnetic ordered phase occurs for $J_s < J_w$, $J_{ws}/2$ at $T = 0$ and thus it is not an artefact of the strong-coupling limit $J_{ws} \rightarrow \infty$. Finally, the intermediate regime $0 < J_{ws} < \infty$ at finite temperature has also been investigated using analytical (e.g. chain mean-field [228]) and numerical (e.g. Monte Carlo [94]) methods.

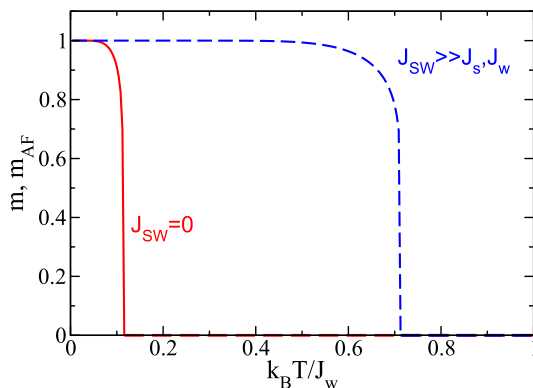


Fig. 8. Magnetization as a function of temperature in the bi-layer Ising model for wires on a substrate: substrate magnetization m (solid red line) for $J_{ws} = 0$ and staggered magnetization m_{AF} in the wires (blue dashed line) for $J_{ws} \rightarrow \infty$ and $J_w > 2J_s$. (For interpretation of the references to color in this figure legend, the reader is referred to the Web version of this article.)

Preliminary results agree with the scenario deduced from the limit cases.

In conclusion, in the bi-layer Ising model the substrate favors a 2D ferromagnetic order at low temperatures. The wires favor a 1D antiferromagnetic order, which is unstable at any finite temperature in the absence of the wire-substrate coupling but is stabilized at low temperatures as a quasi-1D order when this coupling is strong enough. Therefore, this model demonstrates the idea of a surface-mediated stabilization of a quasi-1D long-range order. This mechanism could explain the observation of various symmetry-breaking long-range ordered phases in atomic wires on semiconducting surfaces at relatively large temperature although the direct coupling is probably weak in these 2D systems of well-separated wires. Moreover, we note that a strong coupling between wires and substrate is favorable to the observation of quasi-1D physical properties as found for the correlated wires discussed above.

1.5.4. Summary: influence of substrate

The role of the substrate is clearly important but far from being understood. Some features of 1D physics survive the coupling to the substrate and can even be strengthened by it e.g. Luttinger liquid behavior and quasi-1D symmetry-breaking long-range ordering as discussed above. Assuming a weak wire-substrate coupling is not necessary as quasi-1D properties can be preserved even when this coupling is very strong.

An important observation is that theoretical results for wire-substrate systems depend on details of the models considered, as for coupled chain systems. Thus quasi-1D systems that are embedded in the 3D environment do not seem to exhibit “universal” features contrary to the theoretical predictions for strictly 1D systems. Consequently, we also expect experimental results for atomic wires on surfaces to vary significantly for different materials. Therefore, material-specific studies are required to predict the experimental signature of 1D physics in the presence of a substrate. We will present two such studies in the next two sections about the relevance of the Peierls physics for In/Si(111) and of the Luttinger liquid phenomenology for Au/Ge(100).

1.6. Grand-canonical Peierls theory

The Peierls theory [1,4,5,10,17,28,34] is often invoked to explain features of atomic wires deposited on surfaces. A well-known example is the low-temperature phase and the transition observed in indium wires on the Si(111) surface. The interpretation of the experimental observations is still intensively debated, however [16,46–56]. Experiments and first-principles simulations for this material are presented in detail in sec. 2.3 and 3.

Indium wires on Si(111) surfaces build a 2D array of weakly-coupled chains. A chain is made of 4 parallel strands of indium atoms. In the high temperature “uniform” phase a unit cell contains 4×1 atoms. A metal-insulator transition and a structural transition occurs at a temperature $T \approx 120$ K. The commensurate structural transition changes the unit cell from 4×1 at high temperature to 8×2 (or 4×2) at low temperature.

There is a well-established theoretical framework to describe quasi-1D Peierls-CDW systems at a fixed electronic density [1,4,5,10,17,28,34]. The simplest theory for a commensurate Peierls-CDW is based on a static mean-field approximation without interchain coupling, thus neglecting spatial and thermal fluctuations. It explains how a metal-insulator transition occurs from the degenerate insulating CDW state at low temperature to a metallic state with uniform density at high temperature. Simultaneously, a structural transition takes place from the distorted lattice (i.e. with a larger unit cell) to the uniform lattice (i.e. with a smaller unit cell). This Peierls transition is continuous and the distortion amplitude or the electronic gap can be used as an order parameter.

Thus it seems that a simple multi-band, multi-mode generalization of the canonical Peierls theory [4] could describe the In/Si(111) system. However, experimental evidence shows that the transition is first order

[47,48,50,53,55]. First-principles simulations offer further evidence for a first-order transition [54]. At least the uniform metallic state seems to remain metastable below the critical temperature.

Therefore, we have generalized the Peierls theory to take into account the peculiarities of atomic wires on surfaces. To this end we have pursued two complementary approaches based on the SSH lattice model and the Ginzburg-Landau theory, respectively. The key idea is that the substrate acts as a charge reservoir and thus the phase transition must be described in the grand-canonical ensemble. This insight has allowed us to explain the first-order Peierls-like transition observed in In/Si(111) theoretically.

1.6.1. SSH model for In/Si(111)

In a first step, we have constructed an effective quasi-1D model for indium wires [52] in the spirit of the Su-Schrieffer-Heeger (SSH) model [18,34,61,62]. This lattice model described originally a Peierls-CDW system with one electronic band and a variation of the distance between atoms coupled to a CDW on the bonds between these atoms (i.e. a BOW). We have generalized it to describe all relevant electronic and lattice degrees of freedom in In/Si(111) using the atomic and electronic structure predicted by first-principles calculations [16].

This model has allowed us to demonstrate that the low-temperature phase of In/Si(111) is a Peierls-CDW insulator with two lattice distortion modes made of the shear and rotary eigenmodes [52]. The doubling of the unit cell in the wire direction can be interpreted as the dimerization of three weakly-coupled chains, two outer linear chains and one central zigzag chain, as shown in Fig. 9. We have compared variations of the lattice distortion and electronic band structure predicted by our model with first-principles calculations to determine the appropriate model parameters for In/Si(111).

In a second step, we have investigated the thermodynamics of this generalized SSH model in the grand canonical ensemble using a mean-field approximation. We have found that the transition between the low and high temperature phases can be interpreted as a grand canonical Peierls transition: i.e., the substrate acts as a charge reservoir for the indium wire subsystem and sets the chemical potential μ . The grand-canonical Peierls physics is much richer than the canonical one. In particular, a thermodynamically metastable uniform state can coexist with a stable doubly-degenerate dimerized state for a narrow range of the chemical potential, but over a wide temperature range below the critical temperature. The existence of this phase agrees qualitatively with the energetics of the phase transition in In/Si(111) calculated from first principles [48]. A significant difference with the usual (i.e.,

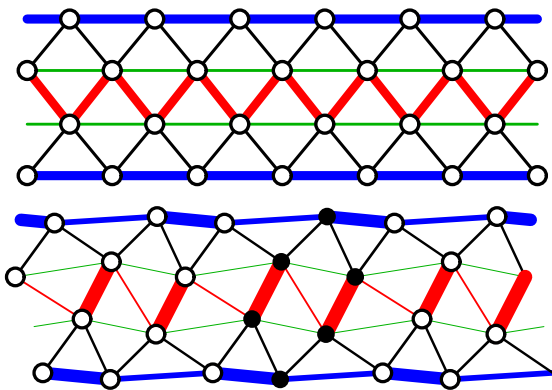


Fig. 9. Uniform (top) and dimerized (bottom) lattice of the generalized SSH model for one indium wire. Circles represent the indium atoms. Their positions are given by first-principles calculations. The line widths are proportional to the bond density. Red bonds define the inner zigzag chain while blue bonds correspond to the two outer linear chains. Solid circles outline one hexamer in the dimerized lattice. (For interpretation of the references to color in this figure legend, the reader is referred to the Web version of this article.)

canonical) Peierls theory is that the phase transition can become first order, in agreement with the interpretation of experiments and first-principles calculations for this material [47,48,50,53–55]. This model also explains naturally the sensitivity of the transition to doping [229–231].

1.6.2. Generic theory

The generalized SSH model discussed above is intractable for analytical methods and thus has been studied mostly numerically because it includes several electronic bands and lattice deformation modes to reproduce the specific atomic and electronic structure of In/Si(111). The original SSH model (like other basic models for Peierls-CDW systems) includes one site per unit cell of the uniform lattice (i.e., one electronic band) and one lattice distortion mode [18,34,61,62]. This simplicity allowed researchers to derive the generic canonical Peierls theory analytically decades ago.

Therefore, we have derived a generic one-band one-mode 1D SSH model from the generalized SSH model for In/Si(111) [52,232]. This amounts to assuming that the two outer and the single inner strands of indium atoms build separate 1D electron systems, which are coupled to one (shear or rotary) lattice deformation mode only. The appropriate model parameters for In/Si(111) are simply given by the generalized SSH model in first approximation. We have systematically investigated the simpler SSH model in the grand-canonical ensemble using mostly analytical methods in order to obtain generic results for period-doubling commensurate Peierls-CDW (i.e., for dimerization, see Fig. 10) [232]. Our study reveals a rich mean-field phase diagram, which is shown in Fig. 11 for parameters representing In/Si(111). In particular, the high-temperature uniform metallic state can remain thermodynamically metastable below the critical temperature for the dimerized state. Thus the structural Peierls phase transition between regions with metastable uniform and dimerized states can be first order as a function of temperature for a fixed chemical potential. Moreover, a first-order metal-insulator transition can occur at a lower temperature than the continuous structural transition.

Various aspects neglected in this simple model should be investigated in the future, but we are confident that our main findings will remain relevant. First, as discussed in sec. 1.4 the coupling between wires is necessary to stabilize long-range-ordered phases like a Peierls-CDW at finite temperature, but this effect is well understood. The extension of the 1D SSH model to a 2D array of wires is straightforward, and we have actually used it to obtain parameters for the generalized SSH model from first-principles simulations [52] as well as for simulations of the non-equilibrium dynamics (see below). However, the direct coupling between wires is very weak. Our estimate is 10^{-3} eV for the direct hopping terms between nearest-neighbor wires in the generalized SSH model. This weak direct coupling cannot explain the experimental critical temperature $T \approx 10^2$ K. Therefore, it is likely that an effective coupling mediated by the substrate plays an important role in the stabilization of the dimerized structure in In/Si, as discussed in sec. 1.5. Second, the substrate could act as a static external field driving a CDW and a lattice distortion in the wires with a particular wave vector set by the surface periodicity rather than the Fermi nesting $2k_F$ as discussed in sec. 1.5.1. Finally, the dimerized states of the 1D SSH model are

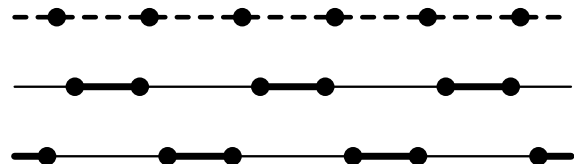


Fig. 10. Uniform lattice (top) and the two dimerized lattices (middle and bottom) of a generic 1D SSH model. Disks represent the sites (atoms) while the different line widths represent the bond strength (bond density or hopping term).

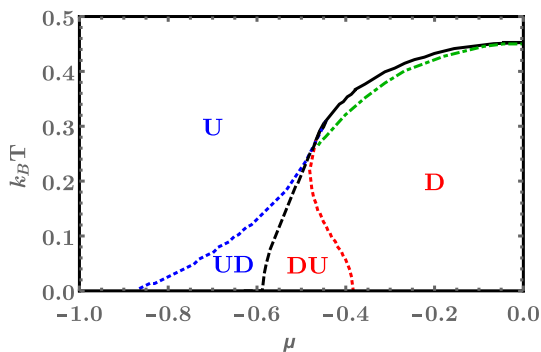


Fig. 11. Grand-canonical phase diagram (μ, T) of the 1D SSH model in the mean-field approximation. The four phases are: uniform phase (U), dimerized Peierls-CDW phase (D), phase with one stable uniform state and two metastable dimerized states (UD), and phase with two stable dimerized Peierls-CDW states and one metastable uniform state (DU). The solid line indicates the usual continuous Peierls phase transition while the dashed line indicates the first-order transition between the UD and DU phases. Metastable states exist below the dotted lines. The green dot-dashed line indicates the position of the first-order metal-insulator transition within the dimerized phase. The energy unit is set by the intrachain hopping t_x . (For interpretation of the references to color in this figure legend, the reader is referred to the Web version of this article.)

probably unstable with respect to the formation of domain walls between dimerized regions with different phases (i.e. the two possible dimerized lattices in Fig. 10) [18,34,61–64]. Topological solitons and solitonic excitations have been reported for the In/Si(111) material [131–137]. However, the substrate periodic potential is probably unfavorable to the formations of domain walls and incommensurate distortions. Therefore, the substrate should be taken into account beyond its role as a charge reservoir to improve the present Peierls theory for atomic wire materials. For instance, substrate effects could be studied in the future using the method discussed in sec. 1.5.2 for correlated wires.

Nevertheless, we have derived a generic grand-canonical Peierls theory using a mean-field solution of the 1D SSH model. This theory allows us to explain the occurrence of first-order Peierls transitions as found experimentally in In/Si(111). It also allows us to determine parameters for the Ginzburg-Landau theory.

1.6.3. Ginzburg-Landau theory

The presence of the metastable uniform phase should be visible in some experiments. Two examples are the phonon spectrum measured in Raman spectroscopy [233] and photoexcited phase transitions [234] (see also sec. 3). To study these properties we have to calculate the time evolution of (grand-canonical) Peierls systems out of equilibrium.

1.6.3.1. SSH dynamics. The nonequilibrium dynamics of Peierls insulators can be calculated within the SSH theory using the adiabatic approximation for the electronic degrees of freedom and a semiclassical approximation for atom displacements. This approach was already used in the original SSH works to simulate solitons in polyacetylene [61,62]. We have applied this approach to 2D arrays of SSH chains coupled by an interchain hopping assuming that electrons remain in a (grand-canonical) thermodynamical equilibrium for each instantaneous atomic configuration. Although the model is too complicated for an (even approximate) analytical solution, its dynamics can be investigated numerically. We have found that it is dominated by long-lived metastable domain walls between finite-length segments of the three configurations illustrated in Fig. 10. Consequently, extremely long simulation times are necessary to obtain accurate numerical results and we have not been able yet to gain information that could be compared to experiments.

1.6.3.2. Ginzburg-Landau dynamics. Thus we have turned to a simpler theoretical approach to study the nonequilibrium dynamics of grand-canonical Peierls-CDW systems. The Ginzburg-Landau theory [110, 111] is a well-established approach to study thermal fluctuations and nonequilibrium dynamics of the order parameter in systems undergoing a continuous phase transitions with a spontaneous symmetric breaking described by an order parameter [112]. It has been extensively applied to explain the properties of Peierls-CDW [4,5,28,108], in particular for the continuous Peierls transition occurring in the canonical ensemble. If one focuses on the vibration spectrum or the structural phase transition, it is convenient to use the amplitude of the lattice distortion q as the order parameter. This order parameter is a real because phase modes are locked (or gapped) for commensurate Peierls-CDW. Within the adiabatic approximation, this quantity is proportional to other common order parameters, e.g. the amplitude of the CDW $\delta\rho$ in Equ. (9) or the single-particle gap 2Δ , see Equ. (10).

The 1D dynamical Ginzburg-Landau equation is

$$m \frac{\partial^2 q}{\partial t^2} = -\kappa \frac{\partial^2 q}{\partial x^2} - \frac{\partial V}{\partial q} - \gamma \frac{\partial q}{\partial t} \quad (17)$$

for the spatial and temporal variations of the order parameter $q(x, t)$, where m can be interpreted as the effective mass of the amplitude mode, κ as the stiffness for spatial variations of the amplitude, and γ as a friction coefficient. In the Ginzburg-Landau theory for continuous phase transitions, $V(q)$ is the Landau free energy, which is usually approximated by

$$V(q) = aq^2 + bq^4 \quad (18)$$

with a temperature-dependent coefficient $a = \alpha \cdot (T - T_c)$, ($\alpha > 0$) and a constant coefficient $b > 0$. Fig. 12 shows the two typical shapes of the Landau free energy for the dimerized and uniform phases of a Peierls-CDW system. In principle, all parameters but the friction coefficient can be derived from microscopic models for Peierls-CDW systems, such as the SSH model discussed above. Alternatively, they can be determined from first-principles or experimental data for a specific material. The Ginzburg-Landau approach can also be applied to 2D or 3D arrays of chains [228,235,236] and several lattice distortion modes [4] as required for a more realistic description of In/Si(111).

An external harmonic perturbation $g \sin(\omega t) \cos(kx)$ can be added to the Ginzburg-Landau equation (17) to generate collective excitations involving both the lattice distortion and the electronic charge distribution. The linear response function $S(\omega, k)$ (for $g \rightarrow 0$) is obtained through

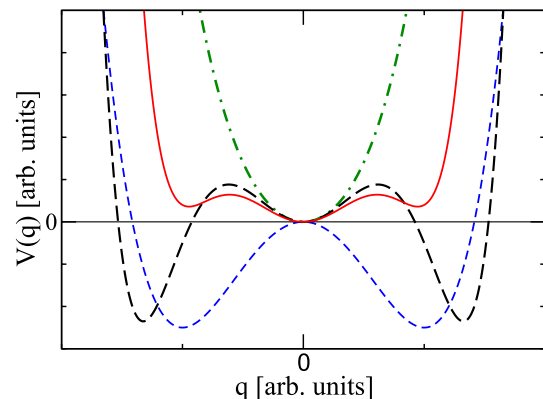


Fig. 12. Typical shapes of the Landau grand-canonical potential (19) as a function of the order parameter q for the four phases in Fig. 11. The green dash-dotted curve corresponds to the uniform phase (U), the blue dashed curve to the dimerized Peierls-CDW phase (D), the black long-dashed curve to the phase with two stable dimerized Peierls-CDW states and one metastable uniform state (DU), and the red solid curve to the phase with one stable uniform state and two metastable dimerized states (UD). (For interpretation of the references to color in this figure legend, the reader is referred to the Web version of this article.)

the Fourier transform of the resulting trajectory $q(x, t)$ at long times t . Moreover, one can use the Langevin dynamics [237] to simulate thermal fluctuations. For this purpose a memoryless random force $\sqrt{2\gamma k_B T} R(t)$ is added to the equation of motion (17), where $R(t)$ is a normalized random variable. This allows one to study dynamical structure factors for collective excitations as a function of temperature and nonequilibrium phase transitions [238]. Alternatively, finite-temperature properties can also be calculated using statistical ensemble averages [239]. For instance, the dynamical structure factor was calculated using Monte Carlo simulations [118].

One can simulate photoexcitation experiments using excitation pulses or metastable initial conditions with the Ginzburg-Landau equation (17). In particular, this method can be used to mimic the photoinduced structural transition found in In/Si(111) [48,240–245]. For ultrafast spectroscopy experiments, however, it is questionable whether the electronic charge density follows the lattice motion adiabatically. It may be necessary to allow for retardation effects and thus to treat the electron CDW $\rho(x, t)$ and the lattice distortion $q(x, t)$ as two separate (but coupled) fields in a generalization of the Ginzburg-Landau theory [246]. For instance, this separation of electronic and lattice fluctuations has been recently used to discuss femtosecond time-resolved spectroscopy experiments in a quasi-1D blue bronze [247,248].

1.6.3.3. Grand-canonical theory. We have generalized this nonequilibrium Ginzburg-Landau theory to the grand-canonical first-order Peierls transition. The Landau free energy (18) is replaced by an expansion of the grand-canonical potential in power of $|q|$

$$V(q) = aq^2 + b|q|^3 + cq^4 + d|q|^5 + fq^6 \quad (19)$$

in the Ginzburg-Landau equation (17). The typical potential shapes are sketched in Fig. 12 for the four phases found in the grand-canonical phase diagram. The parameters a, b, c, d and f depend on the temperature T and the chemical potential μ but they can be derived from the grand-canonical potential of the SSH model [52,232], at least numerically, and thus indirectly from first-principles calculations or experimental data. Similar generalizations of the Landau free energy were used to study the interplay of commensurate and incommensurate CDW within the Ginzburg-Landau theory [249,250].

Nevertheless, dynamical structure factors and relaxation dynamics are largely unknown for the regime corresponding to the grand-canonical Peierls theory. Thus we have solved the dynamical Ginzburg-Landau equations numerically under various conditions (e.g., with and without thermal or spatial fluctuations). We have found that physically interesting quantities, e.g. the linear response function $S(\omega, k)$, depend not only on these precise conditions but also on minute changes of model parameters or initial conditions. In particular, the linear response function fluctuates widely with the external perturbation frequency ω . From a mathematical point of view these dynamical systems exhibit spatiotemporal chaos [112] for various parameter regimes. From a physical point of view, this erratic behavior (as well the SSH dynamics discussed above) reveals that the present approach is not able to describe the nonequilibrium dynamics of Peierls-CDW in atomic wire systems. In contrast to the real materials, it seems to lack a mechanism stabilizing the 2D Peierls-CDW order with respect to thermal and spatial fluctuations. This could be the pinning of domain walls by the periodic substrate potential discussed in sec. 1.5.1. Therefore, we have obtained few relevant results for the nonequilibrium dynamics so far. Below we discuss only results for the Raman spectrum of collective amplitude oscillations that can be obtained assuming that thermal and spatial fluctuations are negligible.

1.6.3.4. Amplitude oscillation mode. Raman spectroscopy is a powerful experimental method for determining vibration eigenmodes of low-dimensional self-organized surface structures [233]. The Peierls theory predicts the existence of Raman-active collective excitations (electronic

CDW and lattice vibrations), which correspond to amplitude oscillations of the order parameter q around its equilibrium configuration [4,18,28,34,118,129,130]. They have been observed experimentally in various quasi-1D bulk material, e.g. blue bronze [251] and polyacetylene [252]. For continuous transitions, the canonical Peierls theory predicts a softening of the eigenfrequency Ω for the Peierls wave number $Q = 2k_F$ close to the critical temperature T_c (Kohn anomaly). If we neglect thermal and spatial fluctuations in the Ginzburg-Landau theory, we recover the well-known mean-field result for the frequency associated to amplitude oscillations

$$\Omega(T) \sim \sqrt{|T - T_c|} \quad (20)$$

for $T \rightarrow T_c$. In the dimerized phase (i.e., for $T \rightarrow 0$) the softening is given by $\Omega^2 = 2\lambda\omega_0^2$ where $\lambda(\ll 1)$ is the electron-phonon coupling constant and ω_0 is the bare phonon frequency (i.e. without the electronic CDW) [18,34,232,253].

We have studied the behavior of these amplitude oscillations through the first-order transition in the grand-canonical Peierls theory. Fig. 13 shows the frequency Ω as a function of temperature. We see that the oscillation frequency in the thermodynamically stable dimerized states diminishes progressively as the temperature rises. At the critical temperature it jumps to the lower oscillation frequency around the thermodynamically stable uniform state, then it varies non-monotonically but smoothly as the temperature increases further. This discontinuous behavior is in strong contrast to the complete softening (20) through a continuous transition in the canonical Peierls theory. In Fig. 13 we also see that oscillation frequencies in the metastable configurations extend smoothly the curves obtained for the stable states. Note that amplitude oscillations have the wave number $Q = 2k_F = \pi/a$ but they appear at $Q = 0$ in experiments in the dimerized phase because of the Brillouin zone folding.

Raman scattering experiments for In/Si(111) [52,53], in particular the temperature dependence of the Raman resonance frequencies, agree qualitatively with these theoretical predictions and thus confirm that the transition observed in In/Si(111) can be seen as a first-order grand-canonical Peierls transition. The Peierls amplitude modes, which are essentially the shear and rotary modes, appear at the Γ point below T_c and show a significant but incomplete softening close to the transition

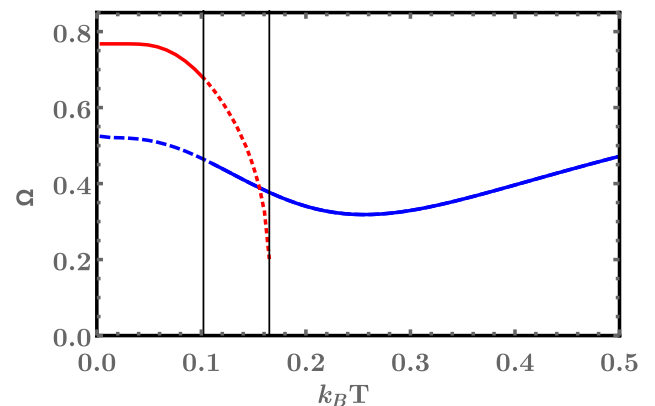


Fig. 13. Eigenfrequency Ω for amplitude oscillations of the order parameter in the dimerized state (red) and in the uniform state (blue) as a function of temperature. The left vertical line indicates the critical temperatures for the first-order Peierls transition while the right vertical line indicates the temperature above which the dimerized state vanishes. The solid lines show the frequency in the thermodynamically stable states with a jump at the first order transition. The dashed lines show the frequency for the metastable states. The frequency Ω is given in units of the bare phonon frequency ω_0 and the temperature is given in units of the intrachain hopping t_s , see Ref. [232] for details. (For interpretation of the references to color in this figure legend, the reader is referred to the Web version of this article.)

between the 4×1 and 8×2 phases. To explain the temperature dependence of the line shapes observed in the Raman spectrum (position and width of resonances), we probably would have to take into account thermal and spatial fluctuations [4,118,254] as well as non-adiabatic effects [247,248].

1.6.4. Summary: Peierls theory

In summary, we have shown that the low-temperature phase and transition observed in In/Si(111) can be explained by a simple model of Peierls-CDW insulators in the grand-canonical ensemble. We think that the ongoing controversy about the nature of the low-temperature physics in In/Si(111) can be solved by interpreting experiments and first-principles simulations within a grand-canonical Peierls theory. More generally, the present work suggests that the substrate-induced chemical potential is a key mechanism for understanding the properties of quasi-1D physics in atomic wires on surfaces.

1.7. Dimensionality of metallic atomic wires

As explained in sec. 1.3.5 the low-energy long-wavelength properties of strictly 1D metallic systems obey the universal Luttinger liquid phenomenology. Experimental signatures of Luttinger liquid have been observed in various atomic wires on semiconducting surfaces such as Au/Ge(100) [37], Bi/InSb(001) [174], and Pt/Ge(001) [175]. We have seen in sec. 1.5 that Luttinger liquids can survive the coupling to a gapped substrate. Although the interchain coupling is generally detrimental to a Luttinger liquid, we have argued in sec. 1.4 that characteristic Luttinger liquid features may be observed in quasi-1D systems due to a dimensional crossover. However, a question remains as to whether metallic phases found experimentally in atomic wire systems can be seen as 2D arrays of weakly-coupled Luttinger liquid chains or whether strongly anisotropic 2D Fermi liquids provide better theoretical descriptions.

For instance, the nature and dimensionality of the metallic state in gold wires on Ge(100) surfaces is controversial. On the one hand, Au/Ge(100) exhibits highly anisotropic properties and the power-law behavior of the density of states at the Fermi energy (14) that is predicted by the Luttinger liquid theory [37–40]. On the other hand, Au/Ge(100) exhibits an anisotropic 2D metallic dispersion at the Fermi energy, which seems to rule out a quasi-1D electronic system [41–44].

To shed some light on this issue we have investigated the low-energy collective charge excitations in 2D correlated models representing strongly anisotropic lattices or weakly coupled chains using well-established theoretical approaches [205,255]. These excitation modes are called plasmons in the theory of ordinary metals and can be described in the framework of the Fermi liquid theory in reduced dimensions. Their counterparts are called holons in the Luttinger liquid theory of correlated strictly 1D systems, see sec. 1.3.5. It is often assumed that the long-wavelength dispersion of plasmons $E(\vec{k})$ reveals metallic states with reduced dimensions because $E(\vec{k}) \propto \sqrt{|\vec{k}|}$ in an isotropic 2D metal [256] but $E(k) \propto |k|$ in a 1D metal [30] for $k, |\vec{k}| \rightarrow 0$. However, theoretical results are less clear for anisotropic systems or systems made of coupled chains [202–204,257–260]. Experimentally, low-dimensional plasmons have been observed in various atomic wire systems, such as Au/Si(557) [259], In/Si(111) [261,262], Pb/Si(557) [263], Ag/Si(557) [264], Au/Si(553) [265,266], and Au/Ge(100) [255], as well as in ultrathin metallic silicide wires [267]. See also sec. 2.5.

First, we have used the random phase approximation to study a lattice model with the anisotropic 2D single-particle dispersion (5) and a general isotropic interaction between electrons [28,30]. This approach reproduces the usual results for plasmons in 1D Fermi liquids ($t_x/t_y = 0$) and in isotropic 2D Fermi liquids ($t_x = t_y$) in the case of an unscreened Coulomb interaction. Second, we have used field theory to study a

system of coupled Luttinger liquid chains with the intrachain dispersion (13) plus low-momentum-transfer processes (forward scattering) of a general long-range and isotropic interaction between electrons [6,204]. As interchain hopping is omitted, the Luttinger liquid phase is stable and the model can be solved using a simple bosonization method. Some resulting holon dispersions are shown in Fig. 14. We see that this approach is able to reproduce the peculiar plasmon dispersion measured in the Au/Ge(100) material with electron energy loss spectroscopy [255], albeit with an *ad hoc* Gaussian interaction potential and Luttinger liquid parameters that are incompatible with photoemission experiments [38,44]. This Gaussian interaction potential results in a dimensional crossover in the holon excitation spectrum from a 2D dispersion for low energy and long wavelength to a 1D dispersion for high energy and short wavelength. Additionally, we have studied strongly correlated spinless fermion ladders coupled by short-range interactions using the exact Bethe Ansatz solution in a special case and the numerical DMRG method for the general case (see sec. 1.2.4).

We have found no qualitative difference between the theoretical predictions for the dispersion of collective charge excitations (plasmons and holons) at long wavelengths in strongly anisotropic 2D Fermi liquids and quasi-1D Luttinger liquids [205], as already reported for strictly 1D systems [268]. With both approaches the dispersion $E(\vec{k})$ is anisotropic and its behavior for $\vec{k} \rightarrow 0$ depends mostly on the screening of the Coulomb interaction between charge carriers. The dispersion can have a significant bandwidth in both the chain direction and the interchain direction even when the system is a strongly anisotropic (i.e., quasi-1D) conductor. Thus a 2D holon dispersion could be visible in the spectral function (and thus in ARPES experiments), similarly to the 1D case discussed in sec. 1.3.5, while the system also exhibits some Luttinger liquid properties, such as the power-law behavior (14) of the density of states at the Fermi energy (visible in STS experiments).

In summary, we are not able to distinguish between a strongly anisotropic 2D Fermi liquid and a system of weakly-coupled Luttinger liquid chains. Moreover, the dispersion of plasmons or holons at long wavelengths does not reveal the system dimension. Obviously, these theoretical findings are based on approximate methods and simplified models. In particular, this study neglects other aspects that are known to be important for atomic wire systems, such as the interchain hopping (see sec. 1.4.2), the substrate coupling (sec. 1.5.2), and the role of the

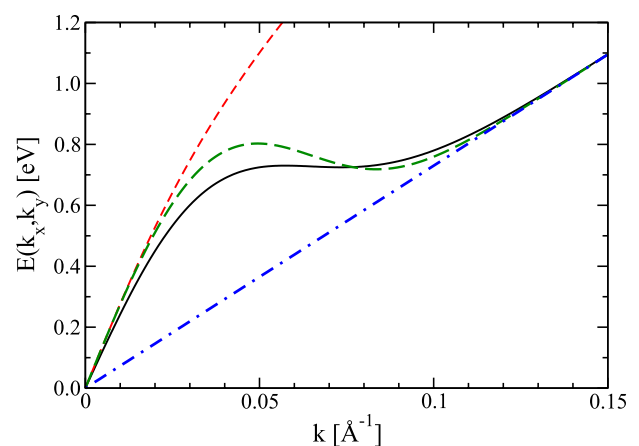


Fig. 14. Upper edge of holon dispersions in 2D arrays of Luttinger liquids as a function of the wave vector norm. The red dashed and green long-dashed curves correspond to a screened Coulomb potential and a phenomenological Gaussian potential, respectively. The blue dash-dotted curve is the intrachain dispersion of uncoupled Luttinger liquids (13). The solid black curve represents a fit to experimental data for plasmons in Au/Ge(100) [255]. In all cases model parameters are chosen so as to fit this “experimental curve”. (For interpretation of the references to color in this figure legend, the reader is referred to the Web version of this article.)

substrate as a charge reservoir (sec. 1.6). Nevertheless, these findings offer a simple explanation for the controversy about the dimensionality of Au/Ge(100). Metallic phases of atomic wire materials could exhibit signatures of both anisotropic 2D Fermi liquids and quasi-1D Luttinger liquids depending on the experimental conditions. This may be the counterpart of the dimensional crossover found in quasi-1D crystalline materials and discussed in sec. 1.4.3.

1.8. Summary phenomenological theory

At first sight, atomic wires deposited on semiconducting surfaces seem to be the ultimate realization of 1D electron systems. In reality, they build 2D arrays of coupled chains and they are inherently 3D systems due to the presence of the substrate. Thus theory must take into account the coupling of atomic wires to their environment to explain the existence of quasi-1D electron systems and to identify their experimental signatures.

In this chapter we have reviewed our theoretical understanding of strictly 1D physics and quasi-1D physics, which is based on effective theories for the relevant low-energy degrees of freedom. This approach reveals that the coupling of atomic wires to their environment (coupling between wires and wire-substrate coupling) does modify their theoretical properties. Nevertheless, the peculiar physics of strictly 1D electron systems (e.g., Peierls transition or Luttinger liquid phenomenology) can survive this coupling and be experimentally observable in atomic wire materials.

An important observation is that theoretical results for quasi-1D systems depend on details of the effective models considered. Consequently, we do not expect atomic wires on surfaces to exhibit “universal” features, contrary to (hypothetical) strictly 1D systems. Thus material-specific theoretical studies are required to describe quasi-1D physics in atomic wire systems, even when one uses a theoretical approach based on effective low-energy models. Here we have discussed two examples: the Peierls theory for indium wires on the Si(111) surface and the Luttinger liquid theory with a view to gold wires on the Ge(100) surface.

In conclusion, atomic wire materials offer unprecedented opportunities to observe and control real quasi-1D electron systems. This calls for a major effort to understand these materials theoretically and to advance our knowledge of 1D physics in the real world.

2. The role of spin and charge in quasi-1D experimental systems: order, entanglement, conductivity, phase transitions

2.1. Introductory remarks

In this section we turn to experimental realizations of 1D or quasi-1D systems. From the large variety of possibilities such as quantum wires, nanowires, nanorods, or nanotubes [144,269,270], we have chosen the class of atomic wires with a height of just one atomic or molecular unit, adsorbed on insulating single crystalline substrates of silicon and germanium. These wires can be generated as perfectly ordered arrays of single, double or multiple strands of atoms with high precision. They thus offer an attractive approach towards quasi-1D physics.

Necessarily, as explained in the previous section, quasi-1D objects need stabilization by interaction with their 2D and 3D environment in order to be experimentally accessible. Indeed, stabilization of such quasi-1D systems by interaction with an (insulating) substrate is one of the most common strategies pursued in the recent past [144,146,271, 272]. As also shown in the previous section, these interactions in higher dimensions may both stabilize, but in most cases modify or even destroy typical phenomena of 1D physics such as Peierls transitions, charge and spin density waves [205]. On the other hand, unexpected new phenomena may appear due to electronic correlations between adsorbed 1D chains and substrate, such as spin-orbit density waves [139] or enforced geometric long range order induced by a randomly distributed adsorbate

[273].

Therefore, it is the aim of this experimental section, not only to identify typical 1D phenomena that have survived despite of 3D interactions, but also to get more insight into such interactions on the atomic scale by close collaboration between experiment and theoretical simulation, thereby also explaining part of the new and unexpected phenomena that are associated with these interactions in higher dimension. The knowledge of these mechanisms opens perspectives towards precise manipulation of the properties of such objects, but no “universality” can be claimed (see also sec. 1.4). Thus these systems may offer attractive perspectives towards technological applications in nanoscale devices (e.g., as building blocks for nanoscale electronics).

Regarding the electronic properties, this section deals with quasi-1D wires in which the wire states interact with substrate states that are decoupled from the bulk [274]. In other words, 1D electronic states of the chain system hybridize with surface electronic states that are located in the energy gap of the substrate band structure [274,275].

The most prominent class of these systems consists of metallic stripes or chains formed by self-organization on flat [46,276] or regularly stepped Si crystal surfaces [16,277,278]. On the latter, submonolayers of Pb [279] and Ag [264] mostly fill the whole mini-terrace, whereas Au forms self-organized single or double-atomic chains. These ordered arrays of atomic chains on the Si mini-terraces of varying width provide a widely variable playground to study various quantum phenomena [280]. The entanglement of hybrid bands of the Si surface and Au chain states, e.g., lead to adsorbate-induced non-local changes of charge distribution, with corresponding consequences to electrical conduction and its temperature dependence [281,282]. On the contrary, the interaction of rare earth metals with Si surfaces is so strong that they form surface silicides. Nevertheless, the uni-directional match of unit cells leads to extremely anisotropic growth. Thus wires of varying width are formed depending on metal concentration and growth conditions.

This section we will give an overview of recent experimental and simulational results on such atomic wire systems, starting with Au atomic wires on stepped Si(hhk) surfaces. This class of systems is an illustration how non-local hybridization between adsorbate and surface states leads to electronic correlation, giving rise to quasi-1D modifications of the Si step edges that dominate the electronic properties close to the Fermi level. Latest results on the paradigmatic system In/Si(111) are discussed in section 2.3 with emphasis on the vibrational properties of this system. In fact, these results are crucial for an understanding of the dynamics and phase transition in this system described in section 3. The Pb/Si(557) system, discussed in section 2.4, is characteristic for strong electronic interactions of fairly long range leading both to reversible and irreversible phase transitions as a function of temperature. While the latter are manifested by refaceting of this surface, reversible anisotropic quasi-1D conductance, crucially depending on small changes in Pb concentrations, and formation of a spin-orbit density wave *normal* to the wire direction are observed. Plasmons in these quasi-1D systems, discussed in section 2.5, turn out to be strongly modified compared with pure 1D systems, and turn out to be sensitive to the unoccupied part of the quasi-1D bandstructure close to the Fermi level, which opens possibilities for a new kind of spectroscopy. Finally we turn to the properties of rare-earth silicide wires in section 2.6, in which we consider not only the geometrical, electronic and conductive properties, but also describe attempts to embed these wires completely into an Si environment.

2.2. Si(hhk)-Au: spin ordering vs. charge ordering²

There is a large family of Au-stabilized Si surfaces miscut from (111) toward or away from the [001] direction [16,283], collectively known as Si(hhk)-Au, see Fig. 15.

² Authors mainly responsible for this section: W.G. Schmidt, S. Sanna, M. Horn-von Hoegen, H. Pfnür

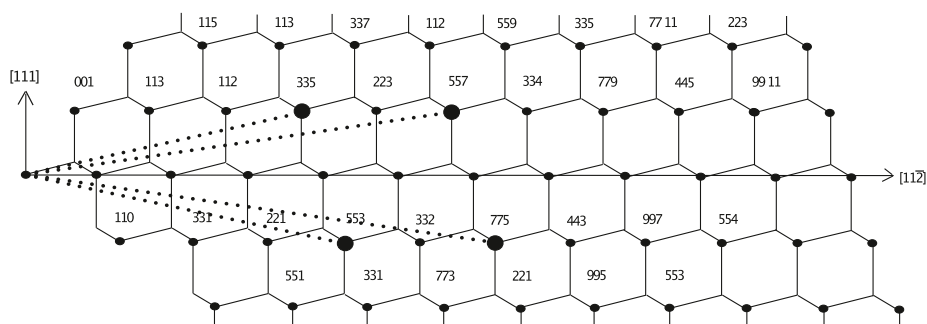


Fig. 15. Schematic view of the silicon lattice indicating the orientation of some relevant miscuts discussed in the following. Adapted from ref. [283].

They are all characterized by an alternation of terraces and steps and a small set of recurring structural motifs, as pointed out by Aulbach and co-workers [284]: The step edge is always a single-honeycomb graphitic strip of silicon. The terrace width varies according to the Miller indices (hhk). A chain of gold atoms, either one or two atoms wide, is incorporated on each terrace. In case of sufficiently wide terraces, a row of silicon adatoms is also present. These building blocks provide a fascinating playground to explore and induce spin and charge ordering phenomena in low-dimensional systems. Already in 1999, the Si(557)-Au surface was proposed to host a real-world example of spin-charge separation in a Luttinger liquid [285]. While the proposed spinon-holon splitting has later been ruled out by the observation of two separate Fermi level crossings [286], the Si(557)-Au surface is also discussed as a model system for the Rashba-type splitting of quasi one-dimensional electronic states due to spin-orbit coupling [287]. Pronounced Rashba-like spin textures have also been calculated for Si(335)-Au [288] and were in fact detected for Si(553)-Au [289,290]. Moreover, superstructures at the Si step edges have been explained in terms of antiferromagnetic spin order at supposedly singly occupied Si dangling bonds in case of Si(553)-Au [144,291]. In addition, structural transitions are observed as a function of STM current and temperature [146,292,293]. In contrast to Si(553)-Au, where spin polarization of the Si step edge dangling bonds had been proposed, spin order at Si(775)-Au is predicted to occur in the Si rest atom dangling bonds [294]. Obviously, as shown by the examples discussed above, the Si(hhk)-Au surface is indeed a source of an inspiring multitude of surface ordering phenomena. On the one hand, this is related to the fact that the interchain coupling and the band filling can be adjusted systematically by varying the step spacing via the tilt angle from Si(111) [283]. On the other hand, a further degree of freedom is added by the Au chain itself, which acts as an electron reservoir [295]. Additionally, defects and dopants such as O and H severely affect the spin and charge order at the surface, as explored, e.g. for Si(775)-Au [284], Si(557)-Au [296], and Si(553)-Au [295].

One member of the family of Si(hhk)-Au surfaces has found particular attention: The Si(553)-Au provoked much interest in the scientific community by the suggestion that it is an example for the existence of intrinsic magnetism at a silicon surface due to nano-structuring [144]. While the integration of single-spin magneto-electronics into standard silicon technology is crucial for technologies involving spin-based computation and storage, typically magnetic transition metals with a large atomic magnetic moment or rare earths are used to induce magnetic order in non-magnetic materials. Therefore the prediction of spin chains [144] or spin liquids [280] in Si(553)-Au seemed interesting from a technological point of view. Moreover, they are also scientifically interesting, since quantum fluctuations should prevent any magnetic ordering in strictly one- or two-dimensional systems [13].

The Si(553)-Au surface is formed by Si(111) terraces separated by single atomic steps and is stabilized by 0.48 monolayers (ML) of Au. Its main geometrical building blocks, i.e., the double Au chain running in the middle of the terrace and the Si honeycomb chain at the step edge, cf.

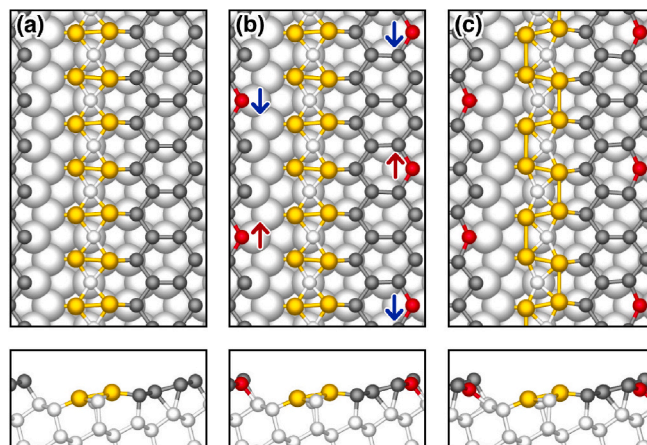


Fig. 16. Structure models of Si(553)-Au: (a) model proposed by Krawiec (K) [305], (b) spin-chain (SC) structure due to Erwin and Himpsel [144], and (c) rehybridized (R) surface proposed here. Yellow and (dark) gray balls indicate Au and (honeycomb chain) Si atoms. The structurally and electronically salient step-edge $\text{Si}_{\times 3}$ atoms characteristic for the SC and R surfaces are red. Arrows indicate spin polarization. Adapted from Ref. [306]. (For interpretation of the references to color in this figure legend, the reader is referred to the Web version of this article.)

Fig. 16, have been established by scanning tunneling microscopy (STM) [146,280,283,297–302], X-ray diffraction [303], low-energy electron diffraction (LEED) [280,298], and density-functional theory (DFT) [144, 280,283,301,304,305].

Au chain dimerization lowers the surface energy [305] and gives rise to a $\times 2$ periodicity parallel to the steps, see Fig. 16 (a). A further energy reduction is realized by the formation of an antiferromagnetic spin chain by spin-polarized electrons that singly occupy every third Si dangling bond (dangling bond) along the Si step edge [144]. This corresponds to the formation of a SDW as explained in the previous chapter and schematically represented in Fig. 3. Fig. 16(b) shows this spin-chain (SC) model. It accounts naturally for the $\times 2$ and $\times 3$ periodicities found by LEED [280] as well as by STM [146,298,299,302], as shown in Fig. 17. The primitive (1×1) unit cell of the (553) substrate is indicated in the diffraction pattern of Fig. 17 and reflects the terrace width of 14.8 Å and the atomic distance in the $[110]$ direction, i.e., along the steps, of $a_0 = 3.84$ Å in real space. The $\times 2$ periodicity of the dimerized Au double chain manifests itself in the streak-like intensity exactly between the chains of integer order spots along the $[112]$ direction. The streaks, if unmodulated, reflect the complete lack of correlation of the dimerization of Au chains on adjacent terraces. The $\times 3$ periodicity originating from the Si dangling bond chains at the step edge is apparent in the chain of slightly elongated spots at 1/3 and 2/3 position between the chains of

integer order spots. From the positions of $1/3$ spots along the $[3310]$ direction a centered correlation of the $\times 3$ periodicity of partially filled dangling bonds was concluded, as sketched in Fig. 16(c). It is important to note that no traces of LEED intensity were observed at $1/6$ or $5/6$ positions between the chains of integer order spots as evident from the LEED line profile in Fig. 17 and thus excluding a $\times 6$ periodicity along the Si step edges: the structural elements of the $\times 3$ periodicity of the Si step edge atoms and of the $\times 2$ periodicity of the Au rows act as independent scatterers during diffraction, i.e. they are not correlated. Also in STM the $\times 3$ periodicity is the dominant feature as shown in Fig. 17 where at positive bias voltage the empty states of the Si step edge dangling bond chain are imaged.

This structure model just described also nicely explains the metallic Au bands observed by ARPES [271,283,289,298,307]. However, there is so far no experimental evidence for the appearance of spin chains at Si(553)-Au, e.g., by spin-polarized STM, nor for the existence of half-occupied Si dangling bonds. Surfaces of covalent materials typically undergo relaxation or reconstruction, which allow the broken bonds to be either eliminated, emptied, or doubly occupied with spin-paired electrons [57,308–314]. This prompted Braun et al. [306] to question the formation of spin chains at Si(553)-Au. They performed density-functional theory (DFT) calculations within the

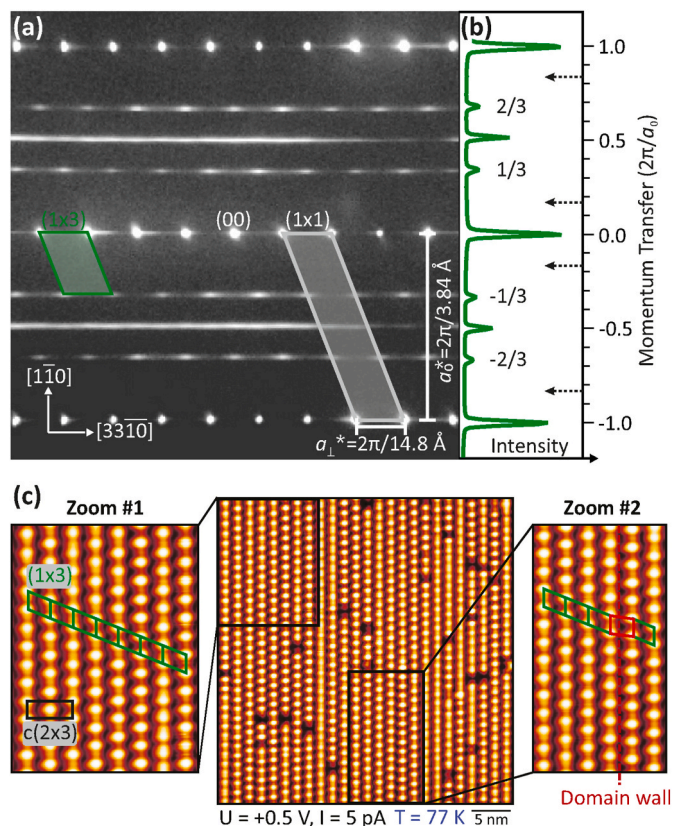


Fig. 17. (a) LEED pattern of the Si(553)-Au surface taken at 150 eV and $T = 80$ K. Half way between the rows of sharp integer order spots streaks are found originating from dimer Au rows along the terraces. Located at $1/3$ and $2/3$ positions slightly elongated spots from the tripled periodicity of the Si step edge atoms indicate a clear long-range ordering. (b) The integrated line profile taken along the $[110]$ direction does not show any intensity at positions for $\times 6$ periodicity (dashed arrows). (c) STM image of the Si(553)-Au surface at 77 K depicting the empty states. The tunneling bias was chosen $U = +0.5 \text{ V}$ to highlight the $\times 3$ periodicity of the Si step edge atoms with partially filled dangling bonds. Zoom #1 shows a well ordered area with the (1×3) unit cell. Zoom #2 depicts two ordered (1×3) domains separated by a linear domain wall.

generalized-gradient approximation (GGA) using the PBE [315] as well the PBEsol functional [316] to explore the Si(553)-Au surface energetics. In addition, local-density approximation (LDA) calculations [317] as well as hybrid DFT calculations were performed to explore the potential energy surface. In particular, a surface energy lowering due to $sp^3 \rightarrow sp^2 + p$ rehybridization of every third Si edge atom, and subsequent charge transfer from the Si p orbital to the Au chain was probed. This mechanism appeared plausible, because the Au chain acts as an electron reservoir that readily provides and accepts charge [295]. Moreover, a similar re-hybridization gives rise to asymmetric dimers at the Si(001) surface [310]. We remark that as the Au chain acts as an electron reservoir, the phase transition must be described in the grand-canonical ensemble, as discussed in section 1.6.

In order to probe that mechanism for Si(553)-Au, Braun et al. [306] started from the Krawiec (K) structure (cf. Fig. 16 (a)) and gradually lowered the vertical height of every third Si edge atom ($Si_{\times 3}$). The energy profile of this reaction path along with the corresponding surface magnetization is shown in Fig. 18. The lowering of $Si_{\times 3}$ reduces the surface energy and increases the surface magnetization, which assumes its maximum when the $Si_{\times 3}$ atoms are about 0.3 \AA below the neighboring step-edge atoms. In this configuration, a charge redistribution along the Si step edge takes place: The $Si_{\times 3}$ dangling bond carries about one electron and the neighboring step-edge atom dangling bonds are fully occupied. The surface is stabilized by an antiferromagnetic spin order along the chain of $Si_{\times 3}$ dangling bond electrons. The resulting structure, shown in Fig. 16 (b), corresponds to the spin-chain model proposed by Erwin and Himpsel [144].

According to the calculations in Ref. [306] it is a local, but not the global minimum on the potential-energy surface (cf. Fig. 18 and Table 1). The latter is reached upon passing an energy barrier of about 5 meV and is characterized by $Si_{\times 3}$ atoms about 0.8 \AA below the neighboring step-edge atoms. In this configuration, they assume a planar, sp^2 -like bonding configuration with respect to their Si neighbors, cf. Fig. 16 (c). As a result, a dangling bond wire forms, where two filled Si dangling bonds at the step edge alternate with single empty dangling bonds, see Fig. 19.

The formation of this rehybridized structure is thus accompanied by a surface charge transfer. About 1.6 electrons per 1×6 surface cell are shifted from the Si step edge to the Au chain. This corresponds to the magnetization calculated for the SC model, i.e. it is equivalent to the spin polarized charge in the $Si_{\times 3}$ dangling bonds. The charge redistribution is visualized in Fig. 20 (a), where the electron density difference between the SC and the R model is shown. The electron transfer from the $Si_{\times 3}$ dangling bonds to the Au dimers is clearly seen. The additional charge at the Au chain strengthens its dimerization, which increases from 5 % to 14 %. The finding that an increase in Au chain dimerization

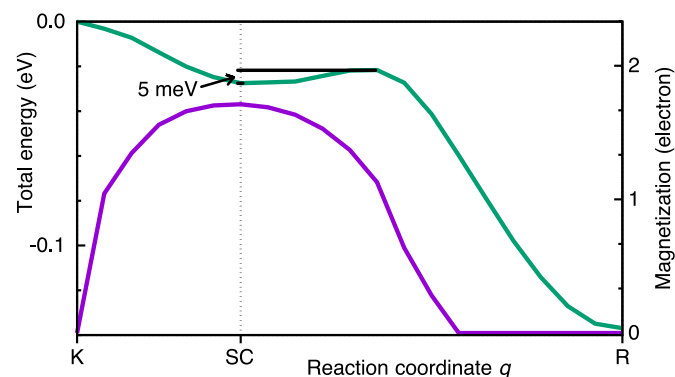


Fig. 18. Calculated (DFT-PBEsol) surface energy (solid line) and surface magnetization (dashed line) per 1×6 surface unit cell vs the reaction coordinate given by the $Si_{\times 3}$ vertical position. Its respective position for the Krawiec (K), spin-chain (SC) and rehybridized model (R) is indicated. Adapted from Ref. [306].

Table 1

Surface formation energies (in meV per 1×6 unit cell) with respect to the Krawiec model calculated in Ref. [306] for the spin-chain (SC) and the rehybridized surface (R), using different XC functionals. The energies* refer to calculations for the respective PBEsol structures.

	LDA	PBE	PBEsol	HSE
SC	–36	–2*	–26	–419*
R	–114	+191*	–137	–457*

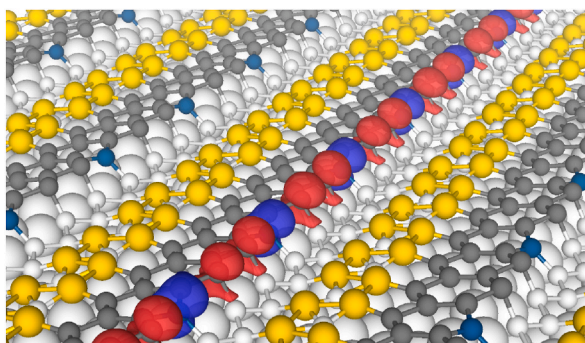


Fig. 19. Filled and empty dangling bonds in the ground state (2,2,0) configuration of the 1×6 reconstructed Si(553)-Au surface are shown (only at one step edge) in red and blue, respectively. (For interpretation of the references to color in this figure legend, the reader is referred to the Web version of this article.)

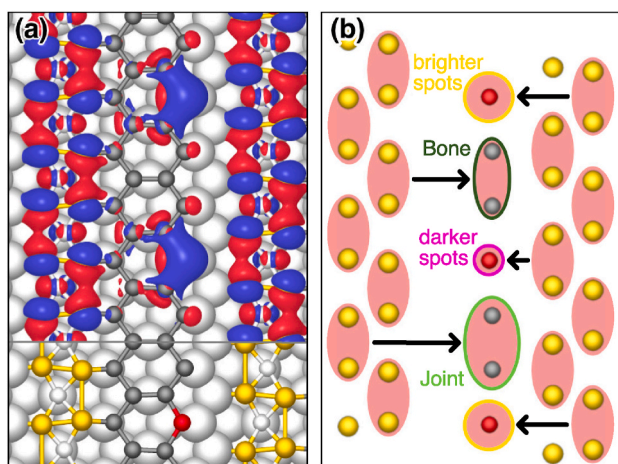


Fig. 20. (a) Difference between the charge densities calculated for the spin-chain (SC) and the rehybridized (R) surface. The relative electron accumulation/depletion at the R surface is shown in red/blue. (b) Schematic model for the parity breaking of the Si step edge due to the Au dimers, see text and Fig. 22. Adapted from Ref. [306]. (For interpretation of the references to color in this figure legend, the reader is referred to the Web version of this article.)

takes place upon electron uptake is in agreement with earlier results by Hogan et al. [295].

The spin-spin exchange constant along the chains has been estimated to be about 15 meV [280], i.e., roughly two orders of magnitude smaller than the Si hybridization energy. Therefore it might at first seem obvious that the energy gain due to rehybridization and emptying the $\text{Si}_{\times 3}$ p orbitals outweighs the stabilization due to the antiferromagnetic spin order. However, the energy balance is as well affected by the charge transfer and strain accompanying the rehybridization. In fact, the energy difference between the R and the SC model (cf. Table 1) is small and depends on the treatment of the electron exchange and correlation effects: PBEsol and HSE calculations predict a lower surface energy for the spin-paired compared to the spin-chain surface. The PBE calculations, in

contrast, failed to identify a local energy minimum for the R model. PBE calculations based on frozen PBEsol geometries yield a higher surface energy for the R than for the SC structure. On the other hand, LDA calculations predict the rehybridization to lower the surface energy, but fail to provide an antiferromagnetically ordered state. In summary, the total-energy calculations in Ref. [306] suggest the rehybridization of the surface, but they are not fully conclusive. Obviously, the energy landscape is rather flat. In order to arrive at a conclusive picture, the calculated electronic properties of the SC and R model should be compared with the available experimental data.

The different electron distributions of the SC and R models lead to somewhat different surface band structures, as shown in Fig. 21. The SC model is characterized by spin-polarized states at the singly occupied $\text{Si}_{\times 3}$ dangling bonds that form two very flat bands about 0.1 eV below and 0.2 eV above the Si valence-band maximum (VBM). These bands are pushed away from the VBM upon rehybridization, accompanying the electron transfer from the $\text{Si}_{\times 3}$ dangling bonds towards the Au chain. At the same time, the strongly dispersive, partially occupied Au bands shift down in energy and are now below the empty Si dangling bond band throughout the Brillouin zone.

Although the calculated Au bands seem to match the experimental data slightly better in case of the rehybridized compared to the spin-chain structure, their modification is not sufficiently strong to allow for discriminating between the models. This holds also with respect to the non-dispersing unoccupied state 0.62 eV above the Fermi level observed by two-photon photoemission [319]. Given the DFT band gap underestimation, this state is well explained by the Si dangling bond states predicted for both the R and the SC geometry. The situation is different in case of the prominent flat band assigned to the single electrons at the $\text{Si}_{\times 3}$ atoms, calculated for the SC model. This band, about 0.1 eV below the VBM, has not been identified clearly experimentally. The disappearance of this state for the R model supports the spin-paired structure.

Additional support for the spin-paired structure is provided by the comparison between the high-resolution low-temperature STM data [302] and the simulations in Ref. [306], as shown in Fig. 22. Both models clearly account for the $\times 2$ and $\times 3$ periodicities observed experimentally for voltages of 0.7 V. These periodicities are due to the Au chain dimerization and the $\text{Si}_{\times 3}$ atoms that stand out structurally and electronically. For biases close to the Fermi level, at 0.2 V, however, the measurements show a $\times 6$ periodic structure reminiscent of "bones" linked by bright "joints" (see labels in Fig. 22). Aulbach et al. [302] suggested these features to be related to the parity breaking of the Si step edge due to the Au dimers. This interpretation is corroborated by the calculations, as shown schematically in Fig. 20 (b): The charge accumulation in the Au dimers affects the electron localization at the Si step-edge atoms in their vicinity. This effect increases with increasing dimerization. Therefore it should be more pronounced and better visible for the R than for the SC model. This is in fact what can be clearly seen in the simulated STM images. The experiment at intermediate voltages corresponds roughly to a superposition of the low and high tunneling bias appearance: The bones and joints are still visible, while the $\text{Si}_{\times 3}$ atoms start to become prominent, but with different intensities ("darker" and "brighter spots" in Fig. 22). This intensity variation is again excellently reproduced by the simulations based on the diamagnetic surface, but not accounted for by the spin-chain model. This shows that the ideal Si (553)-Au surface – considered as a prototypical example for intrinsic magnetism at silicon surfaces – is in fact diamagnetic, at least in the zero temperature ground-state: DFT calculations [306] demonstrate that a structure, where all Si dangling bonds either host spin-paired electrons or are empty, is more favorable and in better agreement with experiment than antiferromagnetically ordered spin chains, at least at 0 K.

Does this now mean that intrinsic surface magnetism can be generally ruled out for Si(hhk)-Au? Perhaps not. An enhanced spin-spin interaction resulting from smaller dangling bond distances as well as a reduced Au coverage – both realized, e.g., at Si(557)-Au – may shift the

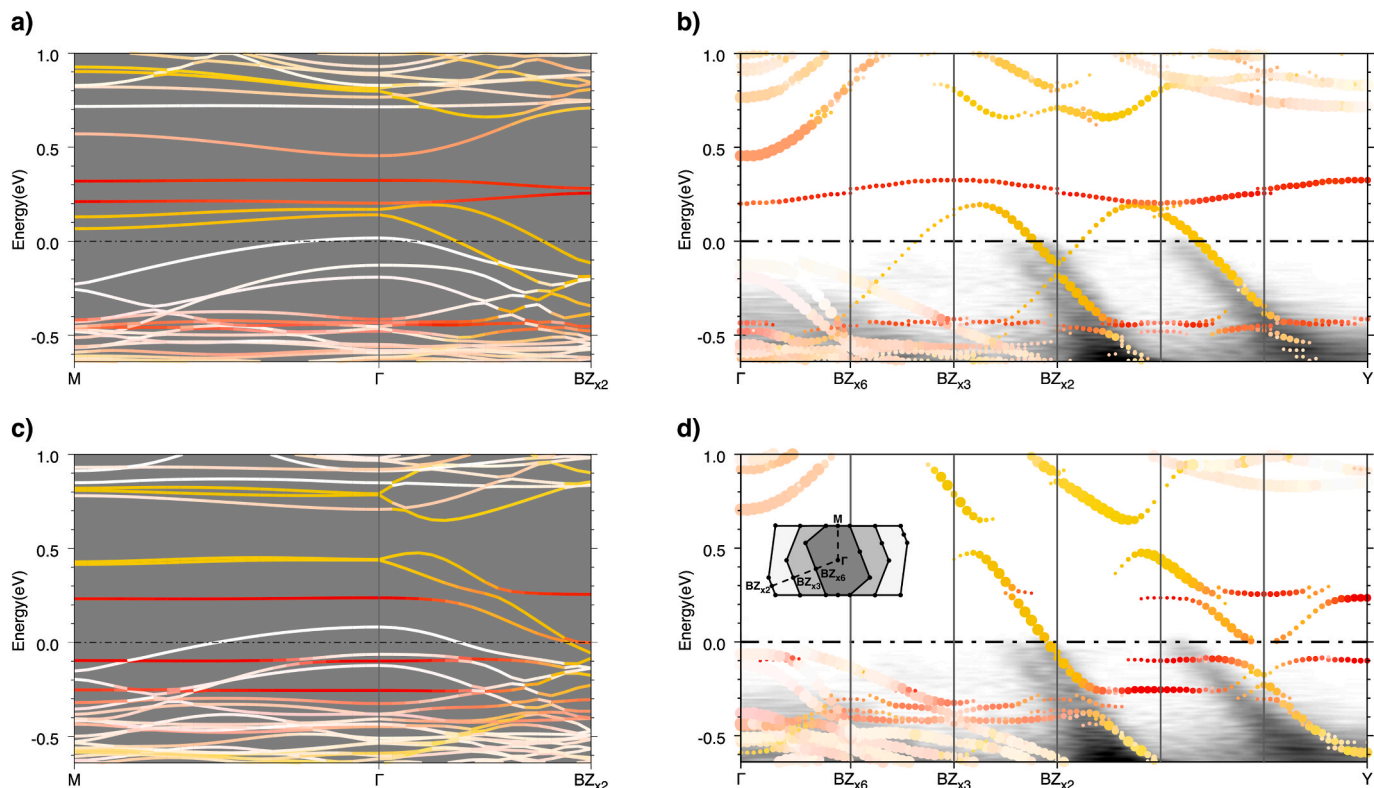


Fig. 21. Si(553)-Au surface band structures: The bands calculated (PBEsol) for the rehybridized (R) and the spin-chain (SC) model with 1×6 periodicity are shown in a) and c), respectively. In b) and d) the respective bands are unfolded (following the procedure proposed in Ref. [318]) into the Brillouin zone with primitive 1×1 lattice periodicity and compared with the ARPES data from Ref. [283]. The spectral weight is indicated by the symbol size. The color scale indicates the localization at Si step-edge (red) and Au atoms (yellow). Adapted from Ref. [306]. (For interpretation of the references to color in this figure legend, the reader is referred to the Web version of this article.)

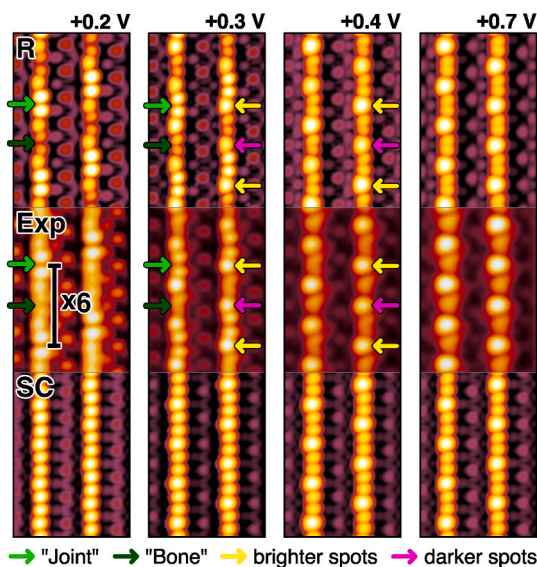


Fig. 22. Comparison of simulated (PBEsol) STM images for the Si(553)-Au surface with experiment. The simulations performed in Ref. [306] for the rehybridized (R) and the spin-chain model (SC) are shown above and below the data measured in Ref. [302]. Adapted from Ref. [306].

energy balance in favor of intrinsic magnetism. In fact, PBEsol calculations for Si(557)-Au [306] indicate a slightly reduced – from 68 to 43 meV per rehybridized Si surface atom – energy gain upon rehybridization compared to Si(553)-Au. At the same time, the energy gain due to spin

polarization is increased considerably from 13 to 56 meV per surface spin. Thus, at least within DFT-PBEsol, the spin-chain structure proposed by Erwin and Himpsel is stable for Si(557)-Au, in contrast to Si(553)-Au and to Si(335) [288]. Spin-chain structures are also predicted by zero-temperature calculations for Si(775)-Au [294]. However, in the latter case they are supposed to involve the Si rest atom dangling bonds rather than the Si step-edge atoms. In both cases, the experimental proof for spin ordering is still pending. Nanostructure engineering, e.g., Si adsorbate induced electron doping [284,294,320], may be another possibility to induce and modify intrinsic magnetism at Si(hhk)-Au.

2.2.1. Temperature effects

Much attention has been paid to phase transitions in Si(hhk)-Au [16]. In case of Si(557)-Au, a metal-insulator transition occurs at 270 K [321]. It has originally been interpreted within the classical Peierls picture [321,322]. Molecular dynamics calculations by Riikonen and Sanchez-Portal [323] showed, however, that the increase of the vibrational amplitudes of the Si step edge atoms at higher temperatures lead to metallic configurations that may as well explain the measured metal-insulator transition.

An even more intriguing example for complex phase transitions at Si(hhk)-Au is provided by the Si(553)-Au surface [298,299]. This is due to the shallow potential energy surface of Si(553)-Au, see Table 1, which in conjunction with the existence of evenly placed Si empty dangling bonds and the charge reservoir provided by the Au chain, makes this system very susceptible to thermal excitations. Indeed first conductivity experiments found that rising temperature leads to a sudden conductivity increase along the step edge at around 65 K (more details and an extension of these measurements will be described in sec. 2.2.4). A further temperature increase quenches first the $\times 3$, i.e., the Si step edge related, and subsequently the $\times 2$, i.e., the Au chain related periodicity

of the surface [281].

This increase in surface conductivity has been attributed to an Au \rightarrow Si dangling bond charge transfer [281]. Such a charge redistribution characterizes the spin chain (or spin-liquid in two dimensions) structure suggested by Erwin et al. [144,280] for Si(553)-Au: It has a (2,2,1) electron configuration, i.e., two fully occupied dangling bonds alternate with one singly occupied dangling bond along the step edge. The occupation of the formerly empty Si p orbital causes a $sp^2 + p \rightarrow sp^3$ rehybridization and moves the respective Si atom out of the planar sp^2 configuration [306]. This is clearly an activated process, see Fig. 18.

Along the reaction path a metastable structure appears that locally corresponds to the (2,2,1) structure [144]. The energy barrier hindering such a local (2,2,0) \rightarrow (2,2,1) transformation amounts to 58 meV, far above the thermal energy at 65 K, i.e., about 6 meV. The energy barrier may be reduced at finite temperatures due to entropy effects [276]. According to Braun et al. [282], entropy effects indeed ease the (2,2,0) \rightarrow (2,2,1) transition, as indicated in Fig. 23. The effect is not sufficiently large, however, to explain a transition close to 65 K. Alternatively, a concerted movement involving a variety of atoms might cause the $sp^2 + p \rightarrow sp^3$ rehybridization and the accompanying charge transfer. In order to probe that scenario, *ab initio* molecular dynamics (AIMD) calculations were performed in Ref. [282]. The time evolution (after equilibration) of the Si step edge atom vertical positions is shown in Fig. 24. Here it is discriminated between three configurations: sp^2 hybridized Si with an empty p orbital dangling bond, partially sp^3 hybridized Si hosting a single electron in its dangling bond, and completely sp^3 hybridized Si with fully occupied dangling bond. The 1×6 surface unit cell considered in the calculations is nearly entirely characterized by (2,2,0) structures at 50 K. In fact, there are only two very short occurrences of singly occupied Si dangling bonds. These occurrences get more frequent and last longer at 100 K. Also an emptying of originally doubly occupied dangling bonds is observed at this temperature. Still, the (2,2,0) configuration is the most dominant structural motif at 100 K. However, strong vertical vibrations of the Si step edge atoms occur. These vibrations get more pronounced for higher temperatures and quench the dominance of the (2,2,0) structure. Increasing disorder is observed and singly occupied dangling bonds occur frequently for temperatures in excess of 200 K. The AIMD results clearly show an order-disorder type phase transition.

How likely is a local transition to such an electron-doped (2,2,1) configuration? In order to answer this question, Braun et al. [282] used DFT-PBESol to calculate the total energy along a reaction path where –

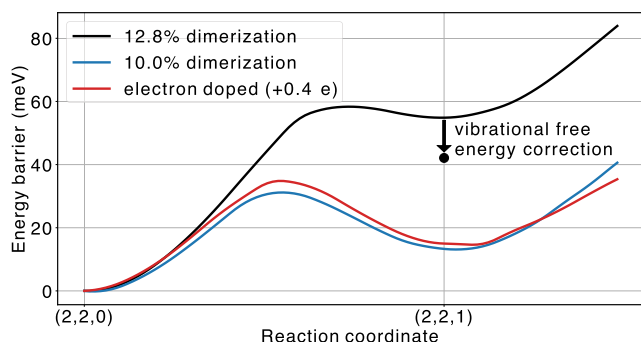


Fig. 23. Calculated potential energy surface from the (2,2,0) ground state to the self-doped (2,2,1) configuration for the AIMD calculated average dimerization at 100 K (12.8 %, black), a reduced dimerization (10 %, blue) and a 0.4 electron doped 1×6 supercell (red). The dimerization is defined as $d = |a - b|/a$, where a and b are the Si lattice constant and Au–Au bond length in chain direction, respectively. The reduction of the total energy difference between (2,2,0) and (2,2,1) structures due to vibrational free-energy corrections at 100 K is indicated. Adapted from ref. [282]. (For interpretation of the references to color in this figure legend, the reader is referred to the Web version of this article.)

within the 1×6 surface unit cell – a single Si atom with an originally empty dangling bond is raised from the flat sp^2 coordination to the sp^3 configuration, see Fig. 23. Here the Au chain dimerization was fixed at its average value at 100 K. The movement of the Si edge atom is accompanied by an Au \rightarrow Si dangling bond charge transfer, opposite to the lateral charge transfer observed upon lowering an originally sp^3 hybridized Si step edge atom, see Fig. 20.

The distribution function of the Si edge atom vertical positions in Fig. 25(a) provides additional details. At 50 K the distribution is bimodal, with cluster points for completely filled and empty Si dangling bonds. A third, very weak accumulation point in between appears for $T > 50$ K. It corresponds to the occupation of the local energy minimum of the reaction path shown in Fig. 23, i.e., singly occupied dangling bonds. For higher temperatures, the distribution gets broader and the Si vertical positions scatter broadly. This shows that the description of the phase transition in terms of solitons and anti-solitons [324], i.e., binary occupancy shifts along the dangling bond wire, simplifies the actual surface dynamics.

Why does the order-disorder transition start at far lower temperatures than expected from the rehybridization barrier (black line in Fig. 23)? The answer is related to the electron chemical potential of the Au chain. A strongly dimerized chain has a stronger electron affinity than a weakly or undimerized chain [295]. Therefore, a reduced dimerization favors the Au \rightarrow Si charge transfer required for the rehybridization. In Fig. 23 it can be seen that a reduction of the dimerization from 12.8 % (average value at 100 K) to 10.0 % reduces the $sp^2 + p \rightarrow sp^3$ transition barrier (blue line) as strongly as doping the 1×6 unit cell with 0.4 electrons (red line). While the average dimerization is larger than 10.0 % even at 400 K, already for temperatures above 50 K Au chain segments with 10.0 % dimerization occur temporarily, cf. distribution in Fig. 25(b). With increasing temperature, even lower dimerization values occur and reduce locally the energy barrier for the Si $sp^2 + p \rightarrow sp^3$ rehybridization. Due to the nonlinear dependence of the reaction rate on the energy barrier, the rehybridization probability depends not only on the average dimerization, but on its entire distribution function. The probability for the occurrence of self-doped (2,2,1) structures derived from the temperature-dependent dimerization distribution under the assumption of thermodynamic equilibrium between (2,2,0) and (2,2,1) surface domains is shown in Fig. 25(c). Its rise for temperatures above 50 K is – even quantitatively – consistent with the AIMD findings discussed above and explains the disorder along the Si step edge already at moderate temperatures.

2.2.2. Experimental evidence: Raman and LEED

Are these computational findings in agreement with the actual surface dynamics and with DC electron transport? The temperature-dependence surface Raman data [282], described in this section, helps to answer this question, as well as the dc transport data that follow in sec. 2.2.4: In Raman two signatures that are particularly strongly affected by temperature are shown in Fig. 26(a): There is a low-frequency phonon mode at around 41 cm^{-1} that softens considerably with rising temperature. A phonon mode at around 415 cm^{-1} appears slightly below 100 K and strongly gains intensity with rising temperature. Both signatures show a continuous rather than an abrupt change in energy or intensity, respectively. This supports the interpretation of the AIMD results in terms of an order-disorder transition.

Frozen-phonon calculations for Si(553)-Au surfaces [282] provide a microscopic interpretation of the Raman data. The calculations show the existence of a Au chain dimerization mode at 41 cm^{-1} for the (2,2,0) ground state, see Fig. 26(d). Its thermal frequency shift – obtained by projecting the AIMD atomic velocities on the phonon eigenvector – is in close agreement with the low-energy Raman signature described above, see Fig. 26(c). The phonon-mode softening with rising temperature roughly parallels the reduction of the dimer strength, i.e., is caused by the reduction of the average Au–Au bond strength. Due to its very low frequency, the Au chain mode is occupied already a low temperature. It

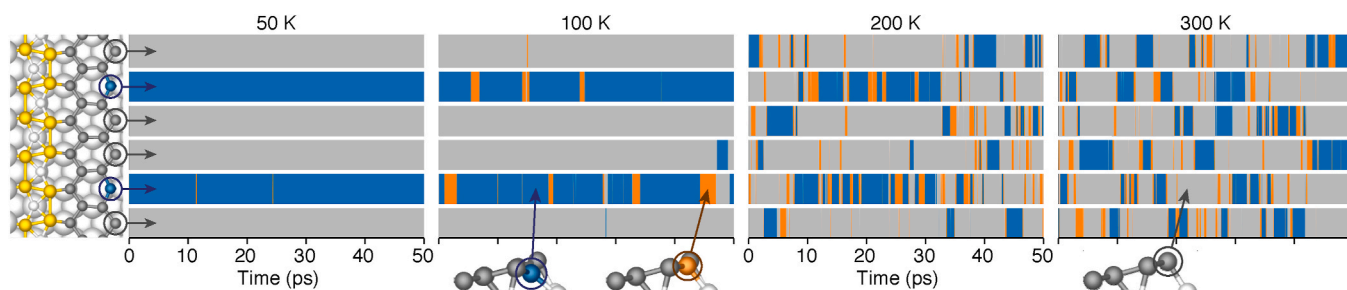


Fig. 24. Projection of the AIMD calculated Si step edge atom vertical positions on the heights corresponding to Si with empty ($q < 0.5e$, blue), singly occupied ($0.5e \leq q \leq 1.5e$, orange) and doubly occupied ($q > 1.5e$, gray) dangling bonds. Adapted from Ref. [282]. (For interpretation of the references to color in this figure legend, the reader is referred to the Web version of this article.)

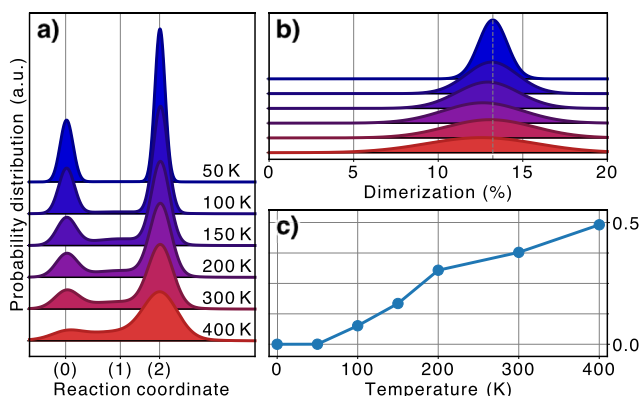


Fig. 25. (a) Distribution of the Si step edge atom vertical positions for various temperatures. Equilibrium positions of Si with empty (0), singly (1) and doubly (2) occupied dangling bonds are indicated. (b) Temperature dependent distribution of Au chain dimerization. Color coding as left. (c) Probability of (2,2,1) ordered surface domains derived from the dimerization distributions shown in (b), see text. Adapted from Ref. [282]. (For interpretation of the references to color in this figure legend, the reader is referred to the Web version of this article.)

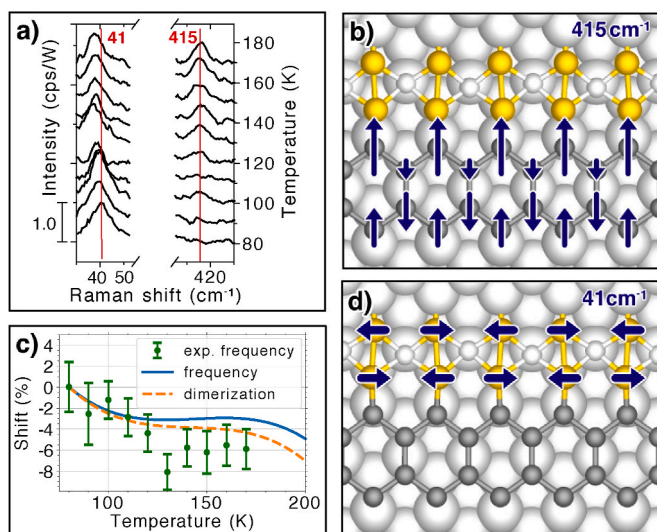


Fig. 26. (a) Temperature dependent Raman spectra, focusing on a Raman mode located at the step edge at 415 cm^{-1} depicted in (b) and one located at the Au chain at 41 cm^{-1} depicted in (d). The measured frequency shift of the 41 cm^{-1} mode is compared in (c) with the calculated shift and the relative change in dimerization. Adapted from Ref. [282].

reduces temporarily the Au chain dimerization and thus lowers – as discussed above – the $sp^2 + p \rightarrow sp^3$ activation energy.

Frozen-phonon calculations for the (2,2,1) surface predict a transversal shear mode along the Si honeycomb chain with a frequency of 415 cm^{-1} , see Fig. 26(b). Its frequency coincides with that of the high-temperature mode seen by Raman spectroscopy. This mode is replaced by localized Si vibrations for the (2,2,0) structure, due to the stronger variation of the force constants along a step edge where sp^3 and sp^2 hybridized Si atoms alternate. This explains, why the measured mode disappears upon cooling the sample below 100 K.

The calculated surface geometries are furthermore consistent with the evolution of the LEED intensity as function of temperature, see Fig. 27. Here the $\times 3$ and $\times 2$ LEED intensities measured in Ref. [281] are compared with the squared structure factors including Debye-Waller effects obtained from AIMD. Both the measured data and the calculations show a gradual loss of order starting below 100 K, which first affects the $\times 3$ signatures and subsequently the $\times 2$ features, in agreement with earlier STM observations [298,299]. The quenching of the $\times 3$ signals is well reproduced by the calculated order-disorder transition at the Si step edge, whereas the measured disappearance of the $\times 2$ intensities clearly precedes the calculated Au chain order-disorder transition. This is, however, to be expected: While the AIMD calculations find a broadening of the dimerization distribution, cf. Fig. 25(b), they cannot correctly account for disorder arising from dimerization phase shifts. The relatively small 1×6 unit cell leads to an overestimation of the defect/antidefect interaction that blueshifts the calculated critical temperature. Since the Au atoms are directly bonded, this effect is more relevant for the Au chain than for indirectly interacting step edge Si. Hafke et al. performed a spot profile analysis of the (1×3) spots for further insight into the order-disorder transition. The change from an ordered to an disordered state is obvious from the LEED patterns taken at 60 K and 180 K, see Fig. 28. The (1×3) spots – clearly visible in Fig. 28(a) at 60 K – are completely smeared out 180 K as shown in Fig. 28

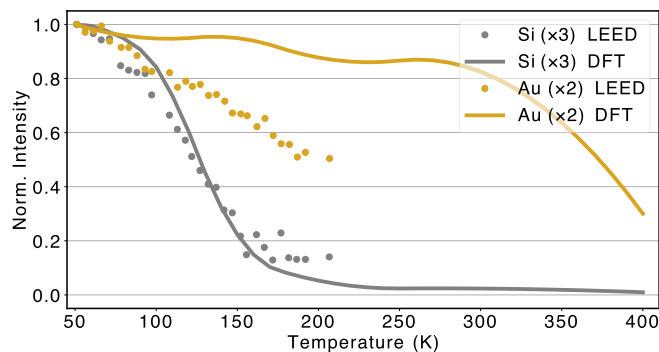


Fig. 27. Temperature-dependent $\times 3$ and $\times 2$ LEED spot intensities from Ref. [281] vs. average structure factors including Debye-Waller effects obtained from the AIMD geometries. Adapted from Ref. [282].

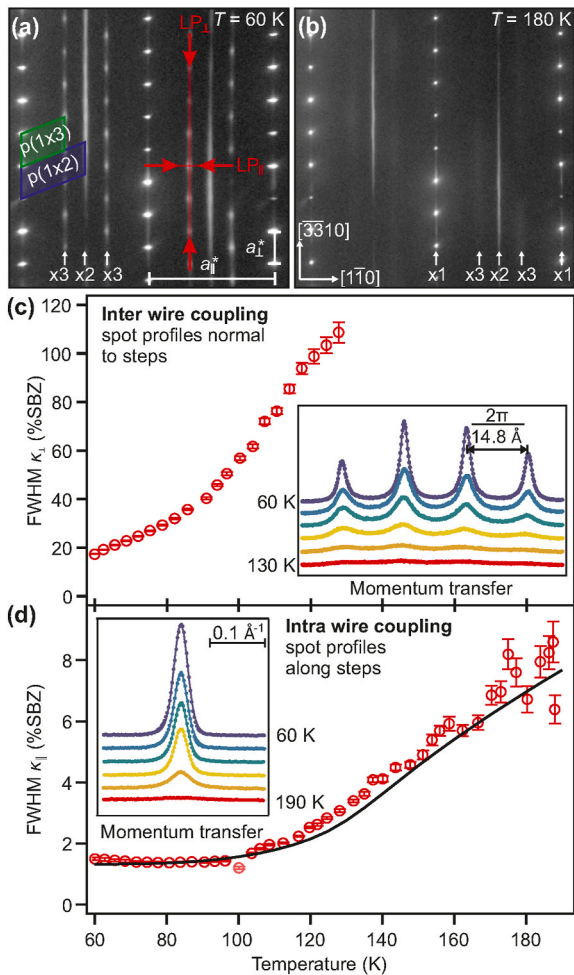


Fig. 28. LEED patterns of Si(553)-Au at an electron energy of 150 eV and temperatures (a) 60 K and (b) 180 K. The $\times 2$ streaks between the rows of sharp integer-order spots arise from dimerized Au double rows on the (111)-oriented terraces. (c) FWHM of the $\times 3$ diffraction spots (red data points) as a function of temperature in the $[3\ 3\ 10]$ direction and same in the $[1\ 1\ 0]$ direction (d). Insets in (c),(d): Line profiles for both directions at various temperatures (shifted vertically for better visibility). Adapted from Ref. [324]. (For interpretation of the references to color in this figure legend, the reader is referred to the Web version of this article.)

(b). Line profiles along and perpendicular to the chain of (1×3) spots are shown as function of temperature in the insets of Fig. 28(c + d). The profiles are described by a Lorentzian or a sum of Lorentzians reflecting the geometric length distribution of the ordered (1×3) domains. The FWHM for both directions increase with temperature. The interwire coupling between adjacent dangling bond chains is lifted much faster than the intrawire coupling. The emergence of disorder along the $\times 3$ periodicity of the dangling bond chains exhibit a clear onset at 100 K.

Hafke et al. constructed an exactly solvable three state Potts model describing the dynamics of coupled wires and the resulting steady-state FWHM of the $\times 3$ spots as a function of temperature:

$$H = \sum_i [-b\delta_{u_i, u_{i+1}} - a\delta_{u_i, c}] \quad (21)$$

Here δ_{ij} denotes the Kronecker delta. A single unoccupied dangling bond can take three positions within each unit cell i : left, center, and right, $u_i = \{l; c; r\}$. The first term, with parameter b , describes the energy needed to displace neighboring unoccupied dangling bonds relative to each other: specifically, the energy needed to create a soliton-antisoliton pair within one wire is $2b$. The second term, with parameter a , favors the

occupation of the central position and arises from the coupling of the wire to neighboring wires (for further details see Ref. [324]). The model fits best to our experimental data for $a = 2.1$ meV and $b = 21$ meV. These fitted values are also consistent with DFT results: a should be equal to the calculated energy difference per unoccupied dangling bond, 2.1 meV, between $(2,2,1)$ configurations in staggered and centered alignments, and b corresponds to half of the formation energy $E_0 = 30$ meV of an elementary excitation, which can be viewed as a soliton-antisoliton bound pair. The resulting FWHM, convoluted with a Gaussian instrumental response function, describes the experimental results, see black solid curve in Fig. 28(d).

The DFT calculations and Raman measurements in Ref. [282] together with the LEED results in Ref. [324] thus provide a consistent description of the experimentally observed two-stage Si(553)-Au surface phase transition up to temperatures of 180 K. In addition, they reveal a novel mechanism for the self-doping of dangling bond nanostructures: Thermally excited vibrations of the Au charge reservoir lead to transient changes of its electron affinity and thus facilitate electron doping at low temperatures. This mechanism can be expected to be relevant beyond the family of gold-stabilized Si surfaces, and to be conveniently tuned by modifying the species of the charge reservoir, the metal coverage, and the dangling bond density.

2.2.3. Vibrational properties

A thorough characterization of the surface-localized phonon modes of the Si(553)-Au system, above and below the phase transition temperature, has been performed combining Raman measurements and DFT calculations [326]. As shown in the following, the comparison between theory and experiment enables the assignment of measured spectral features to the calculated eigenmodes. Thus, the combined experimental and theoretical analysis of the vibrational properties turns out to be quite useful for a distinction between the different structure models. It is found that the calculated Raman spectra of the double Au strand [305] and the $sp^2 + p$ rehybridized [306] models are compatible with the high temperature (HT) and low temperature (LT) measured spectra, respectively.

Fig. 29 shows the measured Raman spectrum of the Si(553)-Au surface (after subtraction of a clean Si(553) surface spectrum) for two different scattering geometries, i.e. $z(yy)-z$ (parallel polarization) and $z(yx)-z$ (crossed polarization). According to the Raman polarization selection rules the two scattering geometries yield fundamentally different spectra: in $z(yy)-z$ A' modes are symmetry allowed (conserving the mirror plane symmetry of the surface structure) while in $z(yx)-z$ A'' modes are allowed (breaking the mirror plane symmetry of the surface structure) [325,326].

The experimental Raman frequencies as obtained from fitting using Voigt profiles (indicated by red lines) are listed in Tables 2 and 3 together with calculated surface eigenmode frequencies (see Table 4).

The vibrational properties of the Si(553)-Au system at 300 K and the according Raman spectra are computed with the structural model proposed by Krawiec [305]. Although the Si(553)-Au surface at 300 K was shown to fluctuate thermally between the double chain [305], rehybridized, and spin-chain phases, the system at RT is for the vast majority of the time in the double chain configuration [282], which is therefore employed to describe the high temperature phase of the Si(553)-Au surface. Accordingly, the calculated phonon spectra, shown in Fig. 30, closely reproduce the measured spectra. Generally, both the frequency and the relative intensity of the spectral features are in satisfactory agreement with the experiment, although the most intense vibrational signatures in the (yx) crossed configuration are somewhat red shifted within PBEsol in comparison with the experiment.

The comparison between measured and calculated spectra allows to assign the calculated phonon eigenmodes to measured Raman peaks on the basis of phonon energy, phonon symmetry, and Raman scattering intensity. The result of this procedure is shown in Tables 2 and 3. Displacement patterns of the corresponding eigenmodes can be found in

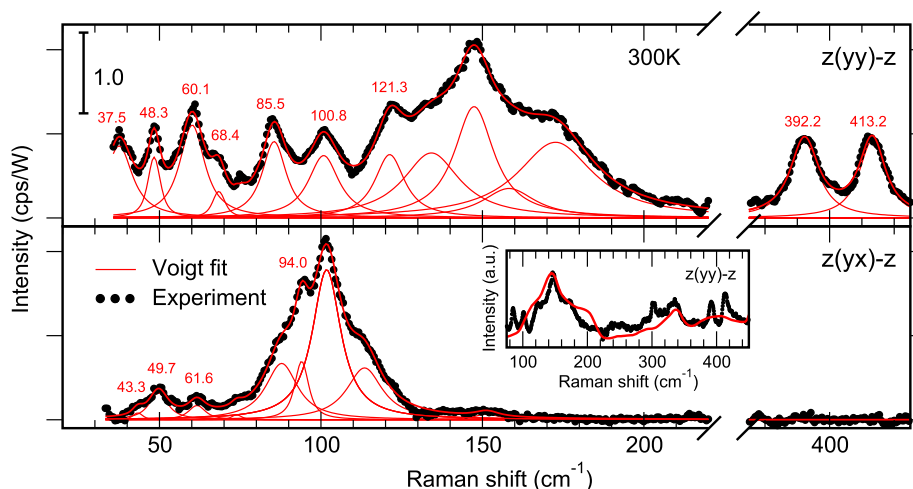


Fig. 29. Raman spectra of the Si(553)-Au surface, measured at 300 K (after subtraction of a clean Si(553) surface spectrum) for two different scattering geometries, i. e. $z(yy)-z$ (parallel polarization) and $z(yx)-z$ (crossed polarization). According to the Raman polarization selection rules the two scattering geometries yield fundamentally different spectra: in $z(yy)-z$ A' -modes are symmetry allowed (conserving the mirror plane symmetry of the surface structure) while in $z(yx)-z$ A'' -modes are allowed (breaking the mirror plane symmetry of the surface structure) [325,326]. The spectra were fitted using Voigt profiles with the Gauss FWHM fixed to the spectrometer resolution of 1.3 cm^{-1} and variable Lorentz FWHM. The inset shows a comparison of the measured Raman intensity with the PBEsol calculated phonon DOS of bulk Si.

Table 2

Raman frequencies (in cm^{-1}) measured at 300 K and calculated (0 K frozen phonon calculations performed with the double chain model) for the $z(yy)-z$ configuration. PBEsol calculated frequencies are listed (Theo.), along with the highest and lowest frequency calculated with other XC-functionals. Char. and Loc. indicate whether the phonon has Au or Si character, and the surface localization of the atomic displacement vectors, respectively. Modes with calculated Raman efficiency below 1 % of the main peak are not listed.

Exp.	Theo.	Theo. Min-Max	Char.	Loc.
37.5	{	47.7–52.9	Au + Si	93 %
48.3 ± 0.1		52.7–59.8	Au	91 %
60.1 ± 0.1	64.9	64.9–66.5	Au + Si	68 %
68.4 ± 0.3	69.8	66.1–72.9	Au	92 %
85.5 ± 0.1	84.2	84.1–86.2	Au + Si	88 %
100.8 ± 0.2	109.4	109.4–113.1	Si	74 %
121.3 ± 0.4	122.0	122.0–129.4	Si	55 %
134.1 ± 1.4	131.9	131.8–141.1	Si	50 %
147.4 ± 0.7	140.2	140.2–144.0	Si	47 %
158.4 ± 4.7	165.1	165.1–167.5	Si	55 %
172.6 ± 1.9	169.8	169.7–171.3	Si	51 %
392.2 ± 0.1	386.2	379.8–388.3	Si	40 %
413.2 ± 0.1	411.5	410.1–415.7	Si	50 %

Refs. [325,326]. The displacement patterns are in agreement with the measured Raman selection rules, i.e. symmetry properties of calculated and experimentally observed modes are taken into account as well. A detailed discussion of the individual eigenmodes is given in Refs. [325, 326].

The Si(553)-Au system is supposed to undergo an order-disorder type structural transition starting below 100 K [282]. According to the present knowledge of the system, the double Au strand model of (5×2) periodicity [305] describes the high-symmetry RT phase, while the (centered) spin-chain [144,280] and rehybridized [306] models of (5×6) periodicity have been proposed for the description of the lower symmetric LT phase. Between RT and LT the morphology of the step edge of the Si terraces fluctuates among the configurations of the different phases, establishing an interplay (via charge transfer) with the Au chain that continuously enhances the chain dimerization from RT to LT [282].

The structural differences of the surface models must be mirrored in

Table 3

Raman frequencies (in cm^{-1}) measured at 300 K and calculated (0 K frozen phonon calculations performed with the double chain model) for the $z(yx)-z$ configuration. PBEsol calculated frequencies are listed (Theo.), along with the highest and lowest frequency calculated with other XC-functionals. Char. and Loc. indicate whether the phonon has Au or Si character, and the surface localization of the atomic displacement vectors, respectively. Modes with calculated Raman efficiency below 1 % of the main peak are not listed [325, 326].

Exp.	Theo.	Theo. Min-Max	Char.	Loc.
43.3 ± 0.9	44.2	44.2–46.1	Au	58 %
49.7 ± 0.4	52.7	52.7–59.8	Au	91 %
61.6 ± 0.5	62.4	61.7–64.6	Au	91 %
73.9 ± 1.1	65.4	65.4–67.6	Si	47 %
87.4 ± 0.9	79.7	79.7–86.2	Si	57 %
94.0 ± 0.2	{	82.1–86.1	Au	77 %
		84.4–94.9	Au	77 %
101.7 ± 0.2	96.8	96.2–98.8	Au	72 %
113.5 ± 0.5	111.4	111.4–115.3	Si	52 %

Table 4

Measured frequencies at 300 and 30K in the $z(yx)-z$ scattering geometry. The uncertainty in frequency is obtained from the Voigt line fit (with 90 % confidence) and the error from the spectral calibration with laser plasma lines.

	Exp. 300K	Exp. 30K	Diff.
low range	37.5 ± 0.4	40.5 ± 0.2	3.0
	48.3 ± 0.2	47.8 ± 0.4	–0.5
	60.7 ± 0.3	61.2 ± 0.2	0.4
	68.4 ± 0.4	–	–
	–	82.7 ± 1.4	–
	85.5 ± 0.3	88.0 ± 0.4	2.5
	–	99.1 ± 1.5	–
high range	100.8 ± 0.2	105.5 ± 0.4	4.7
	392.2 ± 1	396.2 ± 1	4.0
	413.2 ± 1	–	–

Table 5

Raman frequencies of selected modes discussed in the text calculated within PBEsol according to different structural models.

Exp.	R	SC	CSC
40.5 ± 0.2	42.0	8.7	16.7
82.7 ± 1.4	77.3	69.4	70.7
99.1 ± 1.5	91.0	65.0	64.8

their vibrational properties. Modes associated with the Au chain are expected to change their eigenfrequency upon cooling from RT to LT, while modes localized at the Si step edge cannot exist in the same form in the different phases. As the RT and LT structural models differ in the dimerization of the Au chain and in the local structure of the Si step edge, the frequency ranges in which the vibrations related to the Au chain and to the Si step edge occur are crucial for the investigation of the temperature effects.

The LT Raman spectra of Si(553)-Au are shown in Fig. 31, along with the RT Raman spectra for comparison. The experimental frequencies of the relevant modes are summarized in Table 4. The modes at 68.4 and 413.2 cm⁻¹ (assigned to distortions of the Au chain and of the step edge)

are only observed at RT, while modes at 82.7 and 99.1 cm⁻¹ are exclusive to LT.

To understand the changes in the measured spectra, the vibrational properties of the Si(553)-Au system at LT have been calculated with all structural models that have been proposed in the literature for the description of this phase, namely the spin-chain (SC) [144] and centered spin-chain model (CSC) [280], as well as the rehybridized model (R) [306]. Unfortunately, the calculation of the Raman scattering efficiency for the LT structural models is an exceptionally demanding task, due to the system size. However, the knowledge of the calculated Raman frequencies and displacement patterns can still be used to interpret the experimental data.

There are three categories of phonons expected among the calculated modes: (i) modes which are common to the RT and LT phases, (ii) modes that occur both in the RT and in the LT phase, however with a different frequency, and (iii) modes that exist either only in the RT or only in the LT structure. Most of the modes calculated with the RT model can be identified in all three candidate models within a few cm⁻¹. However, several important exceptions are found in the experimental spectra, corresponding to the LT-RT structure differences.

The first particular mode is the Au dimerization mode shown in Fig. 32 (a), which exists in both the RT and LT structure, yet at different frequencies. This mode is predicted at 18.8 ± 5 cm⁻¹ with the RT model,

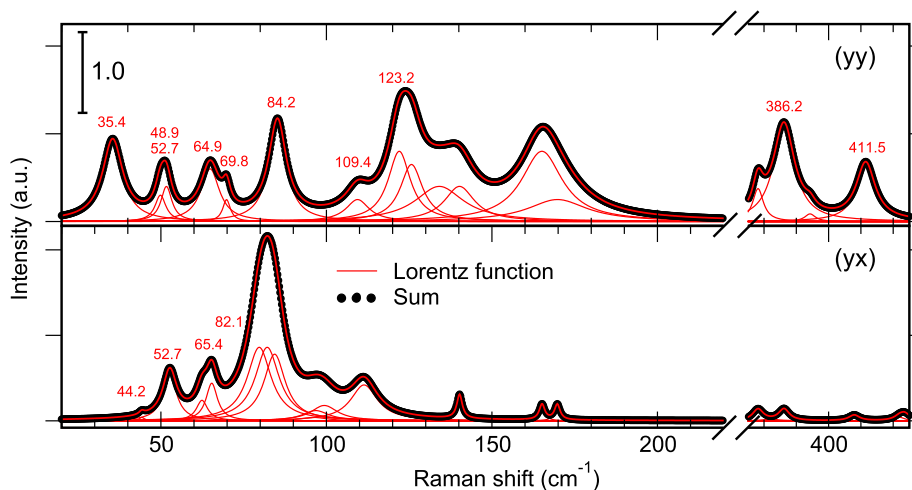


Fig. 30. Raman spectra of the Si(553)-Au surface calculated within DFT-PBEsol for the (yy) and (yx) polarization with the structural model by Krawiec [305].

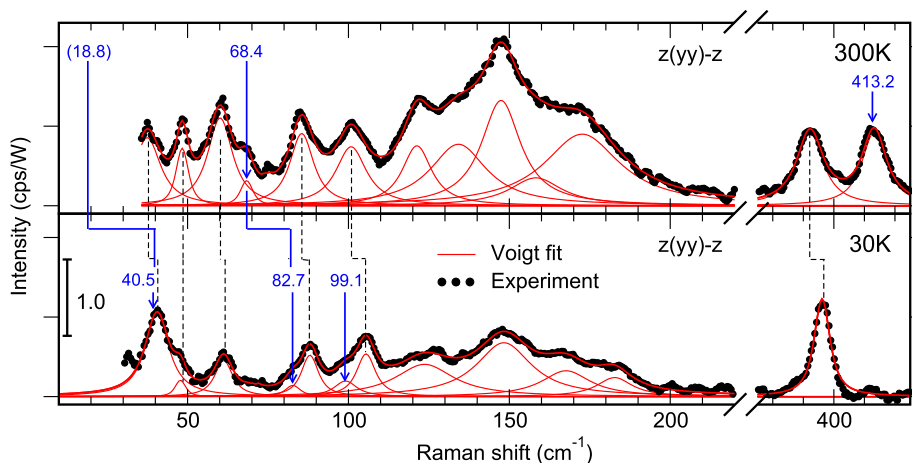


Fig. 31. Raman spectra of the Si(553)-Au surface after subtraction of the bulk scattering, measured at 300 K and 30 K in parallel polarization. The measured Raman spectra were fitted using Voigt profiles with Gauss FWHM fixed to the spectrometer resolution of 1.3 cm⁻¹ and variable Lorentz FWHM. Blue arrows mark features with strong temperature dependence, while dotted black lines join features observed at both temperatures. (For interpretation of the references to color in this figure legend, the reader is referred to the Web version of this article.)

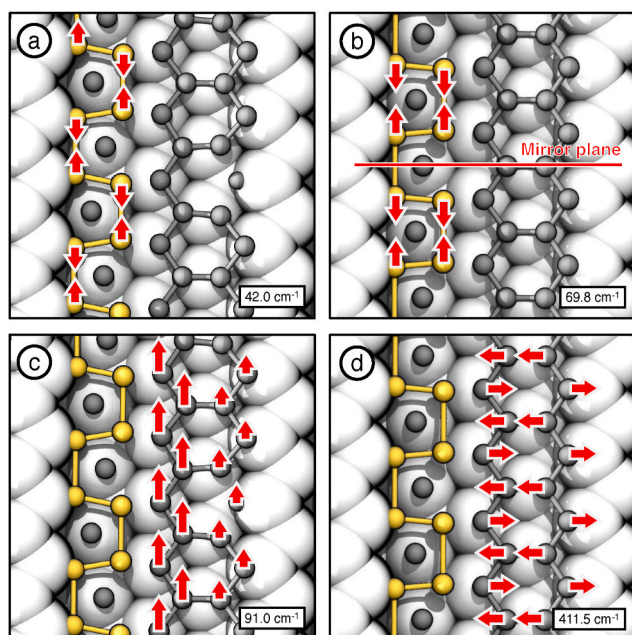


Fig. 32. Schematic representation of the displacement pattern of the dimerization modes (a) and (b), of the honeycomb translation mode (c) and the step edge mode (d). The displacement patterns are calculated within DFT-PBEsol according to the rehybridized model [306] of the LT phase.

and is thus not experimentally accessible. However, it becomes much harder (42.0 cm^{-1}) within the rehybridized model, which features a more pronounced dimerization. As this mode shortens the Au–Au bond length, it requires more energy for a strongly dimerized Au chain. In the experimental spectrum, a noticeable peak shift from 37.5 to 40.5 cm^{-1} is observed in this energy region between 300 K and 30 K along with a strong increase of the Raman intensity. Yet, this is surprising, as the peak at 37.5 cm^{-1} [vertical translation of the Au chain [325,326]] is not expected to be much affected by temperature. Indeed theory predicts a small shift of about 1.5 cm^{-1} in the opposite direction for this mode. This suggests that the peak observed at LT at 40.5 cm^{-1} is the overlap of a weakly temperature dependent mode at 37.5 cm^{-1} and the strongly temperature dependent dimerization mode at about 42 cm^{-1} [325,326].

The second particular mode with strong frequency shift is the mode calculated at 69.8 cm^{-1} shown in Fig. 32(b). Similarly to the dimerization mode, this mode shortens the Au–Au bond length and becomes much harder by about 8 cm^{-1} for the rehybridized model. This mode is associated to the low-intensity Raman peak at 68.4 cm^{-1} at high temperatures, which seems to disappear at 30 K . Comparison with theory suggests that this mode shifts at higher frequencies and can be assigned the mode at about 82.7 cm^{-1} which is not observed in the RT Raman spectrum [325,326].

A third particular mode refers to the feature at 99.1 cm^{-1} in the measured LT Raman spectra, which we associate to the displacement pattern calculated with the rehybridized model and displayed in Fig. 32 (c). At LT, this mode is visible in the parallel polarization Raman spectrum via charge density fluctuation scattering, according to its symmetry. This mode is not existent in the RT structure, but closely related to the chain translation modes predicted at 65.4 cm^{-1} and at 79.7 cm^{-1} at RT, which are visible via deformation potential scattering in the crossed polarization Raman spectrum. This mode is a translation of the HT chain, which is strongly hindered by the LT modification of the step edge pinning the outer atoms and therefore making this mode much harder [325,326].

A fourth particular mode appearing at 413 cm^{-1} only in the RT Raman spectra is associated to the theoretically predicted step edge mode at 411.5 cm^{-1} [see Fig. 32 (d)]. Due to the different symmetry of

the Si step edge in the structural models associated to the LT and RT phases, this lattice vibration has no low temperature counterpart. In the rehybridized model, this mode is decomposed into local vibrations of the step edge, as previously pointed out by Braun et al. [282].

Overall, the rehybridized model can well explain the observed temperature shifts. On the contrary, in the spin-chain model [144,280] the dimerization is not as pronounced as in the rehybridized model [306] and therefore the frequency shifts with respect to the high temperature model cannot be reproduced. For example, the dimerization mode [see Fig. 32 (a), and Table 5] is predicted by DFT-PBEsol at 8.7 and 16.7 cm^{-1} , for the spin-chain and centered spin-chain models, respectively. This value is far from the value of 42.0 cm^{-1} calculated with the rehybridized model and assigned to the peak measured at 40.5 cm^{-1} . Similarly, the mode that couples the Au dimers [see Fig. 32 (b)] calculated at 68.9 cm^{-1} for the RT structure, does not significantly shift at LT in the SC and CSC model (69.4 and 70.7 cm^{-1} , respectively) and cannot explain the behavior of spectral feature measured at 82.7 cm^{-1} . Thus, the comparison of the calculated vibrational properties with the measured spectra yields a strong argument for the rehybridized model for the description of the low-temperature phase.

2.2.4. Electron transport

In this section, we turn to experimental studies of the electronic DC transport in atomic wire systems, concentrating on Si(553)-Au. By measuring dc conductance we probe the scattering properties of electrons globally close to the Fermi level in an energetic range given by the Fermi distribution and kT . Depending on contact distance electron transport phenomena can be tested on a mesoscopic to macroscopic scales [138,327–330].

Four-tip STM-based transport experiments have previously been performed on Si(553)-Au and Si(557)-Au [331]. It was shown there that the wire system is conducting. Several 1D transport channels contribute to the conductivity of Si(hhk)-Au, which could be modified by adatoms like oxygen. Interestingly, as also confirmed by plasmon spectroscopy experiments on Si(557)-Au [332], e.g., metallicity is preserved under all oxidation conditions that are experimentally accessible in UHV. These experiments demonstrate together with hydrogen adsorption experiments on Si(553)-H [296] that changes in conductance are not mainly due to a local adsorption-induced distortion. Rather, non-local changes like the modification of band structure, e.g. by H adsorbed at the Si step edges, yields a better description of the modification of the transport properties. They indicate the existence of strong electronic correlations that comprise a whole mini-terrace.

Extending earlier measurements on the clean Si(553)-Au system with the four-tip STM [281], a detailed view on the temperature dependence of the strongly anisotropic dc conductance in the Si(553)-Au system [333] reveals even more closely the fascinating interplay between the increasing hybridization between spin polarized Au and Si edge states. Indeed, our conductance results are fully in line with the theoretical scenarios outlined above in the first part of sec. 2.2. In other words, the main contribution to conductance stems from the Si dangling bond states at the step edge, which due to temperature dependent partial filling become conducting, first as a transient between the two insulating phases described by the models of Braun [282] and Erwin [144], but finally opening a permanent new 1D conduction channel at high temperatures. Thus all three models turn out to be relevant as thermal excitations at various stages, unifying and corroborating the picture already developed so far.

The conductance along the wires as a function of temperature, after subtraction of the conductance perpendicular to the wires, which was taken as isotropic background, is shown in Fig. 33 for an Au concentration of 0.48 ML . Two pronounced maxima of conductance are seen at 155 K and at 250 K , respectively.

In qualitative agreement with our earlier study [281], a small residual, presumably metallic, conductance ($\approx 10^{-7} \text{ S}$) remains, as shown in the inset of Fig. 33. This conductance curve changes little when the Au

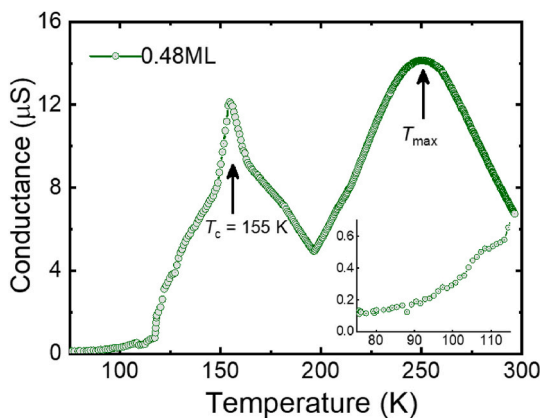


Fig. 33. Conductance along the wires at an Au concentration of 0.48 ML as a function of temperature after subtraction of the conductance perpendicular to them. Inset: magnification of low-temperature range.

concentration deviates by (± 0.02 ML) from the optimal concentration, i. e. it is robust against Au vacancies or surplus atoms. More details can be found in ref. [333].

The conductance maximum originally found around 90 K appears now at 155 K, which is in agreement with ref. [275], while the second maximum was previously not seen at all. This difference to earlier measurements is most likely related to the absence of a significant isotropic background conductance in the data shown here up to 200 K. Such a background may be caused by a sub-surface concentration of C atoms, acting as an 2D-isotropic p-type space charge layer with a strong temperature dependence already below 100 K [334]. Contrary to this earlier situation, the isotropic background is dominated by Au doping during sample preparation, since temperature dependent analysis of this background quantitatively yields the activation energy for Au interstitials in Si [333].

The two distinct conductance maxima represent a rather unusual and puzzling behavior that need further detailed explanation. Interestingly, they are not directly linked to the phase transitions described above in sec. 2.2.1, as deduced from experiments of the temperature dependence of LEED, and further explained in ref. [333]. E.g. the 2D-1D transition for $\times 3$ order, identified in Ref. [324], clearly happens far below 100 K. Also a contribution by the generation of mobile fractionally charged 1D solitons at the step edge that sets in at around 95 K [324,335] will be small due to their small mobilities. While they clearly disturb $\times 3$ 1D long range order, they can thermally only be generated as soliton/anti-soliton pairs with opposite signs of charges.

As shown in the following, the two conductance maxima can indeed be understood within the framework already developed and described above as transitions between the R, SC, and CSC models. They take place over a wide temperature range. For this reason, the stability range of the different phases represented by these models are only rough estimates. Based on the AIMD results, the phase transition from the R phase to the spin liquid is completed at 150 K, at which the spin liquid has the highest probability. At this temperature, the second phase transition with local configurations described by the CSC model sets in, which we consider to be complete at 250 K. As already mentioned, the structural changes between these phases only affect dimerization of the Au chains and small variations of positional heights of Si step edge atoms (see Fig. 16), but these minor structural differences have a large impact on the electronic band structure, especially close to the Fermi level, as illustrated below.

Fig. 34 shows the projected DOS of the Si step edge at various temperatures close to the Fermi level. The topmost panel corresponds to the pure R model, in which no step edge state crosses the Fermi energy, since in the (2,2,0) configuration the dangling bonds are either fully occupied and below the Fermi energy, or fully empty and above the Fermi energy. Correspondingly, the step edge related DOS at the Fermi energy

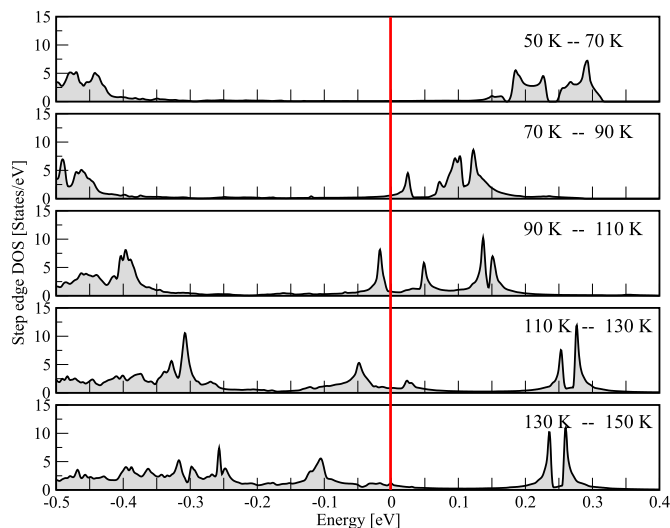


Fig. 34. Projected density of states of the Si step edge in the Fermi level region for different temperatures. At 50 K (top panel), the DOS is that of the rehybridized (R) model [282], while at 150 K (bottom panel) it corresponds to the spin chain (SC) model [144]. The panels in between represent intermediate configurations. The Fermi energy is marked by a red line. (For interpretation of the references to color in this figure legend, the reader is referred to the Web version of this article.)

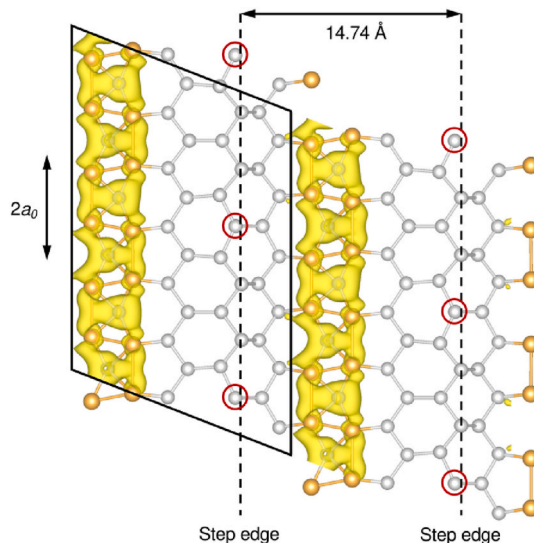


Fig. 35. Squared wavefunctions associated to electronic states within an interval of 0.1 eV around the Fermi energy calculated with the R model [306]. As only Au-related states cross the Fermi energy, a single conduction channel localized at the Au chain is formed. The surface unit cell is highlighted, the Si step-edge atoms with empty orbitals located below the other step-edge atoms are marked by red circles. (For interpretation of the references to color in this figure legend, the reader is referred to the Web version of this article.)

vanishes, while the peaks related to the occupied and empty states can be seen at the left and at the right end of the panel, respectively. Thus the conductivity of the system is exclusively due to the metallic Au chain. A real space representation of the squared wavefunctions in an interval of 0.1 eV around the Fermi energy (see Fig. 35) shows that the states which are important for conduction are indeed localized at the Au chain. They form a 1D conduction channel.

The higher probability for spin-liquid configurations to appear as a function of increasing temperature has direct consequences to conductance. Please note that the full occupation of a (2,2,1) state represents a

configuration in which the spin-polarized electronic states of each spin channel are either fully occupied or fully empty. Therefore, this state is insulating again (see bottom panel of Fig. 34). The conductivity of a system in this state is again solely due to the Au related states, which are not strongly affected by the R-to-SC transition.

However, the modification of the step edge occupation from (2,2,0) to (2,2,1) is coupled with a shift of one of the previously empty states to lower energies, from above to below the Fermi energy (for details, see next section). This transition is well represented in Fig. 34, in which the DOS of the unoccupied step edge states splits for increasing temperatures. One part remains roughly at the original position, while the other part moves below the Fermi energy. In the simulation, a step-edge state crosses the Fermi energy at a temperature of about 110 K, causing a *transient enhancement* of the DOS at the Fermi level. This crossing is expected to generate a resonance-like feature in the conductance, in agreement with the experimental observation of a sharp conductance peak, which in experiment is close to 155 K. Once the step-edge state passes the Fermi energy, the conductance decreases again, in agreement with the experimental observation.

As AIMD also shows [282], the second conductance maximum at around 250 K is related to a second phase transition from the (already disordered [324]) spin chains to a system well described by the Krawiec (CSC) model. Also in this case the phase transition is a continuous process with marginal modifications of the atomic structure, but a large impact on the electronic structure, as shown in Fig. 36. During this second transition, the increasing hybridization between Au and step edge states causes the original band gap of the spin chain system to shrink. Similar to the first transition, mainly the unoccupied states change shape and shift during this transition. Thus again, the previously unoccupied states become more and more filled at temperatures above 200 K. When this transition of the structure described by the CSC model is fully established, the step-edge states are localized at the Fermi energy (see last panel of Fig. 36), increasing the DOS of the states which are relevant for the electronic conduction. Importantly, in this way a truly new conduction channel, spatially separated from the one at the Au chain is formed, as shown in Fig. 37. Correspondingly, a broad and high conductance maximum is predicted and also measured. Due to its nature as a high temperature phase, it is also robust against small changes of Au concentrations, in agreement with experiment. At even higher

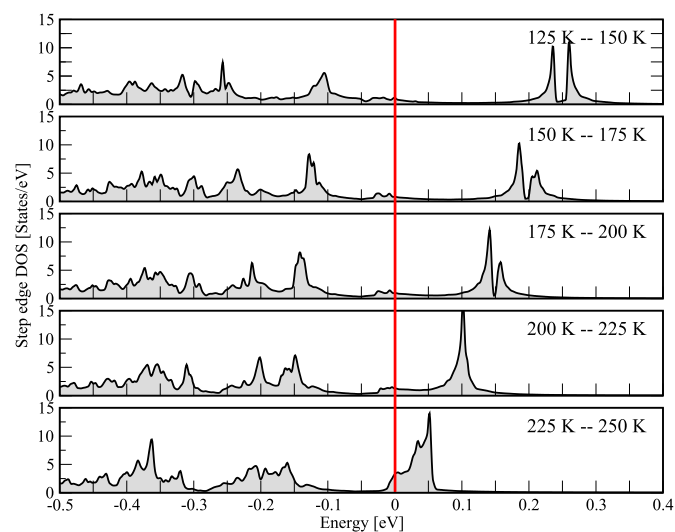


Fig. 36. Projected density of states of the Si step edge in the Fermi level region for different temperatures. At 150 K (top panel), the DOS is that of the SC model [144], while at 250 K (bottom panel) it corresponds to the CSC model [305]. The panels in between represent intermediate configurations. The Fermi energy is marked by a red line. (For interpretation of the references to color in this figure legend, the reader is referred to the Web version of this article.)

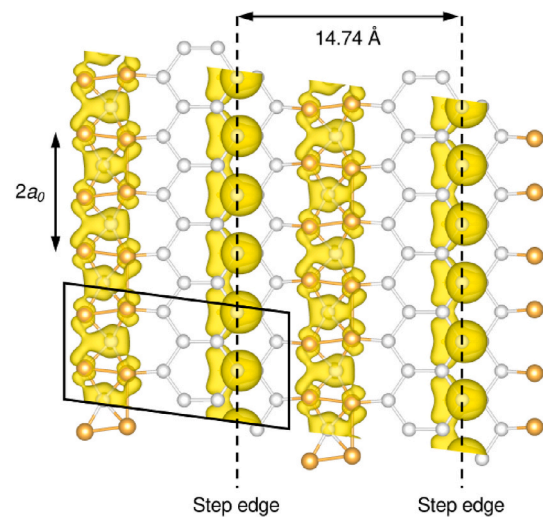


Fig. 37. Squared wavefunctions associated to electronic states within an interval of 0.1 eV around the Fermi energy calculated with the CSC model [305]. As Au related and Si step-edge states cross the Fermi energy, two spatially separated conduction channels are formed, localized at the Au chain and at the Si step-edge, respectively. The surface unit cell is highlighted.

temperatures, the step-edge oscillates with a higher amplitude [282], thus reducing conduction in this channel, as observed.

Summarizing, the already established atomistic models turn out to represent thermally excited states of the Si(553)-Au system at different temperatures with the configuration of the R model as the lowest energy state. The transitions between them are not only compatible with the measured DC conductance, but can also explain the origin and form of the different features including sensitivity to defects. This study not only shows that all three models suggested for this chain system Si(553)-Au are relevant and valid, but at different temperatures, it also highlights the role of the Au chains in this system. While the Au chains provide some metallic conductivity and modify the electronic surface states strongly, the main part of conductance stems in fact from charge transfer to partially occupied Si step edge states. This is the - somewhat counterintuitive - result of correlations between Au and Si states.

2.2.5. Transition from 2D to 1D

As already outlined in chapter 1, one-dimensional wires are inherently unstable, but can be stabilized by interaction with their higher dimensional environment. Thus, strictly speaking, a pure one-dimensional description of the systems discussed here is not appropriate. Lateral charge transfer between the Au chain and the Si step edge dangling bond wire, for example, is instrumental for the surface phase transition of Si(553)-Au, as discussed above [282] and shown in Fig. 38. The failure of a strict one-dimensional description of the highly anisotropic Si(553)-Au surface has also been demonstrated by the measured plasmon dispersion relations [266].

In general, excitations are expected to wash out the effect of the surface anisotropy and hence to suppress the indications of one-dimensional behavior. Interestingly, the Si(553)-Au shows the opposite: Thermal excitation induces a crossover from the lateral, i.e., two-dimensional coupling between neighboring dangling wires to a more one-dimensional behavior. As discussed above, the ground-state structure Si(553)-Au is characterized by Si dangling-bond wires, where two filled dangling bonds alternate with one empty dangling bond [306]. The dangling-bond structure in different rows are in registry. As shown by SPA-LEED and STM, the lateral interactions lead to a centered arrangement of $p(1 \times 3)$ unit cells [280]. For temperatures above around 100 K, however, the $\times 3$ diffraction spots broaden, due to increasing disorder in the arrangement of the dangling bond wires. Hafke *et al.* [324] attribute this disorder to occupation changes in the dangling bond

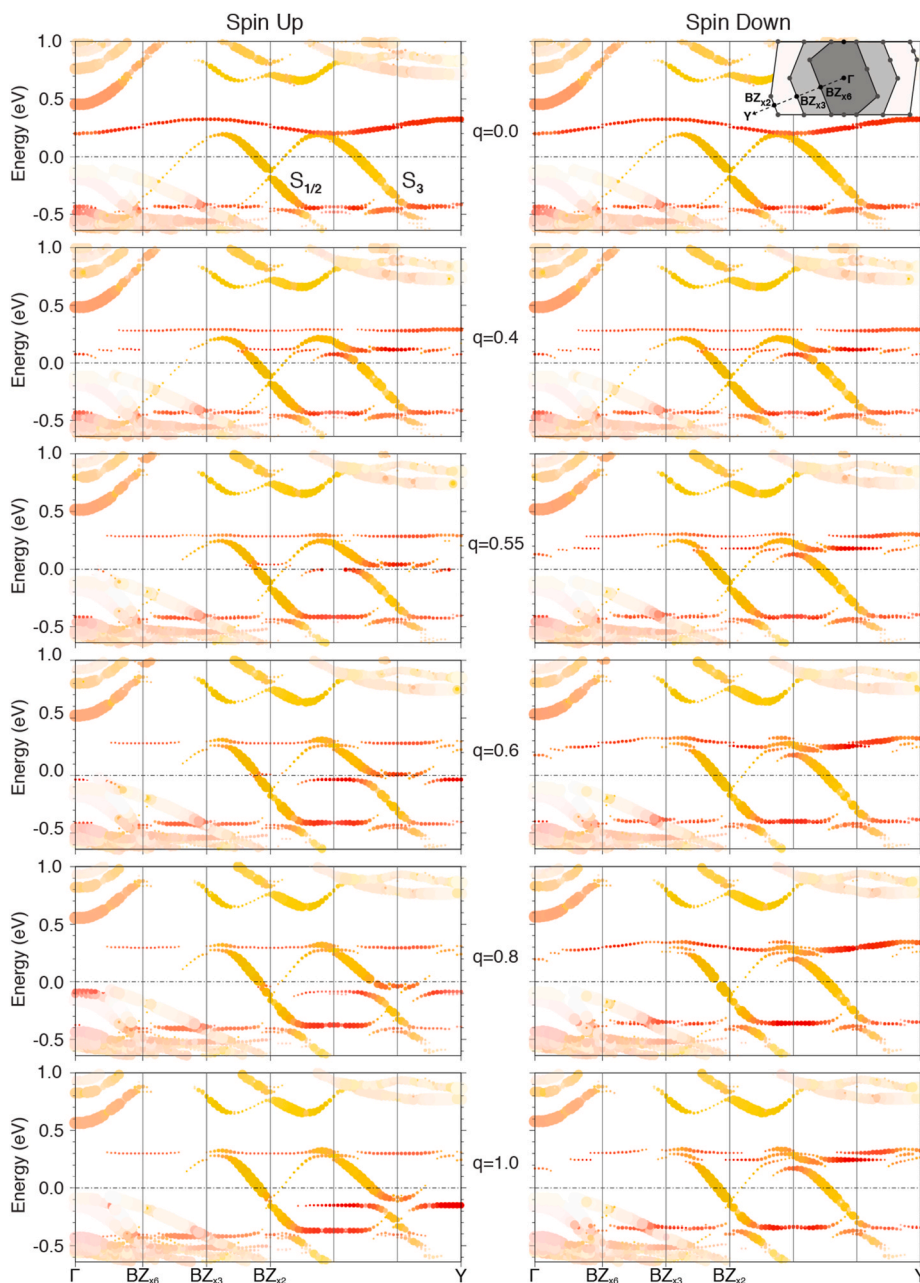


Fig. 38. Si(553)-Au surface band structures calculated along the reaction path from local (2,2,0) ($q = 0.0$) to (2,2,1) ($q = 1.0$) configurations. To ease the interpretation, the bands are unfolded into the 1×1 Brillouin zone (see inset) following Medeiros et al. [318]. Yellow and red colors denote electron localization at Au and Si step edge atoms, respectively. Adapted from ref. [282]. (For interpretation of the references to color in this figure legend, the reader is referred to the Web version of this article.)

wires, which interchange the positions of filled and empty dangling bonds, see Fig. 39. This elementary excitation can be viewed as a soliton-antisoliton bound pair. The formation of soliton defects leads with increasing temperature to a growing fraction of dangling bond wires that undergo registry shifts with respect to each other and hence the two-dimensional low temperature state begins to behave like a collection of uncoupled one-dimensional wires.

Experimentally, this transition from 2D to 1D behavior has been determined by Hafke et al. through a change of the shape of the spot profile in LEED as shown in the insets of Fig. 40. At temperatures above ≈ 120 K, the $\times 3$ diffraction spots are well described by a standard Lorentzian, indicative for 1D behavior. At temperatures below ≈ 90 K, the 2D character of the diffraction is more pronounced and hence the spot profiles are described by a Lorentzian to the power $3/2$ [44].

A well-defined transition from an exponent $\nu = 1.5$ to $\nu = 1.0$ between $T_- = 93$ K and $T_+ = 128$ K is shown in Fig. 40. The transition sets in at the temperature for which the FWHM along the steps begins to increase (see Fig. 27). Fitting the spot profiles without allowing ν to vary leads to significantly worse fits (insets to Fig. 40). The transition is completed at T_+ , where the FWHM κ_{\perp} across the wires exceeds the size of the surface Brillouin zone as seen in Fig. 27, reflecting the complete loss of long-range order perpendicular to the wires.

Very recently, those solitons were directly proven by STM and it could be shown that their motion is activated above 100 K [335]. Indeed, various mobile defects could be identified in Ref. [335] and were attributed to fractional topological solitons, which possibly provide a new platform of robustly-protected informatics potentially with extraordinary functionalities. Thus, while the Si(553)-Au surface is

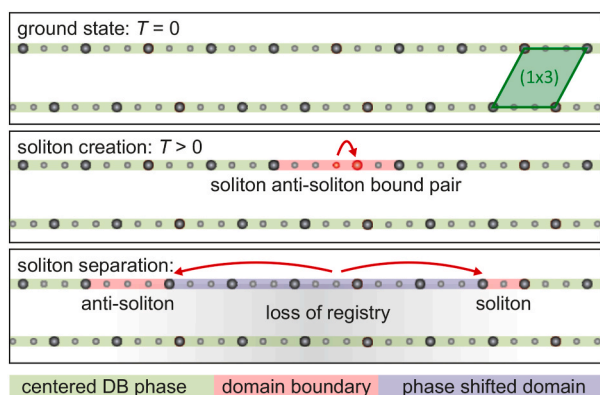


Fig. 39. Schematic model of creation and separation of a soliton-antisoliton pair. Charge is transferred from a filled dangling bond to an empty dangling bond, generating a hop of the empty dangling bond to a neighboring site and creating a soliton-antisoliton pair. If this pair separates then a phase-shifted domain with $\times 3$ periodicity is formed. Adapted from ref. [324].

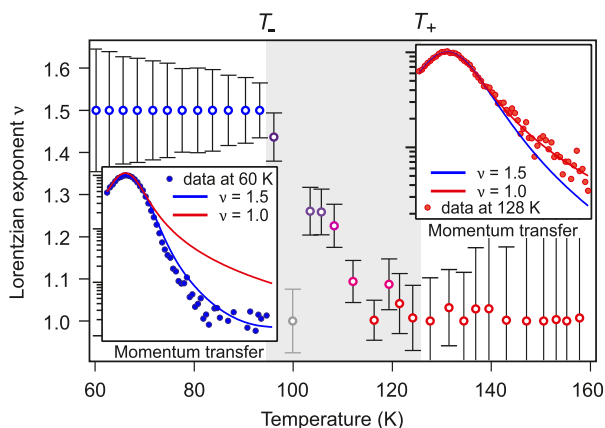


Fig. 40. Change of shape of spot profile. Plotted is the exponent of the Lorentzian describing the spot profile of the 1×3 spot as function of temperature. Left inset: at low $T = 60$ K the spot profile is described by an exponent $\nu = 1.5$ indicative for two dimensional order. Right inset: at high temperatures $T = 128$ K the spot profile is described by an exponent $\nu = 1.0$ indicative for one dimensional order. Adapted from ref. [324].

clearly a two-dimensional object, it still gives rise to fascinating one-dimensional phenomena.

2.3. Indium on Si(111): phonons, structure and their relation to phase transitions³

The system In on Si(111) was not only historically one of the first systems, in which the spontaneous break of symmetry induced by adsorption of submonolayers of In lead to quasi-1D structures, it also turned out to exhibit particularly rich physics in low dimensions. The adsorption of indium on Si(111) in the submonolayer range is known to result in various ordered surface reconstructions, as found for a variety of metals on silicon and germanium surfaces [336,337].

One of these adsorbate phases is the In/Si(111) (4×1) structure formed by a full monolayer of indium, mimicking the geometry of a π -bonded chain-structure of Si(111) (2×1) with the outermost Si plane being replaced by In atoms [338,339]. The discovery of a metal-insulator-phase transition into a (8×2) reconstruction by cooling below 130K, as reported by Yeom and coworkers in 1999 [46], led to an

enormous scientific interest in this particular structure with regard to the nature of a Peierls transition in quasi-one-dimensional structures. So far, In/Si(111) (4×1) is the only 1D- or quasi-1D-surface structure which exhibits a Peierls transition. These observations, in conjunction with the fact that In/Si(111) forms an atomically sharp interface, has motivated numerous experimental as well as theoretical works in order to elucidate the nature and microscopic mechanisms of the phase transition. As a matter of fact In/Si(111) represents a unique realization of a 1D Peierls structure, which is accessible with reasonable experimental and theoretical effort. In particular, the investigation of the intertwinement between lattice vibrational properties (surface phonons) and electronic structure have finally led to a consistent and very detailed understanding of the structure and the phase transition in this prototypical system.

It is now commonly accepted that the (8×2) reconstruction observed at low temperature represents the ground state structure, while the (4×1) phase observed at room temperature is a metastable structure with slightly different atomic coordinates of the surface atoms. Upon cooling the system undergoes a reversible transition from the metallic high temperature state to the insulating ground state [340–342] at $T_c = 130$ K [50,343,344] which is accompanied with the opening of a band gap of $E_{\text{gap}} = 0.2$ eV [48,244,343] and the formation of a charge density wave (CDW). Fig. 41 shows the atomic structure of both the (4×1) and (8×2) reconstructions. The formation of the charge density wave along the In chain direction leads to period doubling, accompanied with a small displacement of atomic coordinates in the respective unit cells that causes the mentioned energy barrier in between [345]. Wippermann et al. [276] showed that the balance between the lower total energy of the stable (8×2) structure and the larger entropy of the metastable (4×1) structure drives the phase transition. Moreover, two phonon soft shear and rotational phonon modes of the (4×1) and (8×2) structures were identified which transform the respective atomic positions by superposition of the phonon displacements [53,276]. Within a

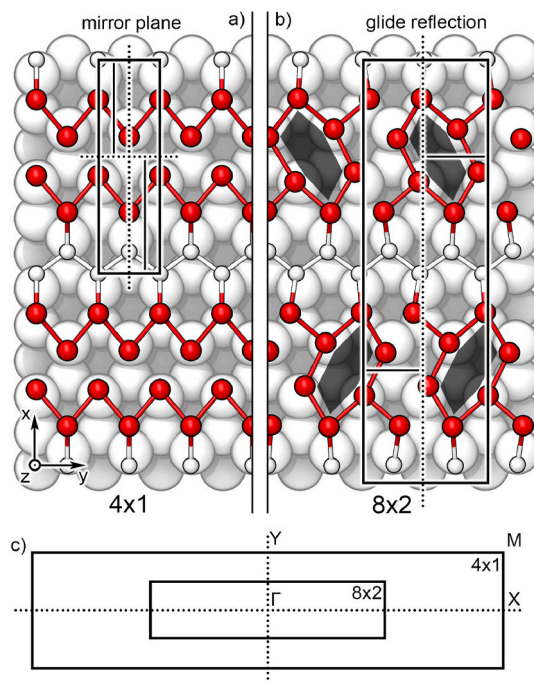


Fig. 41. Atomic structure (top view) of the room temperature (4×1) (a) and low temperature (8×2) phase (b) of In/Si(111), respectively. The surface unit cells and the respective mirror plane/glide planes in the unit cells are indicated. The (4×1) structure has in addition a C_2 rotational symmetry (not shown). (c) shows the corresponding surface Brillouin zones of the (4×1) (red) and (8×2) (blue) periodicities. (For interpretation of the references to color in this figure legend, the reader is referred to the Web version of this article.)

³ Author mainly responsible for this section: Norbert Esser

thermodynamical approach the phase transition was described as a grand canonical Peierls transition [52]. In the grand canonical ensemble the Si substrate is acting as a charge reservoir in contact with the surface structure. It explains the Peierls-transition in the quasi-1D-structure and also its dependence on charge transfer by e.g. doping of the Si substrate [51,346] or adsorbates [229,230].

The strong correlation between electron and lattice degrees of freedom is indicated by phonon softening and the formation of coupled charge density - phonon modes, called amplitudon modes, in the (8×2) phase, which is the correlated phase at low temperature [52]. This strong electron-lattice coupling arises for two particular phonon modes which transform between the structures by a linear combination of the respective phonon displacement vectors. As shown below, these two modes refer to amplitudon modes in the correlated ground state. It was shown that the two amplitudon modes arise from a shear phonon distortion accompanied with a charge accumulation in the inner indium rows and a rotary phonon distortion accompanied with charge accumulation in the outer indium rows. In the following we will focus on the microscopic understanding of the phonon modes and their role in the phase transition.

In recent years, a number of concerted experimental and theoretical studies of the lattice dynamical, electronic and thermodynamical properties of the structure has led to a very detailed understanding of the underlying mechanisms [52,53,233]. By Raman spectroscopy and ab-initio calculations of the surface structure and phonons a fully consistent picture of the surface vibrational modes of both phases was finally achieved [53,233,276,347]. Surface vibrational modes, i.e. characteristic fingerprints of both structures, were identified by Raman spectroscopy in a spectral range from 10 cm^{-1} – 500 cm^{-1} and subsequently related to microscopic eigenmodes from frozen phonon calculations. For the assignment, both eigenfrequencies and symmetry properties of the modes were considered. In particular, the low frequency eigenmodes in the spectral range up to 70 cm^{-1} were shown to involve atomic displacements within the outermost In–Si layer and thus strongly depend on the surface structure.

Fig. 42 shows Raman spectra of the low-frequency range in parallel and crossed polarization configuration. According to the C_{2v} - and C_s symmetry of the In/Si(111) (4×1) and (8×2) structures, respectively, A' denote the symmetry-conserving modes which appear under parallel polarization conditions, while A'' denote symmetry-breaking modes showing up under crossed polarization conditions [53,233]. Consequently, both types of phonon modes can be experimentally distinguished via their Raman polarization selection rules.

In Fig. 43 eigenvectors of the modes of the (4×1) and (8×2) structures corresponding to the major Raman lines are shown. Modes of the (4×1) are indicated by numbers 2, 5, and 6 as discussed in Refs. [53, 233]. The A' mode 2 corresponds to a shear displacement along the In rows, breaking the mirror plane symmetry. Please note that the Raman peak 2 is associated with mode 2 at the Brillouin zone center, while the displacement pattern shown in Fig. 43 refers to the according mode at the Y point of the Brillouin zone. At the Brillouin zone center the respective mode shows an in-phase shear displacement of adjacent indium double chains. The A' mode 5 corresponds to a vertical displacement of In atoms and A' mode 6 to a shear displacement perpendicular to the In rows, both conserving the mirror plane symmetry.

Upon transition to the (8×2) structure, additional modes show up in the Raman spectra, see Fig. 42. Additional modes are indeed expected to arise from backfolding from the (4×1) zone boundaries. In addition to the backfolding, the structural arrangement within the unit cell is slightly different for the (4×1) and (8×2) structures. Thus, the eigenvectors and eigenfrequencies of the modes may change due to the structural rearrangement within the unit cells.

The relation of the (8×2) and (4×1) -modes has been discussed by Speiser et al. [53,233] in detail and will be briefly summarized here. Fig. 43 shows the eigenvectors of five eigenmodes of the (8×2) structure at the Brillouin zone center, together with their respective

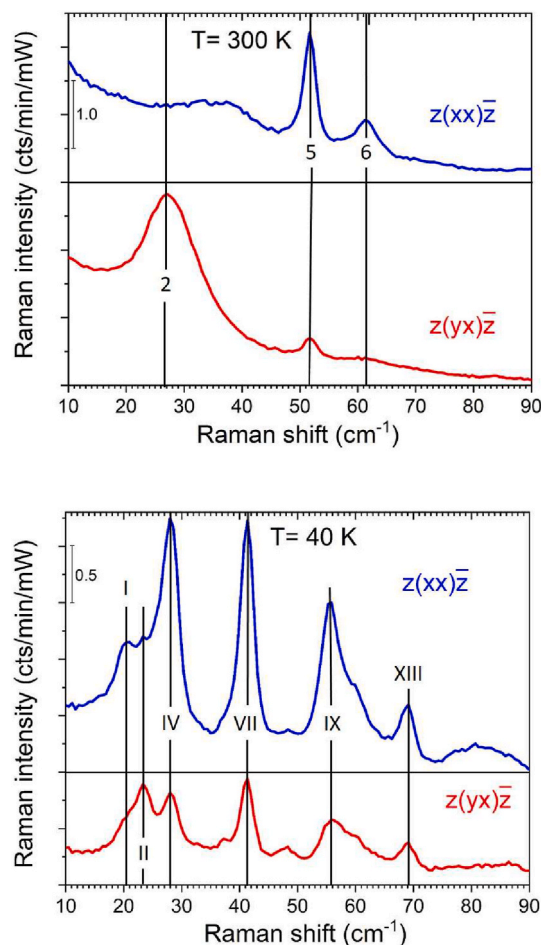


Fig. 42. Raman spectra of the (4×1) (a) and (8×2) (b) structures for parallel ($z(xx)\bar{z}$) and crossed ($z(yx)\bar{z}$) polarization configurations, corresponding to A' and A'' -modes, respectively. The assignment of Raman peaks to phonon eigenmodes is indicated by Greek (for (4×1)) and Roman numbers (for (8×2)). The assignment is adapted from Refs. [53,233]. The eigenvectors of the labeled modes are shown in Fig. 43.

counterparts in the (4×1) structure. The A' shear and rotary modes I and IV of the (8×2) structure refer to those two modes which strongly couple with the electronic system. The (4×1) counterparts of the strongly coupled modes I and IV refer to modes at the zone boundary, at \bar{Y} and \bar{X} points, in the (4×1) structure. A'' mode 2 in the (4×1) structure is the shear mode at Γ , while the according mode at the Y-point is the counterpart of the strongly coupled shear mode I. The shear mode 2 at Γ corresponds to the A'' mode II in the (8×2) structure (not shown here, displacements according to mode I but with inverted directions in adjacent In chains). The modes showing vertical displacements, i.e. A' modes VII and IX, and the shear perpendicular A' mode XIII, on the contrary are not strongly coupled to the electronic system and have phononic character.

Summarizing, the modes I and IV in the correlated ground state phase, refer to amplitudon modes of the correlated phase and show the atomic displacements within the In rows associated with the respective charge density excitations [52,233]. The associated modes of the (4×1) structure are zone boundary phonons and correspondingly not visible in Raman spectra due to the momentum conservation rule.

Raman spectra for different temperatures across the phase transition are shown in Fig. 44, together with an evaluation of phonon frequencies as a function of temperature. The five low frequency Raman lines observed in the spectral range refer to the eigenmodes I, IV, VII, IX and

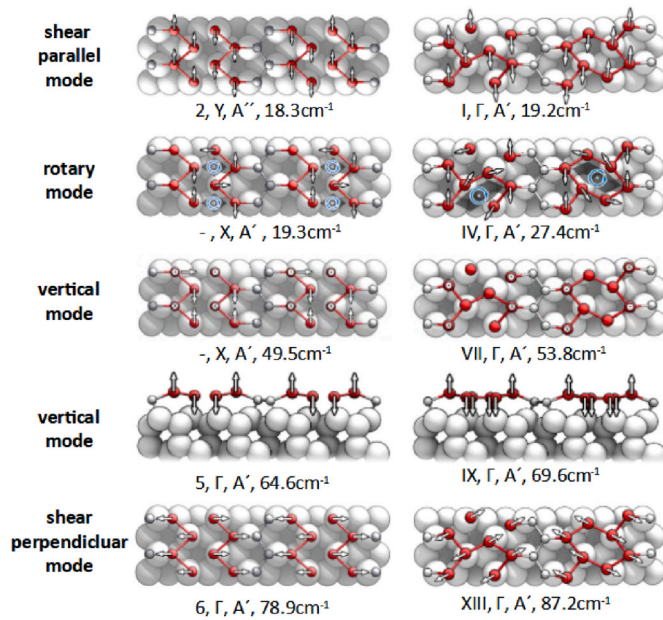


Fig. 43. Displacement patterns of corresponding phonon eigenmodes of the Si (111)-In (4×1) (left hand side) and (8×2) structures (right hand side). The displacement patterns are shown in a common (8×2) unit mesh to allow for an easy comparison for the (4×1) and (8×2) surface modes. The labelling by Greek and Roman numbers for (4×1) and (8×2) structures refers to the Raman modes shown in Fig. 42. Symmetry and related Brillouin zone points are denoted as well for each mode. The assignment is adapted from Refs. [53,233].

XIII shown in Fig. 43. Approaching the phase transition temperature of 130K, the shear and rotary modes I and IV at 20 cm^{-1} and 28 cm^{-1} show a remarkably strong phonon softening of more than 10 % of their respective frequency at 45K (the lowest temperature achieved in the experiment), and vanish with the phase transition in the Raman spectrum. The vertical modes VII and IX, however, do not show any indication of phonon softening, since they are not strongly coupled with the electron system of the quasi-1D In-nanowires. The mode at 55 cm^{-1} lowers by less than 1 % up to T_c , while the mode at 42 cm^{-1} remains constant in frequency and even shows a very slight hardening. Nevertheless, mode VII vanishes from the spectrum since the corresponding mode of the (4×1) structure is located at the X-point of the Brillouin zone.

Indeed, the Peierls theory predicts amplitudon modes to be Raman active excitations of the correlated phase [109]. The amplitudon modes of the correlated phase refer to a charge density modulation accompanied by a lattice distortion with periodicity of $2a_0$ of the uncorrelated phase [109,254,348,349]. The amplitudons show a strong softening according to $\omega^2(T) \propto |T - T_c|$ when approaching the phase transition temperature T_c . Above T_c , in the uncorrelated phase, the excitations refer to phonon modes at the zone boundary, due to the change in periodicity accompanied with the Peierls transition. The according zone boundary modes of the uncorrelated phase show also a strong phonon softening when approaching T_c , called Kohn anomaly.

A microscopic picture of the phase change in terms of electronic band structures and bond strengths has been derived from ab-initio calculations as well as calculations within the crystal orbital Hamiltonian scheme [52,233,345]. The shear distortion is found to open a bandgap at the zone center while the rotary mode distortion does the same close to X-point of the (4×1) Brillouin zone (see Fig. 45). The shear mode distortion yields a modification of electronic charge mainly between the inner In-atom rows, while rotary mode distortion yields an accumulation of charge between pairs of In-atoms of the outer chains. Both effects are indicative of bond strengths changing continuously with the displacement, according to the re-structuring from zig-zag-chains in the

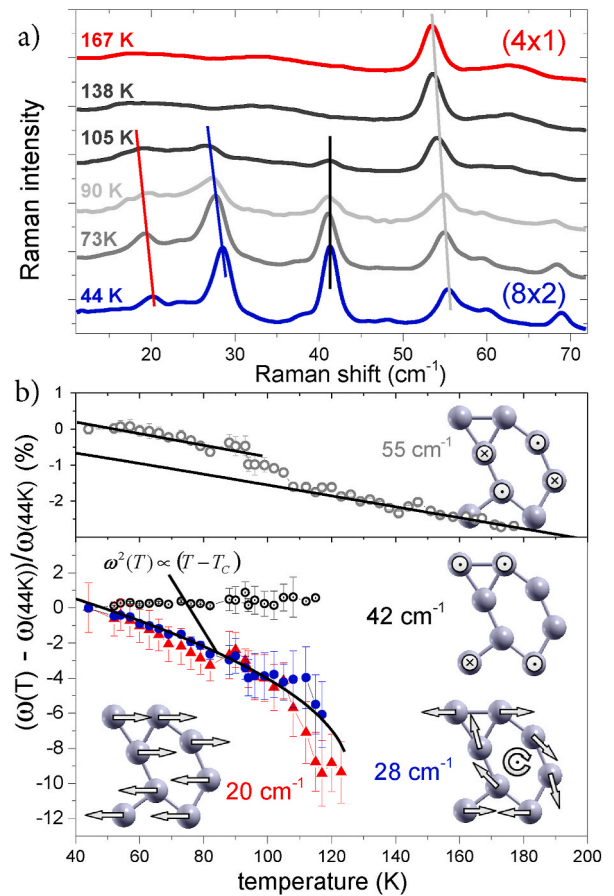


Fig. 44. Phase transition in vibrational spectra: (a) Raman spectra for different temperatures across the phase transition, (b) frequency of modes I (20 cm^{-1}), IV (28 cm^{-1}), VII (42 cm^{-1}) and IX (55 cm^{-1}) as a function of temperature. Modes I and II are the strongly coupled amplitudon modes, IV and VII are phonon modes. Modes I, IV and IX refer to zone boundary phonon modes in the (4×1) structure.

uncorrelated phase to hexagons in the correlated phase (see Fig. 45). The structural transition is accompanied with an energy barrier of approximately 100 meV per (8×2) unit cell.

The predicted behavior of the amplitudon modes of the correlated phase is exactly reflected in the temperature dependent Raman spectra discussed above and becomes microscopically perceptible by the ab-initio calculations of lattice and electronic excitations. While the shear and rotary modes in the correlated phase refer to the atomic displacements associated with charge density fluctuations in the surface, also termed charge density waves (CDW), they refer to zone boundary phonons in the uncorrelated phase. The Kohn anomaly, on the other hand, cannot be observed with Raman scattering since Raman is restricted to zone center modes due to momentum conservation in well-ordered structures.

Thus, a full microscopic understanding of structural, bonding, vibrational and electronic properties of both correlated and uncorrelated phases is achieved. In section 3, the structural and electronic dynamics of the phase transition are discussed.

2.4. Si(557)-Pb: strongly interacting nanowires⁴

The spin degree of freedom of electrons attracted much attention

⁴ Authors mainly responsible for this section: Christoph Tegenkamp and Uwe Bovensiepen

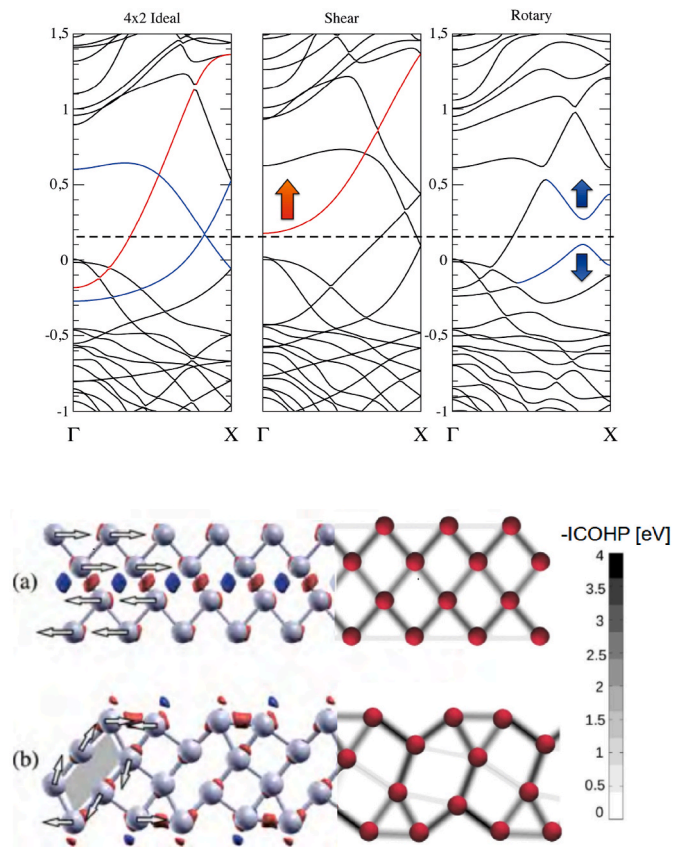


Fig. 45. DFT-LDA electronic band structure of In/Si(111) in the (4×1) phase, after a shear distortion, and after a rotary distortion. Gaps open at Γ between

two red bands and close to X between four blue bands. (b) and (c) show the respective changes in charge density associated with the displacements. In (c), left panel, the bond strengths as determined by an analysis within the crystal orbital Hamiltonian population scheme (COHP) are shown. The thickness of lines represents the bond strength. (For interpretation of the references to color in this figure legend, the reader is referred to the Web version of this article.)

over the last years. The electron spin plays a central role in the spin Hall effect [350,351], topological insulators [352], Rashba-type surface or interface states [353,354], and spintronic device structures [355]. Typically the propagation of electrons is treated as a single particle problem. This simple concept fails, however, when electronic correlation effects in low dimensional systems become important and spin- and orbit-effects are entangled like in hard-magnets [356], $j = 1/2$ Mott-insulators [357], or in new emergent topological superconductors [358,359]. So far, for the formation of 1D atomic chains induced by adsorption of the high-Z elements Au and Pb, spin-orbit signatures in spectroscopy and transport were found, which we highlight in the following.

Compared to many adsorbates on Si-surfaces, Pb does not alloy with the substrate and forms various surface phases on Si(111) [360,361] with intriguing properties. As an example, 2D superconductivity was found [362]. Pb structures with coverages close to the physical monolayer (ML) grown on vicinal silicon substrates attracted much interest during the last decades as they host peculiar spin properties. For instance, Pb/Si(553) was reported to arrange in a well-ordered nanowire array, which electronically has a purely 1D character with metallic surface states showing a giant Rashba-type spin-orbit splitting [363–365]. Similar effects were observed for the partially embedded zigzag Pb chains on Si(113), which exhibit substantially spin-orbit-split one-dimensional electron bands [366]. This enhanced spin-orbit coupling is due to the strong 2D anisotropy and not present in

isotropic 2D phases [367].

The Pb/Si(557) system presented here exhibits a peculiar inherent instability. Growth of Pb structures leads to a local refaceting of the surface. Depending on the exact Pb coverage in the range of 1.2 and 1.6 ML, various facets are formed, e.g. (112), (335), or (223) [279,368]. The deviation from the overall (557) orientation is compensated by wider (111) terraces, or non-periodic step bunches. In the case of the particular Pb coverage of 1.3 ML, the surface undergoes a refaceting to a facet with (223) orientation. The (111) mini-terraces of this phase reveal a width of $4\frac{2}{3} a_{\text{Si}} = 1.55$ nm corresponding to a spot splitting in diffraction of $\Delta k_y = 21.3$ % SBZ (Surface Brillouin Zone) observed with SPALEED [279]. Moreover, the terraces host densely packed Pb atoms revealing a reconstruction close to $(\sqrt{3} \times \sqrt{3})$ with four Pb atoms per unit cell [369]. Despite the existence of several STM images published in literature, see, e.g., refs. [139,368,369], high resolution images revealing details of the atomic positions were obtained only recently [370].

Interestingly, the system reversibly switches between 1D and 2D conductance as a function of temperature [371]. Below a critical temperature, T_c , of ≈ 78 K, a 1D metallic state with high a conductance along the Pb wires is present, while the anisotropic ensemble is insulating in the direction perpendicular to the wires. Above T_c , the system reveals anisotropic 2D conductance [369,372] (see sec. 2.4.4). This one-directional metal-insulator transition is explained by the formation of a spin-orbit density wave (SODW), due to a delicate interplay between spin-orbit coupling (SOC) and electronic correlation of the system [198], as outlined in section 2.4.5.

The formation of Pb wires on Si(557) is a delicate process in two aspects. Usually, 2 ML of Pb was evaporated first at a substrate temperature of 605 K. Thereafter, the substrate temperature was lowered to 575 K and an additional 1.5 ML Pb was deposited. During the first step, the Pb atoms do not stick to the surface at the elevated temperature, but induce the refaceting to a singly stepped surface, which is then stabilized by Pb adsorption on the (111)-mini terraces throughout the second stage of the recipe [279,327]. The resulting total coverage is approximately 1.3 ML. The Pb evaporator was carefully calibrated, e.g., using the α - and β - $\sqrt{3} \times \sqrt{3}$ phases of Pb on Si(111).

2.4.1. Atomic structure of densely-packed Pb nanowires

Due to the miscut of 9.5° off [111] towards the $[112]$ direction, the clean Si(557) reveals, besides the integer spots and the (7×7) reconstruction of the Si(111) surface, further characteristic signatures: the spots are split along the mirror plane of the uniaxial surface. The correlation effects of the steps are seen best for the (1×1) spots, whereas the 7th-order spots of the reconstruction are only streaky indicating a weaker correlation. Although the (7×7) reconstruction is isotropic, the Si(557) surface is not equally stepped, i.e. the (557) surface, with a nominal terrace width of $5\frac{2}{3} a_0$ ($a_0 = 3.32$ Å, row distance), consists of (111) and (112) facets.

The situation changes completely when Pb is adsorbed on Si(557): The spot splitting along the $[112]$ direction increases dramatically, i.e. only four spots appear between (00) and (10). This splitting along the $[112]$ direction of $k_y = 21.3$ % SBZ, indicated by the blue arrows in Fig. 46(a), corresponds to an equally stepped surface with a step distance of $d = \left(\left(4\frac{2}{3}a_0 \right)^2 + (0.314 \text{ nm})^2 \right)^{1/2} = 1.58$ nm, i.e. a (223) facet structure with a miscut angle of 11.5° . The (7×7) reconstruction is not visible any longer. Instead a new superstructure at the $\sqrt{3}$ -spots appears, i.e., these spots are split by ≈ 10 % SBZ along the $[110]$ direction (along the terraces, green circle). This splitting corresponds to a $s = 10$ -fold periodicity along the Pb-chain direction and is nicely seen in STM

(panel b). The mini-terraces of the (223) facets have sufficient width to allow formation of ordered $\sqrt{3}$ -units, indicated by the yellow diamond on Fig. 46(b).

The coverage dependence of the Pb reconstruction and its modulation along the terraces reveal strong similarities with the Devil's staircase phases reported on Pb/Si(111) [373]. These so-called linear (m, n)-phases, a combination of $m\sqrt{7} \times \sqrt{3}$ and $n\sqrt{3} \times \sqrt{3}$ units, appear in our case only as a single domain structure and the 10-fold periodic structure is denoted as a (1,5) phase. As already mentioned, the $\sqrt{3} \times \sqrt{3}$ phase consists here of four Pb atoms (one on the centered H3 and three on off-centered T1 sites), i.e. the coverage of the non-split structure is $\frac{4}{3}$ ML. Accordingly, the $(\sqrt{7} \times \sqrt{3})$ cell contains six Pb atoms (one on H3, five on off-centered T1) per five Si atoms. With these two units, a coverage of 1.31 ML results for the (1,5) phase, strictly yielding a 10-fold periodicity along the terraces. Based on a contrast enhanced STM image of a (223) terrace, a slightly optimized atomistic model is proposed and shown in Fig. 46(c). Compared to the (5,1)-phase revealing strictly a 10-fold periodicity, the new model is rather based if a compressed $\sqrt{3} \times \sqrt{3}$ unit cells giving rise to a 11-fold periodicity. However, as shown by our former LEED experiments [279], the splitting is not exactly 10 % SBZ and sensitively depends on minutes amounts of excess coverage. To remain consistent with previous work, we therefore

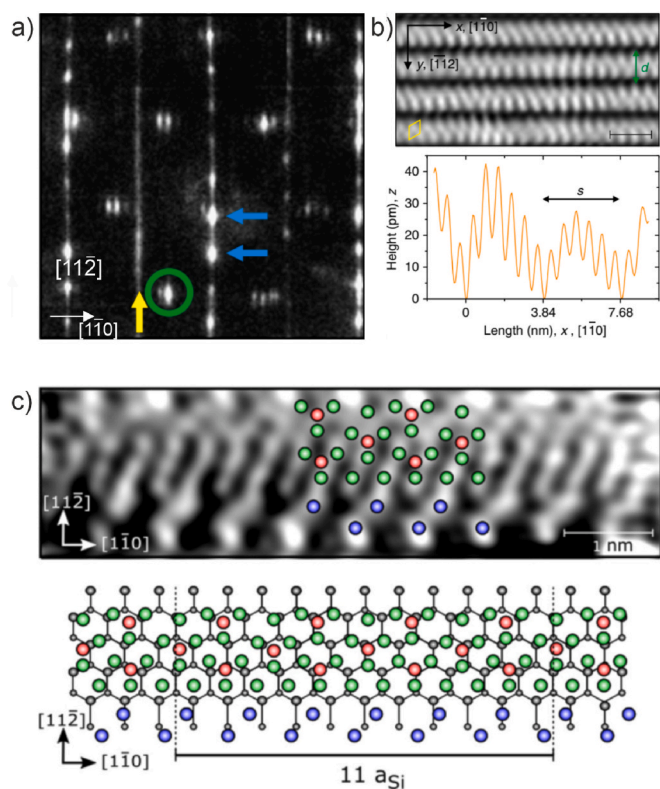


Fig. 46. a) SPALEED pattern (99 eV) with 1.31 ML Pb on Si(557) forming a (223) facet structure (blue arrows). b) STM (+1 V, 80 K) revealing the interwire spacing of $d = 1.58$ nm of a (223) facet structure (scale bar, 2 nm). The period of $5.8 \text{ \AA} = \sqrt{3} \times a_{\text{Si}}$ correlates with formation of a $\text{Pb-}\sqrt{3} \times \sqrt{3}\text{R}30^\circ$ reconstruction (size of unit cell indicated by yellow trapeze). The superimposed modulation s results in spot splitting in a) (green circle) of around 10 % SBZ [139]. c) Contrast enhanced LT-STM image (+0.5 V, 0.3 nA, 10 K) of a Pb nanowire and top view of a new atomistic model of this dense $\text{Pb-}\sqrt{3}$ phase. It consists of tetramers marked by red and three adjacent green circles. Blue circles denote Pb atoms arranged in two rows along the step edge. The Si lattice is shown by gray-colored circles [370]. (For interpretation of the references to color in this figure legend, the reader is referred to the Web version of this article.)

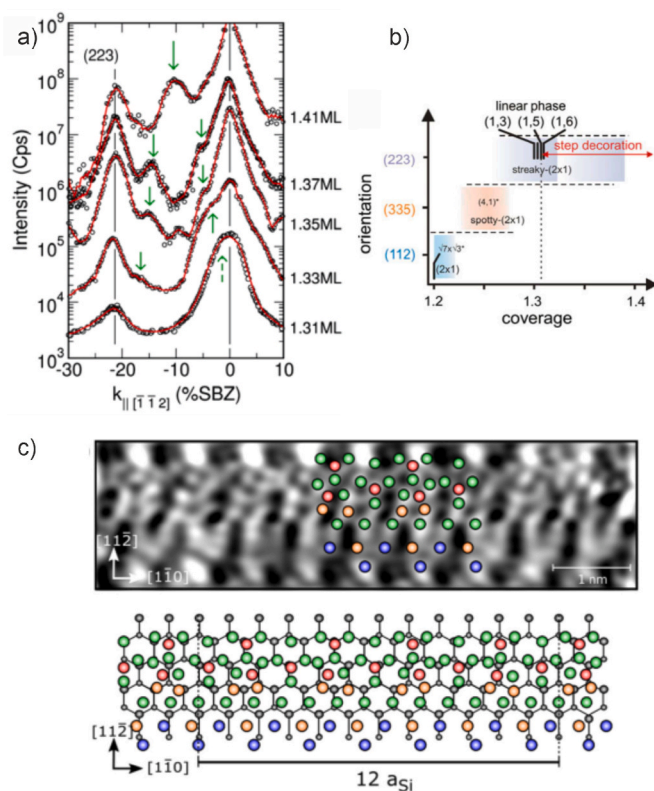


Fig. 47. a) Line scans taken along the $[112]$ direction for Pb coverages between 1.31 and 1.41 ML. The curves are shifted for better visibility. b) Phase diagram of Pb/Si(557) for various Pb coverages. The (223) phase is stable within 0.1 ML of excess coverage [374]. c) STM image of Pb nanowire with a local excess coverage of 0.2 ML Pb (orange circles), leading to a tilting of some of the tetramers [370]. (For interpretation of the references to color in this figure legend, the reader is referred to the Web version of this article.)

refer to the modulation as a quasi-10-fold periodic structure in the following. For this structural model, the underlying silicon lattice was calibrated by means of a nearby larger (111) terrace hosting the SIC phase. The Pb atoms on top are arranged as tetramers that form a compressed $(\sqrt{3} \times \sqrt{3})$ reconstruction to fit the observed pattern. Although the central atom of the tetramers remains hidden as in the case of Pb/Si(111) [367], it is a suitable approach as the $(\sqrt{3} \times \sqrt{3})$ diffraction spot is split due to varying modulation lengths [279]. At the 1.31 ML coverages, the step edges were assumed to be still uncovered by Pb so that the dimerized Si bonds remain present at step edges giving rise to the half-order diffraction lines in Fig. 46(a) (yellow arrow) [279]. Indeed, a periodicity of roughly $2a_{\text{Si}}$ is observed by STM at the step edges, but it seems to be modulated in the same fashion as the $\sqrt{3}$ reconstruction. Therefore, the dimerization feature in diffraction is rather due to two rows of Pb atoms with reduced density compared with the terrace (see Fig. 46(c)). In any case, the Pb-induced formation for extended (223) facet areas with a higher step density compared to the initial (557) surface orientation already points towards an electronic stabilization of this phase (see also section 2.4.4).

This stabilization of the structure is supported by decoration experiments with excess Pb coverage giving rise to atomic chain ordering with ultra-long periods [374]. Instead of a random step decoration, periodicities up to six (223)-terrace widths (28 atomic Si rows, 93 Å) were found. Diffraction profiles taken along the $[112]$ direction show for Pb excess coverage besides the (223) spots additional satellite spots, which are characteristic for the additional chain ordering (cf. green arrows in Fig. 47). These depend inversely on excess Pb concentration and end at a

concentration of 1.52 ML when all terraces are decorated with a line density equal to the Si density at steps. Within 0.1 ML excess coverage the Pb-induced (223) facet structure is stable, as shown by the diagram in Fig. 47(b). Based on the contrast-enhanced STM image, shown in panel c), we suggest a model how the excess Pb is incorporated. Due to the excess coverage, also the modulation length along the wires become larger, in agreement with high resolution SPALEED investigations [279].

2.4.2. Interaction of electrons with phonons in Pb films and with steps of the Si substrate

Interactions of electrons with deviations of the crystal periodicity results in e-ph coupling and scattering of electrons at superstructures or defects. Both aspects were investigated experimentally here in low dimensional Pb structures grown on single crystal Si surfaces. The e-ph coupling was analyzed for epitaxial monolayer films on Si(111) by a photoelectron emission spectroscopy linewidth analysis as a function of temperature [375]. The electronic scattering with quasi-one dimensional superstructures became accessible at vicinal Si(557) surfaces on which Pb nanowire arrays were prepared as described above, see Figs. 48–52, in femtosecond time-resolved two-photon PES [376].

Fig. 48 shows in the top panel the laser PE spectrum obtained with photon energies of 6 eV. The main spectral feature observed is the electronic quantum well state which originates from confinement of the Pb $6p_z$ electrons to the 2D film at a thickness of 5 ML [377,378]. From the comparison of the two spectra shown for temperatures of 31 K and 120 K one can conclude on thermally induced broadening due to e-ph

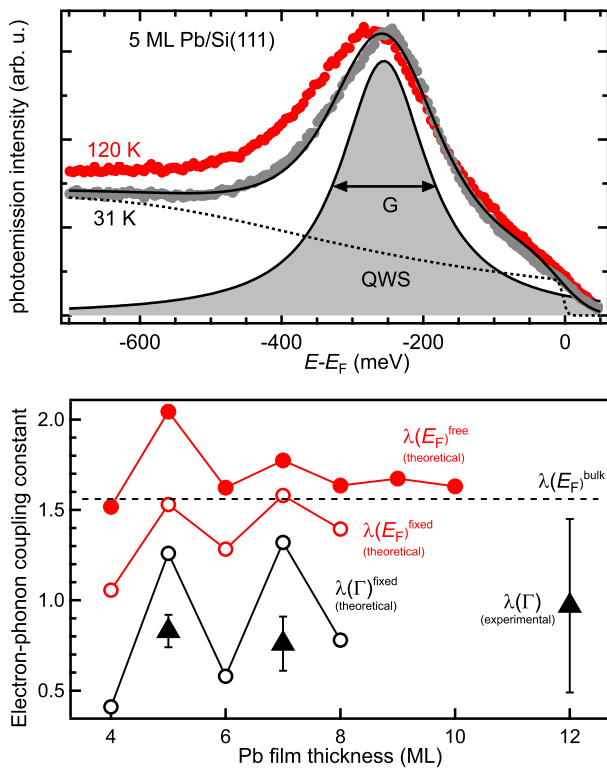


Fig. 48. Top: Laser-excited PE spectrum in normal emission geometry for a 5 ML thick lead film on Si(111) for two different temperatures as indicated. The filled area represents the highest occupied quantum well state contribution to the spectrum with the linewidth G of a Lorentzian line, the dashed line represents the considered background including the Fermi–Dirac distribution function. The solid line is a fit to the measured spectrum which consists of a sum of the background and the Lorentzian line. Bottom: Electron–phonon coupling parameter $\lambda(E_F)$ averaged over electron momentum at the Fermi energy as a function of Pb film thickness. All theoretical data were obtained with spin–orbit interaction included.

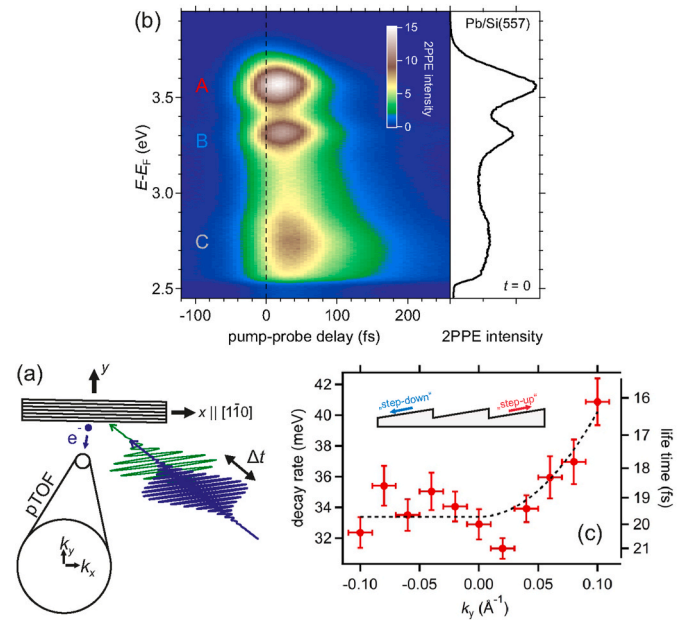


Fig. 49. (a) Sketch of the experimental geometry. Pump and probe femtosecond laser pulses used for the 2PPE process were p-polarized parallel to the step edges of Si(557). PE spectra were recorded by a position-sensitive time-of-flight spectrometer [380] that records PE events along k_x and k_y simultaneously. (b) Momentum-averaged 2PPE intensity as a function of pump-probe delay t in a false-color representation. Positive delay times refer to the situation in which the intermediate states are populated by the UV pulse ($h\nu_1 = 3.8$ eV) and probed by the VIS pulse ($h\nu_2 = 1.9$ eV). The right panel shows the momentum averaged 2PPE spectrum recorded at $\Delta t = 0$. (c) Population decay rates for state A, see panel (b), as a function of step-perpendicular in-plane momentum k_y . Error bars along the momentum axis indicate the integration windows used for data analysis. The dashed line is a guide to the eye. The inset sketches “step-down” and “step-up” processes with respect to the macroscopic sample surface. (For interpretation of the references to color in this figure legend, the reader is referred to the Web version of this article.)

coupling. As discussed in Ref. [379] the analysis of the temperature dependent linewidth provides direct access to the e-ph induced mass enhancement and the e-ph coupling constant λ . Our temperature dependent linewidth analysis showed a linear increase in linewidth with temperature above 60 K up to 175 K. At higher temperature the wetting Pb films become unstable. Fig. 48 reports the obtained values for λ in the bottom panel for 5, 7, and 12 ML thick films. These experimental findings are compared to calculations of λ by DFT including spin orbit interaction. The red data points refer to two sets of results for momentum averaged values of λ for the case of free standing films and an atomic structure fixed according to the structure of the substrate. Both clearly overestimate the experimentally found value. We obtain better agreement with the experimental result for the calculation of momentum selective λ . The open black circles assume the fixed structure and contributions from the Γ region in the Brillouin zone probed in experiment. The respective reduction in λ is a consequence of the restriction to the $6p_z$ bands. The $6p_{xy}$ bands will also contribute to e-ph coupling but are not tested in the present experiment since they are further out in the Brillouin zone in regions that do not contribute to the spectral line analyzed here. The remaining discrepancy between experimental and theoretical coupling constant is attributed to structural effects of the Si substrate that were not included in the fixed structure assumed for free standing films here [378]. We expect that a future calculation for larger unit cells which include the Si substrate explicitly will improve the agreement.

We now turn to the experiments discussing the interaction with the steps in the Pb/Si(557) nanowire arrays. Time-resolved two-photon photoelectron emission spectroscopy is carried out as described in Refs.

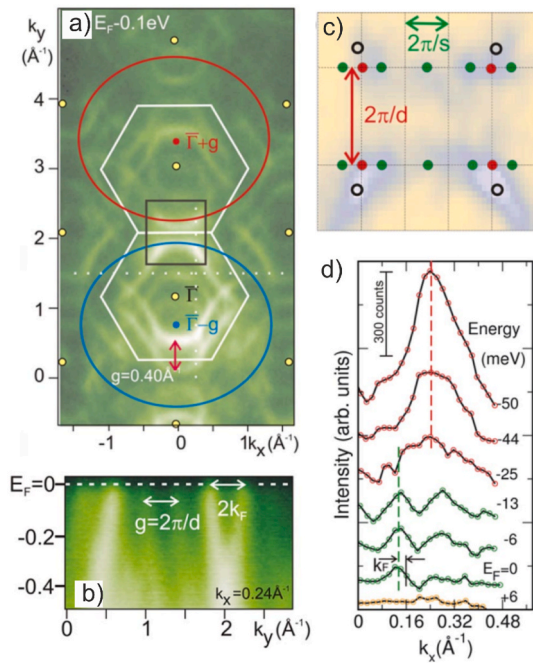


Fig. 50. a) Constant energy map (CEM) taken at $E_F - 0.1$ eV of 1.3 ML Pb on Si (557). The intensity distribution is well described by a set of ellipses centered at the Γ points of the (111) terraces and at centers shifted by the reciprocal lattice vector $g = 2\pi/d$, where d is the interchain distance. The area marked by the black square is shown in c). b) Energy dispersion along the $[112]$ (y) direction showing the nesting at E_F . c) Schematic drawing of the nesting points overlaid on the CEM taken at $E_F - 30$ meV. d) Sequence of momentum distribution curves (MDCs) along k_x ($[110]$ -direction) and $k_y = 2.25$ $1/\text{\AA}$ at various energies around E_F . The ARPES experiments were performed at $T = 40$ K and a photon energy of $h\nu = 160$ eV [327].

[381,382]. As illustrated by Fig. 49(a) a unique time-of-flight spectrometer with a position sensitive anode was used [380], which facilitated parallel detection of momentum dependent and time-resolved two-photon PE spectra perpendicular and along the steps of Si(557). Fig. 49(b) shows typical experimental results as a function of time- and

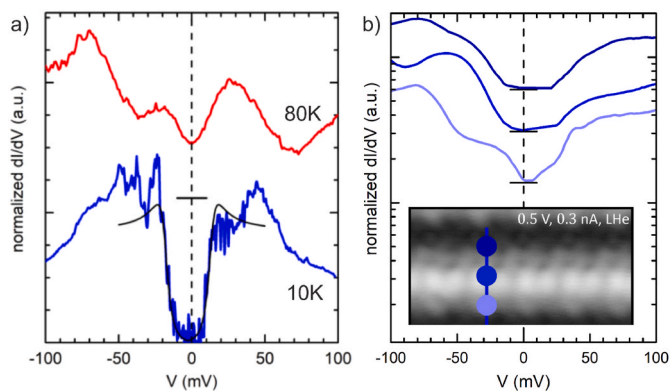


Fig. 51. a) STM dI/dV spectra for 1.3 ML Pb on Si(557) taken below (blue) and above (red) T_c . The spectra are shifted vertically for clarity, the horizontal black lines mark the origin for each curve. The low temperature spectrum is fitted by the Dynes function, shown in black. b) Spatially resolved (averaged) spectra across the ribbons. The gap size is gradually reduced towards the outward edge of the Pb nanoribbon. The inset shows the Pb nanowire like in Fig. 46(c) [370]. (For interpretation of the references to color in this figure legend, the reader is referred to the Web version of this article.)

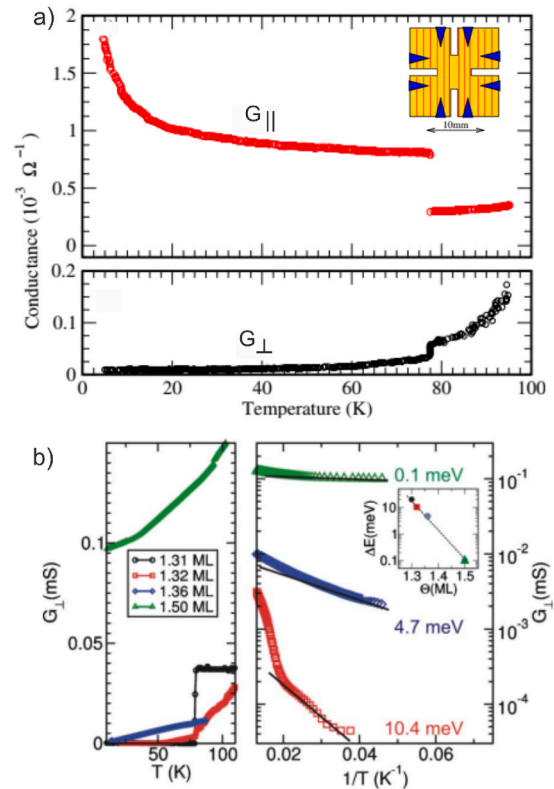


Fig. 52. a) Conductance for 1.31 ML Pb on Si(557) as a function of temperature and the crystallographic direction. G_{\parallel} and G_{\perp} refer to the conductance measured along the $[110]$ and $[112]$ directions, respectively. The inset shows a modified van der Pauw geometry, which allows for symmetrization of the current with respect to the step structure [371]. b) Temperature dependence of conductance G_{\perp} across the wires for various Pb coverages between 1.3 and 1.5 ML on almost perfect (223) facet structures on a linear scale (left) and as semilog plot versus $1/T$ (right). The inset shows the effective activation energies ΔE for electronic transport derived from these data and that obtained from ARPES (black circle, shown in Fig. 50) [329].

energy in case of momentum averaging. Above the Fermi energy three spectral features A, B, C are identified. Features A and B are well defined, unoccupied interface states that are assigned to electronic bands of the interface calculated by density functional theory [376]. Feature C is a spectrally broad continuum that most likely involves momentum dependent scattering at lower energy. The momentum averaged analysis of the time-dependent spectra shown in Fig. 49(b) resulted in combination with a rate model description in a determination of lifetimes $\tau_A = 24(3)$ fs, $\tau_B = 35(3)$ fs, and $\tau_C = 65(3)$ fs. The momentum dependent analysis revealed two interesting results, see Syed et al. [376] for details. (i) Intraband scattering in the band of state A: Here a high energy electron at large k scatters via interaction with an electron below the Fermi energy to smaller k within the band. In a direction perpendicular to the step edges along k_y we identified the symmetry break induced by the presence of the steps in these intraband scattering rates. The experimental results are shown in Fig. 49(c) as lifetimes (right axis) or decay rates (left axis) for positive and negative k_y , i.e. step-up and step-down, respectively. We observe that the decay rate is about 20 % larger (and the lifetime correspondingly shorter) for the step up direction than for the step down direction. This observation provides microscopic information on the scattering potential at the steps. In comparison with related work on the step induced scattering in image potential states on vicinal Cu(001) surfaces [383] the observed changes in the scattering rates up and down the steps are much larger in the case of the stepped metal-semiconductor interfaces studied here. This

highlights the stronger and more localized dipolar scattering potential at these interfaces. This finding is very plausible, since the chemical bonding of Pb–Si at the interface involves local bonds and charge transfer contrary to a metal-vacuum surface where Bloch electron density variations determine the step dipole responsible for scattering at the steps.

2.4.3. Fermi nesting in a quasi 2D system

The overall 2D character is supported by ARPES measurements and obvious from the constant energy map (CEM), shown in Fig. 50(a) [327]. The intensity distribution in k-space 0.1 eV below E_F can be reconstructed by ellipses around the Γ points of the (111) terraces and, in addition, by shifted replicas along the $\begin{bmatrix} 1 & 1 & 2 \end{bmatrix}$ direction. The ellipses resemble those of a free electron gas system that is modified by the anisotropy of the system in its metallic state, and by the periodic step structure. Metallicity is also seen by plasmon spectroscopy (see sec. 2.5.7) and surface transport (see sec. 2.2.4).

This simple picture, however, does not contain the full truth for two reasons. First, the periodic step array results in a shift vector of the ellipses, g , which corresponds exactly to the reciprocal lattice vector $g = \frac{2\pi}{d} = 0.40 \pm 0.01 \text{ \AA}^{-1}$, where $d = 1.58 \text{ nm}$ is the interchain distance. Such repeated structures also have been found for a variety of vicinal metallic surfaces [384,385]. From the energy distribution curve shown in panel b) the interrelation between the (223) facet and the filling factor of the Pb-induced electronic states becomes obvious: Complete filling of the topmost band is demonstrated by the coincidence of the reciprocal lattice vector g with $2k_F$ at E_F and gives rise to Fermi nesting.

Second, when going close to the Fermi level, deviations from the elliptical form towards more straight sections become visible, which are in fact necessary in order to get efficient Fermi nesting. This renormalization of the Fermi surface due to nesting is illustrated in Fig. 50(c), which shows the section of Fig. 50(a) marked by a square. In this part of the phase space Umklapp scattering by $+g$ and $-g$ becomes most pronounced. In order to facilitate interpretation, a SBZ grid based on the interchain distance d and the modulation s along the wires is superimposed. In the central part of this figure, the two nearly straight sections are separated by exactly the reciprocal lattice vector g , and the ARPES intensity is fully concentrated at the zone boundary in the k_y direction, i.e., the Fermi surface is nested. In terms of transport, this causes an insulating behavior in this direction, as we will show below. In k_x -direction, this intensity can be grouped into two contributions, marked by red and green dots. While the intensity at the red dots appears at the zone boundary in both directions, the intensity marked green corresponds to intensity modulations with a period of $f = 2\pi/s = 0.16 \text{ \AA}^{-1}$, and is located close to the zone centers. This quasi-tenfold periodicity along the chains marks the crossing of a (repeated) doublet of split bands with the Fermi level at these points, as seen in Fig. 50(b)). As obvious from the MDCs shown in Fig. 50(d), only the bands marked by the green dots in Fig. 50(c) have a finite intensity at E_F , i.e., only these bands cross the Fermi level and are the only ones that can contribute to electron transport in the $\begin{bmatrix} 1 & 1 & 0 \end{bmatrix}$ direction. From this analysis we can also estimate a 1D band gap of approximately 20 meV, in agreement with transport and STS measurements (see below) [370,371]. This electronic gap protects the (223) facet structure and makes it immune to some extent against Pb excess coverage, as discussed in context of Fig. 47(a)). The intensity close to the open circles marked in panel c), on the other hand, is the result of an intersection of three ellipses, i.e., it is not affected by structural details of Pb ordering. Therefore, it is not of relevance here.

The importance of electronic correlation in this system is corroborated by recent STM measurements [370]. As shown in Fig. 51(a), below T_c the density of states at E_F vanishes coming along with the opening of a gap. This change of DOS comes along with a metal-insulator transition,

which we discuss in detail in sec. 2.4.4. At low temperatures, we see the formation of a BCS-like gap structure. This phase was analyzed in detail using the Dynes function [386,387], including the gap energy 2Δ as well as an additional broadening with a linewidth due to inelastic electron-electron scattering. This function is appropriate for modeling STS spectra of electronically correlated materials, e.g., superconductors but also for Mott states, e.g., Sn/Si(111) [388] and or a spin-orbit Mott insulator Sr_2IrO_4 [389]. As the comparison with the ARPES and transport data will show (see below), the Dynes function can also be used to quantify the spin orbit density wave in our case. For the Pb nanowire without excess coverage on the (223) facet we obtain $2\Delta = 31.8 \pm 0.5 \text{ mV}$, which is in the same order as the gap size of around 20 meV deduced from the ARPES measurements shown in Fig. 50(d) [327]. Using the transition temperature of $T_c = 78 \text{ K}$, measured with DC surface transport and SPALEED [371,390], the ratio $2\Delta/k_B T_c$ is ≈ 4.7 , which is very close to the BCS ratios of 4.4 and 4.3 obtained for superconducting Pb monolayer films on Si(111) and Pb bulk, respectively [362]. As obvious from Fig. 51(b), the electron gap is completely formed in the center of the ribbons and is reduced at its edge. We will address this edge feature, when we discuss the magnetotransport experiments in sec. 2.4.5.

In accordance with the ARPES and transport finding, our STS signal is compatible with the signatures of a not fundamental band gap. The local spectroscopy probes the conductance across the surface and samples the electronic states within a certain momentum range mainly around the Γ point. In agreement with ARPES measurements, the spectral weight in this region of the phase space at E_F is very low. Apparently, the most intense features found at $(k_x, k_y) \approx (0.14 \text{ \AA}^{-1}, 2.25 \text{ \AA}^{-1})$ (cf. Fig. 50) are not effectively contributing to the tunneling process.

In addition, STS experiments on Pb-nanowires with an excess coverage were also performed (not shown) [370]. Compared to the case shown above, the electronic gap on the wire excess coverage is still visible, but vanishes completely when approaching the step edge, where additional Pb is present. Here, the local density of states exhibits an additional state close to E_F , which does not exist in nanowires without extra Pb coverage. At the step edge of the lower terrace, this state gets even more pronounced with its tail crossing E_F . It rather resembles the asymmetric line shape of a Fano resonance [370,391]. Apparently, there is increased scattering in the presence of excess Pb coverage. The electrons along the delocalized channel scatter resonantly with the localized states induced by the excess Pb, which marks the crossover to a 2D behavior, as, e.g., seen in DC transport and plasmon spectroscopy (cf. sec. 2.5.7) [263,372].

2.4.4. Quasi-Peierls transition into 1D

The Pb/Si(557) system was also investigated by surface transport [371]. For this purpose, an extended four-contact geometry with eight pre-deposited macroscopic TiSi_2 contacts, approximately 50 nm thick, was used. They are separated pairwise by slits machined into the samples, as shown in the inset of Fig. 52(a)). By switching between equivalent sets of contacts, the conductance was measured sequentially parallel and perpendicular to the steps. The separation between equivalent contacts was approximately 10 nm. In all measurements contributions of the clean Si substrate were subtracted.

The DC conductance measured parallel and perpendicular to the steps at 1.31 ML is shown in Fig. 52(a). This curve is reversible and dominated by an abrupt change at a temperature of 78 K separating a high temperature region with small conductance anisotropy from the low-T region, where 1D metallic transport along the wire direction is seen. This 1D metal-insulator transition is in line with the change of the density of states at E_F probed by STS and discussed in context of Fig. 51(a). In view of the nesting conditions discussed in the previous section (sec. 2.4.3), this 1D transport is a result of the gap opening along the $\begin{bmatrix} 1 & 1 & 2 \end{bmatrix}$ direction, i.e. of Fermi nesting, as seen in Fig. 50(b). Moreover,

due to the modulation along the wires, band backfolding results in states crossing E_F close to the Γ points. Thus the mesoscopic Fermi wavelength makes the propagating electrons rather robust against scattering at atomic defects, so that metallic behavior is found along the wires even in a macroscopic experiment.

Before we explain the 1D/2D transition, we want to point out that this transition depends strongly on the initial coverage, and on details of the preparation method. Both the exact concentration of a physical Pb monolayer and the transition into a long-range ordered (223)-facet structure are required in order to see the transition in transport [230, 329,371]. Moreover, we performed also transport measurements with Pb concentrations in excess of 1.31 ML. The effect of the formation of periodic chain ordering, i.e. terrace modification due to the excess coverage, can be monitored also by surface transport, as shown in Fig. 52(b). Starting from 1.31 ML of Pb with the small gap of around 20 meV [327], the 1.32 ML curve still shows the abrupt transition, which apparently has disappeared for 0.06 ML Pb excess coverage. At the same time, the original insulating state below 78 K becomes gradually more conducting as the coverage is increased with a clear signature of activated transport. The quantitative evaluation of the temperature dependence of conductance (right part of this figure and inset) indeed reveals a continuously decreasing effective activation barrier for electronic transport, which results in purely metallic behavior at a Pb concentration of 1.50 ML. Thus, interpreting these activation energies ΔE as the gradual decrease in the band gap, these findings from transport nicely fit into the nesting model presented above. Once 1.5 ML is deposited, all steps are completely decorated, and fully metallicity is reached, as expected [279].

The 1D/2D transition seen in transport is induced by a refacetting transition. Adsorption of 1.3 ML Pb on Si(557) results in the formation of a long-range ordered (223) facet structure, as impressively shown by the $(k_{\parallel}, k_{\perp})$ -plot for electron energies ranging between 80 and 230 eV in Fig. 53(a). We have analyzed the rods as a function of temperature around the (1 0)-spot. Fig. 53(b) shows exemplarily two line scans along the $[112]$ direction in reciprocal space for temperatures below (75 K) and above (80 K) T_c . Below T_c , the part of the profiles shown there is well described by three diffraction peaks (blue curves, denoted by 1 and 2 and (1 0) spot). The electron energy of 96 eV is close to an out-of-phase scattering condition for the first-order spot with respect to a step height of 3.14 Å between (111) terraces, as can be seen by the almost symmetric relative positions of the step train peaks with respect to the (1 0) peak. This small (1 0) peak, serving as calibration point here, exists due to small inhomogeneities on the surface or due to pinned steps yielding

larger and uncorrelated (111) terraces (less than 10 %). Above T_c , the diffraction peaks of the step train shift, but are also split and/or broadened (cf. Fig. 53(b)). Peak 2 shifts closer to the Bragg peak so that splitting into two peaks can be observed. The splitting is around 3 % SBZ. On the other hand, a splitting of peak 1 cannot be resolved due to broadening. The detailed analysis revealed a transition from the (223) facets to an average (17,17,25) orientation [390]. These shifts, splitting (Δk_y), and broadenings (FWHM) are reversible and the results as a function of temperature are shown in panel c). The discontinuity at T_c is evident.

The critical temperature of this so-called refacetting transition fits very nicely to the T_c measured in transport (cf. Fig. 52(a)). No local expansions of lattice constant are involved in this phase transition and all atoms remain on their crystalline sites. It is thus a order-order phase transition, in which only the average inclination of the facets on the surface changes at T_c . Apparently, at this temperature the excitation of electrons across the 20 meV gap is obviously coupled with the destabilization of the (223) facet in favor of the (17,17,25) facet with a lower step density. This small change in periodicity leads to a breakdown of the Fermi nesting ($2k_F = g$) condition along the $[112]$ direction and a transition from 1D to 2D conductance. It directly demonstrates the strong coupling between electronic and vibrational degrees of freedom and fits into the (generalized) model of a Peierls transition.

2.4.5. Correlation of spin and charge: formation of a spin-orbit density wave

In order to address the role of electron spin in this system, magnetotransport measurements were performed. The superconducting split coil magnet used here reaches magnetic fields of ± 4 T, which were directed perpendicular to the sample surface. The samples were mounted on a cryostat at allowed temperatures between 9 and 300 K at the sample. Further details, also about the evaluation of the transport data, can be found in Refs. [393,394].

Magnetotransport for Pb multi- and monolayer structures on Si(111) reveal a decrease of the conductance with increasing magnetic field, a hallmark for weak antilocalization (WAL). The elastic and spin-orbit scattering times, τ_0 and τ_{SO} , respectively, are in the range between 10^{-13} - 10^{-15} s [395,396]. The peculiar DC-transport behavior below 80 K of the perfectly ordered Pb-chain structure after deposition of 1.3 ML was already discussed in context of Fig. 52(a). A special signature at this Pb concentration is also seen in magnetotransport measurements and shown in Fig. 54(a). While in the perpendicular direction WAL is seen, as for all other Pb concentrations between 1.2 and 1.5 ML the magnetoconductance for the parallel direction is reversed to weak localization (WL). This anomaly disappears for coverages at and above 1.5 ML, where all mini-(111) terraces of the (223) facet have incorporated the

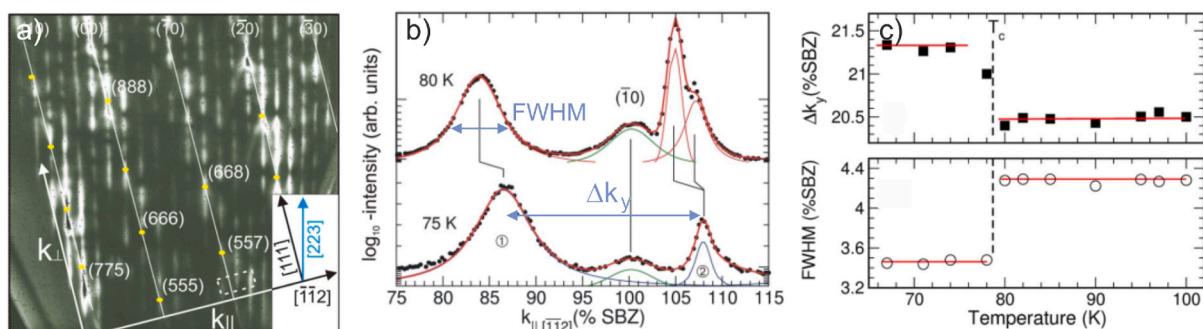


Fig. 53. a) $(k_{\parallel}, k_{\perp})$ -plot along the $[112]$ direction showing the regular step train of a (223) facet after adsorption of 1.3 ML Pb on Si(557) for electron energies between 80 and 230 eV. The measurements are taken at $T = 40$ K. The dashed square around $S = 5$ marks the range in k -space for the line scans shown in panel b).

There, two exemplary line scans at fixed k_{\perp} close to the (1 0) spot below and above T_c are shown. c) Variation of the spot splitting Δk_y and the FWHM, as defined in b), as a function of temperature. In both cases, the discontinuity at T_c is clearly visible [390].

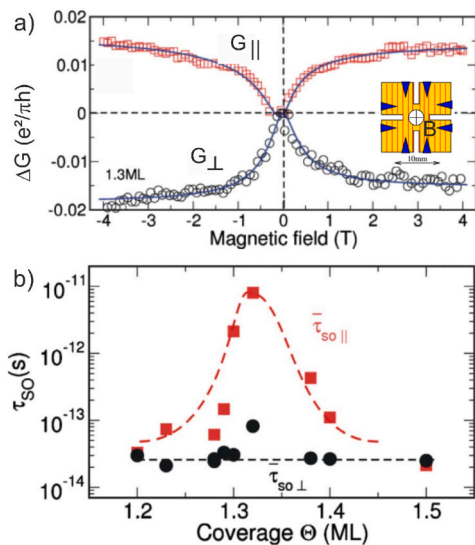


Fig. 54. a) Magnetoconductance ΔG of 1.3 ML Pb on Si(557) measured at 50 K along (squares) and perpendicular (circles) to the step direction. The magnetotransport measured along the steps switches from positive to a negative MR. The solid lines represent results from a Hikami analysis. b) Spin-orbit scattering time τ_{SO} derived from the Hikami analysis of magnetoconductance curves for different Pb coverages [392]. In contrast, the elastic scattering times τ_0 (not shown) reveal no dependence on Pb concentration. The dashed lines are guides to the eye.

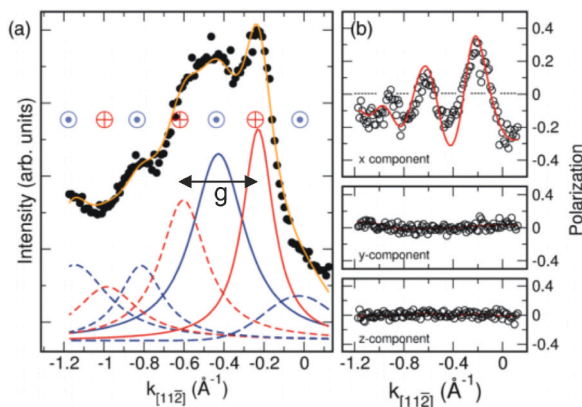


Fig. 55. a) Momentum distribution curve measured at $E_F - 100$ meV with the Mott detectors for 1.3 ML Pb on Si(557) across the Pb wires ($[112]$ direction) [138]. The reciprocal lattice vector g , shown in Fig. 50, is plotted for one spin-component. (b) Spin polarizations measured with the Mott detectors for each spatial component. The pronounced polarization along the $[112]$ direction for the x component is indicated by \otimes and \odot in panel a).

maximum amount of excess coverage (see model in Fig. 47(c)), and WAL was found for both directions.

From the Hikami analysis we derive a spin-orbit scattering time, which around the Pb concentration of 1.3 ML is larger by 3 orders of magnitude than outside this coverage range. The results of τ_{SO} for both directions are shown in Fig. 54(b)). Contrary to the behavior of τ_0 , spin-orbit scattering seems to be sensitive predominantly in the direction along the wires. The elastic scattering times are independent of Pb coverage and the ratio $\tau_{0,||}/\tau_{0,\perp} = 4$ is in good agreement with the anisotropy in conductance above T_c , i.e., the elastic scattering rates are essentially controlled by the steps.

As a first rational of these findings in magnetoconductance, we recall that for the 1D quasi-Peierls transition at 78 K the split-off states are

mainly responsible for the transport along the wires. Moreover, if these bands are spin polarized, it is obvious that scattering of electrons close to the Fermi level from $+k$ to $-k$ requires spin Umklapp. This results in an effective suppression of spin-orbit scattering under these conditions. Spatially resolved STS experiments revealed, that the gap vanishes when the spectra are taken close to the step edge of the Pb nanoribbon (cf. Fig. 51(b)). However, whether the transport channels are related to topologically protected edge states, e.g. like in epitaxial sidewall zigzag graphene nanoribbons [397], remains unclear at moment and demands further investigations.

In order to capture the spin degree of freedom spectroscopically, spin- and angle resolved PE experiments were performed [138]. As a consequence of the broken inversion symmetry, SOC leads inevitably to spin-polarized states in these low-dimensional systems at surfaces [398]. The experiments were performed with p-polarized light (mostly $h\nu = 24$ eV) at 60 K at the Swiss Light Source.

In contrast to the measurements with spin integration at $h\nu = 160$ eV (shown in Fig. 50), the MDCs shown in Fig. 55 a) along the $[112]$ direction, measured with a lower photon energy and with a Mott detector, reveal a characteristic substructure that is shifted by around 0.2 \AA^{-1} with respect to the dominant replica structure. Nearly perfect modeling of the intensity distribution is possible by pseudo-Voigt peaks separated by half the reciprocal lattice vector g . The corresponding spin asymmetries measured with the Mott detectors and weighted with the system-specific Sherman function are shown in Fig. 55(b) for (P_x , P_y , P_z). Thereby, a spin polarization of around 40 % was measured for the component perpendicular to the direction of the momentum, i.e., along the $[110]$ direction for P_x , while the y and z components do not show a clear polarization signal. The (Rashba) splitting $\Delta k_0 = 0.2 \text{ \AA}^{-1}$ found along the $[112]$ direction is extremely large and, interestingly, half the size of the reciprocal lattice vector g ; i.e., it takes its maximum possible value. For comparison, the Rashba-splitting measured for the isotropic 2D phase is $\Delta k_0 = 0.04 \text{ \AA}^{-1}$ [367].

It was shown that inherent spin splitting such as Rashba-type SOC yields Fermi surfaces (FS) with nesting between opposite helical states causing a so-called spin-orbit density wave (SODW) state, which cannot be characterized by independent local order parameters. This new emergent phase of matter arises without breaking time-reversal symmetry above a critical value for the Coulomb potential U . Its order parameter, i.e. the energy gap Δ , is determined by the energy scales of both the SOC strength l and the interaction U [198]. In essence, the finite gap Δ protects the SODW from spin dephasing against external perturbations like magnetic fields, thermal excitation and doping by excess coverage. In case that the interaction energy is large compared to SOC, however, the SODW can be overturned at the expense of a spin density wave. Experimentally, a SODW can be identified by the difference between charge and spin order, the nesting of spin-polarized states and the concomitant opening of a gap, and the depolarization of the spin order as a function of Coulomb screening due to the dephasing of spin states.

Whether this concept holds can be tested by looking at excitations of the ground state represented by the spin order at the critical Pb concentration of 1.31 ML. Regardless of the protection of the SODW phase, the spin polarization of the surface bands should be affected by the excess coverage since the spin dephasing time is proportional to the size of the electronic gap [198]. Fig. 56(a) shows the S_x -polarization curves obtained along the $[112]$ direction, revealing a pronounced spin polarization along the wires. Up to an excess coverage of 0.1 ML the polarization curves reveal a harmonic but damped oscillatory behavior. The period of 0.2 \AA^{-1} as well as the almost symmetric amplitudes, are giving rise to a vanishing net polarization within the Brillouin zone, indicating the presence of time-reversal symmetry. This observation excludes the possibility of a spin density wave and further favors the

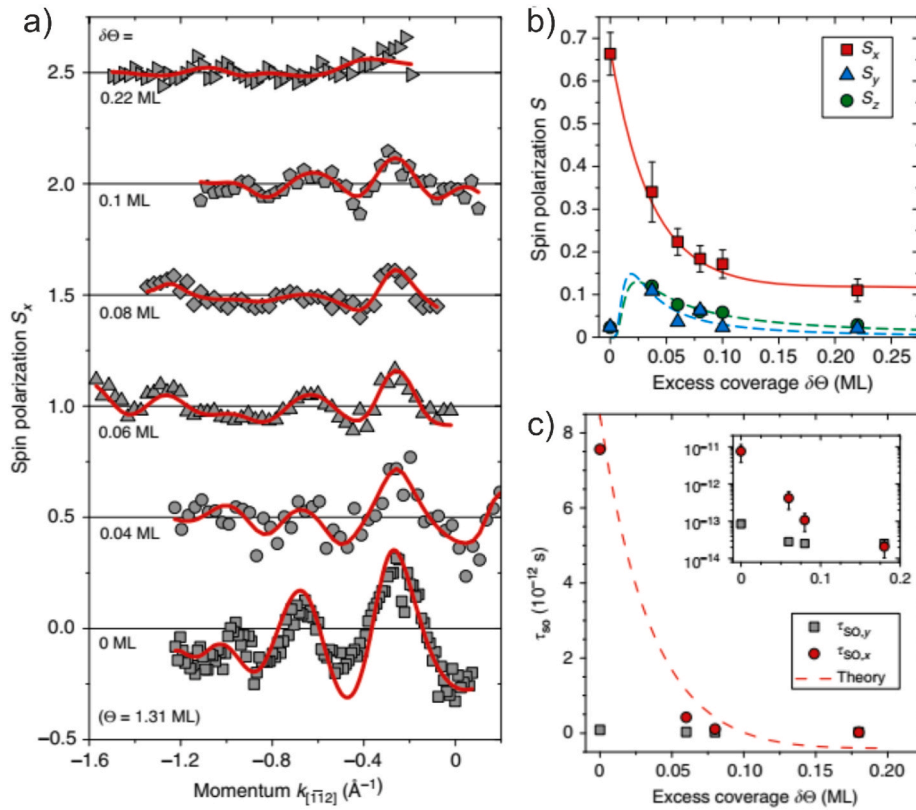


Fig. 56. a) Spin polarization along the wires measured along the $[11\bar{2}]$ direction for different amounts of excess coverage. The spectra are shifted for better visibility. b) Peak-to-peak maximum values of all three polarization vectors as a function of excess coverage. The (solid) line is deduced from theory. The dashed lines are guide to the eyes. The error bars are deduced from least mean square fits to the spin-polarized ARPES data. c) Spin-orbit scattering times as a function of excess coverage deduced from magnetotransport measurements (cf. Fig. 54) [392]. The dashed line is a fit according SODW theory for $\tau_{SO,x}$ along the wires. For reference also the scattering time $\tau_{SO,y}$ for direction across the wires is shown. Inset: log scale.

SODW scenario [198].

The spin depolarization can be further quantified. As shown in Fig. 56(b), the S_x component decreases exponentially and can be described by $S_x(\delta\Theta) = 0.56 \cdot \exp(-q\delta\Theta) + const.$, with $q = 27.8$. We want to emphasize that the gradual decrease of the band gap Δ deduced independently from DC-transport measurements (cf. inset of Fig. 52(b)) reveals an almost identical q value. Based on these findings and the fact that within first order the spin lifetime τ_s is given by the spin-orbit scattering time τ_{SO} in a strongly spin-orbit-coupled system, the spin dynamics can be described by a kinetic equation [399]: $\frac{\delta S_k}{\delta t} + S_k \times \Omega_k = \frac{\langle S_k \rangle - S_k}{\eta} + P$ where S_k is the spin polarization vector, P is any external spin source, and η is the scattering time. Ω_k is the effective Larmor frequency defined in our case by $\Omega_k = (\Omega_R k_x / k_F, 0, \Omega_{SODW})$, where $\Omega_R = 2\alpha_R k_F / \hbar$, and $\Omega_{SODW} = 2\Delta / \hbar$ are the frequencies corresponding to Rashba-type SOC and SODW, respectively. In our case, $P = 0$, and the initial condition for the spin is $S_k(0)_x$ (the other components of the spin polarization are negligibly small), so we can solve this equation analytically in the limit of $\Omega_R < \Omega_{SODW}$ at the Fermi momentum, and get $S_x(t) = S_x(0) \cdot \exp(-t/\tau_{so})$, where the spin dephasing time is $\tau_{so} = (1/\Omega_R^2 \eta) \left(1 + \sqrt{1 + \Omega_{SODW}^2 \eta^2} \right) + const.$ Inserting the exponential dependence of the SODW gap on the excess coverage and keeping all other parameters constant, we get a good fit of the spin dephasing time τ_{so} to the experimental value for a reasonable parameter set of SODW gap $\Delta = 20$ meV, $\eta = 1 \times 10^{-12}$ s and $\Omega_R = 2.6 \times 10^{12}$ Hz which is small compared to Ω_{SODW} up to $\delta\Theta = 0.1$ ML. Using the value of $\alpha_R = 1.9$ eV Å as the Rashba parameter found in our previous study [138], this refers to an extremely

small Fermi-wave vector component along the wires ($k_{F,x} \approx 10^{-4} \text{ \AA}^{-1}$). This in turn explains the insensitivity of the propagating electrons along the wires against atomic sized defects [139,371].

2.4.6. Conclusions

Ensembles of Pb nanowires on vicinal Si substrates are an interesting, albeit complicated, system for studying the interaction of (atomic) structures and electronic properties. The formation of the (223) facet structure on a Si(557) surface highlights this interplay in a striking manner. Due to Fermi nesting below 80K perpendicular to the chains, the system becomes one-dimensional and therefore seems to be immune to the typical instabilities in 1D systems, as introduced in sec. 1.3.1 and found for the In/Si and Au/Si systems (sec. 2.2, 2.3 and chapter 3). The Pb system is further characterized by its high spin-orbit interaction and we showed that the insulating behavior is caused by a new quantum state, a so-called spin orbit density wave (SODW). In contrast to the submonolayer chain systems, such as Au/Si (cf. sec. 2.2), and the silicide wires (cf. sec. 2.6), Pb on Si surfaces forms true on-surface structures. This fact allows to study doping effects, e.g., by additional adsorbates with high precision, to (de)tune the SODW phase in terms of further reconstructions and stability and to monitor the inequality of the edges of the nanowires on the mini-terraces. Further studies to quantify electron correlation effects in these nanowires will be continued in the future. For instance, measurements of the Kondo resonance due to manganese phthalocyanine (MnPc) molecules physisorbed on the Pb chain systems show strong differences compared to experiments done on the 2D Pb phase.

2.5. Collective excitations in quasi-1D systems: wire plasmons⁵

The long-range Coulomb interaction between valence electrons results in collective plasma oscillations [400,401]. Plasmons exist in all dimensions [402]. Plasmons in low-dimensional systems are characterized by a dispersion that starts at zero excitation energy in the long wavelength limit [256,403] and by group velocities that are typically only of the order of 1 % of the speed of light [259,404]. As a consequence, very short wavelengths of only a few nanometers can be reached, much shorter than those obtained for surface plasmon polaritons, e.g. in graphene [405,406]. Excitation and energy transfer into these modes, on the other hand, is only possible in the near field of appropriate antennas, if electromagnetic radiation is the source of excitation [407], or by charged particles like electrons, which scatter by an impact scattering mechanism [408]. Because of their short wavelengths, they are interesting candidates for energy transfer and local energy transport on the nanoscale, since extreme localization compared with standard surface plasmon modes should be possible. Quasi-1D systems add directionality to these properties and are particularly attractive in this context.

Linear dispersion, necessary for undistorted signal transfer, can be achieved in low-D systems by coupling a 2D electron gas with other 2D or 3D electron gases [409], as seen, e.g., for acoustic surface plasmons (ASP) of Shockley type surface states on surfaces of noble metals [410–415], or for graphene on metallic surfaces [416,417]. The dispersion of the 1D electron gas is already close to linear [418] for an unshielded wire, and therefore particularly attractive. Investigations of metallic arrays of quasi-1D wires, exhibiting quasi-linear 1D dispersion, are still scarce. Examples of the recent past are studies of metallic and of silicide chains on flat and stepped Si substrates [259,263,267,402,419] with intrinsic metallicity.

The 1D properties are not only visible by a combined view at geometry and occupied electronic states, they manifest themselves also in electronic excitations, which in the limit of pure 1D behavior with its strong electronic correlations cannot be discriminated from collective plasmonic excitations [6]. As we will show below, although the identification of purely 1D dispersion is easily possible [259,263,264,267,402], the quantitative properties deviate significantly from simple theoretical models, and explicitly depend on the coupling to the environment. If the wires in arrays are essentially decoupled from each other, the strong confinement perpendicular to the chains leads to generation of electronic subbands. As a consequence, the simultaneous excitation of subbands, plasmons and intersubband plasmons are observed [259,267,420]. In fact, various forms of interwire coupling [263,421] lead in part to crossover to 2D in the quantitative dispersion properties.

For these reasons, this section will mainly concentrate on the consequences of this crossover, evident already from the plasmonic dispersion along the wires. In most systems only this dispersion can be observed. As a counterexample, the system Si(557)-Pb shows 2D dispersion in a limited range of energies above 0.5 eV, for Pb concentrations in which SODWs (see sec. 2.4) still keep the system in its insulating state perpendicular to the steps at low temperature.

We will start out, after a short experimental section, with the system Si(557)-Ag, which exhibits the typical properties of a 2D electron gas confined to thin, electronically independent Ag monolayer stripes on small (111)-oriented terraces that are separated by (112)-oriented minifacets. The special mechanism leading to metallicity of these stripes will be discussed. Furthermore, as a contribution to the discussion of Luttinger liquids (LL), we demonstrate the incompatibility of the plasmonic dispersion with the theory of LL.

One of the central issues of our investigations during the last years was the use of plasmon excitations and their dispersion in conjunction

with quantitative DFT simulations as a spectroscopic tool for the unoccupied electronic band structure in the vicinity of the Fermi level in these quasi-1D systems. Emphasis was put on Au wires on Si(hhk) surfaces. Finally, we will address the Si(557)-Pb system already mentioned.

2.5.1. Experimental aspects

All experiments were carried out in ultra-high vacuum at base pressures around 1×10^{-10} mbar. Since plasmons in low dimensions cannot be excited by light directly, because of momentum conservation, the experiments described here were carried out mostly by HREELS. A combination of a HREEL spectrometer as electron source with a LEED system was used. It provides simultaneously high energy and momentum (k_{\parallel}) resolution [422,423]. Typical operating parameters were 20 meV energy resolution at a k_{\parallel} resolution of $1.3 \times 10^{-2} \text{ \AA}^{-1}$.

A reliable determination of loss peak positions required quantitative fitting of the loss spectra. This was done by combining an exponential Drude tail, describing the metallic continuum of losses, with an instrument function for the elastic peak and exponentially modified Gaussians for the loss peak. Details can be found, e.g., in the appendix of ref. [330].

The evaporation of metals was carried out with crucibles. The metal flux was controlled by a quartz microbalance located at the evaporator. This microbalance was calibrated with another one located at sample position, supplemented by calculated estimates. Furthermore, LEED, partly STM, and plasmon frequencies at fixed k_{\parallel} values were used to absolutely calibrate the metal concentration. While the various procedures allowed an overall precision of about 5 % of the absolute value, the Au concentration could be fixed within 1 % using the abrupt changes of plasmon frequency in Si(553)-Au [424] when the optimum concentration for formation of Au wires in the HCW phase (see below) was exceeded.

2.5.2. A strongly confined 2D electron gas: the Si(557)-Ag monolayer

The Si(557)-Ag system consists of (111)-oriented mini-terraces that are separated by three monatomic steps with (113) orientation (see Fig. 57 [264]). This morphology turned out to be stable after adsorption of Ag at room temperature and annealing up to 600° C. Close to monolayer coverage, Ag forms a $(\sqrt{3} \times \sqrt{3})R30^\circ$ structure, which was thought to be metallic, similar to that on the flat Si(111) surface [423].

Indeed a low-energy plasmon was found in this system close to this coverage, as shown in Fig. 58, which turned out not to be sensitive to the exact concentration exceeding 1 ML. A dispersing loss was found only along the Ag strips, while in the direction perpendicular to them two non-dispersing losses exist. The dispersing loss was identified with the low-energy quasi-1D plasmon, while the non-dispersing losses were identified with inter-subband plasmon excitations. In other words, the plasmons that exist on the strips of (111)-terraces seem to be well separated from each other by the (113) facets acting as spacers so that no dispersion perpendicular to the step edges was seen. However, the plasmons are confined on conducting strips of only 3.6 nm width, which

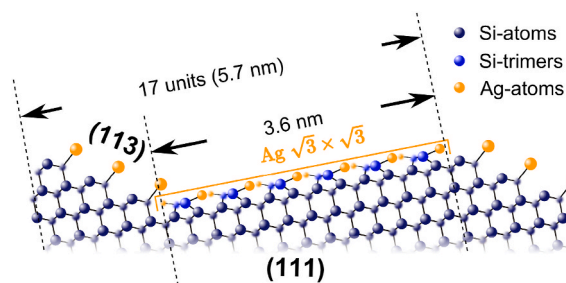


Fig. 57. Schematic of a monolayer of Ag (yellow balls) adsorbed on the Si(557) surface, consisting of flat (111) mini-terraces and strongly stepped (113) minifacets. (For interpretation of the references to color in this figure legend, the reader is referred to the Web version of this article.)

⁵ Author mainly responsible for this section: Herbert Pfnür

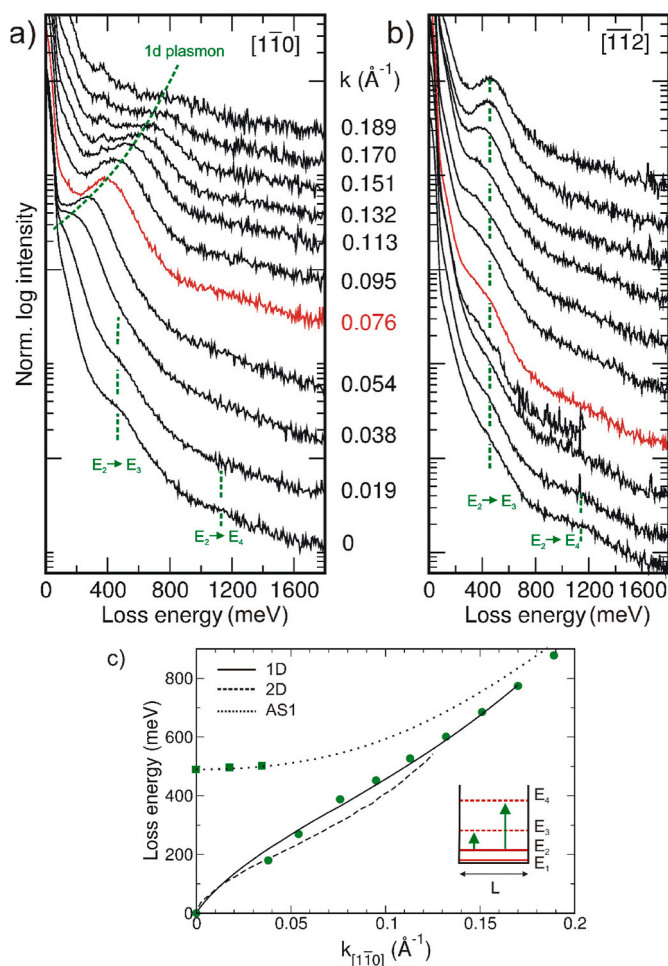


Fig. 58. a) Plasmonic losses at various angles of observation, converted into k_{\parallel} values, as indicated. b) same, but perpendicular to the step direction. c) Plasmon dispersion determined by the peak positions in a). Lines: calculated dispersion for lowest band and first subband excitation. Inset: Scheme of sub-band excitations.

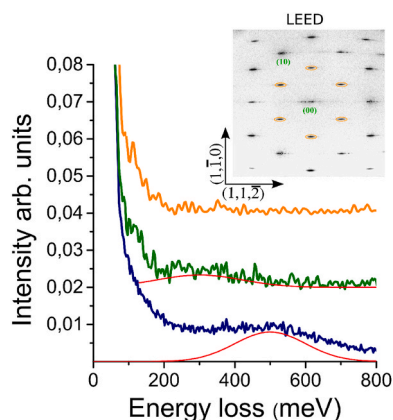


Fig. 59. Annealing experiments to 600 °C leading to shifts and complete disappearance of plasmonic losses, while the LEED pattern, shown in the inset, remains unchanged. Blue: initial spectrum, green: after first annealing cycle, orange: after second cycle. (For interpretation of the references to color in this figure legend, the reader is referred to the Web version of this article.)

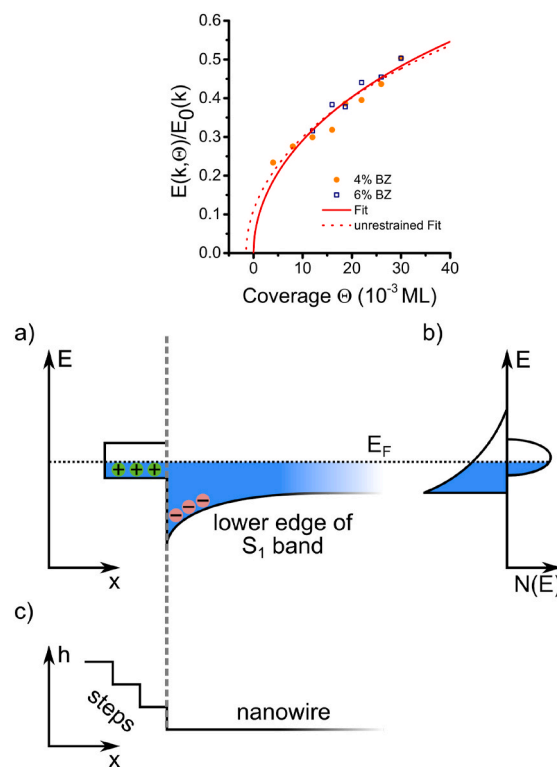


Fig. 60. Self-doping with Ag atoms on the semi-metallic Ag monolayer on Si (557). Top: Dependence of plasmon excitation energy on the post-adsorbed Ag concentration at two values of k_{\parallel} . The data have been normalized to the excitation energy at saturation for the respective k_{\parallel} . Bottom: Model of self-doping by Ag adsorption at the step edges. a), b) charge donation to the terrace due to energetic differences of the topmost Ag level. c) Geometric model.

is the reason for dispersion only along the strips. In $[112]$ direction this width sets boundary conditions for a series of excitations that can be combined with the plasmon excitation resulting in the formation of inter-subband plasmon excitations. The corresponding model, developed by Inaoka [420], is corroborated by fits (lines in Fig. 58). Our experiment allows identification of the zeroth mode that goes to energy zero at $k_{\parallel} \rightarrow 0$, the first mode with a finite energy of 470 meV in this limit, and a small further loss at 1170 meV that is compatible with a second excited mode. Further details are described in ref. [264].

However, these results turned out not to contain the full truth, as shown in later experiments: In order to obtain metallicity, a surplus of Ag atoms is needed that is most likely adsorbed at the step edges of the (113)-facets. The bare monolayer Ag strips are not metallic. Metallicity is only achieved by extrinsic self-doping due to charge donation from the edge atoms to the terraces.

This scenario becomes evident from annealing experiments, in which only a tiny amount of Ag is desorbed at 600 °C so that the LEED image, fully developed and with a negligible loss of superstructure intensity, is essentially unchanged. Nevertheless, this procedure results in complete disappearance of plasmonic losses, as demonstrated in Fig. 59.

This process is fully reversible [425]: After the plasmon loss has disappeared by the procedure just described, it is sufficient to add tiny amounts of Ag at room temperature (less than 1 % of a monolayer) to make the plasmon loss reappear (see Fig. 60). The systematic increase of this amount directly permits verification of the functional dependence of the plasmon excitation energy on (added) electron density, assuming a constant amount of charge per Ag atom to be transferred to the Ag monolayer at these small Ag concentrations. Thus the electron density, n , is proportional to the surplus Ag concentration. As shown in the left part of Fig. 60, the expected \sqrt{n} dependence was found, which proves

the universality of this rule irrespective of dimension.

These findings lead us to the model of self-doping shown in the lower part of Fig. 60. In this model, we assume that due to a smaller binding energy of Ag on the step edges compared to Ag in the monolayer on the flat terrace there is also an energetic difference for the topmost occupied Ag level between steps and flat terrace. In order to reach a common Fermi level, partial charge transfer from the step edge atoms to the terrace is necessary. This charge transfer was estimated to be $1/3 e^-$ per Ag step edge atom. This model has also been tested by simulations as well as by a variation of the terraces width, which is possible due to the instability of the regular step array to Ag adsorption at high temperature (500 °C in this case). It allows controlled widening of the terrace width, which results in a reduction of the maximum doping concentration, as expected for doping from Ag at the step edges [330].

Thus a lateral self-doping mechanism on the nanometer scale is acting in this system due the geometric and electronic inhomogeneity introduced by the sequence of (111) and (113) minifacets. Although dispersion exists only along the Ag strips, these properties are more consistent with a strongly confined 2D system than with a quasi-1D system, as also suggested by ARPES results for this system [426].

2.5.3. Low-energy plasmon excitations in Ge(001)-Au

The Ge(001)-Au system is another prototype system of self-organized atomic chains on insulating or semiconducting surfaces [136,144,240,427,428] that may be able to exhibit quasi-one dimensional properties while being embedded in a two- or three-dimensional environment. On the other hand, it is also exemplary for the difficulties of analyzing such systems. E.g., the many structural investigations of the Au covered Ge (001) surface, mainly with LEED [429] and STM [43,428,430–437] did not allow to uniquely model the structure of this system. While the so-called giant missing row model was able to reproduce some of the experimental properties [438], there are quite different suggestions for the optimal Au concentration leading to the observed $c(8 \times 2)$ structure ranging from fractions of a monolayer (ML) [43,432–434] to about one ML or even higher coverages [41,42,429]. Considerations of the Gibbs free energy in recent modelling [439] show that stabilization of structures is temperature dependent with the consequence that the highly corrugated structures of the giant missing-row models [433] with

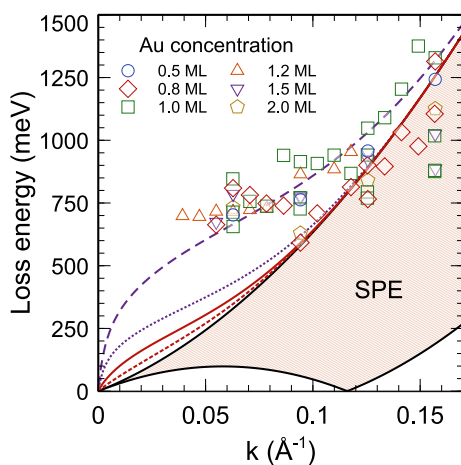


Fig. 61. Plasmon dispersion (open symbols) extracted from loss measurements and comparison with a model of a confined 2D electron gas. No dependence on Au coverage was found, as indicated by the different symbols. The shaded area shows the electron-hole excitation continuum (SPE). Simulated dispersion relations are indicated by colored lines: Plasmon dispersion of a single wire (dashed red) and an array of wires (solid red), both with a width of $w = 5 \text{ \AA}$, as well as for an array of wires with $w = 20 \text{ \AA}$ (dotted purple). Long dashes: Wire array with $w = 20 \text{ \AA}$, same effective mass as before, but twice the electron density. (For interpretation of the references to color in this figure legend, the reader is referred to the Web version of this article.)

concentrations above one ML are significantly more stable at and above room temperature than the dimer-row [430,438,440] or bridged dimer-row models [433]. While this finding may explain some of the ambiguities in the results obtained in the past, it also shows that this system is prone of formation of metastable structures that have not been explored in detail yet.

Also the electronic structure of this system has been a controversial issue. PES and STM data were originally interpreted as being fully compatible with quasi-1D electronic properties [37,39,428,432,436] in form of a LL with strong electron-electron interaction [102,103]. However, other studies carried out with similar methods indicated [41–44, 433] that this system is indeed highly anisotropic, but the Fermi surface is still 2D.

Here we present the results obtained with HREELS for the plasmonic losses, which favor the latter interpretation. More details can be found in ref. [255]. Great care was given to get optimal ordering of the Au-covered Ge surface. It was prepared at room temperature and annealed at 500 °C. After optimization an average terrace width of 350 Å was achieved, and the optimum Au concentration was determined to be 1 ML [429]. Any excess coverage exceeding 1 ML results in growth of small Au-clusters on the surface [437] that are not visible in LEED, and do not lead to low-energy plasmons (see below). At smaller coverages island formation was found so that there is no coverage dependence of the plasmon dispersion (within quite large error bars) between 0.5 and 2 ML. The procedures of measurement and data evaluation were the same as described in section 2.5.1 and will not be repeated here.

The main results are shown in Fig. 61. The extremely weak plasmon loss signal causes relatively large uncertainties compared with the Ag system on Si described above, as obvious from the scatter of the data. For large $k_{\parallel} > 0.1 \text{ \AA}^{-1}$ the measured dispersion is close to the electron-hole excitation continuum derived with a nearly-free electron gas model with the parameters obtained from photoemission [44]. For the levelling-off at $k_{\parallel} < 0.08 \text{ \AA}^{-1}$ a finite-size effect can most likely be excluded, given the large terrace widths in this system. In the analysis of these data both a modified LL model, as the extreme case of a 1D scenario, and a quasi-free laterally confined 2D electron gas model was tested. Details can be found in ref [255].

As it turned out, the LL model is not compatible with our data for several reasons.

- The Fermi velocity determined from the best fit within this model is about twice as large as that determined in PES along the wires.
- The modified electronic screening that had to be used in order to describe the overall shape of the dispersion curve is extremely long range (40 Å), i.e. it is much larger than the interchain distance between wires. Thus 2D-coupling between the wires becomes inevitable.
- Also the limiting slope for $k_{\parallel} \rightarrow 0$ is incompatible with the electron-electron interaction derived from STS [37].

This incompatibility with the LL model can have two origins: First, the 2D and 3D interactions are so relevant that they turn the system into a highly anisotropic 2D system, as suggested by STM and latest PES data [40,441], which in the limit of strong confinement is equivalent to a coupled array of wires. Second, since there are no energy scales known for the validity of the LL model, our plasmonic excitation energies may be too high for its applicability. In view of the most recent experimental results, this is the less likely possibility. Therefore, a quasi-1D quasi-free electron gas model with coupling between wires seems to be more appropriate, but, as it turns out, this model is also not without problems in the present system either.

The latter approach has been successfully applied to systems like Si (557)-Au [259]. Closed expressions for plasmon dispersion including its dependence on a confining potential, have been derived, as explained in detail below, that can be directly used [260]. Here we just present briefly the main results [255].

As shown by the lines in Fig. 61, the data are well described by this model for $k_{\parallel} > 0.09 \text{ \AA}^{-1}$, using the electron density and effective mass along the wire direction derived from PES [44]. Significant deviations, however, were found for smaller k_{\parallel} -values. While there is a clear tendency in the calculated curves to get closer to the experimental values by not only considering wire interactions, but also by making this interaction stronger, approximate agreement was only achieved by doubling the effective electron density. Alternatively, a single wire confined in a square well potential of 15 \AA width generates a very similar curve to that plotted with long dashes in Fig. 61 [255].

This ambiguity illustrates the necessity both to go beyond the nearly-free electron gas model, but, even more important, to be able to establish an accepted geometrical model for this system so that calculated band structures can be compared with experimental results on a more quantitative level. This approach is pursued in the following section.

2.5.4. Plasmon spectroscopy: sensing the unoccupied band structure in quasi-1D systems

Our approach to quasi-1D plasmonic properties starts from a 2D quasi-free electron gas that is confined to a wire of finite width by an appropriate potential. This description has the advantage of demonstrating the close relationship between band structure, single particle and collective plasmonic excitations. Within this model, following ref. [260], the plasmon dispersion for a single isolated wire can be expressed as a function of the upper and lower boundary of the electron-hole continuum of excitations, ω_+ and ω_- , respectively. For a nearly-free electron gas, the values of ω_+ and ω_- can be explicitly given as $\omega_{\pm} = \hbar(k_{\parallel}^2/2 \pm k_{\parallel}k_F)/m^*$. The plasmon dispersion is then given as

$$\omega_p(k_{\parallel}) = \sqrt{\frac{\omega_+^2 e^{A(k_{\parallel})} - \omega_-^2}{e^{A(k_{\parallel})} - 1}} \quad (22)$$

with $A(k) = \hbar^2/(2\pi) \cdot k/(m^*g_s V(k)[1 - G(k)])$. $V(k)$ is the Fourier transform of the confining potential, $G(k)$ the local field correction factor due to electronic correlations, and g_s the spin degeneracy (1 or 2). This formula, which is not limited to a NFEG, shows the intimate relationship between the continuum of e-h excitations and the plasmon dispersion. The latter turns out to be always located above the e-h continuum, and merges into ω_+ in the large k limit.

This model yields to lowest order in k_{\parallel} a dispersion linear in k_{\parallel} , contrary to a 2D nearly-free electron gas. As one sees from eq. 22, the dispersion depends not only on electron density (via k_F) and effective masses, but also explicitly on the form of the confining potential, and on electronic correlations. It can easily be expanded to arrays of wires by appropriate modification of $V(k)$. While for simple forms of the confining potentials, e.g. square well or harmonic potential, analytic expressions can be given, this is not possible for the coupling between wires, but an approximate description of coupling, valid in the limit of small k_{\parallel} [442–444], exists. Fortunately, as shown in Ref. [260], the sensitivity to the form of confining potentials and coupling between wires is not strong and slight modifications of the plasmon dispersion curve are seen mostly at small k_{\parallel} .

A unique comparison and test of validity is possible for quasi-1D band structures with single crossings of the Fermi level. In general, the band structures close to the Fermi level have a unique curvature. If, e.g. the curvature is positive, the lower edge of single particle excitations, ω_- , is that from the occupied states to the Fermi level, while the upper edge, ω_+ is given by the excitations from the Fermi level into the unoccupied states within the same band.

Since $A(k)$ rises very quickly as a function of k in all physical scenarios considered so far [260], $A(k) \gg 1$ is typically already fulfilled at $k_{\parallel} > 0.03 \text{ \AA}^{-1}$, i.e. ω_p follows very closely ω_+ for larger k_{\parallel} values. Thus measured plasmon dispersions can be directly compared with calculated unoccupied band structures and serve as a spectroscopic tool. This property will be exploited in the following in context with Au atomic

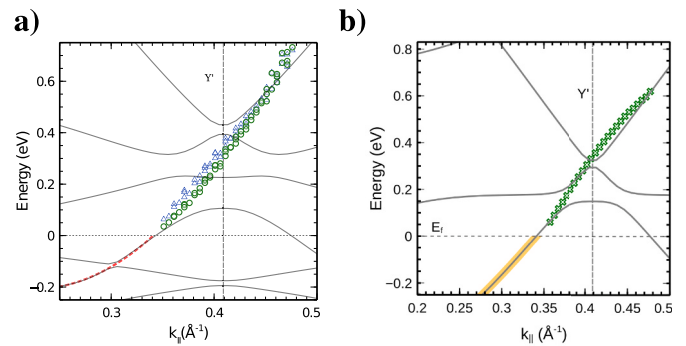


Fig. 62. Comparison of calculated band structures (gray lines) with ω_+ determined from the experimental plasmon dispersion for Si(557)-Au (a) and Si(335)-Au (b).

wires on vicinal Si(hhk) surfaces. We first demonstrate the informational content before we show the most characteristic examples of the many tests performed in the recent past.

As a starting point, we compare calculated band structures for the systems Si(557)-Au and Si(335)-Au with the dispersion of ω_+ determined from the experimental plasmon dispersion curves. The calculations were performed within density functional theory using the GGA correlation functional. Details are described in ref. [332]. Both systems feature one single atomic Au chain per terrace. Due to the hybridization of the Si honeycomb step edge – and the adatom chain for the Si(557)-Au system – with the electronic states of the Au chain, a series of small band gaps appears, particularly in the unoccupied part of the band structure. In both systems, only a single band is crossing the Fermi level, which makes the analysis as simple as possible.

For the determination of ω_+ from eq. 22 also ω_- is needed, which was taken from the calculated band structures, as indicated by the dashed red line in Fig. 62(a) and a parabolic fit. The influence of this particular choice of ω_- is tested by taking into account the negative curvature of the partially filled topmost band in its unoccupied part. This leads to small differences in the determination of ω_+ below $k_{\parallel} = 0.05 \text{ \AA}^{-1}$, as indicated by circles and triangles in Fig. 62(a) (please note that for the plasmons $k_{\parallel} = 0$ corresponds to the value at the Fermi level), and shows that the particular choice of ω_- is not crucial for the application of this method.

As confinement we assume a Gaussian distribution of the electrons in the system with a FWHM of 3.3 \AA , corresponding to a single atomic wire. This width corresponds to a parabolic confinement with ground state width of 1.4 \AA or, approximately, to a square-well confinement of 6.6 \AA . These parameters determine $A(k_{\parallel})$. As tested, the results depend very little on the exact wire width. Even changes of the form of the confining potential to a square potential yields a correction that amounts to a maximum change of slope of 10 % at most at small k_{\parallel} . More details are described in ref. [332].

In both systems shown here, the calculated band structure agrees well for the strongly dispersing bands 0.4 eV above E_F , but the small bandgaps are effectively integrated out by this type of plasmon spectroscopy. While instrumental broadening can be ruled out as the major source of broadening, the small interaction times and the increasing localization in order to transfer the necessary momentum by the impinging electron may play a role. There can, of course, also be true physical effects of integration, since every electron-hole pair with the right energy and k_{\parallel} can be excited by the plasmon, thus effectively filling the gap. Furthermore, it is conceivable that a plasmon as a collective excitation cannot be formed by strongly localized electrons or by electronic hybrids that localize electrons. In other words, such a hybridization may be “ignored” by plasmonic excitations, i.e., only the projection of a wave function on the nonhybridized delocalized contributions is responsible for plasmonic excitations. A definite answer to these questions must be subject to further investigations.

Nevertheless, within these limitations, which are not very dissimilar to methods for the occupied band structure such as PE, valuable new information about the unoccupied band structure can be obtained by this method, as will be demonstrated further below. The plasmon dispersion (and that of ω_+) seems to be strongly determined by matching group velocities between plasmon ω_+ and the unoccupied band structure. This means that flat bands contribute little to the plasmon excitation. Large band gaps, on the other hand, which limit the e-h-continuum, are also visible as limits of plasmon frequency (see below).

2.5.4.1. Application of plasmon spectroscopy: optimal Au concentration in Si(111)-Au(5×2). The submonolayer of Au on Si(111) forms a (5×2) structure over a fairly wide range of coverage, which has been investigated by several authors in the past [445–448]. In fact, it can be considered as a prototype system for an adsorbate-induced spontaneous symmetry break by formation of quasi-1D atomic chains that are metallic. Surprisingly, the geometric structure of these chains is still under debate.

From a comparison of STM data and quantitative DFT calculations [449] an optimal concentration of 6 Au atoms per (5×2) unit cell was suggested, which corresponds to 0.6 ML. In this so-called EBH model [450] the (5×2) structure consists of a single and a dimerized double-atomic Au chain, separated by a Si honeycomb chain (HC). According to the calculations, this structure is further stabilized by Si atoms adsorbed on the Au chain system. The existence of these Si adatoms as well as that of the Si-HC chain was corroborated by optical reflection anisotropy and by DFT [451]. This model was also corroborated by high-energy electron diffraction data [452]. In contrast, Kwon and Kang proposed a model (KK model) with an optimal Au concentration of 0.7 ML, i.e., one Au atom more per unit cell than in the EBH model [453]. With this model a metal-insulator transition, induced by adding additional Au to the optimal concentration, could successfully be modeled [454]. Nevertheless, the optimal concentration suggested by this model is not only at variance with the EBH model, but also with the findings by Kautz et al. using low energy electron microscopy in combination with medium and high energy ion scattering, which fixes this value to 0.65 ± 0.01 ML [455].

Here we show that indeed plasmon spectroscopy, testing the unoccupied band structure, is able to discriminate between the suggested models just mentioned. This is done by comparing the calculated unoccupied band structure close to the Fermi level [450,453] with ω_+ derived from the plasmon dispersion [456] using the procedure just described (see Fig. 63). An almost quantitative agreement is obtained between our data and the undoped model of a Au-induced (5×1)

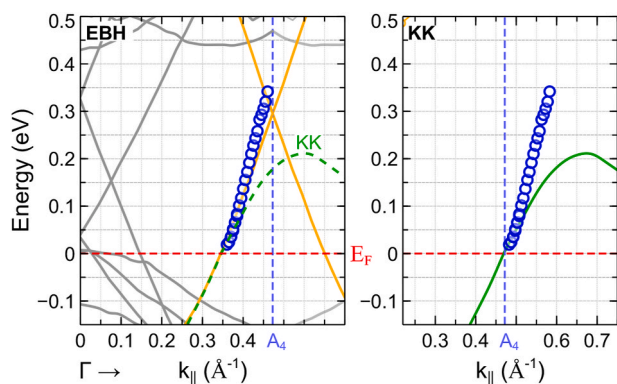


Fig. 63. Comparison of calculated electronic band structures (lines) with experiment (blue circles). The left panel shows the comparison with the EBH model for the case of an undoped (5×1) structure, the right one that with the KK model. The circles mark ω_+ determined from the plasmon dispersion. (For interpretation of the references to color in this figure legend, the reader is referred to the Web version of this article.)

structure of Erwin et al. [450] with a Au concentration of 0.6 ML. Only the experimental slope is slightly higher than in theory. According to Ref. [450] Si adatoms on the Au dimer chain lower the total energy further. While ordered structures of Si adatoms would lead to multiple openings of band gaps [450] that are not compatible with our data, the adlayer consists of single atoms or small clusters, as demonstrated in further studies [457,458]. Thus metallicity is retained in agreement with our findings.

Within the KK model, large band gaps are always present, which does not fit to our data (see Fig. 63). As seen in this figure, also the slope of the dispersion of the unoccupied band structure close to E_F is far off the experimental data points, this model is clearly not able to describe our experimental findings.

Concluding, this example demonstrates once more that the low-lying collective electronic excitations can be directly used as a spectroscopy to obtain information about the unoccupied band structure close to the Fermi level. This part of the band structure turned out to be much more sensitive to differences between various structural models proposed for this system than spectroscopies of the occupied bands such as ARPES. Thus we were able to corroborate the validity of the EBH model that suggests a saturation coverage of 0.60 ML of Au, in agreement with our own coverage calibration and with our LEED investigations.

2.5.5. Electronic coupling of quasi-1D Au-wires on Si(hhk) surfaces to higher dimensions

Already from the preceding sections it became obvious that even quasi-1D gold chains on substrates like Ge or Si are coupled to these substrates by hybridization mainly with surface states. On the one hand, these interactions stabilize the wires, but lead to strong modification of quasi-1D properties. On the other hand, new phenomena, e.g. the enforced strengthening of order by surplus Au atoms in Si(553)-Au [424], appear that are explainable only by the delocalized and partly even non-local interactions between electronic states of the adsorbate and the substrate.

We have systematically investigated these properties mainly on vicinal Si surfaces [265,266,296,332,421,424,460], but will concentrate in the following on the prototype system Si(553)-Au [144]. It contains a double strand of Au chains and exists in two flavors: Upon adsorption of 0.48 ML of Au, a double-chain is formed on each terrace, called the high coverage phase (HCW). This phase has been studied extensively, and the reader is referred to section 2.2. At a Au concentration of 0.19, a second ordered phase (LCW) appears, which can be considered as a 1D version of a strained-layer superlattice structure [459] and in which a double Au chain exists only on every second terrace. Although this system allows to

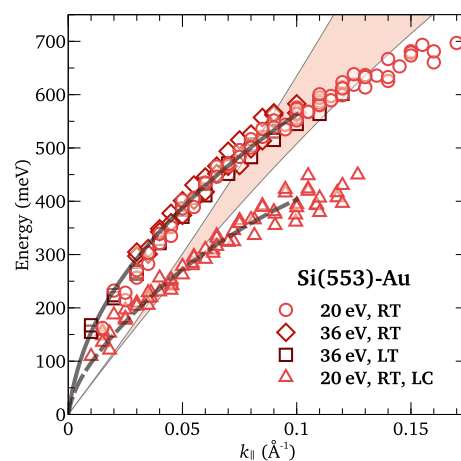


Fig. 64. Plasmon dispersion of the Si(553)-Au HCW and LCW phases. RT, LT: measurements at room-temperature ($T = 293$ K, RT) and at $T < 120$ K \diamond , \square : HCW phase. \triangle : LCW phase. The e-h continuum is derived from ARPES measurements [272,459] within the NFEG model.

separate the Au chains of the Au/Si(553) system and thus possibly study the inter-chain coupling strength, we focus in this section on the coupling of the Au chains with the substrate. Therefore, the electronic band structure was calculated for both phases within DFT, putting emphasis on the unoccupied part, and compared with the experimental plasmon dispersion.

One important question to solve was the obvious discrepancy between PES data and theoretical calculations of the band structures in the past. Although the PES data for the systems under investigation here [272,283] suggest that the Au-induced bands are mostly free-electron like, atomistic calculations using the geometries extrapolated from STM consistently show [272,288] that this interpretation is incorrect. In both systems, there is strong hybridization of the Au-induced band(s) with the Si surface state that originates from the Si honeycomb chain (for more details, see ref. [266]). As a consequence, band gaps of about 0.1 eV open, which partly have been observed in some experimental studies [307]. One of these gaps is located right at the Fermi level, preventing one of the Au-induced bands to cross it [272]. Therefore, a single band actually crosses the Fermi level close to the edge of the Brillouin zone for both phases of Si(553)-Au. This band has a strongly nonparabolic dispersion. Although the LCW structure features an additional terrace, the Au-induced bands are very similar in photoemission. This resemblance makes the two systems a perfect couple for the investigation of properties that are strongly dependent on the interwire distance, such as plasmons.

The relevance of hybridizations between Au and Si states becomes clear by analyzing plasmon dispersion of the Au-induced metallicity by EELS. The measured plasmon dispersion is plotted for both Si(553)-Au systems in Fig. 64. Indeed, only one plasmon dispersion curve was found in both systems, compatible with a single crossing of the Fermi level. Interestingly, as shown by the solid lines, which represent a fit with an empirical model [421], based on the NFEG in the small k_{\parallel} limit [442–444] the system can be reasonably well described by a confined NFEG model of coupled wires. However, although this model gives a satisfactory fit to the measured data, this description cannot be correct: For reasons of stability, the plasmon dispersion must be above the e-h continuum and converges to the upper boundary of the single particle excitation spectrum at large k_{\parallel} , as already explained above. Here,

however, as seen in Fig. 64, the plasmon dispersion fully crosses the e-h continuum derived with the same parameters used for the plasmonic fit. At the highest measured k_{\parallel} values, the plasmon dispersion curve is even below the e-h continuum. This behavior is not unique to this system, but was observed for Au chain on other vicinal Si surfaces as well [332].

A way out of this dilemma is to compare plasmon dispersion with the calculated band structure by use of eq. 22, following the lines sketched in the previous section. The result for ω_{+} is shown in Fig. 65 as blue circles together with the electronic bands calculated by DFT-PBE (in gray). Since there is only one crossing of partially occupied bands with the Fermi level for the HCW phase, ω_{+} is identical to the excitation from the Fermi level to the first Au-induced unoccupied band. Therefore, ω_{+} can be directly compared to the calculated unoccupied band structure. The match, assuming pairing $\Delta d/d$ of the Au atoms within the Au strands of 0.005, is nearly quantitative. The strong curvature at small k_{\parallel} is a clear indication of interwire interactions and thus of the wire coupling with higher dimensions. As expected, and clearly visible from the results of the band structure calculation in the occupied part below the Fermi level, the hybridization of Au-induced bands with the surface state originating from the Si honeycomb chain close to the step edge strongly reduces the value of ω_{-} . Putting all this together, we obtained values for $\omega_{+}(k_{\parallel})$ from the measured plasmon dispersion, which fit the calculated unoccupied band structure in the range up to about 0.75 eV.

Not surprisingly, the comparison of plasmon dispersion with calculated band structures reveals some structural sensitivity. As an example, the curvature and flattening of ω_{+} at large k_{\parallel} indicate the appearance of a band gap at about 0.70 eV, which is also seen in STS [146]. The dispersive electronic bands originating from the Au states are characterized by the previously discussed anticrossing interaction, resulting in the occurrence of an electronic band gap of about 0.1 eV around $k_{\parallel} = 0.3 \text{ \AA}^{-1}$, which is sensitive to the degree of dimerization of the Au atoms within the Au chains. Indeed, as shown in ref. [266], there is a linear relationship between dimerization and the size of this bandgap.

The same procedure can now be applied to the Si(553)-Au LCW phase. The main changes between HCW and LCW appear in the unoccupied band structure, as the reduced slope in Fig. 64 compared with the HCW phase suggests. Generally, the calculated bands exhibit a slightly smaller overall slope, and the band crossing at E_F is significantly more curved in the unoccupied section. It levels off at a smaller energy, thus reducing the dispersion of this band as a whole. For this reason, the originally postulated “spill-out” effect due to unoccupied adjacent terraces [459] can now be pinned down to a shift of E_F coupled with slight modifications of the electronic interaction with the ionic potentials. As a result, small changes in the band structure, mainly in the unoccupied part, become obvious, resulting in a reduction of the plasmon frequency, as observed.

These examples show that a pure 1D description is not adequate, although these systems are among the narrowest possible quasi-1D objects that can be realized. Hybridization between the electronic Si surface state and Au-induced states results in a breakdown of the NFEG model. Because the coupling with higher dimensions through the substrate is relevant, HCW and LCW are more appropriately described as extremely anisotropic 2D objects. On the other hand, the very satisfactory agreement between atomistic calculations and plasmon spectroscopy validates the calculated band structure, in particular the unoccupied part. Furthermore, it shows that plasmon spectroscopy contains important information about the excitation spectrum of an electronic system that is not easily accessible otherwise.

2.5.6. Modification of plasmons by adsorption and environment

Due to the polarization effects, plasmon frequencies are known to be modified when the plasmonic structure is embedded into an environment [256,461], leading in general to a reduction of plasmon frequencies compared to a hypothetical free-standing system.

This is, however, by far not the only effect in quasi-1D structures. Here we concentrate on the effect of simple adsorbates like atomic

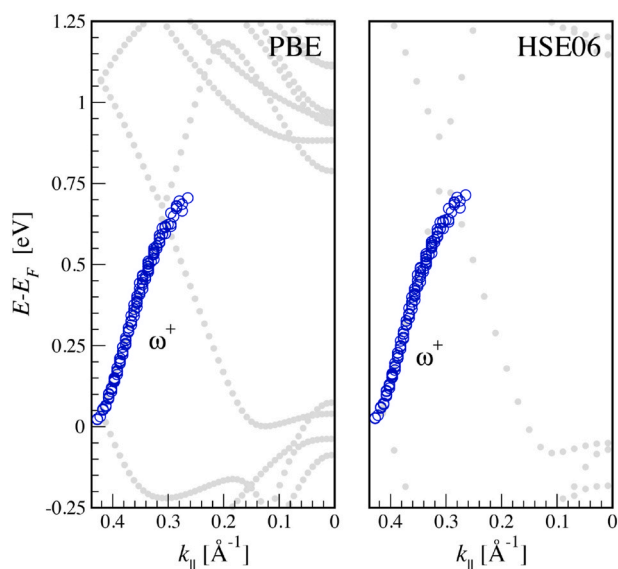


Fig. 65. DFT band structure (gray lines) calculated without SO interaction for the Si(553)-Au HCW phase. The blue circles show the positions of ω_{+} calculated from the plasmon dispersion with the procedure described in the text. Left panel: DFT-PBE calculations. Right panel: DFT-HSE06 calculations. (For interpretation of the references to color in this figure legend, the reader is referred to the Web version of this article.)

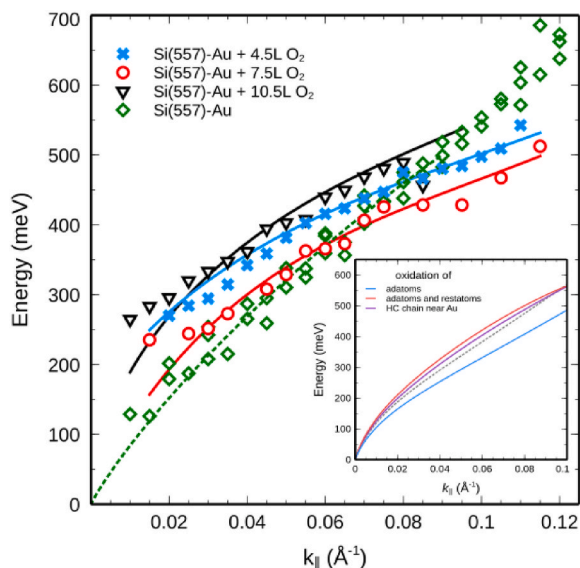


Fig. 66. Modification of plasmon dispersion of Si(557)-Au (diamonds) by various exposures of oxygen, as indicated. Solid lines are guides to the eye with the assumption that the curves have to start at $E = 0$ in the long wavelength limit. Inset: Calculated plasmon dispersion using the band structures shown in Fig. 67 for oxygen adsorption at the sites indicated.

hydrogen and oxygen on Au atomic wires on vicinal Si surfaces, but again also on adsorption of surplus Au atoms. Their interaction, as we showed recently [296,424], goes far beyond simple doping as in the Si(557)-Ag system discussed above and influences dimerization of Au atoms, their energetics, and thus long-range order.

2.5.6.1. Chemical modifications. Before we discuss this topic, we address the effect of chemical modification of band structures by adsorbates as well as their role as additional scattering centers, which lead to the formation of plasmon standing waves, but also, again in combination with changes in band structure, to plasmon localization. In this context, the Si(557)-Au system is one of the most interesting and most reactive since, according to the well-established geometrical structural

model [283,288], there is a single atomic chain of Au, but in addition a Si adatom chain on each terrace, which can be oxidized.

In Fig. 66 the modification of the plasmon dispersion as a function of oxygen exposure is shown. As seen from Fig. 66, oxydation with exposures up to 10 L, that are expected to almost saturate the monolayer, the plasmon does not disappear, the plasmon loss energy at small k_{\parallel} even increases. In other words, metallicity is not lost by oxidation, in agreement with surface conductance measurements, in which conductance was only reduced by about 20 % in this range of exposures [331]. Compared with the pristine dispersion curve, the position of the dispersion even changes non-monotonically as a function of exposure. This result can be understood for small k_{\parallel} by a comparison with infrared absorption data measured for the Si(553)-Au system [462] that shows very similar effects at small k_{\parallel} , though slightly less pronounced. The whole dispersion is compared with quantitative DFT simulations putting oxygen atoms as 1D rows on various adsorption sites, as indicated in the inset of Fig. 66.

The simulated results for the band structures of the Si(557)-Au after oxidation of the chains of adatoms, the honeycomb (HC) chain and Si atoms close to the Au atoms (for details, see ref. [296]) are shown in Fig. 67 in an extended zone scheme, with a restriction to those bands with clear contributions from the Au chain, adatoms, and the HC chain. In (a) the complete adatom row has been oxidized. As expected, modifications of the bands associated with the adatoms and the restatoms were observed due to the admixture of oxygen orbitals, but changes to the band with preferential Au character are surprisingly small, as obvious by the comparison with the bands of the pure Si(557)-Au system, which are shown as thin dotted lines in this figure. A single band still crosses the Fermi level, and the Fermi wavevector slightly changes from 0.35 \AA^{-1} to 0.37 \AA^{-1} . These changes get stronger with increasing oxygen concentration, as seen in panel (b). Although the configuration of (c) is energetically not very favorable, i.e. these sites will only be filled after those of (a) and (b), it was used to test the effect of oxidation of Si atoms in the immediate vicinity of the Au chain. As seen in Fig. 67(c), even under these conditions the system remains metallic, even though the whole band structure is strongly modified. These results match well with the experimental findings.

When looking at the plasmons, also the small changes of plasmon dispersion can be understood in detail, using the procedures for the determination of ω_+ and ω_- described above. The expected plasmon

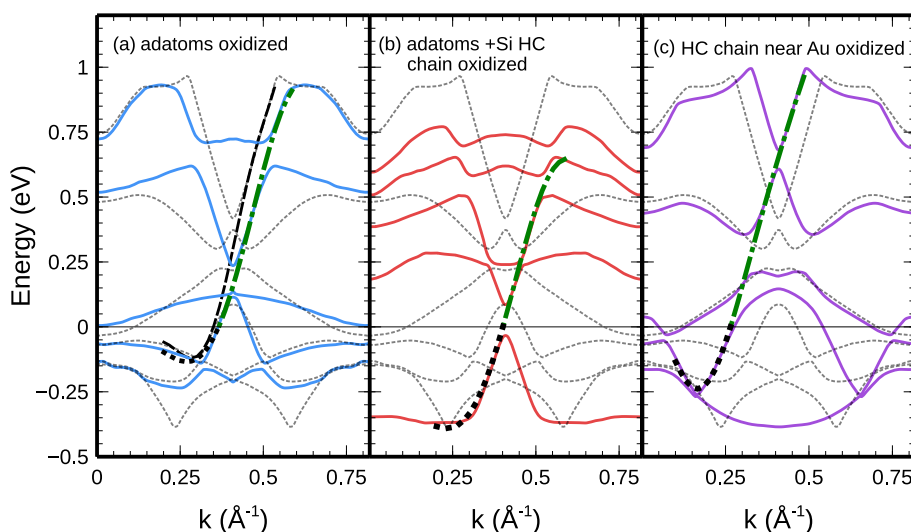


Fig. 67. Band structures calculated in an extended zone scheme along ΓY (Y at 0.82 \AA^{-1}) for the indicated oxygen adsorption sites. For details of geometrical models, see Ref. [296]. The black dashed lines below E_F (energy zero) correspond to the assumed ω_- . Above E_F ω_+ is plotted (dashed-dotted, green) that was calculated from the experimental plasmon dispersion and ω_- . The black dashed line in (a) indicates the analogous result for the clean system. (For interpretation of the references to color in this figure legend, the reader is referred to the Web version of this article.)

dispersions are plotted in Fig. 67 as dashed-dotted lines, neglecting again the small bandgaps. The results in more detail are shown as inset in Fig. 66, which agree qualitatively well with the experimental data. From the results of the simulation we can even learn that the oxidation seems to start with the HC chain, followed by the adatoms.

In conclusion, although strong modifications of the band structure by oxidation are found, metallicity turns out to be quite robust. On the other hand this system is an example of strongly delocalized interactions over several atomic distances so that the electronic bands of the Au atoms, including the Fermi surface, are modified both on the clean and on the oxidized Si surface.

An extreme example in this context, going far beyond doping of charge by an adorbate [463], is the charge redistribution over the whole terrace induced by adsorption of atomic hydrogen on Si(557)-Au [460]. In this system, we observed band gap opening in the measured plasmon dispersion at large momenta that limits the plasmonic excitation to an energy of 0.43 eV in presence of H. DFT shows that Si surface bands strongly hybridize with those of Au so that H adsorption on the energetically most favorable sites at the Si step edge and the restatom chain causes a significant shift of bands but also strongly changes the character of hybridization. Together with H-induced changes in band order, the result is band gap opening and reduced overlap of wave functions. These mechanisms were identified as the main reasons for plasmon localization that act independent of disorder (see below). Interestingly, although the whole electronic system is modified by H adsorption, there is no direct interaction between H and the Au chains.

2.5.6.2. Plasmon standing waves, disorder, localization. Let us now turn our focus to small k_{\parallel} . Infrared absorption is known to be sensitive only to infrared active modes in the limit $k_{\parallel} \rightarrow 0$ [464]. Since low-D plasmons have zero excitation energy in this limit, these plasmons are not expected to be detectable by IR spectroscopy. However, because of finite wire lengths, the wires serve as antennas as a whole, and the plasmon resonance becomes optically detectable due mixing in of a dipolar contribution to the excitation [465,466]. It is thus a very valuable tool, complementing HREELS, that is also important to discriminate between finite size effects of wire lengths and possible adsorbate-induced band gap openings. With both HREELS and IR we see a minimum energy loss (or absorption) peak already for the pristine Si(553)-HCW system around 100 meV that systematically shifts to higher energy with an increasing amount of adsorbed oxygen [462]. If we identify the energy of the IR absorption minima with the energy of the ground state of a plasmon standing wave on wires with an average length l , this wavelength cannot be exceeded at a given oxygen concentration so that no dispersion is possible for smaller k_{\parallel} . With this assumption in mind, we

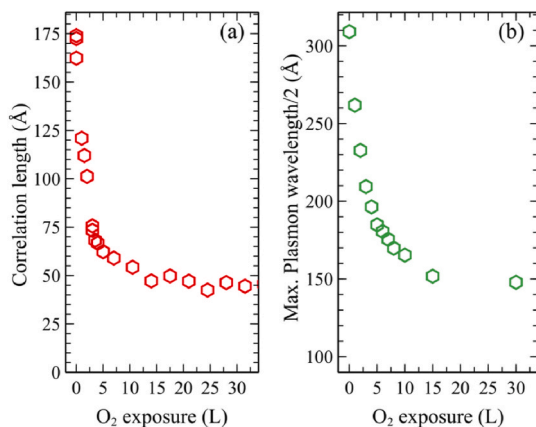


Fig. 68. (a) Correlation lengths of $\times 2$ streaks in LEED, determined as inverse FWHMs, as a function of oxygen exposure in Si(553)-Au. (b) Maximum plasmon wavelengths, divided by 2, determined from the energetic positions of the absorption minima and the plasmon dispersion (for details, see text).

took the energies of the IR absorption minima and determined their corresponding minimum k_{\parallel} values as the intersection of a nondispersing state of this energy with the actual dispersion of the pristine surface.

In Fig. 68, the average wire lengths, as obtained from the maximum wavelengths determined by the procedure just described, are compared with those obtained from the inverse halfwidths of the LEED profiles of the $\times 2$ streaks present in these systems. As expected, both strongly decrease as a function of oxygen exposure from the initial value of about 31 nm, obtained from IR. From these results it is obvious that random adsorption of oxygen introduces new scattering centers. Although oxidation directly at the Au chains is unfavorable [296], oxidation at the HC Si chain still has a significant influence also on plasmon scattering by defects, so that the effective wire length for plasmons decreases.

A very similar trend is seen when taking the inverse FWHMs of the $\times 2$ streaks along the $[112\ 1]$ direction in LEED (see Fig. 68(a)). The reduction of the correlation lengths of $\times 2$ -order along the wires as a function of oxygen exposure is even more pronounced than that in IR and starts at a significantly smaller value, indicating different sensitivities of IR and LEED to various types of disorder introduced by oxygen atoms. These different sensitivities to defects can at least be qualitatively understood. Plasmons generally have wavelengths much larger than the lattice constant and exhibit a pronounced wavelength dependence [416] that makes the scattering probability at defects of atomic size small at long wavelengths. On the contrary, stacking faults in the dimerization of the Au chains, e.g., clearly cause phase changes in LEED and thus limit the correlation length in LEED, whereas they are expected to represent weak scatterers for the plasmons with long wavelengths. Kinks in the Au chains, on the other hand, caused by roughness of step edges or slight azimuthal misalignment of the sample, should also scatter plasmons more efficiently. Therefore, we always expect a higher sensitivity to structural defects in LEED than with plasmons.

The formation of plasmonic standing waves induced by defects is a common phenomenon in all these systems. As an extreme case, it can lead to plasmon localization, as observed for the Si(775)-Au system [424].

2.5.7. Dimensional crossover: Si(557)-Pb

As discussed above in sec. 2.4, the Si(557)-Pb system is the prototype system for temperature switchable 1D-2D metallicity [371], but also for highly correlated electrons leading to SODWs [139]. The critical concentration for pure 1D electrical conductance at low temperature is 1.31 ML of Pb relative to the Si(111) surface concentration.

For this critical Pb concentration of 1.31 ML a clear dispersing loss along the terrace edges was observed (shown in Fig. 69(a)), and no such loss was found in perpendicular direction - evidence for a 1D dispersion at this coverage. No temperature dependence could be observed comparing measurement at room temperature with those during ℓ He

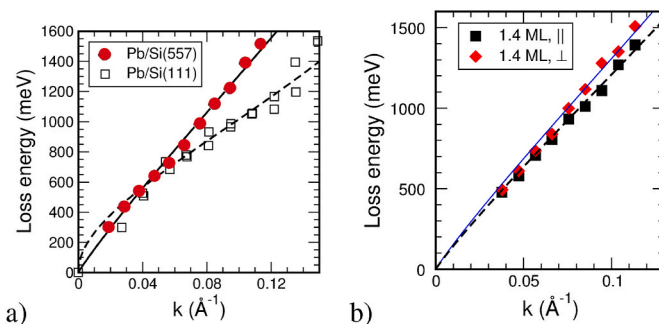


Fig. 69. a) Comparison of the dispersion for 1.31 ML Pb on Si(557) parallel to the steps (red balls) with that obtained for the same coverage of Pb on Si(111). b) Dispersion in both directions with 1.40 ML of Pb. The dashed line corresponds to the result at 1.31 ML. (For interpretation of the references to color in this figure legend, the reader is referred to the Web version of this article.)

cooling.

As seen from Fig. 69(a), the measured data points can be naturally extrapolated to zero momentum and zero energy. The dispersion can quantitatively be described by a model of a confined 2D electron gas with local field corrections and correlations [420] using a single, four atoms wide metallic strip that is confined in a parabolic potential. More details can be found in ref. [263]. There is a clear qualitative difference between these quasi-1D data and the 2D system of Si(111)-Pb that is also shown in this figure. Furthermore, the almost linear dispersion of Pb/Si (557) was taken as the typical signature for a quasi-1D system [443].

Contrary to the Ag/Si(557) system described above, however, no indications for quantum well confinement were detected. Already the missing temperature dependence of the 1D plasmonic dispersion is an indication that the physical mechanism for decoupling the plasmonic excitation on the various terraces cannot be related to Fermi nesting and opening of the 1D band gap alone. A large contribution to effective decoupling may, however, originate from the high resistance between steps [370].

However, as it turns out, the quasi-linear dispersion is no unique signature for a 1D property [461]: Increasing the Pb coverage, e.g. to 1.4 ML, leads to appearance of a plasmonic loss also in the direction perpendicular to the steps (see Fig. 69(b)). At this Pb concentration, about half of the Si step edges originally not covered by Pb are decorated with Pb chains [370,374]. While these added chains increase coupling between different terraces, also the effective band gap is reduced [329]. These changes in coupling between terraces may explain the appearance of propagating plasmons at energies much higher than the measured gap. Nevertheless, the small anisotropy of about 10 % between directions parallel and perpendicular to the steps is quite puzzling, as well as the non-detectability of a loss signal for wavelengths above 15 nm, which corresponds to 10 times the terrace width.

In both directions there is still a quasi-linear dispersion. For geometric reasons, this coupling must still be strongly anisotropic. It may also linearize the dispersion, in a quite analogous manner as the coupling of 2D layers [409] or of surface state plasmons with bulk electrons [414]. Thus we have here a clear crossover behavior from 1D to 2D induced by a very small change of surface concentration of Pb. At this moment there is no clear understanding yet of the underlying physical mechanism for the crossover nor is there a quantitative theory for the plasmonic excitations in these anisotropic low-D systems.

2.5.8. Conclusions

This section has demonstrated that the study of plasmonic excitations is a quite versatile and valuable tool in order to characterize quasi-1D systems on insulating substrates. The identification of quasi-1D behavior, however, turned out not to be straight forward.

While the Si(557)-Ag system seems to consist of an array of well decoupled individual Ag strips on each mini-terrace, there is no sign of the typical 1D instabilities described in sec. 1.3. Instead, the substrate seems to provide a 3D confining potential in this case so that the description by a strongly confined 2D electron gas fits the data well. This confining potential may be the reason that no signs of quasi-1D behavior show up, in agreement with scenarios described in sec. 1.7. The data of Ge(100)-Au and their comparison with theory point in a similar direction so that it is very difficult to discriminate between 2D and quasi-1D behavior, as already discussed in sec. 1.7.

Furthermore, all systems studied here suffer from limitations by substrate imperfections. These generally lead to limited lengths of the quasi-1D objects and to typical finite size effects, so that the behavior for $k_{\parallel} \rightarrow 0$ can only be extrapolated. At the same time, these finite size effects limit the accessible range of low-energy plasmonic excitations to finite values that may already be too large for the observation of, e.g., Luttinger liquid behavior.

Nevertheless, the study of plasmon dispersion turned out to be directly sensitive to the interactions in 2D and 3D. By comparing plasmon dispersions with theoretical unoccupied band structures close to

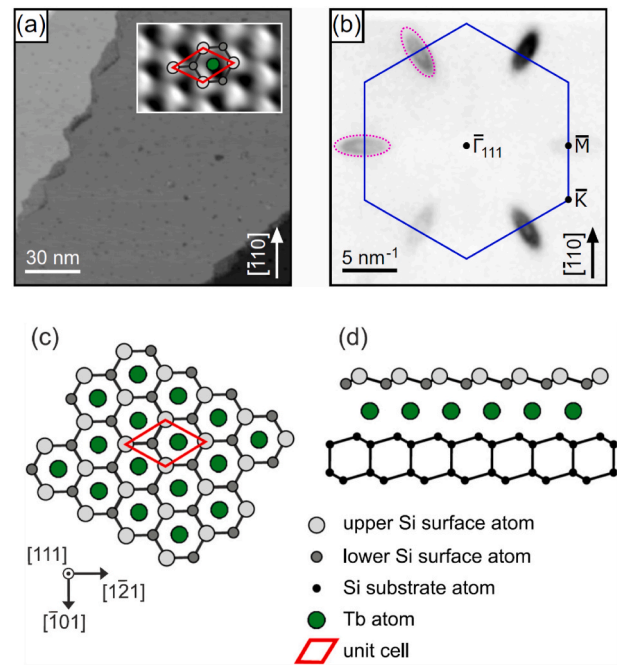


Fig. 70. (a) STM data of the TbSi_2 monolayer on Si(111) with an atomically resolved image in the inset, (b) the corresponding Fermi surface observed by ARPES at $h\nu = 100$ eV, and (c,d) the related structure model (c) in top view and (d) in side view. From Refs. [499,506].

the Fermi level, calculated with ab-initio methods, these dispersion curves were shown to be useful as a new spectroscopic tool. This method was tested on a variety of Si(hhk)-Au systems and revealed strong coupling between electronic Au and Si surface states including strong electronic correlations involving both spin and charge (see section 2.2.4).

A particularly intriguing system in this context is the Si(557)-Pb system, which shows a clear crossover in dispersion from 1D to anisotropic 2D induced by a small increase of Pb concentration that most likely also changes coupling between terraces even for excitation energies much higher than those relevant for electrical conductance and the formation of SODWs (see sec. 2.4). At this point there is no theoretical description yet.

2.6. Strongly interacting systems and embedding: rare earth silicides⁶

In the previous sections, the properties of atomic wires were presented, which are mainly characterized by metal induced surface reconstructions, governed by the intensive interaction of the deposited metal atoms with the semiconductor surfaces. In the present section, we will mainly discuss the properties of nanowire structures, which are based on existing bulk compounds — the rare earth silicide nanowires. These 1D structures have been intensively studied in the last two decades, in particular on Si(001) surfaces [467–489], but also on other orientations of the silicon substrate [479,486,490–500].

Rare earth silicide nanostructures on silicon surfaces are usually prepared by deposition of the rare earth metal and simultaneous or subsequent annealing at temperatures of 500–750 °C. In this way, a solid state reaction accompanied by atomic diffusion processes leads to the formation of a silicide. Because of the silicon surplus from the substrate, usually the most silicon-rich silicides are formed, which are the hexagonal or tetragonal disilicides RESi_{2-x} (RE stands for a trivalent rare earth).

⁶ Author mainly responsible for this section: Mario Dähne

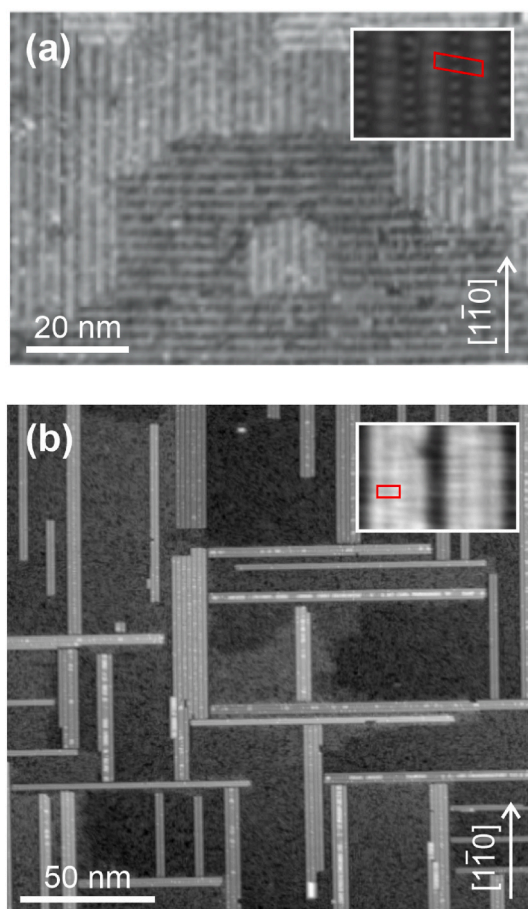


Fig. 71. STM images of (a) the terbium induced wetting layer on Si(001) and (b) the terbium silicide nanowires on Si(001). The magnifications in the insets show (a) the 2×7 periodicity of the wetting layer and (b) the 1×2 periodicity of the nanowire top surface, as marked by the red unit cells. Adapted from Ref. [486]. (For interpretation of the references to color in this figure legend, the reader is referred to the Web version of this article.)

2.6.1. Planar rare earth silicide films on Si(111)

On a planar Si(111) surface, wide 2D films of the hexagonal silicide can be formed in this way [501–507]. In Fig. 70, STM and ARPES results of such a monolayer-high TbSi₂ film are shown together with the corresponding structure model. As revealed from atomically resolved STM data [e. g. in the inset of Fig. 70(a)], the film has a quasi-hexagonal structure with a 1×1 periodicity, composed of a hexagonal terbium layer underneath a silicon bilayer with a threefold symmetry because of its buckling [Fig. 70(c and d)]. The electronic band structure with its Fermi surface, shown in Fig. 70(b)—is characterized by a metallic behavior with elliptical electron pockets at the *M* points [499].

Furthermore, a star-like hole pocket is located at the Γ point [506,507], which is, however, not visible at the photon energy used here because of photoemission matrix element effects.

In the case of thicker, more bulk-like films, a strain induced defect structure develops, which leads to a Tb₃Si₅ stoichiometry with a $\sqrt{3} \times \sqrt{3}$ periodicity [506,507]. Other trivalent rare earth metals such as dysprosium or erbium form very similar structures with almost identical electronic properties, a behavior that is related to the chemical similarity of the rare earths [501–505,507].

These hexagonal silicide structures will play a major role in the following presentation of rare earth silicide nanowires on differently oriented silicon surfaces.

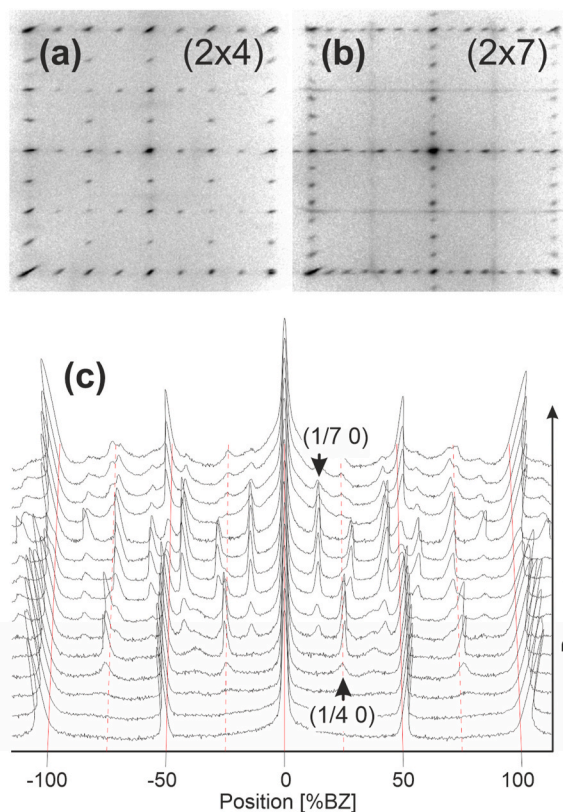


Fig. 72. (a,b) Selected LEED patterns and (c) a sequence of line scans for the development of the dysprosium induced wetting layer on Si(001) with increasing dysprosium coverage taken at $E_{kin} = 52$ eV, showing the transition from 2×4 building blocks to the ordered 2×7 structure. Adapted from Ref. [508].

2.6.2. Rare earth silicide nanowires on Si(001)

When rare earth metals are deposited on Si(001), accompanied or followed by thermal activation, mainly two low-D structure types are formed, the so-called wetting layer and the nanowires, as shown exemplarily in Fig. 71(a) and (b), respectively. Now these two structure types will be presented in detail.

2.6.2.1. The wetting layer.

The first structure, observed at sub-monolayer rare earth coverages on Si(001) and/or rather low formation temperatures, is a wetting layer, which finally shows a 2×7 periodicity. As shown in Fig. 71(a) for the case of terbium, it is characterized by a periodic arrangement of long structures appearing like wires. However, since this structure is formed by submonolayer coverages and covers the entire surface, it should rather be considered as a rare earth induced surface reconstruction, in analogy to the ones from gold, indium, or silver that were discussed in sections 2.2, 2.3, and 2.5.

Before the formation of this continuous wetting layer, an arrangement of 2×4 building blocks develops, and the typical LEED pattern of this preliminary structure is shown in Fig. 72(a). With increasing coverage, these building blocks form the continuous film with 2×7 periodicity and a characteristic LEED pattern is observed [Fig. 72(b)]. The successive development from the 2×4 to the 2×7 structure when increasing the rare earth coverage was observed for the case of dysprosium using a series of LEED patterns, and the corresponding sequence of line scans between the 1×1 main LEED reflexes is shown in Fig. 72(c) [508].

Despite of several studies addressing these wetting layer structures, conclusive structure models could not be developed up to now [486].

2.6.2.2. Formation of the nanowires.

The second structure formed on Si

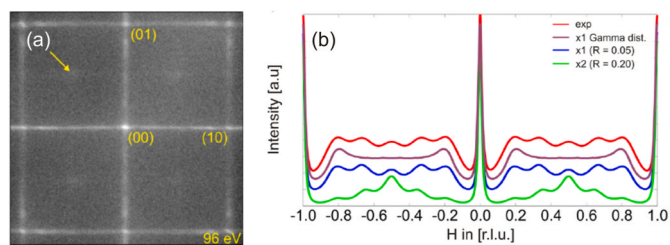


Fig. 73. (a) LEED pattern from a planar Si(001) surface with dysprosium silicide nanowire bundles taken at $E_{\text{kin}} = 81$ eV. Only negligible diffraction spots due to a 2×2 reconstruction of the nanowires are visible (see arrow). (b) Line scan of streaks (red line) between the $(1\ 0)$ and (10) fundamental diffraction spots of (a), exhibiting a fine structure. The experimental data are compared to calculated fine structures with 1×2 and 1×1 periodicities presented by green and blue lines, respectively. Best agreement is obtained assuming nanowires with a 1×1 periodicity. For comparison, the violet line shows the calculated fine structure for Gamma distributed widths of nanowires, being far from satisfactory. Adapted from Ref. [484]. (For interpretation of the references to color in this figure legend, the reader is referred to the Web version of this article.)

(001), shown in Fig. 71(b) for the case of terbium, is an arrangement of much wider and in particular also higher nanowires. They are aligned in $\langle 110 \rangle$ directions, can reach lengths up to $1\ \mu\text{m}$, are only a few nm wide, and have typical heights around $0.5\ \text{nm}$. Moreover, they tend to form nanowire bundles in particular at higher rare earth coverages, with characteristic grooves between the nanowires. At monoatomic surface steps, the direction of the nanowires turns by 90° , which is due to the corresponding change of the dangling bond directions of the Si(001) 2×1 substrate, so that two domain types with different nanowire orientations develop. As shown in the inset of Fig. 71(b), the surface structure of the nanowires is characterized by parallel lines in nanowire direction with a corrugation, which is compatible with a 1×2 periodicity. Again, very similar structures were found for other trivalent rare earth metals [467–471,475].

Comparative LEED experiments on planar Si(001) surfaces with dysprosium induced nanowire bundles were performed after a dysprosium deposition of less than 2 ML at $500\text{--}600\ ^\circ\text{C}$ [484]. Fig. 73(a) shows the LEED pattern of such a two-domain sample. It is characterized by streaks between the fundamental diffraction spots caused by diffraction from nanowire bundles due to their shape with large aspect ratios.

From literature it is well known that dysprosium induced nanowires can show 1×1 , 1×2 , or 2×2 reconstructions [470,472]. In the present case, the 2×2 reconstruction can practically be excluded due to an only negligible intensity of the related diffraction spots [see arrow in Fig. 73(a)].

The line scan along the streaks of the LEED pattern in Fig. 73(b) (red line) demonstrates that the streaks are not structureless but show some fine structure. This has been analyzed using binary models to calculate the diffraction pattern and to model the distribution of nanowire bundles on the Si(001) surface [484]. The main fit parameters were the widths of both nanowires and nanowire bundles as well as the spacing between nanowire bundles. Best agreement between the experiment and the calculated fine structure [blue line in Fig. 73(b)] was obtained using a categorical distribution of nanowire widths (average width of $4.4\ a$, where $a = 0.384\ \text{nm}$ is the Si(001) surface lattice constant), a geometric distribution of nanowires per bundle (in average seven nanowires per bundle), and an average spacing between bundles of $37\ a$. In addition, this analysis shows that the nanowires predominantly have a 1×1 structure, while no significant indications for a 1×2 periodicity were found [green line in Fig. 73(b) for a pure $\times 2$ periodicity]. However, this discrepancy to the STM results [inset of Fig. 71(b)] may be assigned to the dominating $\times 1$ periodicity within the nanowire bulk as mainly probed by LEED, while the $\times 2$ periodicity only occurs at the nanowire

surface dominating the appearance in STM images.

The properties of these rare earth silicide nanowires on Si(001) will now be discussed in detail, and it will be shown that they consist of the above-mentioned hexagonal disilicide and are characterized by a 1D metallicity.

Since the first observation of these nanowires more than two decades ago [467], structure models were developed, which were mostly based on strain considerations and on the appearance in STM images. Since the hexagonal RE_3Si_5 bulk crystal, which is the most frequent form of RESi_{2-x} with an ordered assembly of silicon defects, is almost lattice-matched to the Si(001) substrate with its a -axis, while its c -axis has a mismatch of around 7%, it was widely assumed that the nanowire direction corresponds to the a -axis of this silicide, allowing an almost strain-free and therewith practically unlimited extension in this direction. The c -axis, in contrast, was assumed to be oriented along the substrate surface but perpendicular to the nanowires, and the resulting strain would then limit the growth in this direction. In this way, the nanowire formation was attributed to anisotropic strain. And the appearance of the nanowire surface in STM images with the 1×2 periodicity could be well described by a dimerization of the uppermost silicon atoms. Also the bundle formation could be explained by misfit dislocations formed due to the anisotropic strain.

However, this model was based on the lattice parameters of the defected RE_3Si_5 layers, but did not take into account that the STM images of the nanowires usually did not show any indication of such defects. Recently the internal structure of the nanowires could be determined using high-resolution transmission electron microscopy (HRTEM) after nanowire capping and it could be demonstrated that the actual nanowire structure is different [487,489], as will be discussed in the following.

2.6.2.3. Capping of the nanowires. An important aspect of these rare earth silicide nanowires on Si(001) is that their structure may be preserved upon capping with amorphous silicon [482,487,489], in this way

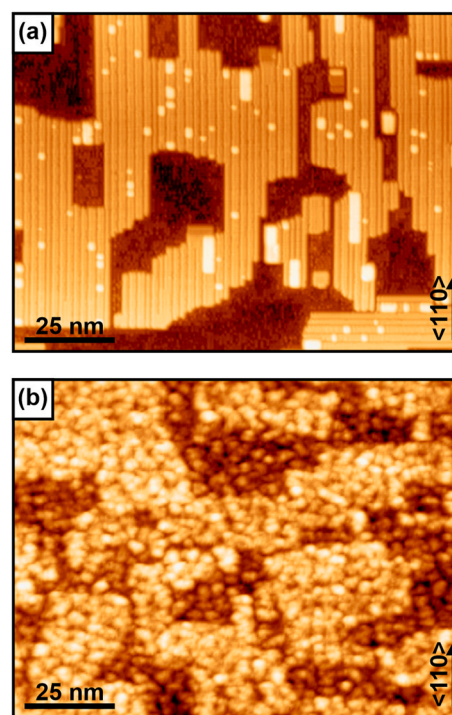


Fig. 74. STM images of terbium silicide nanowires on Si(001) (a) before and (b) after capping with 5 nm amorphous silicon at room temperature. Adapted from Ref. [487]. (For interpretation of the references to color in this figure legend, the reader is referred to the Web version of this article.)

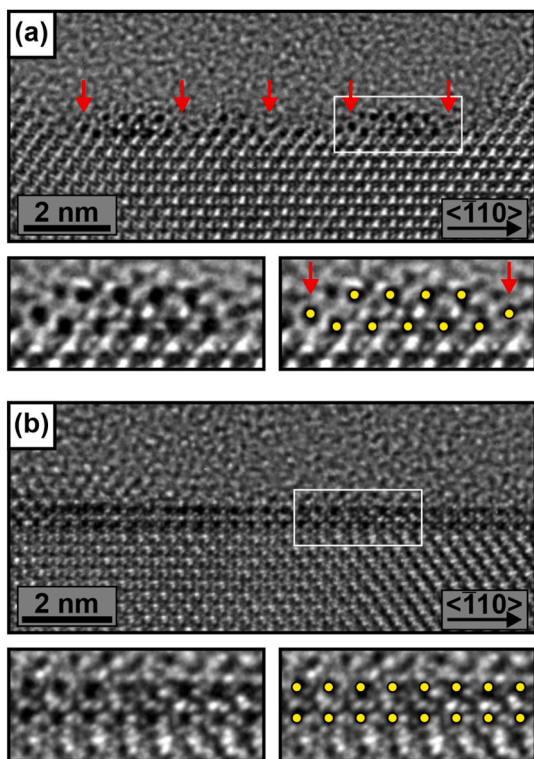


Fig. 75. HRTEM images of terbium silicide nanowires on Si(001) capped with 5 nm amorphous silicon at room temperature (a) in cross-sectional view, i. e. viewed along the nanowires, and (b) in side view. The regions defined by the white rectangles are magnified in the respective bottom images, where the terbium atoms are marked by yellow dots. From Ref. [487]. (For interpretation of the references to color in this figure legend, the reader is referred to the Web version of this article.)

protecting them against ambient conditions. This behavior is related to the fact that the nanowire interior consists of a stable bulk silicide – in contrast e. g. to the gold, indium, or silver induced atomic wires, which are rather very thin metal induced surface reconstructions and will probably show strong modifications or even complete destruction upon capping. Thus the rare earth silicide nanowires are also an interesting candidate for applications in devices. Moreover, the capped and in this way passivated nanowires can be studied by HRTEM, revealing their internal structure.

In Fig. 74, STM images of terbium silicide nanowire bundles on Si(001) are shown (a) directly after growth and (b) after subsequent capping with a 5 nm thick film of amorphous silicon, deposited at room temperature. After capping, the surface is characterized by a rough texture, indicating a lack of crystalline ordering of the capping layer. However, the appearance of the image in Fig. 74(b) already suggests that the nanowire bundles are still present underneath the capping layer, since mesa-like structures are observed, which have very similar shapes and extensions as compared with the nanowire bundles in Fig. 74(a).

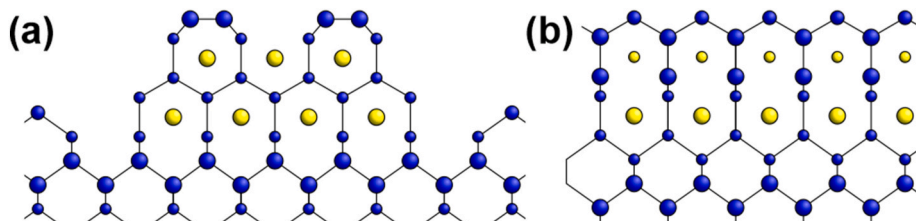


Fig. 76. Structure model of terbium silicide nanowires on Si(001) (a) in cross-sectional view and (b) in side view. Blue and yellow circles mark silicon and terbium atoms, respectively. From Ref. [487]. (For interpretation of the references to color in this figure legend, the reader is referred to the Web version of this article.)

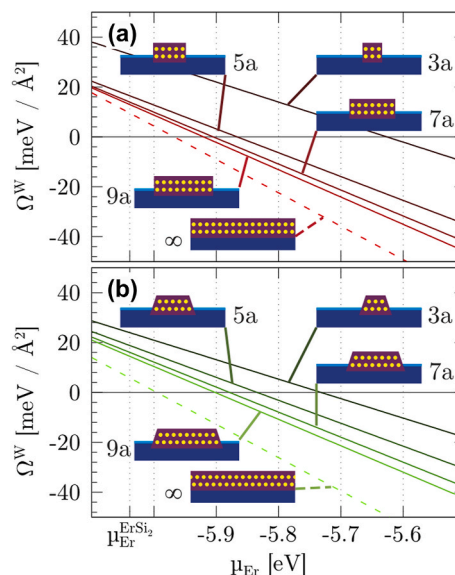


Fig. 77. Variation of the Landau potential for different erbium silicide nanowire structures on Si(001) with the hexagonal c -axis (a) perpendicular to the nanowires and (b) parallel to the nanowires. The nanowires are labeled by their width in units of the Si(001) lattice constant a . Adapted from Ref. [488].

This assumption is verified by the HRTEM images of the capped nanowires shown in Fig. 75. In Fig. 75(a), a cross-sectional view of a nanowire bundle is shown, while Fig. 75(b) shows a side view. It is obvious that the nanowires are still characterized by a crystalline structure. In the following, the atomic structure of the nanowires is studied in detail.

2.6.2.4. Atomic structure of the nanowires. With the acquisition of so-called defocus series and the respective HRTEM image simulations, it could be shown that the large black spots in the images are related to the terbium atoms within the nanowires on Si(001) [487,489]. The terbium atoms are marked by yellow dots in the magnified sections at the respective bottoms of the images. Thus it is obvious that the nanowires consist of two layers of terbium atoms, which is consistent with the heights of around 0.5 nm observed in the STM images. Also the bundle formation can be observed in the cross-sectional image [Fig. 75(a)], with the grooves indicated by the red arrows. Moreover, the terbium atoms show a zigzag pattern in the cross-sectional view [Fig. 75(a)], which is consistent with a hexagonal arrangement viewed in c -direction. In contrast, the side view [Fig. 75(b)] shows an on-top arrangement of the terbium atoms, as expected from a view on the hexagonal silicide structure in a -direction.

These results demonstrate that the nanowires indeed consist of the hexagonal disilicide with the c -axis along the substrate surface. Moreover, the silicide c -axis is oriented parallel to the nanowires. This orientation of the silicide thus deviates by 90° from the one proposed in the previous assumptions.

With this information, a structure model of the nanowires is

developed, as shown in Fig. 76. Their interior is characterized by a 1×1 periodicity, as derived from the LEED data (Fig. 73). The alternating formation of silicon dimers at the nanowire top surface leads to the 1×2 periodicity, as observed in the STM images [inset of Fig. 71(b)].

These results on the nanowire structure can be related to a different mechanism for nanowire formation than previously assumed. Since no indications for the silicon vacancy defects of the hexagonal Tb_3Si_5 bulk silicide could be found in both STM and HRTEM images, the nanowires are formed by a hexagonal silicide with a TbSi_2 stoichiometry. First of all, this results in different lattice constants as compared with Tb_3Si_5 because of the missing defects, so that anisotropic strain may not be the main formation mechanism. Instead, kinetic effects may play a role, since an intense lateral atomic diffusion is required during the thermally activated nanowire formation process. In order to resolve this issue, theoretical calculations were performed.

In a detailed theoretical investigation of a variety of possible erbium silicide nanowire structures [488], which are very similar to those formed with terbium, it could be demonstrated that the experimentally observed nanowires are metastable, while a 2D silicide film represents the energy minimum. This is shown in Fig. 77, where the variation of the Landau potential is displayed for different nanowire structures with (a) the previously assumed structure model and (b) the new model presented here. The solid lines represent the results for the different nanowire widths and the dashed lines the ones for the 2D films. From a comparison of Fig. 77(a) and (b) it is also revealed that the orientation of the c -axis – along or perpendicular to the nanowires – does not influence the formation energy significantly. These results indicate a considerable role of kinetic effects on the formation of the nanowires.

Finally it should be noted that also nanowires higher than two atomic layers were observed occasionally, in particular at higher rare earth coverages. The HRTEM data of such nanowires indicate that they consist of a tetragonal silicide [489]. However, for the majority of the nanowires, which are two atomic layers high, this does not play any role, since the hexagonal and tetragonal silicide structures consist of the same two layers high building blocks [489].

2.6.2.5. Electronic properties of the nanowires. Generally, a fascinating property of the nanowires on Si(001) is their electronic structure, which may be purely 1D in the ideal case. It is thus of particular interest, if the present rare earth silicide nanowires have metallic behavior and if they are electrically insulated from their surroundings, since this could be an important property in device applications.

For the analysis of the electronic properties of individual nanowires, STS experiments were performed [483], as shown in Fig. 78. A non-zero signal at zero voltage is observed in the spectra, corresponding to a finite density of states at the Fermi energy. This indicates that the nanowires are metallic.

For such a 1D system, a strongly anisotropic band structure is expected. A very versatile tool for a determination of the dispersion of the electronic states is ARPES, which, however, averages across a large

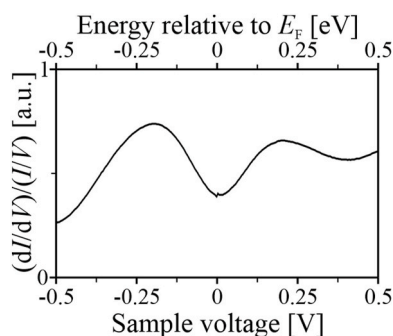


Fig. 78. STS spectrum of terbium silicide nanowire bundles on planar Si(001) taken at room temperature. From Ref. [483].

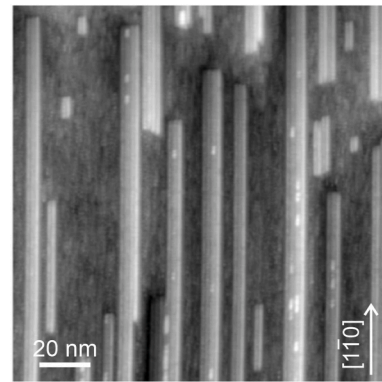


Fig. 79. STM image of unidirectional terbium silicide nanowires on a vicinal Si(001) surface. Adapted from Ref. [480].

surface area and thus does not allow an investigation of individual nanowires. Unfortunately, the present nanowires on the planar Si(001) surface form domains with nanowire orientations perpendicular to each other [see Fig. 71(b)]. In order to study the anisotropy of the band structure with ARPES, however, single domain samples are required.

Such a sample with a single nanowire direction may be prepared using vicinal Si(001) wafers with a misorientation of a few degrees, since here a double-step surface structure is formed, so that the substrate dangling bonds of neighboring terraces have the same orientation, resulting in a single domain sample. As an example, Fig. 79 shows nanowires grown on a vicinal Si(001) surface with 4° misorientation. These nanowires are indeed characterized by a single orientation across the entire sample. Moreover, their overall appearance is very similar to the one on the planar Si(001) surface, indicating a similar atomic structure, as indeed confirmed in HRTEM experiments [482,489].

ARPES results for such a nanowire sample are shown in Fig. 80(a) [483]. In nanowire direction (labeled k_{\parallel}), at least five dispersing bands are observed. Three of them (numbers 2, 4, and 5) cross the Fermi energy, and two further bands (numbers 1 and 3) at least reach the Fermi energy. These observations demonstrate the metallicity of the nanowires and therewith also confirm the STS results presented above. However, these bands are not always visible in the ARPES experiments, but appear and disappear at different values of the in-plane wave vector component perpendicular to the nanowires (labeled k_{\perp}), as revealed by the different plots in Fig. 80(a). This behavior may be related to photoemission matrix element effects.

The derived dispersion curves are shown schematically in Fig. 80(b). A closer inspection of Fig. 80(a) reveals that the dispersion curves do not only show an intensity variation with the perpendicular wave vector component k_{\perp} , but also slight energy variations. This behavior is also visible in the Fermi surface plot in Fig. 80(c), where undulations are observed instead of the straight lines expected for a purely 1D dispersion. This observation could indicate a small electronic cross-talk of neighboring nanowires, e. g. directly between the nanowires within a bundle or even by electronic tunneling through the band gap of the substrate. In this case, the nanowires would not be completely insulated from each other, and their electronic structure would not be purely 1D. On the other hand, the observed variations could also be due to the fact that such samples generally contain nanowires and bundles with different widths [see e. g. Fig. 79], which are expected to vary also in their electronic dispersion curves. These curves could contribute predominantly to the ARPES signal at certain emission angles due to photoemission matrix element effects, in this way also resulting in the impression of a k_{\perp} -dependent energy variation. This issue, however, could not be resolved based on the present ARPES results.

In theoretical band structure calculations, in contrast, it could be demonstrated that individual nanowires separated from each other by a few nm do not show noticeable electronic interactions at all [488]. Here,

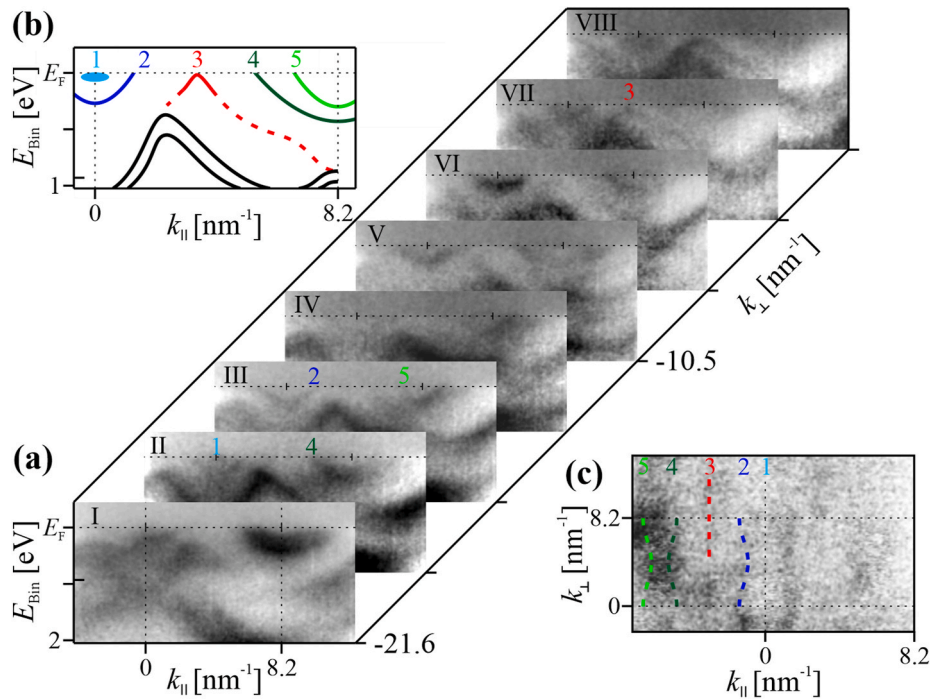


Fig. 80. ARPES results of terbium silicide nanowires on a vicinal Si(001) surface taken at $h\nu = 62$ eV, with (a) a series of dispersion plots for different k_{\perp} values, (b) a schematic plot of the derived dispersion curves close to the Fermi energy in nanowire direction, and (c) a Fermi surface plot showing a possible slight dispersion perpendicular to the nanowires. The zone boundary in k_{\parallel} direction lies at 8.2 nm^{-1} for the $1 \times$ periodicity. Adapted from Ref. [483].

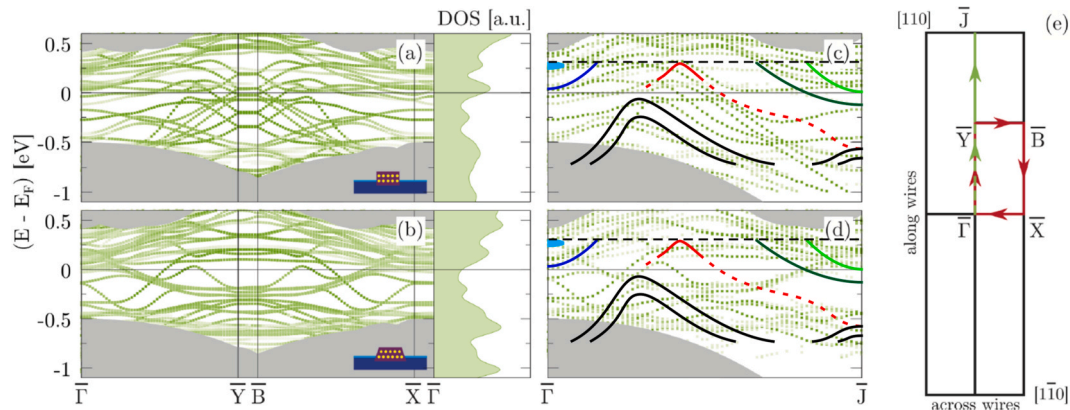


Fig. 81. (a,b) The calculated band structures of the erbium silicide nanowires on a Si(001) surface with the c -axis orientations (a) perpendicular and (b) along the nanowires. (c,d) The respective dispersion curves after unfolding to a $1 \times$ periodicity, and (e) the corresponding SBZ (slightly distorted). The projected silicon bulk band structure is marked by the gray areas. In (c) and (d), the experimentally determined dispersion curves are overlaid, energy shifted to account for a charge transfer from the wetting layer. Adapted from Refs. [483,488]. (For interpretation of the references to color in this figure legend, the reader is referred to the Web version of this article.)

erbium silicide nanowires were separated by a hydrogenated and thus non-metallic silicon surface, which mimics the electronic properties of the non-metallic wetting layer of up-to-now unknown structure and prevents an electronic coupling of neighboring nanowires. The results are shown in Fig. 81(a and b) for the two different orientations of the hexagonal silicide within the nanowires.

It is clearly observed that there is a multitude of bands, which show a strong dispersion in nanowire direction ($\Gamma - Y$ or $X - B$), and many of them are crossing the Fermi energy. In contrast, no significant dispersion can be observed in the direction perpendicular to the nanowires ($\Gamma - X$ or $Y - B$). This demonstrates that these nanowires are characterized by a purely 1D metallicity.

However, at the nanowire flanks, a dimerization of silicon atoms occurred, resulting in a $2 \times$ periodicity of the supercell used for the calculations. In order to derive the pure dispersion of the nanowires with their $1 \times$ periodicity, the calculated band structures were unfolded, as shown in Fig. 81(c and d), so that the SBZ doubles in nanowire direction [see Fig. 81(e)].

Moreover, for a comparison with the experimental data, the Fermi energy had to be shifted slightly to higher energies in order to take into account a charge transfer to the nanowires from the surrounding wetting layer, which could not be considered in the calculations, where a hydrogen terminated silicon surface in between the nanowires was used instead. With this correction, the scheme of the experimentally observed dispersion curves close to the Fermi energy [Fig. 80(b)] is overlaid on the calculated curves, as shown in Fig. 81(c and d). A rather good

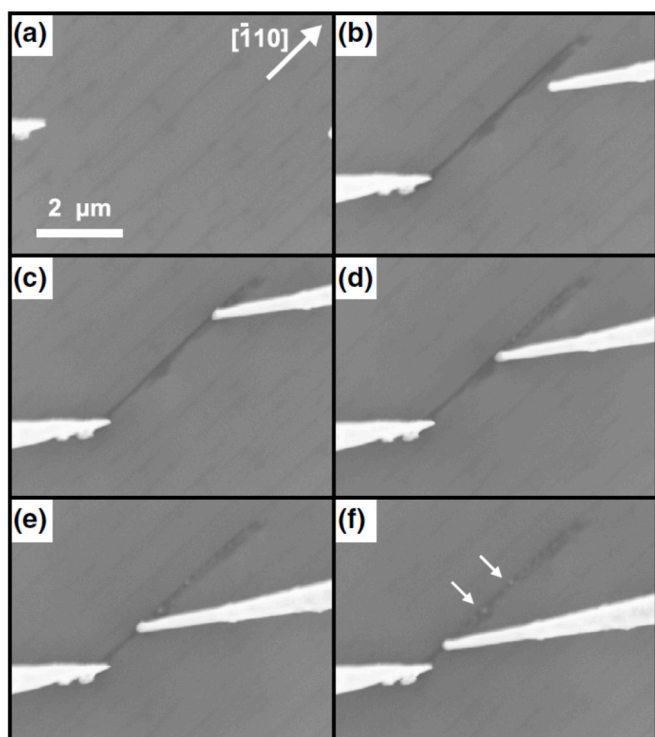


Fig. 82. SEM image sequence of the contacting of a terbium silicide nanowire on Si(001) by two tips and measuring the length dependence of the resistance. From Ref. [481].

agreement is observed in both cases despite the multitude of theoretical curves, when considering that not all theoretically calculated bands are visible in ARPES experiments due to photoemission matrix element effects and that the ARPES signal is further superposed by emissions from the surrounding wetting layer. Thus a decision on the *c*-axis orientation of the silicide in the nanowires is not appropriate on the basis of the comparison in Fig. 81(c and d) alone, while the HRTEM data (Fig. 75) clearly demonstrate that the *c*-axis is aligned along the nanowires.

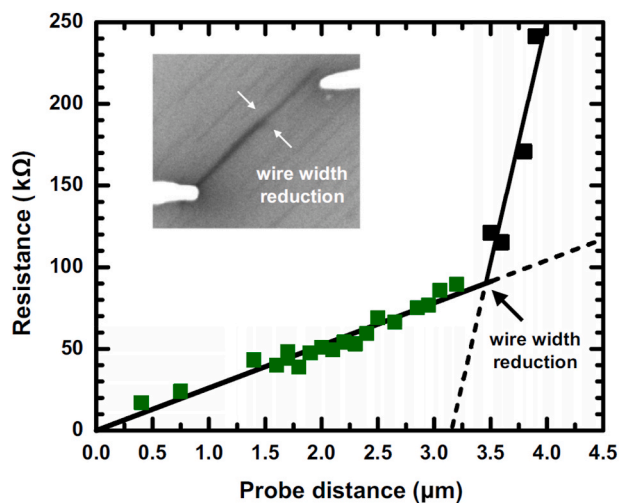


Fig. 83. Resistance variation with probed length of a terbium silicide nanowire on Si(001). The slope increases at a reduction of the nanowire width, as shown in the SEM image in the inset. From Ref. [481].

2.6.2.6. Electron transport properties of the nanowires. An important possible application of these metallic nanowires on Si(001) could be the use as nanoscale electrical connectors within silicon-based devices. In order to investigate the electrical conductivity of the nanowires in detail, multi-tip STM experiments were performed for terbium silicide nanowires with different widths and heights [481].

In Fig. 82, the procedure of this experiment is shown. The movement of the two tips used here is controlled by a scanning electron microscope (SEM). While the nanowire is initially almost invisible [Fig. 82(a)], the contact with the first tip (bottom left in the images) leads to a pronounced SEM contrast because of its biasing [Fig. 82(b)]. Then the second tip can be contacted in order to measure the resistance [Fig. 82(c)]. In this case, linear current-voltage characteristics were observed (not shown here), indicating an ohmic behavior and thus also an electrical conductivity of the metallic nanowire. In contrast, when contacting the substrate with the second tip, a diode-like characteristics was observed, demonstrating that the nanowires are electrically well insulated from the substrate by Schottky barriers.

However, such mechanic contacts lead to small defects at the nanowires, as indicated by the arrows in Fig. 82(f). Thus the length dependence of the resistance was measured by successively approaching the second tip towards the first one, as shown in Fig. 82(c–f), so that the formerly produced defects do not play any role. It turned out that the contact resistances from the tips to the investigated nanowire are so small that they can be neglected, justifying the use of the two-point resistance measurements instead of a four point setup.

In Fig. 83, the length dependence is shown for a specific nanowire. The curve consists of two straight sections with different slopes, amounting to 26 kΩ/μm and 300 kΩ/μm, indicating that the property of the nanowire changes at a certain position. Indeed, the SEM image shows a variation of the nanowire width at the position where the slope changes – for thinner nanowires the length variation of their resistance is larger, as expected.

Thus it is found [481] that the nanowire bundles are insulated from each other as well as from the substrate, and that they show a linear current-voltage characteristics as well as a linear variation of the resistance with the probed nanowire length. Moreover, the resistance decreases with the cross-sectional area of the nanowires. However, the derived resistivity of the narrow and sub-nanometer high nanowires was found to be as high as $11 \times 10^{-6} \Omega m$, being much larger than the bulk resistivity of Tb_3Si_5 of $0.9 \times 10^{-6} \Omega m$, while the resistivities of the thicker and broader nanowire bundles approach the bulk value. This effect was attributed to carrier scattering by defects at the nanowire surfaces, which are e. g. visible in Fig. 71(b), 74(a) and 79 as additional material assemblies on top of the nanowires. These defects contribute more to carrier scattering at lower nanowire heights, leading to the observed higher resistivities. A similar scattering effect of nanowire boundaries on their resistivity was e. g. also assumed for $CoSi_2$ nanowires [509].

2.6.2.7. Optical anisotropy. RAS is a well-established tool for studying the surface induced optical anisotropy. In the case of anisotropic thin films on isotropic bulk substrates or simply its anisotropic surface reconstructions, the optical anisotropy is uniquely linked to the anisotropic layers, irrespective of the much larger penetration depth of light, making this optical technique very surface sensitive [510].

Vicinal Si(001) surfaces represent a prominent example of such substrates, where RAS has been extensively applied to study surface structures and adsorbate induced modifications. The combination of experiment with optical simulations and ab-initio calculations can be used to relate the spectral fingerprint with microscopic structure information [511,512]. In the case of low-D metallic structures, a Drude-like optical anisotropy term can also contribute due to the anisotropic conductivity [513].

The interface of terbium and dysprosium silicides with Si(001)

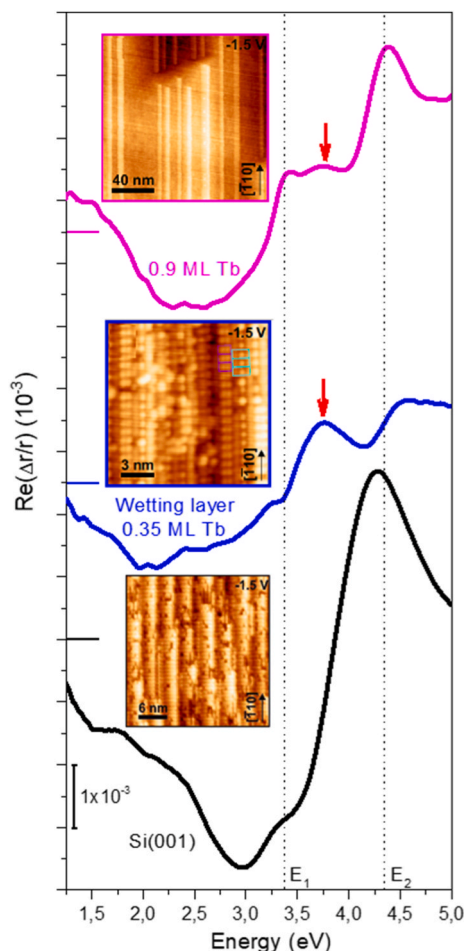


Fig. 84. RAS spectra and corresponding STM images of the clean vicinal Si(001) surface as well as of the terbium induced wetting layer and the nanowires. The interband critical energies of the silicon bulk band structure are indicated by E_1 and E_2 . The red arrows mark the Tb–Si bond related feature. Adapted from Ref. [485]. (For interpretation of the references to color in this figure legend, the reader is referred to the Web version of this article.)

satisfies the condition of structural anisotropy and thus yields characteristic spectroscopic fingerprints in the optical anisotropy. This has been shown in a study of these two nanowire systems on vicinal Si(001) using RAS for optical analysis in combination with structure determination by STM [485].

Fig. 84 shows a set of RAS spectra of clean vicinal Si(001), the 2×7 wetting layer, and the nanowires, obtained with increasing amounts of terbium. The STM images shown were recorded *in-situ* for each coverage to reveal the respective surface morphology. Characteristic for the set of spectra are (I) the bulk features of silicon (E_1 and E_2 band gaps at $h\nu = 3.4$ eV and 4.4 eV, respectively), induced by anisotropic strain imposed by the surface structure onto the bulk silicon, (II) surface electronic transitions ($h\nu = 2.0 - 3.3$ eV) related to surface states at the step edges and to silicon dimers on the clean surface, and (III) a Tb–Si bond related feature at $h\nu = 3.8$ eV (marked by red arrows).

Based on these spectral features, the evolution from the clean surface over the wetting layer to the subsequent formation of the nanowires is traced. In the first step, i. e. the formation of the wetting layer, silicon bulk and surface related features are quenched due to the reaction of terbium with silicon, which breaks the dimer bonds. Thus the surface strain is lifted and the silicon dimer related features are replaced by Si–Tb related features from the building blocks of the 2×7 reconstructed wetting layer. The formation of the anisotropic terbium silicide

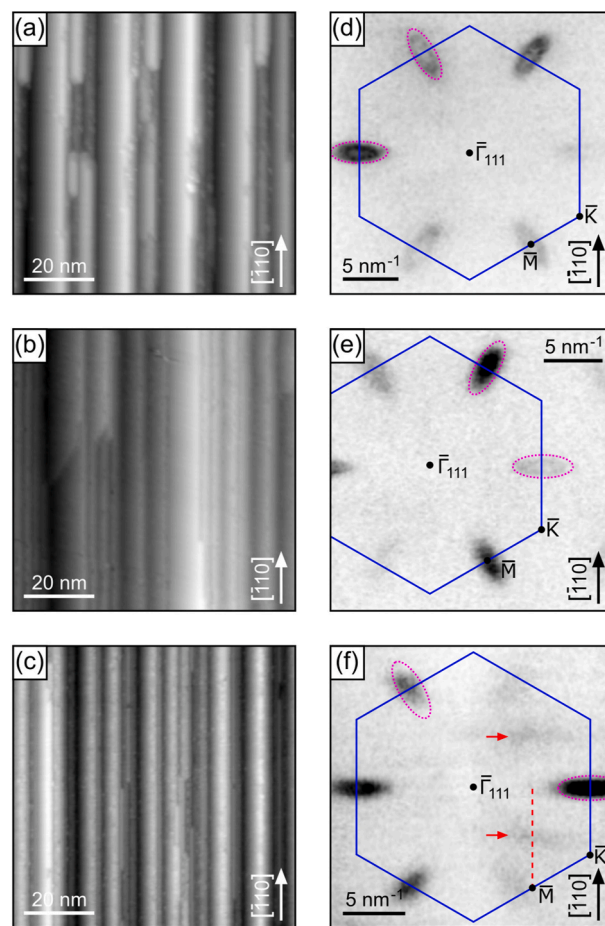


Fig. 85. (a–c) STM images and (d–f) corresponding Fermi surfaces derived by ARPES at $h\nu = 100$ eV of terbium silicide nanowires on vicinal Si(*h**h**k*) surfaces. (a,d) Si(557) with higher terbium coverage, (b,e) Si(557) with lower terbium coverage, and (c,f) Si(335) with lower terbium coverage. The hexagonal Brillouin zone of the 2D TbSi₂ monolayer on Si(111) is marked blue. Adapted from Ref. [499]. (For interpretation of the references to color in this figure legend, the reader is referred to the Web version of this article.)

nanowires upon further deposition restores the strain, due to the lattice misfit of the terbium silicide with the silicon bulk, and exposes small areas of silicon dimer terminated patches in between the nanowires. Thus, the total optical anisotropy is a superposition of the silicon bulk, silicon surface, and Tb–Si related features.

In the case of dysprosium on Si(001) a very similar behavior was observed, which indicates the rather universal interface formation of the rare earth silicides on Si(001) [485]. The optical features related to the re-appearance of strain as well as to the bonds between rare earth and silicon atoms are characteristic for the growth mode and allow both a structure analysis and an optical *in-situ* control of the sample preparation or of the growth processes. Moreover, for terbium as well as dysprosium silicide nanowires a Drude-like increase of the baseline of the RAS spectra towards lower frequencies is observed, which is characteristic for the anisotropic metallic conductivity of the nanowires.

2.6.3. Rare earth silicide nanowires on Si(*h**h**k*) surfaces

Up to now, the rare earth silicide nanowires on the Si(001) surface were discussed, which are probably formed by kinetic effects during growth, while anisotropic strain may also play a role. A different strategy to obtain nanowires is the use of vicinal surfaces. As seen in Fig. 70, an almost strain-free hexagonal silicide monolayer forms on the Si(111) surface, which has metallic properties. When using certain vicinal Si

(111) surfaces instead, which are usually labeled Si(*h**h**k*), the formation of narrow stripes of the monolayer silicide may be expected on the narrow (111)-oriented terraces, with widths tunable by the misalignment angle of the substrate.

Such a behavior is indeed observed for $h < k$, as shown in Fig. 85(a–c) for the case of terbium [491,492,498,499]. For the Si(557) surface, which is characterized by a misalignment angle of 9.5° relative to the Si(111) surface, silicide nanowires are observed, and their widths of a few nm may be adjusted by the amount of deposited terbium [Fig. 85(a and b)]. When using Si(335) surfaces with a higher misalignment angle of 14.4° , even narrower nanowires may be obtained [Fig. 85(c)]. And the surfaces of the nanowires are oriented in the [111] direction, as expected for a growth of TbSi₂ monolayer stripes on the (111) terraces [498,499].

2.6.3.1. Electronic properties. The corresponding electronic properties of the nanowires on Si(*h**h**k*) are shown in Fig. 85(d–f) [499]. On a first glance, the Fermi surfaces appear similar as the one of the silicide monolayer on Si(111) [Fig. 70(b)], supporting the above assumption of a similar structure. However, the shape of the elliptical electron pockets has changed, in particular for the case of the narrowest nanowires on the Si(335) surface [Fig. 85(f)]. Here, the two horizontal ellipses appear extended in the horizontal direction, i. e. perpendicular to the nanowires. This visual result is supported by the comparison with the overlaid pink ellipse, which was derived from the respective horizontal ellipses of the 2D TbSi₂ monolayer on the (111) surface [Fig. 70(b)]. And also the other four inclined ellipses are widened in the same horizontal direction, as illustrated by the comparison with the inclined pink ellipse from the TbSi₂ monolayer on Si(111).

Moreover, additional linear structures are observed in Fig. 85(f)–as marked by the red arrows. Such linear structures indicate a missing or negligible dispersion perpendicular to the nanowires and therewith a purely 1D behavior.

In a first approach, the shape changes of the ellipses can be explained on the basis of Heisenberg’s uncertainty principle: During the ARPES experiment, the electron emission from a narrow nanowire occurs from a spatially confined region, so that diffraction effects occur, similar to the case of an optical single slit. From the typical width of the nanowires on the Si(335) surface of 2.5 nm, as revealed by STM [Fig. 85(c)], the main maximum of the single-slit pattern has a full width at half maximum of about 2.2 nm^{-1} , in nice agreement with the broadening and extension of the ellipses observed in Fig. 85(f).

In detailed theoretical calculations, the atomic structure and in particular the electronic properties of these nanowires were investigated for the case of the Si(557) surface [499]. In order to separate the

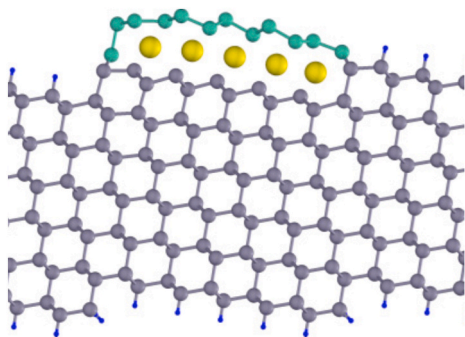


Fig. 86. Calculated structure of about 2 nm wide terbium silicide nanowires on (111) terraces of the Si(557) surface, which alternate with hydrogenated (111) terraces. Yellow circles mark the terbium atoms. From Ref. [499]. (For interpretation of the references to color in this figure legend, the reader is referred to the Web version of this article.)

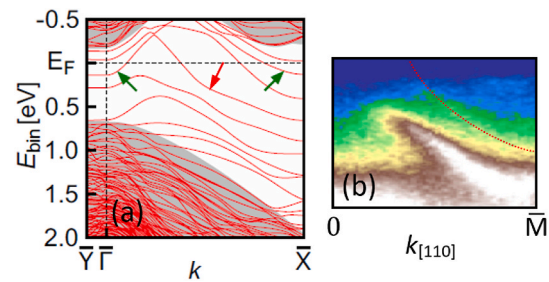


Fig. 87. (a) Calculated dispersion curves of the terbium silicide nanowires on Si(557) and (b) corresponding slice of the ARPES data along the nanowires. Adapted from Ref. [499].

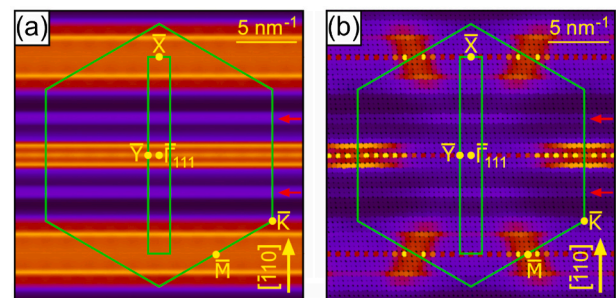


Fig. 88. (a) Calculated Fermi surface of the terbium silicide nanowires on Si(557) and (b) after unfolding onto the SBZ of the TbSi₂ film. The narrow SBZ of the nanowires and the hexagonal one of the 2D silicide film are marked green. From Ref. [499]. (For interpretation of the references to color in this figure legend, the reader is referred to the Web version of this article.)

nanowires electronically, an about 2 nm wide terbium silicide monolayer stripe was assumed only on every second Si(111) terrace, while the terraces in between were hydrogenated, removing the silicon surface states from the band gap. The resulting structure is shown in Fig. 86. It is formed by a stripe of a TbSi₂ monolayer with terbium atoms underneath a buckled silicon bilayer, as also expected from the Si(111) case [Fig. 70(c) and d)]. On its right side the stripe ends at a substrate surface step, and on its left side the last row of terbium atoms is caged by additional silicon atoms.

The calculated electronic dispersion is shown in Fig. 87(a). Here, the X point corresponds to the Brillouin zone boundary in the direction of the nanowires (with the same wave vector component as the M point),

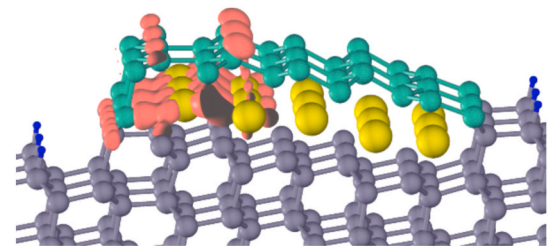


Fig. 89. The spatial localization of the electronic states from the linear structure in the Fermi surfaces of the terbium silicide nanowires on Si(557) [red arrows in Figs. 85(f) and Fig. 88]. From Ref. [499]. (For interpretation of the references to color in this figure legend, the reader is referred to the Web version of this article.)

while the Y point corresponds to the one in the perpendicular direction (see also Fig. 88). For comparison, a slice of the ARPES data along the nanowire direction up to the M point is shown in Fig. 87(b)—as indicated by the dashed red line in Fig. 85(f), where the linear structure is most pronounced. A purely 1D behavior is found in the calculated dispersion in Fig. 87(a), without any dispersion within the silicon bulk band gap perpendicular to the nanowires, i. e. in $\Gamma - Y$ direction. Along the nanowires ($\Gamma - X$ direction), in contrast, a strong dispersion of the bands is observed. In particular the band sections marked by the green arrows correspond to the ellipses in the Fermi surface data from the ARPES experiments [Fig. 85(f)]. Also the band marked by a red arrow in Fig. 87(a) is well represented by the ARPES data in Fig. 87(b), where the corresponding band, slightly scaled in energy, is marked by a dotted red line.

Now the question is discussed why a rather 2D Fermi surface is observed in ARPES, while the calculated electronic band structure is purely 1D. In Fig. 88(a), the calculated Fermi surface is shown, which is indeed purely 1D, as expected from the calculated dispersion curves. However, in an ARPES experiment, the photoemission intensity is strongly influenced by the shapes of the wave functions in real space, which couple to the ones of the measured photoelectrons via the photoemission matrix element. In this way, mostly photoelectrons with the same parallel wave vector component are emitted, as has been demonstrated e. g. for the case of organic molecules on surfaces [514, 515]. In order to take these effects into account, the calculated Fermi surface was unfolded from the narrower Brillouin zone of the nanowire supercell to the hexagonal one of a TbSi_2 film, as shown in Fig. 88(b). In this way, a nice agreement is found between the calculated and the experimental Fermi surfaces [compare Fig. 88(b) with Fig. 85(f)]: The experimentally observed broadening of the ellipses is well reproduced by the calculations, and also the linear structures can be found, as indicated by the red arrows in Fig. 88.

Finally the origin of these linear structures will be determined, which are predominantly found in the most narrow nanowires [Fig. 85(f)]. For this purpose, the isosurface of the probability density of the

corresponding band at the Fermi energy (red arrows in Fig. 88) is displayed in Fig. 89 by the red areas. This wave function is mainly localized at the left edge of the nanowires and can thus be related to 1D edge states. It is now obvious why these edge states are most pronounced in the ARPES data of the narrowest nanowires, since they have the largest relative weight in this case.

2.6.3.2. Thicker nanowires. When the rare earth silicides are formed on $\text{Si}(h\bar{h}k)$ surfaces for higher rare earth coverages of several monolayers, the formation of similar nanowires as already discussed was observed on the $\text{Si}(111)$ terraces by STM [491,492]. The ARPES data, however, indicate that these metallic nanowires consist of the defective RE_3Si_5 multilayer silicide with a $\sqrt{3} \times \sqrt{3}$ periodicity [491,492]. In this way, even higher rare earth silicide nanowires can be produced on $\text{Si}(h\bar{h}k)$ surfaces.

2.6.4. Rare earth induced subsurface stripes on $\text{Si}(111)$

A rare earth induced formation of 1D structures is even possible when using the rather isotropic planar $\text{Si}(111)$ surface as a substrate. For multilayer rare earth coverages, the formation of a structure with a $2\sqrt{3} \times \sqrt{3}$ periodicity was found in combined LEED and STM experiments for dysprosium and terbium induced reconstructions [496]. Here, LEED showed a $2\sqrt{3} \times \sqrt{3}$ reconstructed surface with three rotational domains and $\left(\frac{m-n}{6}, \frac{m+2n}{6}\right)$ diffraction spots, as shown in Fig. 90(a). In addition, the formation of belt-like striped domains was proved by the splitting of certain superstructure spots, as revealed by the line scan through the $\left(\frac{1}{2}, \frac{1}{2}\right)$ diffraction spot (where $m = 3$ and $n = 0$), as shown in Fig. 90(b). Surprisingly, STM studies showed contradictory results on first sight. Here, the surface layer showed a $\sqrt{3} \times \sqrt{3}$ reconstruction [Fig. 90(c)]. However, two different coexisting $\sqrt{3} \times \sqrt{3}$ structures with a hexagonal and a triangular arrangement of surface atoms were observed, as shown in Fig. 90(d) and (e), respectively.

This apparent contradiction of LEED and STM studies was solved by DFT studies. From former studies on the $\sqrt{3} \times \sqrt{3}$ reconstructed rare

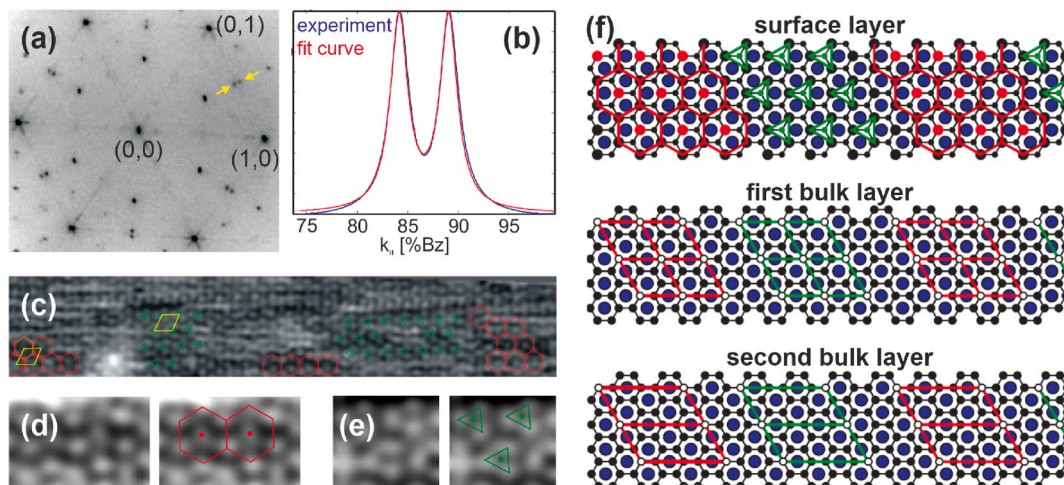


Fig. 90. (a) LEED pattern from the dysprosium induced $2\sqrt{3} \times \sqrt{3}$ reconstruction on $\text{Si}(111)$ taken at $E_{\text{kin}} = 95$ eV. Arrows mark a split $\left(\frac{1}{2}, \frac{1}{2}\right)$ diffraction spot, and (b) shows a line scan through this spot. (c) STM image of the related terbium induced structure showing a $\sqrt{3} \times \sqrt{3}$ reconstruction with domains of coexisting hexagonal (red hexagons) and triangular (green triangles) arrangements of surface silicon atoms. (d) Close up of the hexagonal arrangement of surface silicon atoms and (e) of the triangular arrangement. (f) Model of the complete structure consisting of a surface silicon bilayer with 1×1 periodicity, a first subsurface layer with a $\sqrt{3} \times \sqrt{3}$ reconstruction, and a $2\sqrt{3} \times \sqrt{3}$ reconstructed second subsurface silicon layer. The white dots mark silicon vacancies and the red dots those surface silicon atoms above silicon vacancies in the first subsurface layer. Adapted from Refs. [496,497]. (For interpretation of the references to color in this figure legend, the reader is referred to the Web version of this article.)

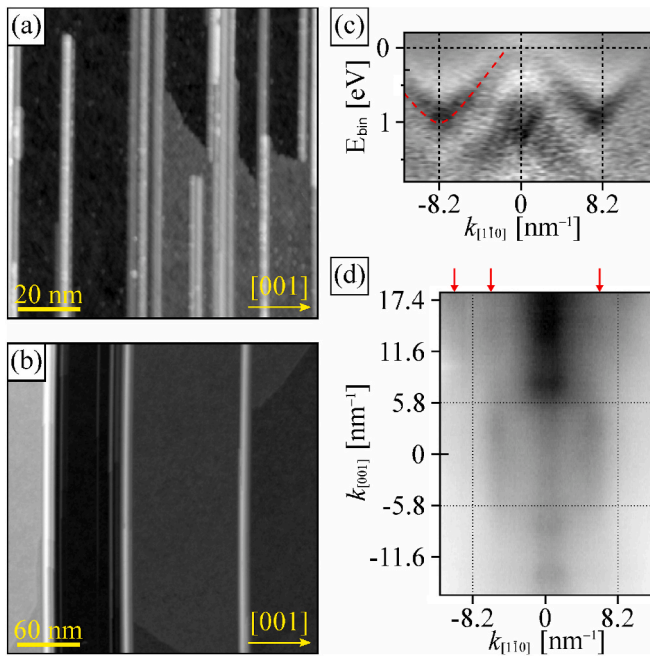


Fig. 91. (a,b) STM images of terbium silicide nanowires on Si(110). (c,d) ARPES data taken at $h\nu = 102$ eV with (c) a dispersion plot along the nanowires (the second derivative is shown to highlight faint structures) and (d) a constant energy surface at a binding energy of 0.7 eV. Adapted from Ref. [500].

earth silicide multilayer films it is well-known that its reconstruction is due to silicon vacancies of the planar subsurface silicon layers, while the surface still consists of a buckled bilayer of silicon atoms [506,507]. The apparent geometry of a triangular or a hexagonal arrangement of silicon atoms can be attributed to silicon vacancies formed underneath either the upper or the lower silicon atoms of the surface bilayer.

The DFT results, taking into account the first and second subsurface silicon layers, clarified that the first silicon subsurface layer indeed has the well-known $\sqrt{3} \times \sqrt{3}$ structure, while the second subsurface silicon layer has a $2\sqrt{3} \times \sqrt{3}$ structure, as shown in Fig. 90(f). In addition, DFT showed the existence of two energetically almost degenerated structures with different arrangements of the silicon vacancies with respect to the buckled silicon surface layer. This explains the coexistence of two different $\sqrt{3} \times \sqrt{3}$ appearances of the surface as observed by STM. Furthermore, the discrepancy between the STM and LEED results can be attributed to the much higher surface sensitivity of STM: Indeed, DFT-based calculated STM images performed for this model with a $\sqrt{3} \times \sqrt{3}$ top layer structure and a $2\sqrt{3} \times \sqrt{3}$ bottom layer structure showed no $2\sqrt{3} \times \sqrt{3}$ signatures. In contrast to STM, LEED can detect also this lower $2\sqrt{3} \times \sqrt{3}$ structure due to its much higher depth sensitivity of a few monolayers.

In addition, the splitting of the superstructure diffraction spots of odd order was analyzed quantitatively [496,497]. In this way, the width of the belt-like striped domains could be determined to ≈ 8 nm, and the structure of the anti-phase domain boundaries between neighboring stripe domains could also be determined in detail.

2.6.5. Rare earth induced atomic chains on Si(111)

1D structures were also found for submonolayer rare earth coverages on Si(111). These structures are characterized by a 5×2 periodicity, and their atomic structure could be determined to be a combination of honeycomb and Seiwatz chains of silicon atoms, with the atomic rare earth chains located in between these silicon chains [495,507]. Furthermore, this 5×2 structure was found to be semiconducting [507].

Thus this chain structure rather represents an atomically thin rare earth induced reconstruction of the silicon surface, similar as the gold, indium, and silver induced nanowire structures presented in previous sections.

2.6.6. Rare earth silicide nanowires on Si(110)

Finally it should be noted that a formation of rare earth silicide nanowires can also occur on Si(110) substrates [490,493,494,500]. STM images of such nanowires prepared with terbium are presented in Fig. 91 (a and b) [500]. They can show extremely high aspect ratios with lengths exceeding 500 nm and widths around 5 nm. Presumably they consist of hexagonal TbSi₂ or Tb₃Si₅ because of the above-mentioned silicon surplus, and thus it is assumed that they grow endotaxially into the surface forming inclined interfaces parallel to the Si{111} planes of the substrate [500]. Because of the twofold symmetry of the Si(110) surface, the nanowires only grow in one direction, which in this case is the $[110]$ direction. Such a unidirectional growth on a planar surface is remarkable, since it can even lead to rather homogeneous grating-like nanowire assemblies across the entire substrate [493].

These nanowires are also characterized by a quasi-1D electronic band structure [500], as revealed from the ARPES data shown in Fig. 91 (c and d). In the dispersion plot along the nanowires [Fig. 91(c)], an electron-like band is clearly visible, which crosses the Fermi energy (marked by the red dashed line). And the corresponding constant energy surfaces clearly reveal the 1D character of the electronic dispersion by straight contours in the [001] direction, i. e. perpendicular to the nanowires, as shown exemplarily in Fig. 91(d) and marked by the red arrows.

2.6.6.1. Conclusions. In this section, the structural and electronic properties of rare earth silicide nanowires, formed by self-assembly on differently oriented silicon surfaces, were presented. It turned out that the nanowires are structurally very close to bulk silicides. They are formed due to specifics in growth kinetics in combination with the unilateral stress in the silicide as well as in the substrate, and they are characterized by 1D physical properties. In particular, the nanowires are metallic with a mostly or even purely 1D electronic dispersion. It was further shown for the nanowires grown on Si(001) that they can be passivated against the ambient by capping with amorphous silicon, and also electric transport along these nanowires could be demonstrated.

3. Dynamics of phase transitions after electronic excitation of quasi-1D systems⁷

3.1. The Peierls system Si(111)-In (8×2) \leftrightarrow (4×1)

Due to its unique and peculiar properties the indium atomic wire system is ideally suited for the study of structural and electronic dynamics. This surface system exhibits an inherent Peierls instability manifesting itself in a 1st order phase transition between an insulating (8×2) ground state and a metallic (4×1) high temperature state. This structural transition can non-thermally be driven through an optical excitation and subsequently is trapped for nanoseconds in a supercooled metastable state.

The indium atomic wire system is prepared by self-assembly under ultra high vacuum conditions [46,340,343,516–519]. In situ deposition of a monolayer (1 ML is equivalent to 7.83×10^{14} cm⁻²) of indium atoms on Si(111) substrates at a sample temperature of 700–750 K creates the (4×1) In/Si(111) reconstruction. Removal of accumulated adsorbates originating from residual gas was possible through short flash annealing to 700–750 K providing a freshly prepared indium atomic wire system [48,50,240,244].

⁷ Authors mainly responsible for this section: M. Horn-von Hoegen, W.G. Schmidt, S. Wippermann

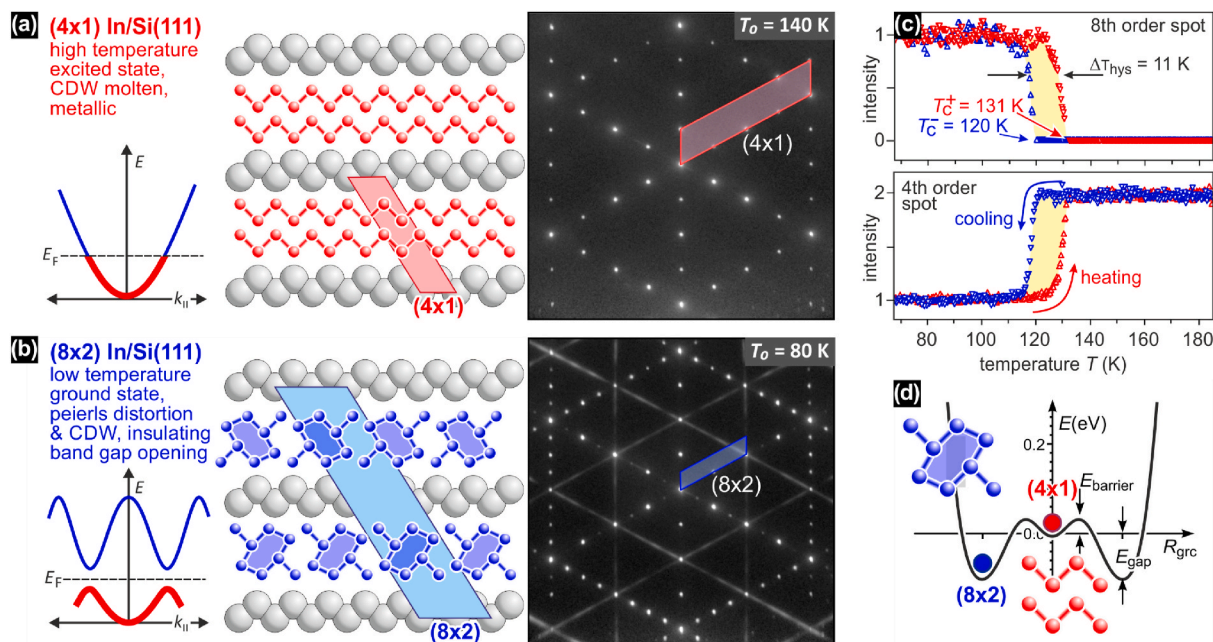


Fig. 92. (a) The metallic high temperature (4×1) state is composed of In atoms arranged in double zig-zag chains. The LEED pattern depicts the (4×1) reconstruction in three rotational domains. (b) The insulating (8×2) ground state exhibits a Peierls distortion with the formation of a CDW and opening of a band gap. The In atoms are rearranged in distorted hexagons. The (8×2) LEED pattern clearly shows the periodicity doubling along and perpendicular to the wires. The 8th order spots and second order streaks are indicative for the ground state structure. (c) RHEED intensity of the (8×2) spots (upper panel) and the (4×1) spots (lower panel) as function of temperature. Upon heating the intensity of the (8×2) spots drops to the background at T_c . Cooling with the same rate leads to the transition back to the (8×2) reconstruction. The intensity of the (4×1) spots rises upon heating at T_c , reflecting the change of atom positions in the unit cell. Temperature cycling exhibits a hysteresis of 11 K. (d) Potential energy surface obtained through DFT calculations as function of a generalized reaction coordinate R_{grc} describing the transition between (4×1) and (8×2) phases. The blue and red dots indicate the (8×2) ground state and the metastable (4×1) state, respectively. (For interpretation of the references to color in this figure legend, the reader is referred to the Web version of this article.)

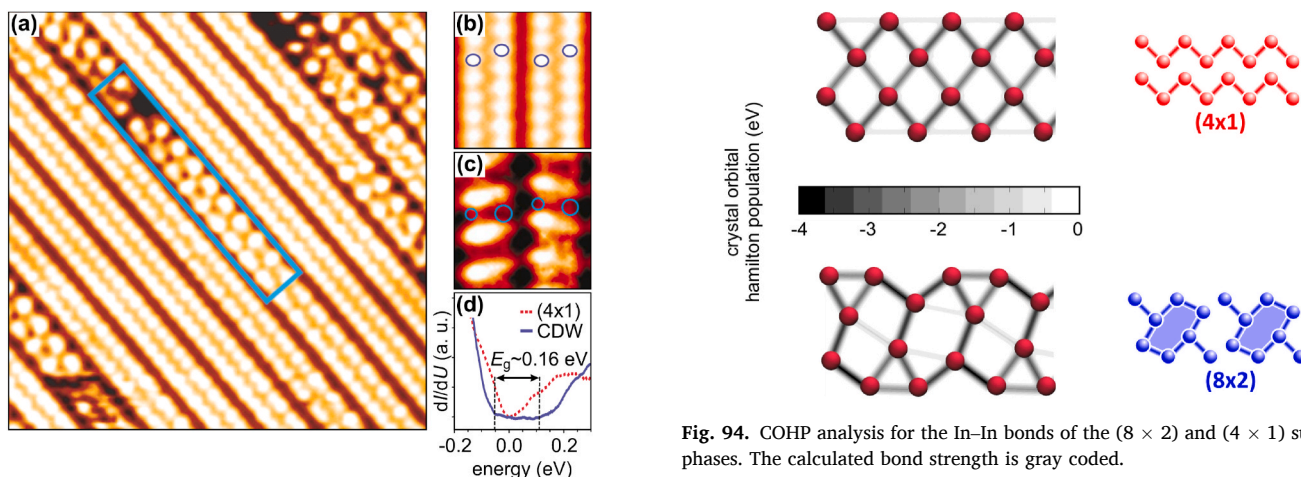


Fig. 93. (a) STM micrograph under constant current conditions taken at 100 K. Both (8×2) and (4×1) reconstructed indium wires can be seen. (b) The metallic (4×1) wires are composed of In atoms arranged in two parallel zig-zag chains. (c) Instead, in the insulating (8×2) wires the chains are broken up and distorted hexagons of In atoms form. (d) STS spectra for the (8×2) and (4×1) reconstructed wires. While the (4×1) exhibit metallic behavior (dashed red line), the (8×2) clearly shows opening of a bandgap of $E_{gap} = 0.16$ eV (solid blue line). Data courtesy of H.W. Yeom and with permission from Ref. [343]. (For interpretation of the references to color in this figure legend, the reader is referred to the Web version of this article.)

The metallic high temperature phase of this atomic wire system is composed of two parallel zig-zag chains of indium atoms with a (4×1) unit cell [276,516] as is sketched in Fig. 92(a). The corresponding LEED pattern is shown in the right panel of Fig. 92(a) with its 3-fold symmetry

Fig. 94. COHP analysis for the In-In bonds of the (8×2) and (4×1) surface phases. The calculated bond strength is gray coded.

arising from three rotational domains at the hexagonal (111) surface.

As already mentioned in section 2.3, the system undergoes a temperature driven reversible transition from the metallic high temperature state to the insulating ground state [340–342] at $T_c = 130$ K [50,343,344], which is accompanied by the formation of a charge density wave (CDW) with the corresponding opening of a band gap of $E_{gap} = 0.2$ eV [48,244,343]. In the ground state the zig-zag chains of indium atoms are broken and they rearrange into distorted hexagons [276,516], as sketched in Fig. 92(b). Upon this phase transition the maximum change of geometric position of the In atoms in the surface unit cell is less than 0.1 Å only [49]. This Peierls-like transition is characterized by symmetry breaking in both directions, which is facilitated through soft shear and rotational phonon modes with frequencies of $\nu_{shear} = 0.54$ THz and

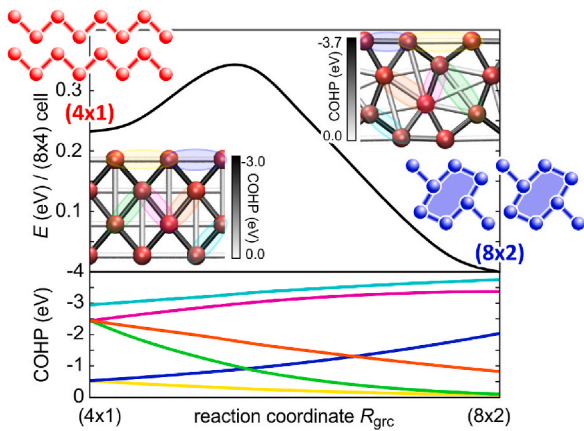


Fig. 95. COHP bonding analysis between nearest neighbors for the two geometries. The darker a bond is drawn, the stronger it is. The black curve depicts the potential energy surface which exhibits two minima belonging to the (8×2) phase and the (4×1) phase. The lower graph shows the bond strength evolution for selected bonds during the phase transition.

$\nu_{\text{rot}} = 0.81$ THz, respectively [52,276,520–522]. The surface periodicity doubles along and normal to the wires and the size of the unit cell increases to (8×2) . This change becomes obvious in the LEED pattern in the right panel of Fig. 92(b) through the appearance of additional spots at 8th order positions between the 4th order spots. The appearance of second order streaks emerge from the broken correlation of the 2-fold periodicity in neighbored wires. The anisotropic nature of the indium atomic wire system becomes immediately apparent in STM. Fig. 93(a) displays a filled-state STM image from Ref. [343] from the indium wire

surface at $T = 135$ K, i.e., at T_c . Extended and parallel wires both with (8×2) and (4×1) reconstruction are present. Employing STS both at the (8×2) and (4×1) structure - as shown in Fig. 93(b) and (c) - reveals the opening of a bandgap of $E_{\text{gap}} = 0.16$ eV for the low temperature (8×2) structure - see Fig. 93(d) - which is indicative for the formation of a charge density wave and the metal to insulator transition [343] (see Fig. 94).

The equilibrium phase transition was recorded during a quasi-stationary rise of temperature from 70 K to 180 K where the sharp drop of intensity of the 8th order spots to zero [see upper panel of Fig. 92 (c)] is indicative for the transition from the (8×2) ground state to the (4×1) high temperature state. At the same time, the intensity of the 4th order spots sharply rises by a factor of two, indicating the structural transition (see lower panel of Fig. 92(c)). During slow temperature cycling a hysteresis of the high temperature (4×1) and low temperature (8×2) states is observed upon heating and cooling as shown in Fig. 92 (c). The width of the hysteresis is independent of the cooling/heating rate dT/dt [50]. Such behavior is evidence of a first-order phase transition, i.e., a non-continuous transition with both states separated by a small energy barrier.

What is the origin of the small energy barrier? In order to answer this question, DFT-based crystal orbital Hamilton population (COHP) calculations were performed [345]. Thereby the band-structure energy is rewritten as a sum of orbital pair contributions. The energy dependent COHP [523] is given by

$$\text{COHP}_{\mu T, \nu T'}(E) = H_{\mu T, \nu T'} \sum_{j, \vec{k}} f_j(\vec{k}) C_{\mu T, j}^*(\vec{k}) C_{\nu T', j}(\vec{k}) \delta(\epsilon_j(\vec{k}) - E), \quad (23)$$

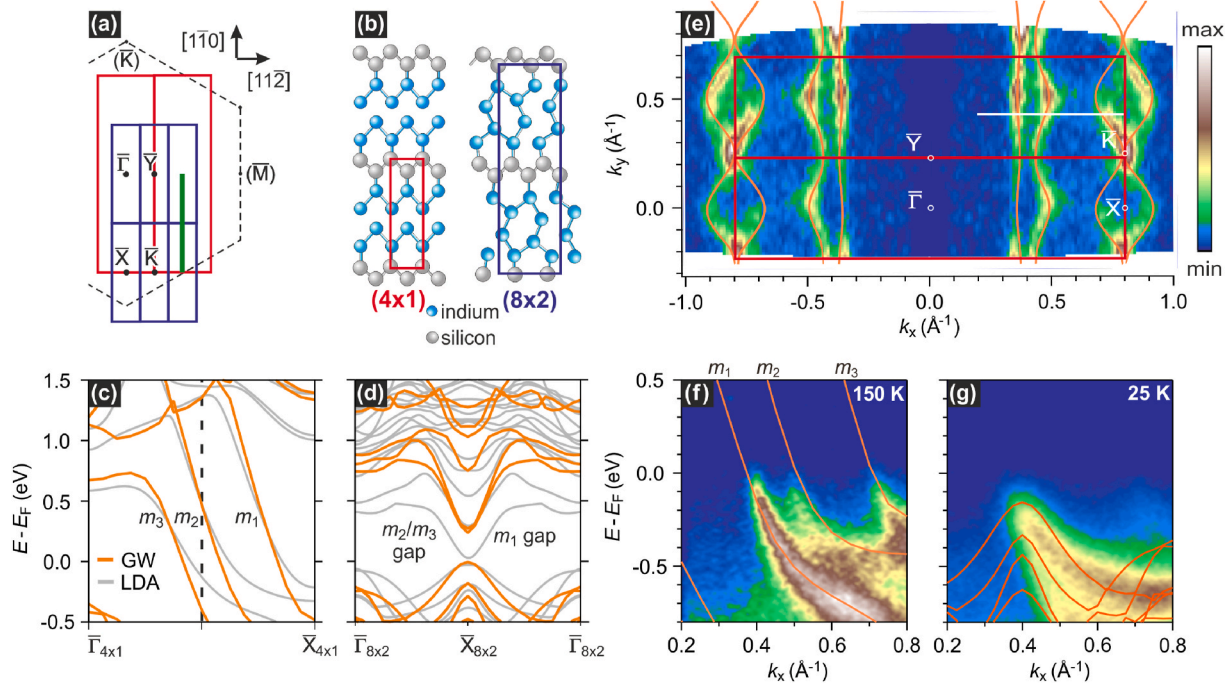


Fig. 96. (a) BZ of the (4×1) (red) and (8×2) (blue) phases of In/Si(111). High-symmetry points are marked for the (4×1) phase. The dashed line marks the SBZ of Si(111). The green solid line shows the $\Gamma - X$ line along which the majority of data was obtained. (b) Schematic real-space structure after ref. [242] in the (4×1) phase and the (8×2) phase revealing the structural motifs of the two phases. The respective unit cells are marked. (c) Electronic band structure calculated within the GW (orange) and LDA (gray) approximations in the (4×1) phase and (d) in the (8×2) phase. The dashed line in (c) is at the position that becomes the $X_{(8 \times 2)}$ point in (d). (e) Symmetrized Fermi surface at 150 K overlaid with the DFT Fermi surface sheets of the (4×1) phase (orange). The (4×1) BZ is overlaid (red). Data reproduced from ref. [242]. (f) E vs k_x cuts through the Fermi surface obtained at $k_y = 0.43 \text{ \AA}^{-1}$ at 150 K revealing the three characteristic bands of the (4×1) phase. Calculated bands in the GW approximation along the $\Gamma - X$ line are overlaid. (g) The same cut as in (f) at 25 K in the (8×2) phase revealing the gapped electronic structure and asymmetric spectral weight. (For interpretation of the references to color in this figure legend, the reader is referred to the Web version of this article.)

where $C_{\mu \vec{T} j}$ is the expansion coefficient of the j th band in terms of the atomic orbital μ at the atomic position \vec{T} . $H_{\mu \vec{T}, \nu \vec{T}'}$ denotes the matrix elements of the Hamiltonian in atomic orbitals, $\epsilon_j(\vec{k})$ is the eigenvalue corresponding to the j th electron state and $f_j(\vec{k})$ its occupation number. The COHP(E) diagram allows for identifying bonding, nonbonding, and antibonding regions within a specified energy range. The energy integral of COHP(E) gives access to the contribution of an atom or a chemical bond to the distribution of one-particle energies and indicates the total bond strength.

The COHP analysis provides the possibility to determine the strength of specific In–In bonds within the complicated nanowire structure and to track quantitatively the bond strength changes during the phase transition. The strengths of the In–In bonds calculated for the (8×2) and (4×1) surface phases of the In atomic wire system are shown in Fig. 94. It can be seen that the bonds in the (8×2) phase give indeed rise to hexagon-like structure motifs. The COHP analysis for the (4×1) phase confirms the typical model of two regular outer zig-zag chains. However, there are also strong bonds between the In atoms of the two neighboring zig-zag rows. Obviously, there are drastic differences in the bond strengths calculated for the (8×2) and (4×1) phases. This suggests that the Peierls transition between the two phases may be interpreted as well in terms of bond-breaking and bond-formation [54]. This explains naturally the energy barrier separating the (8×2) and (4×1) surface phases.

This energy barrier, shown in the top panel of Fig. 95, results from a variety of bond breaking and bond formation processes at the surface: In the bottom panel of Fig. 95 the COHP calculated bond strengths of selected bonds is pursued along the generalized coordinate describing the $(8 \times 2) \rightarrow (4 \times 1)$ phase transition. The bond strengths follow a monotonous behavior: In all cases it is observed that the bond strengths change smoothly rather than abruptly during the phase transition. There are bonds, most notably the ones indicated in green and orange between neighboring In–In zig-zag chains, that soften considerably during the phase transition. Other bonds, in particular the one indicated in blue between outer-row In atoms, gain strength upon the (8×2) phase formation. While the various individual bonds involved in the phase transition experience considerable bond strength changes, in one case even exceeding 2 eV, the overall energy difference between the two surface phases as well as the transition barrier are small. Obviously, bond breaking and bond formation processes compete, resulting in an overall subtle energy balance. This explains many of the peculiarities of the Si(111)-In Peierls system.

Interestingly, the bonds indicated green and blue in Fig. 95 are exactly the bonds that couple most strongly to the shear and rotary phonon modes of the In/Si(111) surface [276], i.e., the two Peierls lattice modes.

The Peierls-like structural transition is accompanied by a clear qualitative change of electronic structure. For the high temperature metallic phase in k -space there are three In bands with p -orbital character that cross E_F , labeled m_1 , m_2 , and m_3 in Fig. 96(c), located in the Si bulk band gap [46,244]. Below T_c the system transforms into the gapped electronic structure of the low-temperature phase [Fig. 96(d)]. While the Peierls-like nature of the phase transition has long been debated [46,54,427,517,518,524], the proposed mechanism [525] is that during the phase transition the initially metallic m_1 band at X moves above E_F , transferring electrons to the m_2 , and m_3 bands, which become unstable toward the formation of a Peierls gap (see Fig. 96). The observed softening of the relevant phonon modes [526] further supported the Peierls-like mechanism driving the phase transition.

Using ARPES, this phase transition was followed in k -space. The Fermi surface of Si(111)-In in the metallic (4×1) phase is shown in Fig. 96(c). The quasi one-dimensional nature of the system is evident from the warped Fermi surface sheets, which imply a certain degree of

inter-wire coupling [527]. The measured data show excellent agreement with previous studies [46,518,528] and with the LDA-calculated Fermi surface. We have characterized the differences between the two thermally stabilized phases, which are shown in Fig. 96(d) and (e) for the high and low temperature phases, respectively. At 150 K, the characteristic bands m_1 , m_2 , and m_3 of the (4×1) phase are clearly seen to disperse up to E_F , in excellent agreement with our GW calculations. Upon cooling into the (8×2) phase, spectral weight is removed from E_F as the system becomes gapped. In the m_2/m_3 region, the resulting band dispersion turns away from E_F , with only weak spectral weight in the renormalized dispersion, as expected for charge-density wave systems [49]. The m_1 region also shows a significant decrease of intensity at E_F , although it is worth noting that a small amount of the original m_1 band intensity still persists, even at lowest temperatures, in contrast to the prediction of theory. Such signatures suggest the presence of small

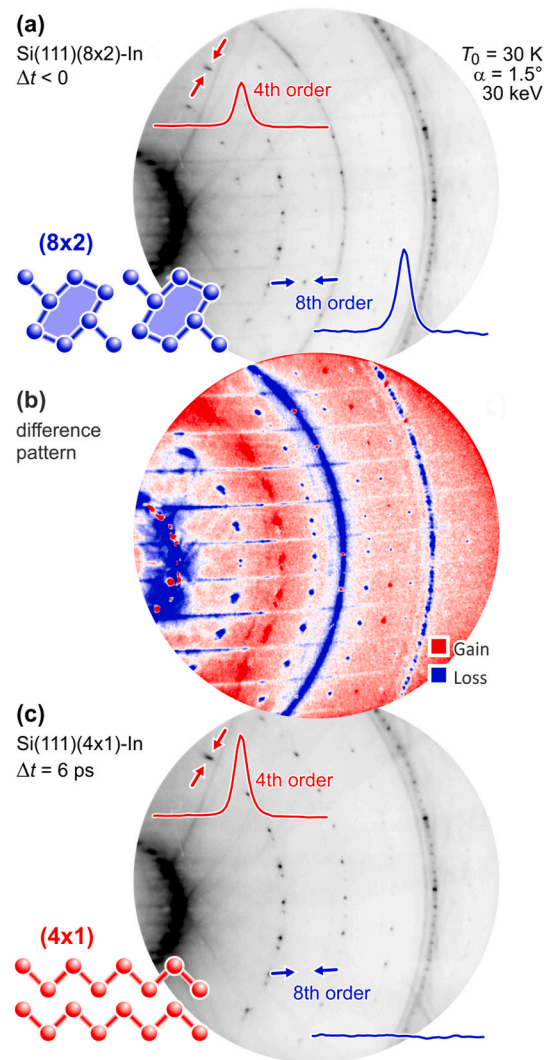


Fig. 97. RHEED patterns for clarity shown in inverted intensity representation (bright spots are shown in dark, background in bright) at 30 K prior and after optical excitation through a fs laser pulse. (a) Pattern exhibiting (8×2) ground state. Spot profiles of a 4th order and an 8th order spot are shown in red and blue, respectively. (c) The pattern 6 ps after excitation has changed to (4×1) . All (8×2) spots and second order streaks disappeared, as evident from the changes in spot profile, indicating the structural transition. (b) The difference pattern in false color representation exhibits systematic changes: all (4×1) spots gain intensity (red) while the (8×2) and second order streaks disappeared (blue). (For interpretation of the references to color in this figure legend, the reader is referred to the Web version of this article.)

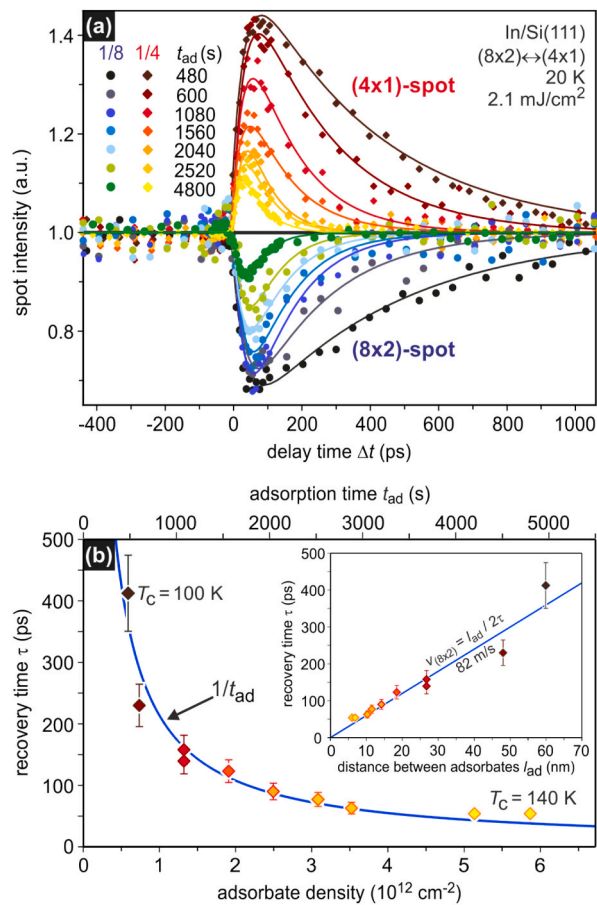


Fig. 98. Recovery of the (8×2) ground state. (a) The recovery of the (8×2) ground state strongly depends on adsorption from the residual gas. With increasing adsorbate density the recovery time constant τ changes from $\tau = 415$ ps for the first experiment after $t_{ad} = 480$ s (dark red data points) to $\tau = 54$ ps after $t_{ad} = 4800$ s (light yellow data points). (b) Time constant τ for the recovery of the (8×2) reconstruction as a function of adsorbate density. The solid line describes a $1/t_{ad}$ behavior. From the slope in the inset we derive a velocity of the propagating phase front of $v_{(8 \times 2)} = 82$ m/s. (For interpretation of the references to color in this figure legend, the reader is referred to the Web version of this article.)

domains of (4×1) even at low temperatures [519,529–531], which may be pinned at defects or step edges [48].

3.2. Photo-induced phase transition

This 1st order phase transition can also be triggered by optical excitation through intense laser pulses (1–10 mJ/cm² on a femtosecond time scale of 20–200 fs). The sudden and massive optical excitation of the electron system transiently changes the potential energy surface for the atom positions in the lattice. This provokes accelerating forces on the atoms ultimately causing the structural transition.

This photo-induced transition (PIPT) is demonstrated in Fig. 97 where panel (a) depicts the RHEED pattern of the (8×2) ground state prior to optical excitation at negative pump-probe delays $\Delta t < 0$ at a temperature $T_0 = 30$ K, i.e., well below $T_c = 130$ K. The pattern taken at $\Delta t = 6$ ps, i.e., after optical excitation through a fs-laser pulse with a fluence of $\Phi = 6.7$ mJ/cm², is shown in panel (c) and exhibits clear differences. The transient changes of spot intensity become more obvious in the difference pattern in panel (b) depicting intensity gains (red) and losses (blue) in a false color representation. All 8th order spots and second order streaks (indicative for the ground state) disappeared while 4th order spots (indicative for the high temperature state) gained

intensity. The complete transition from the (8×2) ground state to the (4×1) excited state is also reflected by the clear changes in the two representative spot profiles shown for a (8×2) and (4×1) spot in blue and red, respectively.

3.3. Supercooled excited state

Surprisingly the excited (4×1) state is stable for ns and only slowly recovers the (8×2) ground state as shown in Fig. 100(f), where the intensity of a (4×1) spot is plotted for long pump-probe delays Δt . As we show later, the indium surface layer cools via heat transport on a $\tau_{cool} = 30$ ps timescale to the substrate temperature of $T_0 = 30$ K. We thus can safely exclude a slow thermal recovery of the (8×2) ground state.

This long lived (4×1) state is explained through the nature of this phase transition: in general, a first-order transition exhibits a barrier between the two states hindering the immediate recovery of the ground state. This picture is corroborated through density functional calculations of the potential energy surface (PES). Fig. 92(d) depicts this PES as function of a generalized reaction coordinate R_{grc} obtained by superimposing the soft shear and rotary phonon eigenvectors that transform between the (4×1) and the (8×2) phase [276,516]. We found the transition from the (4×1) phase to the (8×2) structure to be hampered by an energy barrier of $E_{barrier} = 40$ meV (see Fig. 92). At temperatures below T_c this barrier hinders the immediate recovery to the (8×2) ground state: A long-lived metastable and supercooled excited phase is stabilized and trapped in a state far from equilibrium for few nanoseconds [532].

In analogy to a supercooled liquid, one might even expect the freezing, i.e., the transition back to the (8×2) ground state, to be facilitated by condensation nuclei, possibly in form of adsorbates.

To verify this assumption experimentally, we monitored the phase transition dynamics upon controlled adsorption of molecules from the residual gas. The transient intensity evolution of the (8×2) (black to green dots) and (4×1) spots (red to yellow dots) is plotted in Fig. 98(a) for various adsorption times t_{ad} . With increasing adsorbate coverage, we observed a strong decrease in the time constant, as depicted in Fig. 98(b). The shortest observed time constant was $\tau = 54$ ps for an adsorption time of $t_{ad} = 75$ min. The solid line shows a fit to a $1/t_{ad}$ behavior. Obviously, the adsorption from the residual gas drastically shortens the recovery time of the (8×2) ground state by almost a factor of 10.

Sticking to the analogy with a supercooled liquid, the insertion of seeds, i.e., condensation nuclei, initiates the freezing, which then propagates with constant velocity. Here, freezing means recovery of the (8×2) ground state. Because of the highly anisotropic nature of the indium-induced Si surface reconstruction this phase front propagates only one-dimensionally along the direction of the indium chains. Therefore, the velocity of the phase front $v_{(8 \times 2)}$ within the one-dimensional In wire and the averaged distance l_{ad} between the condensation nuclei determine the time constant τ for the complete recovery of the (8×2) ground state: $\tau = l_{ad}/(2 \cdot v_{(8 \times 2)})$; as sketched in Fig. 99. In addition, assuming a linear relation between adsorbate coverage θ_{ad} and the time t_{ad} , the distance between the adsorbates in one row obeys $l_{ad} \propto t_{ad}^{-1}$; consequently, it holds $\tau \propto t_{ad}^{-1}$. This is indeed the experimental finding shown in Fig. 98(b). An estimate for the distance l_{ad} between adsorbates in one individual row can be obtained from the shift of critical temperature T_c as a function of the adsorbate density θ_{ad} . We observed $\Delta T = +40$ K after adsorption for $t_{ad} = 75$ min. According to Lee and Shibusaki, such a change in T_c is induced by an adsorbate density of $\theta_{ad} = 6 \times 10^{12}$ cm⁻² as determined by STM [344,533]. The distance l_{ad} between the adsorbates, together with the measured time constant τ , are sufficient to determine the lower limit of the phase front velocity $v_{(8 \times 2)}$. The present experimental data result in a value of $v_{(8 \times 2)} = 82$ m/s [48]. This value rests on the assumption that all adsorbates irrespective of species and adsorption site act as condensation nuclei and initiate a phase transition. However, due to the complexity of the (8×2) surface reconstruction, not every adsorbate is likely to trigger a phase

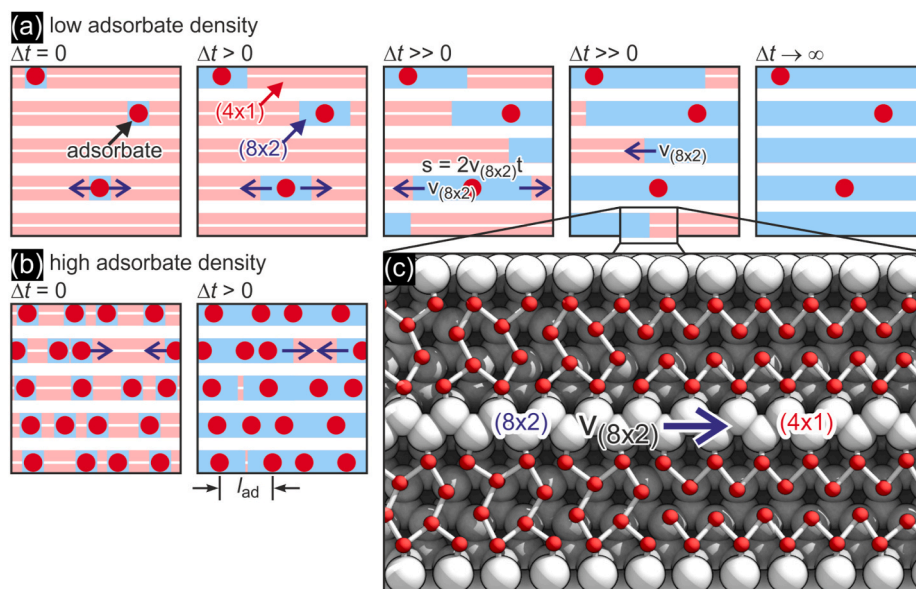


Fig. 99. Propagation of the phase front of the (8×2) ground state. (a,b) Adsorbates with a mean separation l_{ad} act as seeds (red dots). $v_{(8 \times 2)}$ is the velocity of the propagating phase front. Low (a) and high (b) adsorbate densities are shown. (c) A snapshot from the AIMD simulations depicts the transition from the metastable (4×1) phase to the (8×2) ground state. (For interpretation of the references to color in this figure legend, the reader is referred to the Web version of this article.)

transition. In fact, it was found that some adsorbates stabilize the (4×1) phase [231,344,533].

The transition back to the (8×2) ground state may also be facilitated by condensation nuclei in form of the omnipresent steps on the Si(111) substrate [534]. With the knowledge of the mean terrace width between two atomic steps $\langle \Gamma \rangle = 350$ nm and the time constant of recovery to the ground state $\tau_{\text{rec}} = 3$ ns a speed of the 1D-recovery front of 112 m/s was determined experimentally [532], which agrees with the above determined value of $v_{(8 \times 2)} = 82$ m/s.

To obtain microscopic insight into the recovery of the (8×2) ground state, we performed AIMD simulations [535] for the (4×1) surface

phase at 20 K using a (8×12) slab with periodic boundary conditions. The simulations (a snapshot is shown in Fig. 99) confirm that the phase transition starts exclusively from condensation nuclei and propagates by changing the atomic structure of subsequent unit cells one after the other with an average velocity of $v_{(8 \times 2)} = 85$ m/s. The system recovers the ground state like a row of falling dominoes – one unit cell after the other falls back from (4×1) to (8×2) .

3.4. Initial dynamics at the quantum limit

The initial dynamics of this optically driven structural transition was

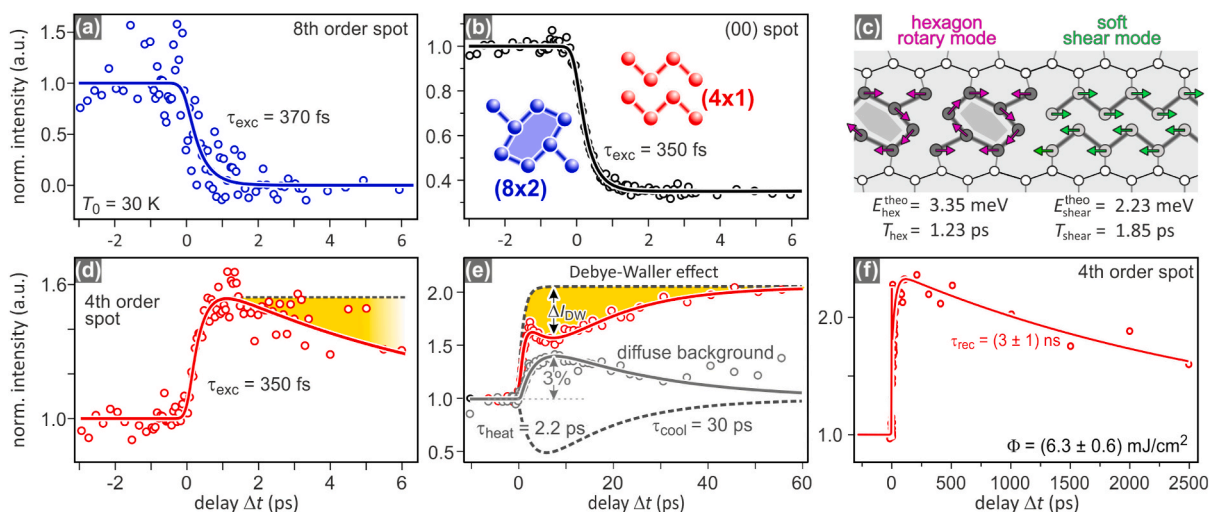


Fig. 100. Time evolution of the diffraction intensities following the fs-photoexcitation as a function of pump-probe delay Δt . (a) The transient intensity of an (8×2) spot at a laser fluence of $\Phi = 6.7$ mJ/cm² vanishes at a rate of $\tau_{\text{exc}} = 370$ fs to the background level. (b) Transient intensity of the (00) spot reflecting the structural transition from (8×2) to (4×1) state at a rate of $\tau_{\text{exc}} = 350$ fs. (c) Characteristic hexagon rotary and soft shear phonon modes facilitating the transition. (d,e) Intensity of a 4th order spot and the thermal diffuse background at a laser fluence of $\Phi = 6.7$ mJ/cm². The transient dip in the intensity of the 4th order spot ΔI_{DW} (yellow shaded area) at $\Delta t = 6$ ps indicates surface heating by $\Delta T = 80$ K, which coincides with the increase in background intensity. The 4th order spot intensity is described (solid red curve) by the superposition of the two dashed lines representing incoherent thermal motion (heating and subsequent cooling with time constants of 2.2 ps and 30 ps, respectively) and the structural transition with $\tau_{\text{exc}} = 350$ fs. (f) metastable state for long timescales. The supercooled (4×1) state recovers slowly on a 3 ns timescale. (For interpretation of the references to color in this figure legend, the reader is referred to the Web version of this article.)

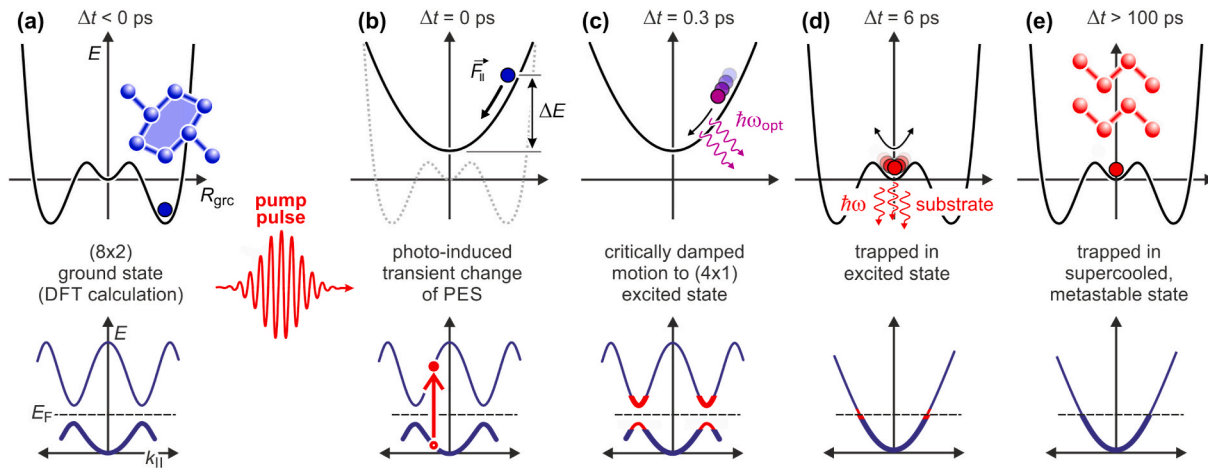


Fig. 101. Basic sketch of transient changes of the potential energy surface (PES, upper row) and simplified band structure (lower row) as function of time delay Δt . (a) Ground state prior to excitation. (b) Photo excitation, generation of electron hole pairs, excitation of the electron system, transient change of PES. (c) Accelerated dispersive structural transition, critically damped motion due to effective energy dissipation to manifold of surface phonon modes. (d) System is trapped in excited high temperature state, electron and lattice system are thermalized. (e) Ground state PES. System trapped in metastable, supercooled state. Energy barrier hinders immediate recovery of ground state for nanoseconds.

followed in the time domain through the transient intensity changes of RHEED spots as function of pump-probe delay Δt as is shown in Fig. 100.

Fig. 100(a) shows that the 8th order diffraction intensity (indicative for the ground state) is quenched in less than 1 ps. Owing to the much higher signal-to-noise ratio as compared to the 8th order spots, the dynamics of the more intense (00) spot was analyzed which follows the same trend as the 8th order spots. The (00) spot decreases with a time constant of $\tau_{\text{trans}} = 350$ fs for a laser fluence of $\Phi = 6.7$ mJ/cm² as shown in Fig. 100(b), i.e., the structural transition is completed in only 700 fs. No oscillatory signatures of the optical phonons connected to the periodic lattice distortion are observed, in contrast to studies on other CDW materials [50,247,536,537].

This structural transition from the initial insulating (8×2) state to the final metallic (4×1) state is driven by transient changes of the ground state PES which is sketched in Fig. 101(a). Photo excitation of the electron system leads to a depopulation of those states at the top of the surface state conduction band which are responsible for the energy gain through the Peierls distortion as sketched in Fig. 101(b). This results in a transient change of the energy landscape, as is sketched in Fig. 101(c) for $\Delta t = 0.3$ ps. Inevitably, the system undergoes a strongly

accelerated dispersive structural transition to the minimum of the transient energy landscape. The experimentally determined value of $\tau_{\text{exc}} = 350$ fs is about 1/4 of the periods of the equilibrium rotational and shear modes, $T_{\text{rot}} = 1.2$ ps and $T_{\text{shear}} = 1.8$ ps, respectively [522]. The transition from (8×2) state to the excited (4×1) state is completed after 0.7 ps.

The temporal fine structure of one of the (4×1) diffraction spots (Fig. 100(d and e)) is determined by two opposing trends. First, the initial increase within less than 1 ps is due to the structure factor enhancement of the (4×1) phase reflecting the change of atomic positions. Second, the subsequent decrease in intensity is explained by the Debye-Waller effect and results from the excitation of incoherent surface vibrations [538]. This leads to a transient minimum at 6 ps, which is confirmed by the rise of the thermal diffuse background and its temporal evolution (gray circles). We find time constants of 2.2 ps and 30 ps for heating and cooling of the indium atoms, respectively. This situation is sketched in Fig. 101(d + e) for $\Delta t = 6$ ps and $\Delta t > 100$ ps.

From the stationary Debye-Waller behavior of the high temperature (4×1) phase and its extrapolation to lower temperatures we determined the maximum transient temperature $T_{\text{max}} = T_0 + \Delta T_{\text{max}} = 30$ K + 80 K = 110 K at $\Delta t = 6$ ps which is well below $T_c = 130$ K. We therefore conclude that the structural transition occurs with $\tau_{\text{exc}} = 350$ fs, well before the initial excitation has thermalized at 6 ps, and is not thermally driven.

3.5. Dynamics of the electron system

The dispersive excitation scenario for the atoms motion during the driven PT relies on transiently changed PES and thus an electronic excitation that last long enough to complete the transition. This expectation was validated through time and angle resolved photo electron spectroscopy (tr-ARPES) at such low fluences $\Phi = 0.25$ mJ/cm² where the PT is not driven in order to avoid intermixture with structurally induced changes of the band structure [539]. Fig. 102(a) shows transient electron population dynamics in selected energy windows $E - E_F$ above the Fermi energy E_F obtained in normal emission geometry ($k \approx \Gamma$) for $\Phi = 0.25$ mJ/cm². The relaxation times were extracted by exponential fits to the trailing edges and are shown in (b) for $k = \Gamma$ (red dots) and $k = k_F$ (blue dots). The areas for momentum integration and the high symmetry directions of Si(111) (4×1 -In are indicated in the inset of (b) depicting the first SBZ. (For interpretation of the references to color in this figure legend, the reader is referred to the Web version of this article.)

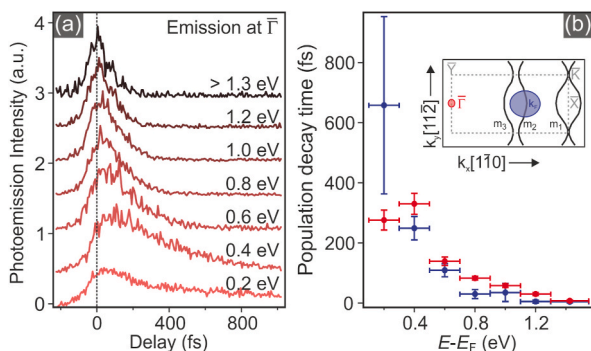


Fig. 102. Transient electron population dynamics in selected energy windows $E - E_F$ above the Fermi energy E_F obtained in normal emission geometry ($k \approx \Gamma$) for $\Phi = 0.25$ mJ/cm². The relaxation times were extracted by exponential fits to the trailing edges and are shown in (b) for $k = \Gamma$ (red dots) and $k = k_F$ (blue dots). The areas for momentum integration and the high symmetry directions of Si(111) (4×1 -In are indicated in the inset of (b) depicting the first SBZ. (For interpretation of the references to color in this figure legend, the reader is referred to the Web version of this article.)

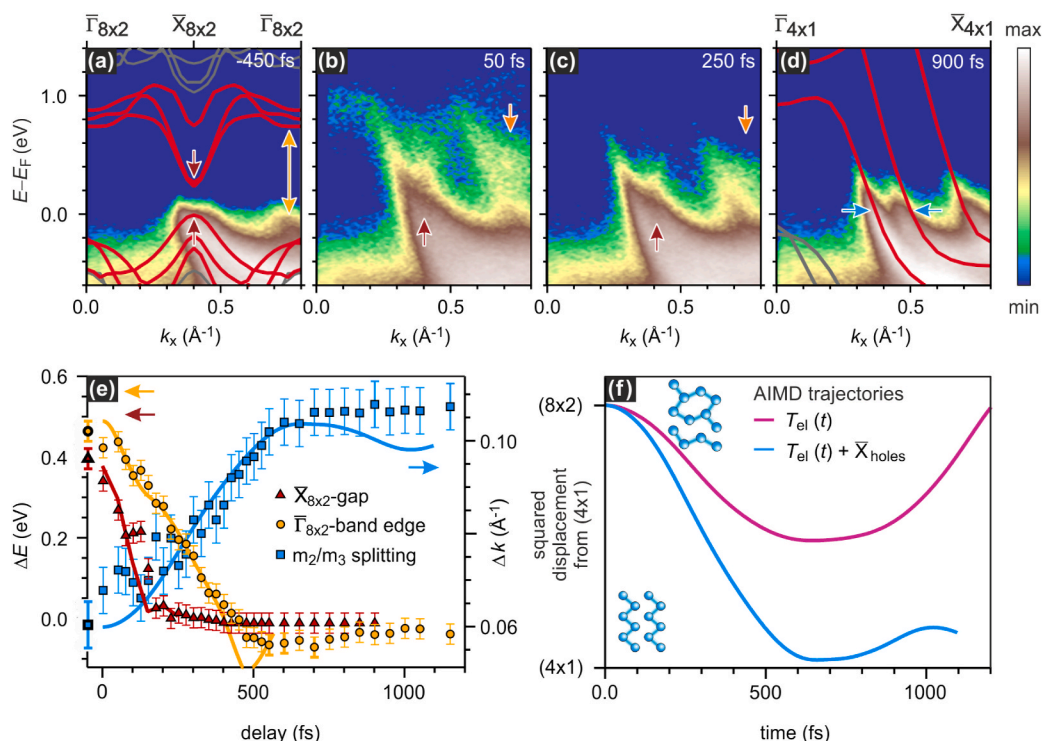


Fig. 103. Electronic and atomic structure during the PIPT. (a) to (d): trARPES data ($\Phi = 1.35 \text{ mJ/cm}^2$) on a logarithmic color scale at selected delays at a base temperature of $T = 25 \text{ K}$. Arrows highlight the positions of the features of interest, which are summarized in (e). (e) Dynamics of the features marked by arrows in (a) to (d). Red data points track the size of the band gap at the zone boundary over time, whereas the orange data points mark the position of the band edge at the zone center with respect to the Fermi level. The blue data reveal the change of splitting between the two innermost bands marked in (d). Solid curves are the dynamics of the relevant spectral features from AIMD simulations, rescaled with respect to the GW band structure. (f) Evolution of the atomic structure (AIMD trajectories) through the PIPT, showing the mean squared displacement of the atomic positions from the (4×1) phase following excitation: $\sum_i |R_i - R_{i,4 \times 2}|^2$. Trajectories for two initial excitation conditions are shown, including (blue) and not including (purple) the observed localized hole population; only the former drives the PIPT. During the PIPT, the relevant atomic modes evolve with an average speed of 0.1 pm fs^{-1} . (For interpretation of the references to color in this figure legend, the reader is referred to the Web version of this article.)

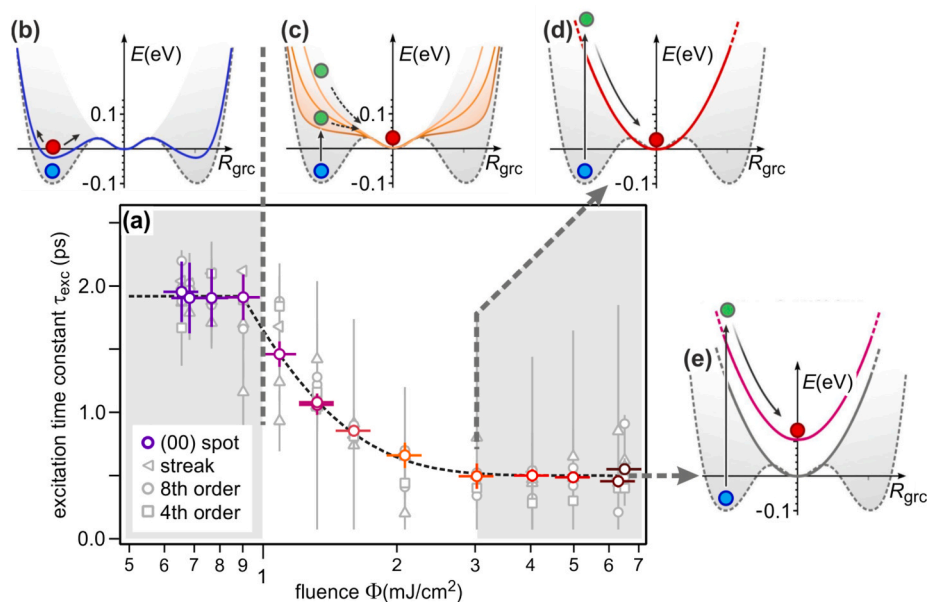


Fig. 104. (a) Fluence dependence of excitation time constant τ_{exc} of driven structural transition. Below $\Phi < 0.9 \text{ mJ/cm}^2$ the (8×2) state is not driven into the excited (4×1) state. The ground state exhibits excitation of the CDW as sketched in (b). For the intermediate regime $0.9 \text{ mJ/cm}^2 < \Phi < 3 \text{ mJ/cm}^2$ the accelerated dispersive structural transition into the excited (4×1) state takes place. The slope of the transient PES increases, i.e., speeding up the transition as is sketched in (c). The transition speed saturates for $\Phi \geq 3 \text{ mJ/cm}^2$. The slope of the transient PES is maximum as sketched in (d) and (e).

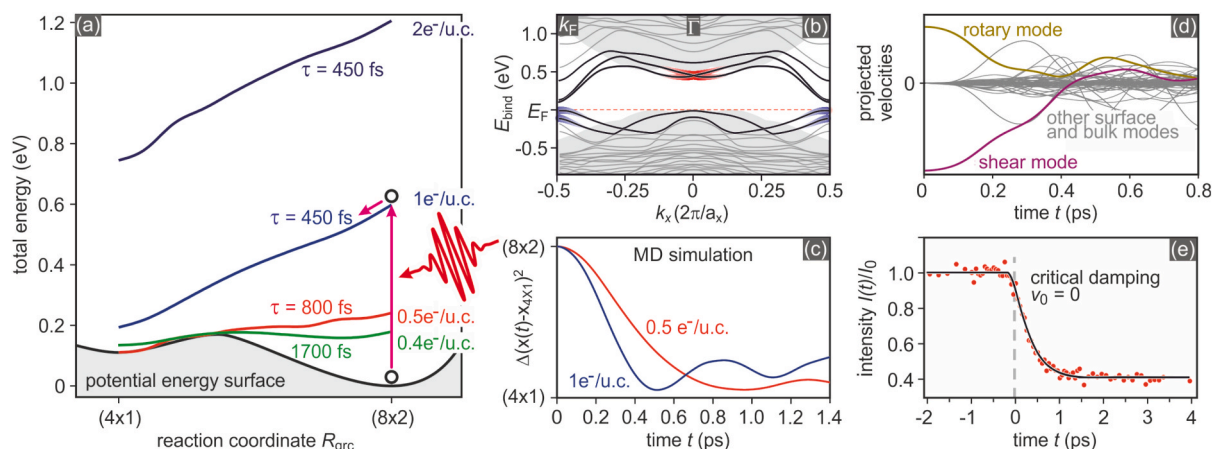


Fig. 105. Potential energy surfaces, electronic surface states, and molecular dynamics. (a) Calculated potential energy surfaces for the ground state (black) and various excited configurations along the $(8 \times 2) \rightarrow (4 \times 1)$ minimum-energy path, i.e., along the generalized reaction coordinate R_{grc} . The open circles and purple and red arrows indicate excitation of the (8×2) phase. (b) Calculated electronic bands of the Si(111) (8×2) -In surface. Here, k_x and a_x are the reciprocal- and real-space lattice vectors in the wire direction; E_{bind} is the electron binding energy relative to the valence band maximum in silicon. The electron occupation of the blue and red shaded surface bands (black lines) is vital for the phase transition. Gray shaded areas show projected silicon bulk bands. (c) Time evolution of the structural deviation from the (4×1) state, obtained from AIMD simulations within the adiabatic approximation, for two excited configurations. Here, $X(t)$ and $X(4 \times 1)$ denote the atomic coordinates of the In atoms, during the molecular dynamics calculation and for the high-temperature phase, respectively. (d) Transient atomic velocities projected onto vibrational eigenmodes. As evident, the rotary and shear modes rapidly transfer their energy to other modes. (e) The transient intensity $I(t)/I_0$ of the (00)-spot is well fitted by the behavior expected for critical damping (solid black line). (For interpretation of the references to color in this figure legend, the reader is referred to the Web version of this article.)

photo-excited electrons thus survive long enough to drive the structural transition, which corroborates the microscopic picture developed above.

Further details of the changes of the electronic band structure during the structural transition were revealed using tr-ARPES using an extreme ultraviolet probe at 22 eV [242]. With a 1.55 eV pump pulse at a sufficiently high incidence fluence $\Phi = 1.35 \text{ mJ/cm}^2$ the indium system was safely driven into the excited (4×1) state, which corresponds to an excitation density in the surface In layer of around one electron per unit cell, implying a homogeneous excitation far from a dilute limit.

Selected snapshots following excitation are shown in Fig. 103(a)–(d). At $\Delta t = -450 \text{ fs}$ (Fig. 103(a)), the XUV pulse arrives before the pump pulse; hence, the band structure reflects the unperturbed (8×2) phase with only states below E_F occupied. Shortly after excitation, at $\Delta t = 50 \text{ fs}$ (Fig. 103(b)), previously unoccupied states above E_F become clearly visible. An evolution of electronic states occurs, most clearly observed for the states around $\Gamma_{8 \times 2}$ ($K_x = 0.75 \text{ \AA}^{-1}$), which shift down in energy between $\Delta t = 50$ and $\Delta t = 250 \text{ fs}$ (Fig. 103(c)). At $\Delta t = 900 \text{ fs}$ (Fig. 103(d)), the system has fully transformed into the (4×1) phase. The overlaid GW band structure for the two phases emphasizes the transition in electronic band structure from insulator to metal.

The dynamics of selected spectral features illustrate the progress of the PIPT (Fig. 103(e)). The arrows in Fig. 103(a)–(d), mark the positions used to obtain the band positions presented in Fig. 103(e) as a function of time delay. The fastest dynamics are found at $\Gamma_{8 \times 2}$ (red arrow in Fig. 103(a)), where the band gap closes within 200 fs, thus defining the ultrafast insulator-to-metal transition. As a second step, the conduction band edge at the BZ center (orange arrow) is found to reach E_F after 500 fs also reflecting the insulator-to-metal transition. Finally, the structural transition, as measured by the splitting between bands m_2 and m_3 (Fig. 103(d), blue arrows), is completed after $\sim 700 \text{ fs}$. This third time scale is in excellent agreement with the structural transition time scale observed by time-resolved electron diffraction, which is completed after $\sim 700 \text{ fs}$ with a time constant $t = 350 \text{ fs}$ [240]. It is notable that even before the structural transition is completed, two physically meaningful electronic transitions have occurred.

3.5.1. Constrained density functional theory and ab-initio molecular dynamics

The structural transition time constant τ_{trans} depends on the laser fluence Φ , as shown in Fig. 104(a). The shortest time constant of $\tau_{\text{exc}} = 350 \text{ fs}$ is observed for $\Phi \geq 3 \text{ mJ/cm}^2$ and the longest of $\tau_{\text{exc}} = 1.9 \text{ ps}$ occurs for $\Phi \leq 0.9 \text{ mJ/cm}^2$. The transition is incomplete, that is, remnants of (8×2) diffraction spots and streaks are observed for $\Phi < 2 \text{ mJ/cm}^2$.

In order to obtain insight into the coupling of the initial electronic excitation and the subsequent local nuclear motion, we employed DFT calculations and AIMD simulations. The modelling of the optically excited electronic configurations in constrained DFT focuses on the long-

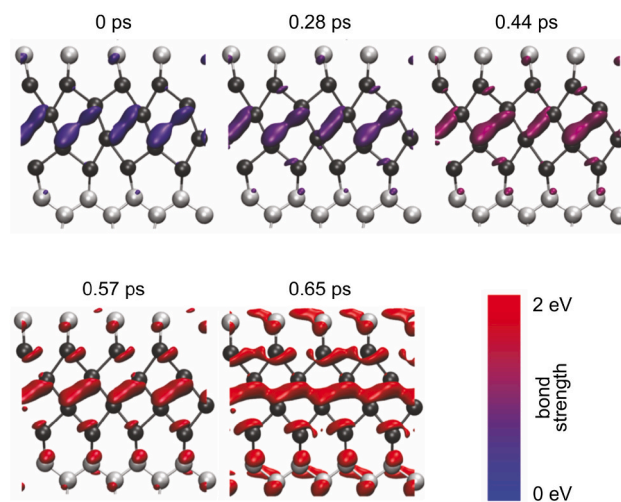


Fig. 106. Time evolution of surface bond formation exemplarily calculated for an In-In bond. Both the shape of the orbital and the COHP calculated bond strength – indicated by the color scale – change during the $(8 \times 2) \rightarrow (4 \times 1)$ phase transition, as a virtual bond across the indium hexagon gets occupied due to optical excitation and transforms into a delocalized metallic state. (For interpretation of the references to color in this figure legend, the reader is referred to the Web version of this article.)

lived excitations of the uppermost valence and lowermost conduction states (for details we refer to Ref. [240]). We analyze the minimum energy path of the $(8 \times 2) \rightarrow (4 \times 1)$ transition for the ground state and for various excited configurations as function of a generalized reaction coordinate R_{grc} , see (Fig. 105(a)). The energy gain upon the Peierls-like transition is due to the bandgap opening at the Fermi wavevector k_F . Depopulation of occupied (shaded blue in Fig. 97(b)) and population of unoccupied states at the BZ boundary destabilizes the Peierls distorted structure and drives the system into the high symmetry state of (4×1) . For sufficiently high excitation densities (for example, 0.5 electrons per (8×2) unit cell), the relative (8×2) and (4×1) energies are inverted; however, the energy barrier that separates the two structural configurations remains. In contrast, hole generation in zone-boundary valence states and population of unoccupied zone-center conduction states (shaded blue and red, respectively, in Fig. 105(b)) yields PESs with decreasing energy along the $(8 \times 2) \rightarrow (4 \times 1)$ generalized nuclear coordinate as depicted in Fig. 105(a). Such PESs can be obtained only by generating electron–hole pairs, not by charging the system.

AIMD simulations in the adiabatic approximation on these excited-state PESs verify the barrier-free $(8 \times 2) \rightarrow (4 \times 1)$ transition as shown in Fig. 105(c). For an excitation of 0.5 electrons per unit cell, the transition is completed in 800 fs. Increasing the excitation to 1.0 electrons per unit cell, results in a complete transformation of the surface within 450 fs, as expected from the steeper PES shown in Fig. 105(a). Higher excitation densities essentially shift the PES without modifying its gradient. For decreasing excitation density, the PES flattens and a threshold for the transition is predicted: 0.4 electrons per unit cell is the weakest excitation that leads to the structural transition.

The chemical rebonding processes that accompany this structural transition can be understood in space and time from the COHP analysis, see Ref. [242]. The formation of a delocalized metallic In–In bond along the nanowire direction upon the insulator-metal transition induced by an one electron excitation is exemplarily shown in Fig. 106. A gradual buildup of bond strength up to 2 eV is observed, encoded in the blue-to-red color scale applied to the orbitals. Combined with the orbital distribution, $t \rightarrow (4 \times 1)$ phase transition, on the same time scale as the closing of the electronic gap. The metal-bond formation, i.e., the transition from a localized molecular orbital (insulator) to a delocalized (metallic) state during the phase transition, parallels the band gap closure.

The DFT calculations [240,242,345] thus provide a clear picture of the microscopic mechanism of the photo-induced phase transition: Upon excitation, holes are created in the bonding states at the BZ boundary. They correspond to In–In dimer bonds between the outer In chain atoms. Consequently, the dimer bonds characteristic for the hexagon structure weaken and break. At the same time, a sizable fraction of excited electrons populates the states at the Brillouin zone center that are formed by a bonding combination of In states from neighboring In chains. Population of these excited states leads to interatomic forces that transform the hexagons into zig-zag chains, resulting in the formation of a delocalized metallic state, as shown in Fig. 106. The electron band related to these bonds is lowered in energy as the In atoms contributing to this bond approach each other, further populating those states and strengthening the bond. It finally crosses the Fermi energy, resulting in the metallic state of the (4×1) phase.

These predictions are nicely confirmed by experiment where the excitation time constant has been analyzed as function of incident laser fluence as shown in Fig. 104(a). We observe a threshold fluence of 1 mJ/cm² below which the system shows some transient response but does not make it into the excited (4×1) state. The excitation of the characteristic shear and rotational phonon modes at 0.82 THz and 0.54 THz has been indirectly observed in a pump-pump-probe experiment addressing coherent control of the phase transition [245]. The resulting amplitude mode is sketched in Fig. 104(b). For an incidence fluence larger than 1 mJ/cm² the potential energy surface of the (8×2) ground state is transiently lifted above the barrier between the two states as sketched in

Fig. 104(c). The surface system undergoes an accelerated transition to the excited (4×1) state in a displacive excitation scenario. Naturally, with increasing laser fluence, i.e., increasing excitation density, the slope of the PES becomes steeper and steeper, resulting in a faster transition to the excited state, as predicted by theory. The transition time constant saturates for incident fluences of 3 mJ/cm² or more as depicted in Fig. 104(d). This behavior nicely confirms the theoretical predictions where higher excitations densities only shift the PES without increasing its gradient as predicted by theory, see Fig. 105(a).

The observed sharp transition from the initial (8×2) state to the final (4×1) state, without any sign of damped oscillatory behavior, is explained through fast mode conversion, dephasing and strong damping of the two characteristic rotary and shear phonon modes [240,540]. Fig. 105(d) shows that the initially excited rotary and shear modes rapidly transfer their energy to a manifold of modes at the surface of the Si substrate. The experimentally determined asymptotic value of $\tau_{\text{trans}} = 350 \pm 10$ fs is about 1/4 of the periods of the equilibrium rotational and shear modes, $T_{\text{rot}} = 1.2$ ps and $T_{\text{shear}} = 1.8$ ps [276], respectively. Consequently, the transition proceeds in the regime of critical damping and cannot be faster than in this limit. All of the surface indium atoms move in a spatially coherent manner: the system undergoes the structural transition in the quantum limit: “Quantum limit is the non-statistical regime of rates in which the nuclear motion is directed and deterministic on the shortest scales of length (0.1–1 nm) and time (10^{-13} to 10^{-12} s)” [525].

Our results demonstrate that structural transitions at surfaces can be driven as fast as those in bulk materials in the non-thermal regime. The optically induced Si(111) (8×2) -In CDW melting relies on transient changes in the PES that arise from the population of very specific electronic states. These directly couple to the two characteristic rotational and shear vibrational lattice modes that drive the structural transition. This melting mechanism is similar to the structural bottleneck mechanism in layered bulk materials [541], which is surprising because the surface system differs from bulk CDWs in one key aspect. Bulk CDWs are formed within layers or chains that only weakly couple to the environment, and so the signatures of low-dimensional physics remain intact. In contrast, the surface CDW analyzed here is characterized by In–In and In–Si bonds that are stronger than In–In bulk bonds. Despite this strong interaction within the surface and between surface and substrate, the Peierls instability remains. The substrate serves as a skeleton that anchors the indium atoms, but with sufficient freedom to adopt different lateral positions. The strong coupling between substrate and adsorbate facilitates the sub-picosecond structural response by dephasing and damping the characteristic phonons after the structural transition. The structural transition of CDW melting at the Si(111) (8×2) -In surface therefore proceeds in a non-thermal regime in a limit of critical damping of the atomic motion. The CDW interaction with the surface enables the transition timescale to be controlled via the coupling strength of surface atoms to the environment, and opens up possibilities for using femto-second switching to control and steer energy and matter [542].

4. Conclusions

At this point it is perhaps worthwhile to have a look back on the experimental results described in chapters 2 and 3 in view of the introductory chapter 1, in which conditions for “survival” of 1D properties in presence of 2D and 3D interactions were investigated. All experimental systems described above were found to be stabilized by interactions in two and partly three dimensions. A clear signature is the formation of ordered arrays of wires that even stabilized or improved the periodicity of substrate terraces, as found for the Si(hhk)-Au systems. Similarly, the spontaneous break of symmetry induced by indium monolayers on Si(111) and the formation of periodic wires on this surface is not possible without such interactions. An extreme case in this respect is the formation of silicide wires on flat and stepped Si(111) surfaces, described in section 2.6. Here the formation of crystalline

quasi-1D wires is due to a chemical reaction with Si atoms of the surface, coupled with the unidirectional match of lattice constants between wire and substrate. Because of this extremely strong interaction, these wires turn out to be so rigid that no phase transitions were observable within the accessible temperature range. Although the Fermi surface is extremely anisotropic, as also reflected by electrical DC conductance, there are no signs of Fermi nesting etc. so that the silicide wires remain within the picture of low-D strongly anisotropic 2D systems.

This situation is somewhat modified when looking at the Si(hhk)-Au systems. The interactions of Au with the Si substrate are not as strong as for the silicides, but they stabilize the periodic terrace structure, as already mentioned. Most importantly, the wires grow by self-organization, i.e. by the combined interactions Si–Au and Au–Au, and form single atomic chains if $h = k - 2$, but double chains for $h = k + 2$ (h, k odd). Since the only difference is the local geometry of steps, this finding can be interpreted as signature of global 3D interactions in these systems, in agreement with findings of $\times 2$ and $\times 3$ order that is correlated across terraces at low temperature. The loss of correlation either between terraces or along the chains (step edges) leads to order-disorder phase transitions and to formation of spin liquids. Nevertheless, highly anisotropic properties were found not only in chain formation, but also in the 1D dispersion of electronic bands, of plasmon dispersion and of DC conductivity. However, in basically all these systems a fully satisfactory description was found within anisotropic 2D models, e.g. for plasmon dispersion (see sec. 2.5).

A peculiarity of the strong anisotropy in these systems is the extreme sensitivity of electronic band structure to small geometric changes at Si step edges as well as in the dimerized Au chains. Dimerization and step edge structure turned out to be directly correlated by hybridization and charge transfer between Au chains and Si step edges. These properties were investigated in most detail in the double-chain system Si(553)-Au. Interestingly and very satisfyingly, the various suggested structural models differ so little in (free) energy that the various states, corresponding to different models, can be excited thermally. While spin turned out to be an essential ingredient, no net spin was detected for the ground state configuration, but the spin liquid phase (spins located at the Si step edges) can be considered as the first excited state before, close to room temperature, all p_z orbitals the Si step edge are occupied at random. The strong changes of electronic band structure associated with these phase transitions result in characteristic vibrational shifts and/or appearance/disappearance of modes. They also lead to two maxima in DC conductance, but only the configuration close to room temperature turned out to be a stable conducting state (located at the Si step edge!), while the conductance maximum at lower temperature appears as transient between two insulating states. These findings underline the importance of long-range correlations in such highly anisotropic systems. Although they consist of single or double chains of atomic wires, i.e. they represent the smallest possible 1D objects, they clearly behave as 2D systems.

Interestingly, and perhaps somewhat against intuition, quasi-1D phenomena were observed in Si(557)-Pb and Si(111)-In with much higher adsorbate concentrations close to one monolayer. Although interactions with the substrate and, indirectly, between adsorbed atoms are large, there are also large compensatory energetic effects when it comes to positional changes during phase transitions, as described in detail in sec. 3.1 for the In system. Therefore, only small thermal energies are required for the $(8 \times 2) \leftrightarrow (4 \times 1)$ phase transition in the Si(111)-In system to occur. For this reason such a phase transition should be considered as a *collective* behavior of adsorbate plus substrate, which in certain limits leads to quasi-1D behavior. Similar properties are expected for the Si(557)-Pb system, although they were not quantified within the studies presented here. These collective properties make universal predictability of 1D behavior very difficult.

In this context, the Si(557)-Pb system is (so far) unique, since due to the Pb-induced instability of the (557) and refacetting to a (223) orientation the Pb layer creates its own nesting condition, i.e., $2k_F$ is

equal to the reciprocal lattice vector g normal to the steps of the (223) facet. Extending the original argument of Peierls [10], only for this orientation nesting leads to a reduction of energy in the electronic system and gap opening in the direction normal to the steps, if a particular concentration of Pb close to a monolayer is present. This nesting condition can be destroyed thermally. Above T_c only tiny, but characteristic changes of the facet orientation turn out to be sufficient, again generalizing the original idea of Peierls.

Furthermore, due to strong spin-orbit interaction and a very large Rashba splitting that corresponds to exactly half of the value of g , instead of separate charge and spin density waves both get entangled to form a spin-orbit density wave, which is protected by the energy gap: It disappears when the gap energy goes to zero, i.e. when the second physical monolayer of Pb is formed. Parallel to the steps high metallic conductance was found. We thus conclude that the combined 2D and 3D interactions in this system lead to a new type of instability, the formation of a spin-orbit density wave across the steps, while along the steps no sign of instability were found, i.e. the system remains conducting.

The system closest to 1D physical models is the Si(111)-In system. From the studies over the last 25 years, including those discussed in detail above, we now understand many details of the $(8 \times 2) \leftrightarrow (4 \times 1)$ phase transition with unprecedented precision, comprising structural, energetic, electronic and vibrational changes, as well as the electron and vibrational dynamics of this (first order) transition on the femto- to picosecond time scales. Mapping of the crucial degrees of freedom, including the role of the substrate, onto a phenomenological model, based on such detailed investigations, may be an important conceptual step towards a general understanding of the still partly puzzling complexity and richness of phenomena involved in such systems.

Summarizing, atomic wires supported by surfaces offer a wealth of fascinating physical phenomena that are related to the coupling of 1D objects with the two and three dimensional environment that stabilizes them, but also strongly modifies their physical properties. Therefore, in retrospect, the initial hope that interactions in 2D and 3D may essentially just act as stabilizers for 1D physics turned out to be a bit too simplistic.

From an experimental point of view, this class of systems is particularly attractive since it allows very precise studies comprising all aspects of geometrical, electronic and dynamic behavior including modifications by adatoms. This precision turned out to be crucial, since small variations of parameters, like material concentration in the wires, e.g., can modify physical properties fundamentally, underlining the importance of precise characterization. On the other hand, this allows tuning and manipulation of these properties in a wide range making them attractive objects for further studies and even for potential applications.

In view of the large variability of phenomena seen in these systems that depend, as it seems, explicitly on material and environment there is still a long way to go to achieve a more or less comprehensive understanding. Since this class of systems is electronically highly correlated, the understanding of these correlation phenomena at the borderline between 1D and 2D that were already a central issue of our studies outlined above, will be crucial. This class of systems is thus opening a wide field of fascinating aspects of correlation physics in strongly anisotropic low-dimensional, but not necessarily purely 1D systems. The latter may turn up as limiting cases, if correlations are sufficiently strong.

One important aspect, so far only touched as a side aspect (see sec. 2.6, ref. [466]), is the long term stabilization of the physical properties of such wires, also in view of potential applications. Since essentially all wires studied so far suffer from chemical modification under ambient conditions, they have to be embedded into protective materials, which by themselves change the physical properties of the wires for reasons outlined above. This topic is largely unexplored, but opens a wide field for interesting studies that combine fundamental physical aspects with more technologically oriented perspectives.

CRedit authorship contribution statement

H. Pfnür: Writing – review & editing, Writing – original draft, Supervision, Project administration, Funding acquisition, Formal analysis, Conceptualization. **C. Tegekamp:** Writing – review & editing, Writing – original draft, Project administration, Investigation, Funding acquisition, Conceptualization. **S. Sanna:** Writing – review & editing, Writing – original draft, Validation, Investigation, Conceptualization. **E. Jeckelmann:** Writing – review & editing, Writing – original draft, Supervision, Project administration, Investigation, Formal analysis, Conceptualization. **M. Horn-von Hoegen:** Writing – review & editing, Writing – original draft, Supervision, Investigation. **U. Bovensiepen:** Writing – review & editing, Writing – original draft, Supervision, Investigation. **N. Esser:** Writing – review & editing, Writing – original draft, Supervision, Investigation. **W.G. Schmidt:** Writing – review & editing, Writing – original draft, Validation, Supervision, Investigation. **M. Dähne:** Writing – review & editing, Writing – original draft, Validation, Supervision. **S. Wippermann:** Writing – original draft, Supervision, Formal analysis. **F. Bechstedt:** Conceptualization, Formal analysis, Software, Validation. **M. Bode:** Writing – review & editing, Supervision, Investigation. **R. Claessen:** Writing – review & editing, Supervision. **R. Ernstorfer:** Writing – review & editing, Supervision, Investigation. **C. Hogan:** Writing – review & editing, Validation, Investigation. **M. Ligges:** Writing – review & editing, Supervision, Investigation. **A. Pucci:** Writing – review & editing, Validation, Supervision, Investigation. **J. Schäfer:** Validation, Supervision, Investigation. **E. Speiser:** Validation, Supervision, Formal analysis. **M. Wolf:** Writing – review & editing, Validation, Supervision. **J. Wollschläger:** Writing – review & editing, Validation, Supervision, Investigation.

Declaration of competing interest

The authors declare that they have no known competing financial interests or personal relationships that could have appeared to influence the work reported in this paper.

Acknowledgements

This work summarizes essential parts of the outcomes of the Research Unit FOR1700 “Metallic nanowires on the atomic scale: Electronic and vibrational coupling in real world systems” funded by the Deutsche Forschungsgemeinschaft (DFG). This work would not have been possible without the continuous engagement of all master and PhD students as well as of the postdoctoral researchers working in the sub-projects of FOR1700. They are not named explicitly here, but are first authors or co-authors in the referenced publications. We acknowledge the computational resources provided at the Lichtenberg high performance computer of the TU Darmstadt, at the Paderborn Center for Parallel Computing (PC²), at the Höchstleistungs-Rechenzentrum Stuttgart (HLRS) and Höchstleistungs-Rechenzentrum Nord (HLRN), and at the HPC Core Facility and the HRZ of the Justus-Liebig-Universität Gießen. We acknowledge the CINECA award under the ISCRA initiative, for the availability of high performance computing resources and support. U.B., M.L., and M.HvH. acknowledge funding by the DFG through Collaborative Research Centers SFB1242 “Non-equilibrium dynamics of condensed matter in the time domain” (Project ID 278162697) and SFB616 “Energy Dissipation at Surfaces”.

References

- [1] S. Kagoshima, H. Nagasawa, T. Sambongi, *One-Dimensional Conductors*, Vol. 72 of Springer Series in Solid-State Sciences, Springer, Berlin, 1982.
- [2] H. Kiess (Ed.), *Conjugated Conducting Polymers*, Springer, Berlin, 1992.
- [3] T. Ishiguro, K. Yamaji, G. Saito, *Organic Superconductors*, Springer Series in Solid-State Sciences, Springer, Berlin, 1998.
- [4] G. Grüner, *Density Waves in Solids*, Perseus Publishing, Cambridge, 2000.

- [5] D. Jérôme, H.J. Schulz, *Organic conductors and superconductors*, *Adv. Phys.* 51 (1) (2002) 293–479.
- [6] T. Giamarchi, *Quantum physics in one dimension*. International Series of Monographs on Physics, Clarendon Press, Oxford, 2003.
- [7] D. Baeriswyl, L. Degiorgi (Eds.), *Strong Interactions in Low Dimensions*, Kluwer Academic Publishers, Dordrecht, 2004.
- [8] M. Springborg, Y. Dong, *Metallic Chains/Chains of Metals*, Elsevier, Amsterdam, 2007.
- [9] S. Roth, D. Carroll, *One-dimensional metals: conjugated polymers, organic crystals*. Carbon Nanotubes and Graphene, Wiley-VCH, Weinheim, 2015.
- [10] R.E. Peierls, *Quantum Theory of Solids*, Oxford University Press, London, 1956.
- [11] F.D.M. Haldane, ‘Luttinger liquid theory’ of one-dimensional quantum fluids. I. properties of the Luttinger model and their extension to the general 1D interacting spinless Fermi gas, *J. Phys. C Solid State Phys.* 14 (19) (1981) 2585–2609.
- [12] E. Ising, Beitrag zur Theorie des Ferromagnetismus, *Z. Phys.* 31 (1925) 253–258.
- [13] N.D. Mermin, H. Wagner, Absence of ferromagnetism or antiferromagnetism in one- or two-dimensional isotropic Heisenberg models, *Phys. Rev. Lett.* 17 (1966) 1133–1136.
- [14] M. Jatochowski, M. Strózak, R. Zdyb, Gold-induced ordering on vicinal Si(111), *Surf. Sci.* 375 (1997) 203–209.
- [15] N. Oncel, Atomic chains on surfaces, *J. Phys. Condens. Matter* 20 (39) (2008) 393001.
- [16] P.C. Snijders, H.H. Weitering, Colloquium: electronic instabilities in self-assembled atom wires, *Rev. Mod. Phys.* 82 (2010) 307–329.
- [17] P. Monceau, *Electronic crystals: an experimental overview*, *Adv. Phys.* 61 (4) (2012) 325–581.
- [18] A.J. Heeger, S. Kivelson, J.R. Schrieffer, W.-P. Su, Solitons in conducting polymers, *Rev. Mod. Phys.* 60 (1988) 781–850.
- [19] R. Saito, G. Dresselhaus, M. Dresselhaus, *Physical Properties of Carbon Nanotubes*, Imperial College Press, London, 2001.
- [20] O.M. Auslaender, A. Yacoby, R. de Picciotto, K.W. Baldwin, L.N. Pfeiffer, K. W. West, Tunneling spectroscopy of the elementary excitations in a one-dimensional wire, *Science* 295 (5556) (2002) 825–828.
- [21] Y. Jompol, C.J.B. Ford, J.P. Griffiths, I. Farrer, G.A.C. Jones, D. Anderson, D. A. Ritchie, T.W. Silk, A.J. Schofield, Probing spin-charge separation in a Tomonaga-Luttinger liquid, *Science* 325 (5940) (2009) 597–601.
- [22] A.M. Chang, Chiral Luttinger liquids at the fractional quantum Hall edge, *Rev. Mod. Phys.* 75 (2003) 1449–1505.
- [23] M. Hashisaka, T. Fujisawa, Tomonaga-Luttinger-liquid nature of edge excitations in integer quantum Hall edge channels, *Reviews in Physics* 3 (2018) 32–43.
- [24] R. Stühler, F. Reis, T. Müller, T. Helbig, T. Schwemmer, R. Thomale, J. Schäfer, R. Claessen, Tomonaga-Luttinger liquid in the edge channels of a quantum spin Hall insulator, *Nat. Phys.* 16 (2020) 47–51.
- [25] J. Jia, E. Marcellina, A. Das, M.S. Lodge, B. Wang, D.-Q. Ho, R. Biswas, T.A. Pham, W. Tao, C.-Y. Huang, H. Lin, A. Bansil, S. Mukherjee, B. Weber, Tuning the many-body interactions in a helical Luttinger liquid, *Nat. Commun.* 13 (2022) 6046.
- [26] I. Bloch, Ultracold quantum gases in optical lattices, *Nat. Phys.* 1 (1) (2005) 23–30.
- [27] T. Stöferle, H. Moritz, C. Schori, M. Köhl, T. Esslinger, Transition from a strongly interacting 1D superfluid to a Mott insulator, *Phys. Rev. Lett.* 92 (2004) 130403.
- [28] J. Sólyom, *Fundamentals of the Physics of Solids*, Volume 3 - Normal, Broken-Symmetry, and Correlated Systems, Springer, Berlin, 2010.
- [29] K. Schönhammer, Luttinger liquids: the basic concepts, in: D. Baeriswyl, L. Degiorgi (Eds.), *Strong Interactions in Low Dimensions*, Kluwer Academic Publishers, Dordrecht, 2004.
- [30] H. Bruus, K. Flensberg, *Many-body Quantum Theory in Condensed Matter Physics*, Oxford University Press, Oxford, 2004.
- [31] P.W. Anderson, *More and Different: Notes from a Thoughtful Curmudgeon*, World Scientific, Hackensack, NJ, 2011.
- [32] K. Schönhammer, *Physics in one dimension: theoretical concepts for quantum many-body systems*, *J. Phys. Condens. Matter* 25 (1) (2013) 014001.
- [33] J. Sólyom, The Fermi gas model of one-dimensional conductors, *Adv. Phys.* 28 (2) (1979) 201–303.
- [34] D. Baeriswyl, D.K. Campbell, S. Mazumdar, An overview of the theory of π -conjugated polymers, in: H. Kiess (Ed.), *Conjugated Conducting Polymers*, Springer, Berlin, 1992.
- [35] D.-J. Choi, N. Lorente, J. Wiebe, K. von Bergmann, A.F. Otte, A.J. Heinrich, Colloquium: atomic spin chains on surfaces, *Rev. Mod. Phys.* 91 (2019) 041001.
- [36] A.A. Khajetoorians, D. Wegner, A.F. Otte, I. Swart, Creating designer quantum states of matter atom-by-atom, *Nat. Rev. Phys.* 1 (2019) 703–715.
- [37] C. Blumenstein, J. Schäfer, S. Mietke, S. Meyer, A. Dollinger, M. Lochner, X. Y. Cui, L. Patthey, R. Matzdorf, R. Claessen, Atomically controlled quantum chains hosting a Tomonaga-Luttinger liquid, *Nat. Phys.* 7 (10) (2011) 776–780.
- [38] S. Meyer, J. Schäfer, C. Blumenstein, P. Höpfner, A. Bostwick, J.L. McChesney, E. Rotenberg, R. Claessen, Strictly one-dimensional electron system in Au chains on Ge(001) revealed by photoelectron k-space mapping, *Phys. Rev. B* 83 (12) (2011) 121411.
- [39] S. Meyer, L. Dudy, J. Schäfer, C. Blumenstein, P. Höpfner, T.E. Umbach, A. Dollinger, X.Y. Cui, L. Patthey, R. Claessen, Valence band and core-level photoemission of Au/Ge(001): band mapping and bonding sites, *Phys. Rev. B* 90 (2014) 125409.
- [40] L. Dudy, J. Aulbach, T. Wagner, J. Schäfer, R. Claessen, One-dimensional quantum matter: gold-induced nanowires on semiconductor surfaces, *J. Phys. Condens. Matter* 29 (43) (2017) 433001.

- [41] K. Nakatsuji, Y. Motomura, R. Niikura, F. Komori, Shape of metallic band at single-domain Au-adsorbed Ge(001) surface studied by angle-resolved photoemission spectroscopy, *Phys. Rev. B* 84 (2011) 115411.
- [42] K. Nakatsuji, F. Komori, Debate over dispersion direction in a Tomonaga-Luttinger-liquid system, *Nat. Phys.* 8 (2012) 174.
- [43] J. Park, K. Nakatsuji, T.-H. Kim, S.K. Song, F. Komori, H.W. Yeom, Absence of Luttinger liquid behavior in Au-Ge wires: a high-resolution scanning tunneling microscopy and spectroscopy study, *Phys. Rev. B* 90 (2014) 165410.
- [44] N. de Jong, R. Heimbuch, S. Eliëns, S. Smit, E. Frantzeskakis, J.-S. Caux, H.J. W. Zandvliet, M.S. Golden, Gold-induced nanowires on the Ge(100) surface yield a 2D and not a 1D electronic structure, *Phys. Rev. B* 93 (23) (2016) 235444.
- [45] H.J. Schulz, Fermi liquids and non-Fermi liquids, in: E. Akkermans, G. Montambaux, J. Pichard, J. Zinn-Justin (Eds.), *Proceedings of Les Houches Summer School LXI*, Elsevier, Amsterdam, 1995, p. 533.
- [46] H.W. Yeom, S. Takeda, E. Rotenberg, I. Matsuda, K. Horikoshi, J. Schaefer, C. M. Lee, S.D. Kevan, T. Ohta, T. Nagao, S. Hasegawa, Instability and charge density wave of metallic quantum chains on a silicon surface, *Phys. Rev. Lett.* 82 (1999) 4898–4901.
- [47] S. Hatta, Y. Ohtsubo, T. Aruga, S. Miyamoto, H. Okuyama, H. Tajiri, O. Sakata, Dynamical fluctuations in In nanowires on Si(111), *Phys. Rev. B* 84 (2011) 245321.
- [48] S. Wall, B. Krenzer, S. Wippermann, S. Sanna, F. Klasing, A. Hanisch-Blicharski, M. Kammler, W.G. Schmidt, M. Horn-von Hoegen, Atomistic picture of charge density wave formation at surfaces, *Phys. Rev. Lett.* 109 (2012) 186101.
- [49] W.G. Schmidt, S. Wippermann, S. Sanna, M. Babilon, N.J. Vollmers, U. Gerstmann, In-Si(111) (4×1)/(8×2) nanowires: electron transport, entropy, and metal-insulator transition, *Phys. Status Solidi B* 249 (2) (2012) 343–359.
- [50] F. Klasing, T. Frigge, B. Hafke, B. Krenzer, S. Wall, A. Hanisch-Blicharski, M. Horn-von Hoegen, Hysteresis proves that the In/Si(111) (8×2) to (4×1) phase transition is first-order, *Phys. Rev. B* 89 (2014) 121107(R).
- [51] H. Zhang, F. Ming, H.-J. Kim, H. Zhu, Q. Zhang, H.H. Weitering, X. Xiao, C. Zeng, J.-H. Cho, Z. Zhang, Stabilization and manipulation of electronically phase-separated ground states in defective indium atom wires on silicon, *Phys. Rev. Lett.* 113 (2014) 196802.
- [52] E. Jeckelmann, S. Sanna, W.G. Schmidt, E. Speiser, N. Esser, Grand canonical Peierls transition in In/Si(111), *Phys. Rev. B* 93 (2016) 241407.
- [53] E. Speiser, N. Esser, S. Wippermann, W.G. Schmidt, Surface vibrational Raman modes of In/Si(111)-(4×1) and (8×2) nanowires, *Phys. Rev. B* 94 (2016) 075417.
- [54] S.-W. Kim, J.-H. Cho, Origin of the metal-insulator transition of indium atom wires on Si(111), *Phys. Rev. B* 93 (2016) 241408.
- [55] S. Hatta, T. Noma, H. Okuyama, T. Aruga, Electrical conduction and metal-insulator transition of indium nanowires on Si(111), *Phys. Rev. B* 95 (2017) 195409.
- [56] J.-H. Choi, S. Liu, W. Zhang, Z. Liu, M.H. Rummeli, Charge density waves driven by Peierls instability at the interface of two-dimensional lateral heterostructures, *Small* 14 (50) (2018) 1803040.
- [57] F. Bechstedt, *Principles of Surface Physics*, Springer, Berlin, 2003.
- [58] N. Toyota, M. Lang, J. Müller, *Low-Dimensional Molecular Metals*, Springer, Berlin, 2007.
- [59] A. Schwartz, M. Dressel, G. Grüner, V. Vescoli, L. Degiorgi, T. Giamarchi, On-chain electrostatics of metallic (TMTSF)₂X salts: observation of Tomonaga-Luttinger liquid response, *Phys. Rev. B* 58 (1998) 1261–1271.
- [60] W. Barford, Electronic and optical properties of conjugated polymers. *International Series of Monographs on Physics*, Oxford University Press, Oxford, 2013.
- [61] W.P. Su, J.R. Schrieffer, A.J. Heeger, Solitons in polyacetylene, *Phys. Rev. Lett.* 42 (1979) 1698–1701.
- [62] W.P. Su, J.R. Schrieffer, A.J. Heeger, Soliton excitations in polyacetylene, *Phys. Rev. B* 22 (1980) 2099–2111.
- [63] E. Jeckelmann, D. Baeriswyl, The metal-insulator transition in polyacetylene: variational study of the Peierls-Hubbard model, *Synth. Met.* 65 (2) (1994) 211–224.
- [64] E. Jeckelmann, Mott-Peierls transition in the extended Peierls-Hubbard model, *Phys. Rev. B* 57 (19) (1998) 11838–11841.
- [65] R. Claessen, M. Sing, U. Schwingenschlögl, P. Blaha, M. Dressel, C.S. Jacobsen, Spectroscopic signatures of spin-charge separation in the quasi-one-dimensional organic conductor TTF-TCNQ, *Phys. Rev. Lett.* 88 (2002) 096402.
- [66] M. Sing, U. Schwingenschlögl, R. Claessen, P. Blaha, J.M.P. Carmelo, L. M. Martelo, P.D. Sacramento, M. Dressel, C.S. Jacobsen, Electronic structure of the quasi-one-dimensional organic conductor TTF-TCNQ, *Phys. Rev. B* 68 (2003) 125111.
- [67] J. Bardeen, Theory of non-ohmic conduction from charge-density waves in NbSe₃, *Phys. Rev. Lett.* 42 (1979) 1498–1500.
- [68] P. Lemmens, P. Millet, Spin-orbit-topology, a triptych, in: U. Schollwöck, J. Richter, D.J.J. Farnell, R.F. Bishop (Eds.), *Quantum Magnetism*, Springer, Berlin, Heidelberg, 2004, pp. 433–477.
- [69] H.-J. Mikeska, A.K. Kolezhuk, One-dimensional magnetism, in: U. Schollwöck, J. Richter, D.J.J. Farnell, R.F. Bishop (Eds.), *Quantum Magnetism*, Springer, Berlin, Heidelberg, 2004, pp. 1–83.
- [70] J. Parkinson, D.J. Farnell, *An Introduction to Quantum Spin Systems*, Springer, Berlin, 2010.
- [71] M. Hase, I. Terasaki, K. Uchinokura, Observation of the spin-Peierls transition in linear Cu²⁺ (spin-1/2) chains in an inorganic compound CuGeO₃, *Phys. Rev. Lett.* 70 (1993) 3651–3654.
- [72] K. Hirota, D.E. Cox, J.E. Lorenzo, G. Shirane, J.M. Tranquada, M. Hase, K. Uchinokura, H. Kojima, Y. Shibuya, I. Tanaka, Dimerization of CuGeO₃ in the spin-Peierls state, *Phys. Rev. Lett.* 73 (1994) 736–739.
- [73] I.A. Zaliznyak, H. Woo, T.G. Perring, C.L. Broholm, C.D. Frost, H. Takagi, Spinons in the strongly correlated copper oxide chains in SrCuO₂, *Phys. Rev. Lett.* 93 (2004) 087202.
- [74] A.C. Walters, T.G. Perring, J.-S. Caux, A.T. Savici, G.D. Gu, C.-C. Lee, W. Ku, I. A. Zaliznyak, Effect of covalent bonding on magnetism and the missing neutron intensity in copper oxide compounds, *Nat. Phys.* 5 (12) (2009) 867–872.
- [75] P. Harrison, *Quantum Wells, Wires and Dots*, Wiley, Chichester, 2005.
- [76] J. Sólyom, *Fundamentals of the Physics of Solids, Volume 1 - Structure and Dynamics*, Springer, Berlin, 2007.
- [77] J. Sólyom, *Fundamentals of the Physics of Solids, Volume 2 - Electronic Properties*, Springer, Berlin, 2009.
- [78] R.M. Martin, *Electronic Structure*, Cambridge University Press, Cambridge, 2005.
- [79] R.O. Jones, Density functional theory: its origins, rise to prominence, and future, *Rev. Mod. Phys.* 87 (2015) 897–923.
- [80] K. Capelle, V.L. Campo, Density functionals and model Hamiltonians: Pillars of many-particle physics, *Phys. Rep.* 528 (3) (2013) 91–159.
- [81] J. Hubbard, Electron correlations in narrow energy bands, *Proc. R. Soc. London, Ser. A* 276 (1963) 238.
- [82] T. Holstein, Studies of polaron motion: Part I. The molecular-crystal model, *Ann. Phys.* 8 (3) (1959) 325–342.
- [83] H. Fröhlich, H. Pelzer, S. Zienau, XX. Properties of slow electrons in polar materials, London, Edinburgh Dublin Phil. Mag. J. Sci. 41 (314) (1950) 221–242.
- [84] H. Fröhlich, Electrons in lattice fields, *Adv. Phys.* 3 (11) (1954) 325–361.
- [85] W. Heisenberg, Zur Theorie des Ferromagnetismus, *Z. Phys.* 49 (9) (1928) 619–636.
- [86] F. Gebhard, *The Mott Metal-Insulator Transition*, Springer Tracts in Modern Physics, Springer, Berlin, 1997.
- [87] L. Cano-Cortés, A. Dolfin, J. Merino, J. Behler, B. Delley, K. Reuter, E. Koch, Spectral broadening due to long-range Coulomb interactions in the molecular metal TTF-TCNQ, *Eur. Phys. J. B* 56 (3) (2007) 173–176.
- [88] H. Bethe, Zur Theorie der Metalle, *Z. Phys.* 71 (3) (1931) 205–226.
- [89] E.H. Lieb, F.Y. Wu, Absence of Mott transition in an exact solution of the short-range, one-band model in one dimension, *Phys. Rev. Lett.* 20 (1968) 1445–1448.
- [90] F. Essler, H. Frahm, F. Göhmann, A. Klümper, V. Korepin, *The One-Dimensional Hubbard Model*, Cambridge University Press, Cambridge, 2005.
- [91] S. Brazovskii, I. Dzyaloshinskii, I. Krichever, Exactly soluble Peierls models, *Phys. Lett.* 91 (1) (1982) 40–42.
- [92] S. Brazovskii, I. Dzyaloshinskii, I. Krichever, Discrete Peierls models with exact solutions, *Sov. Phys. JETP* 56 (1) (1982) 212–225. This paper was first published in Russian in *Zh. Eksp. Teor. Fiz.* 83, 389–415 (1982).
- [93] T.D. Schultz, D.C. Mattis, E.H. Lieb, Two-dimensional Ising model as a soluble problem of many fermions, *Rev. Mod. Phys.* 36 (1964) 856–871.
- [94] D. Landau, K. Binder, *A Guide to Monte Carlo Simulations in Statistical Physics*, fifth ed., Cambridge University Press, Cambridge, 2021.
- [95] J. Gubernatis, N. Kawashima, P. Werner, *Quantum Monte Carlo Methods: Algorithms for Lattice Models*, Cambridge University Press, Cambridge, 2016.
- [96] F.F. Assaad, H.G. Evertz, World-line and determinantal quantum Monte Carlo methods for spins, phonons and electrons, in: H. Fehske, R. Schneider, A. Weiße (Eds.), *Computational Many-Particle Physics*, vol. 739, Springer Berlin Heidelberg, 2008, pp. 277–356, of *Lecture Notes in Physics*.
- [97] S.R. White, R.M. Noack, Real-space quantum renormalization groups, *Phys. Rev. Lett.* 68 (24) (1992) 3487–3490.
- [98] S.R. White, Density-matrix algorithms for quantum renormalization groups, *Phys. Rev. B* 48 (14) (1993) 10345–10356.
- [99] U. Schollwöck, The density-matrix renormalization group, *Rev. Mod. Phys.* 77 (1) (2005) 259.
- [100] E. Jeckelmann, Density-matrix renormalization group algorithms, in: H. Fehske, R. Schneider, A. Weiße (Eds.), *Computational Many-Particle Physics*, vol. 739, Springer Berlin Heidelberg, 2008, pp. 597–619, of *Lecture Notes in Physics*.
- [101] U. Schollwöck, The density-matrix renormalization group in the age of matrix product states, *Ann. Phys.* 326 (1) (2011) 96–192.
- [102] S.-i. Tomonaga, Remarks on Bloch's method of sound waves applied to many-fermion problems, *Prog. Theor. Phys.* 5 (4) (1950) 544–569.
- [103] J.M. Luttinger, An exactly soluble model of a many-fermion system, *J. Math. Phys.* 4 (9) (1963) 1154.
- [104] S. Eggert, One-dimensional quantum wires: a pedestrian approach to bosonization, in: Y. Kuk, S. Hasegawa, Q.-K. Xue (Eds.), *Theoretical Survey of One Dimensional Wire Systems*, (Seoul), Sowha Publishing, 2007.
- [105] C.E. Creffield, W. Häusler, A.H. MacDonald, Spin and charge Tomonaga-Luttinger parameters in quantum wires, *Europhys. Lett.* 53 (2) (2001) 221–227.
- [106] R.M. Lee, N.D. Drummond, Ground-state properties of the one-dimensional electron liquid, *Phys. Rev. B* 83 (2011) 245114.
- [107] A. Gogolin, A. Nersisyan, A. Tsvelik, *Bosonization and Strongly Correlated Systems*, Cambridge University Press, Cambridge, 1998.
- [108] G. Grüner, The dynamics of charge-density waves, *Rev. Mod. Phys.* 60 (1988) 1129–1181.
- [109] G. Grüner, The dynamics of spin-density waves, *Rev. Mod. Phys.* 66 (1994) 1–24.
- [110] V.L. Ginzburg, L.D. Landau, On the Theory of Superconductivity, Heidelberg: Springer Berlin Heidelberg, Berlin, 2009, pp. 113–137. This paper was first published in Russian in *Zh. Eksp. Teor. Fiz. (ZhETF)* 20, 1064 (1950).
- [111] V.L. Ginzburg, On the theory of superconductivity, *Il Nuovo Cimento* 2 (6) (1955) 1234–1250.

- [112] P. Hohenberg, A. Krehkov, An introduction to the Ginzburg-Landau theory of phase transitions and nonequilibrium patterns, *Phys. Rep.* 572 (2015) 1–42.
- [113] C. Itzykson, J.-M. Drouffe, *Statistical Field Theory*, vol. 1, Cambridge University Press, 1989.
- [114] J. Zinn-Justin, *Phase Transitions and Renormalization Group*, Oxford University Press, 2007.
- [115] E. Brézin, *Introduction to Statistical Field Theory*, Cambridge University Press, 2010.
- [116] G. Mussardo, *Statistical Field Theory: an Introduction to Exactly Solved Models in Statistical Physics*, Oxford Graduate Texts, OUP Oxford, 2010.
- [117] K.G. Wilson, J. Kogut, The renormalization group and the ϵ expansion, *Phys. Rep.* 12 (2) (1974) 75–199.
- [118] E. Tutiš, S. Barišić, Dynamic structure factor of a one-dimensional Peierls system, *Phys. Rev. B* 43 (1991) 8431–8436.
- [119] D. Jérôme, T.M. Rice, W. Kohn, Excitonic insulator, *Phys. Rev.* 158 (1967) 462–475.
- [120] A.W. Overhauser, Exchange and correlation instabilities of simple metals, *Phys. Rev.* 167 (1968) 691–698.
- [121] E. Jeckelmann, Ground-state phase diagram of a half-filled one-dimensional extended Hubbard model, *Phys. Rev. Lett.* 89 (23) (2002) 236401.
- [122] E. Wigner, On the interaction of electrons in metals, *Phys. Rev.* 46 (1934) 1002–1011.
- [123] J. Hubbard, Generalized Wigner lattices in one dimension and some applications to tetracyanoquinodimethane (TCNQ) salts, *Phys. Rev. B* 17 (1978) 494–505.
- [124] J.E. Hirsch, E. Fradkin, Phase diagram of one-dimensional electron-phonon systems. II. the molecular-crystal model, *Phys. Rev. B* 27 (1983) 4302–4316.
- [125] E. Jeckelmann, C. Zhang, S.R. White, Metal-insulator transition in the one-dimensional Holstein model at half filling, *Phys. Rev. B* 60 (11) (1999) 7950–7955.
- [126] M. Barborini, M. Calandra, F. Mauri, L. Wirtz, P. Cudazzo, Excitonic-insulator instability and Peierls distortion in one-dimensional semimetals, *Phys. Rev. B* 105 (2022) 075122.
- [127] H. Fehske, G. Hager, E. Jeckelmann, Metallicity in the half-filled Holstein-Hubbard model, *Europhys. Lett.* 84 (2008) 57001.
- [128] H. Fröhlich, On the theory of superconductivity: the one-dimensional case, *Proc. Roy. Soc. Lond. Math. Phys. Ser. C* 223 (1154) (1954) 296–305.
- [129] H.-J. Schulz, Lattice dynamics and electrical properties of commensurate one-dimensional charge-density-wave systems, *Phys. Rev. B* 18 (1978) 5756–5767.
- [130] B. Horowitz, H. Gutfreund, M. Weger, Infrared and Raman activities of organic linear conductors, *Phys. Rev. B* 17 (1978) 2796–2799.
- [131] H. Morikawa, I. Matsuda, S. Hasegawa, Direct observation of soliton dynamics in charge-density waves on a quasi-one-dimensional metallic surface, *Phys. Rev. B* 70 (2004) 085412.
- [132] H. Zhang, J.-H. Choi, Y. Xu, X. Wang, X. Zhai, B. Wang, C. Zeng, J.-H. Cho, Z. Zhang, J.G. Hou, Atomic structure, energetics, and dynamics of topological solitons in indium chains on Si(111) surfaces, *Phys. Rev. Lett.* 106 (2011) 026801.
- [133] H.W. Yeom, T.-H. Kim, Comment on “Atomic structure, energetics, and dynamics of topological solitons in indium chains on Si(111) surfaces”, *Phys. Rev. Lett.* 107 (2011) 019701.
- [134] H. Zhang, J.-H. Choi, Y. Xu, X. Wang, X. Zhai, B. Wang, C. Zeng, J.-H. Cho, J. G. Zhang, Zhenyuand Hou, Reply to a comment on “Atomic structure, energetics, and dynamics of topological solitons in indium chains on Si(111) surfaces”, *Phys. Rev. Lett.* 107 (2011) 019702.
- [135] T.-H. Kim, H.W. Yeom, Topological solitons versus nonsolitonic phase defects in a quasi-one-dimensional charge-density wave, *Phys. Rev. Lett.* 109 (2012) 246802.
- [136] S. Cheon, T.-H. Kim, S.-H. Lee, H.W. Yeom, Chiral solitons in a coupled double Peierls chain, *Science* 350 (6257) (2015) 182–185.
- [137] G. Lee, H. Shim, J.-M. Hyun, H. Kim, Intertwined solitons and impurities in a quasi-one-dimensional charge-density-wave system: In/Si(111), *Phys. Rev. Lett.* 122 (2019) 016102.
- [138] C. Tegenkamp, D. Lükermann, H. Pfnür, B. Slomski, G. Landolt, J.H. Dil, Fermi nesting between atomic wires with strong spin-orbit coupling, *Phys. Rev. Lett.* 109 (2012) 266401.
- [139] C. Brand, H. Pfnür, G. Landolt, S. Muff, J.H. Dil, T. Das, C. Tegenkamp, Observation of correlated spin-orbit order in a strongly anisotropic quantum wire system, *Nat. Commun.* 6 (2015) 8118.
- [140] J.P. Pouget, P. Foury-Leylekan, D.L. Bolloc’h, B. Hennion, S. Ravy, C. Coulon, V. Cardoso, A. Moradpour, Neutron-scattering evidence for a spin-Peierls ground state in (TMTTF)₂PF₆, *J. Low Temp. Phys.* 142 (3) (2006) 147–152.
- [141] S. Fujiyama, T. Nakamura, Redistribution of electronic charges in spin-Peierls state in (TMTTF)₂AsF₆ observed by ¹³C NMR, *J. Phys. Soc. Jpn.* 75 (1) (2006) 014705.
- [142] J.E. Hirsch, D.J. Scalapino, $2p_F$ and $4p_F$ instabilities in the one-dimensional electron gas, *Phys. Rev. Lett.* 50 (1983) 1168–1171.
- [143] H. Seo, H. Fukuyama, Antiferromagnetic phases of one-dimensional quarter-filled organic conductors, *J. Phys. Soc. Jpn.* 66 (5) (1997) 1249–1252.
- [144] S.C. Erwin, F.J. Himpsel, Intrinsic magnetism at silicon surfaces, *Nat. Commun.* 1 (5) (2010).
- [145] P.C. Snijders, P.S. Johnson, N.P. Guisinger, S.C. Erwin, F.J. Himpsel, Spectroscopic evidence for spin-polarized edge states in graphitic Si nanowires, *New J. Phys.* 14 (10) (2012) 103004.
- [146] J. Aulbach, J. Schäfer, S.C. Erwin, S. Meyer, C. Loho, J. Settlein, R. Claessen, Evidence for long-range spin order instead of a Peierls transition in Si(553)-Au chains, *Phys. Rev. Lett.* 111 (2013) 137203.
- [147] N.F. Mott, R. Peierls, Discussion of the paper by de Boer and Verwey, *Proc. Phys. Soc.* 49 (4S) (1937) 72–73.
- [148] N.F. Mott, *Metal-Insulator Transitions*, Taylor and Francis, London, 1990.
- [149] M. Imada, A. Fujimori, Y. Tokura, Metal-insulator transitions, *Rev. Mod. Phys.* 70 (1998) 1039–1263.
- [150] F. Gebhard, O. Legeza, Tracing the Mott-Hubbard transition in one-dimensional Hubbard models without Umklapp scattering, *Phys. Rev. B* 104 (2021) 245118.
- [151] A. Luther, V.J. Emery, Backward scattering in the one-dimensional electron gas, *Phys. Rev. Lett.* 33 (1974) 589–592.
- [152] M. Hohenadler, F.F. Assaad, Excitation spectra and spin gap of the half-filled Holstein-Hubbard model, *Phys. Rev. B* 87 (2013) 075149.
- [153] J. Greitemann, S. Hesselmann, S. Wessel, F.F. Assaad, M. Hohenadler, Finite-size effects in Luther-Emery phases of Holstein and Hubbard models, *Phys. Rev. B* 92 (2015) 245132.
- [154] S. Maekawa, Superconductivity in spin ladders, *Science* 273 (5281) (1996) 1515, 1515.
- [155] J.-P. Song, S. Mazumdar, R.T. Clay, Absence of Luther-Emery superconducting phase in the three-band model for cuprate ladders, *Phys. Rev. B* 104 (2021) 104504.
- [156] P.W. Anderson, Absence of diffusion in certain random lattices, *Phys. Rev.* 109 (1958) 1492–1505.
- [157] B. Kramer, A. MacKinnon, Localization: theory and experiment, *Rep. Prog. Phys.* 56 (12) (1993) 1469–1564.
- [158] A. Auerbach, *Interacting Electrons and Quantum Magnetism*, Springer, Berlin, 1998.
- [159] G. Palle, D.K. Sunko, Physical limitations of the Hohenberg-Mermin-Wagner theorem, *J. Phys. Math. Theor.* 54 (31) (2021) 315001.
- [160] Z.K. Tang, L. Zhang, N. Wang, X.X. Zhang, G.H. Wen, G.D. Li, J.N. Wang, C. T. Chan, P. Sheng, Superconductivity in 4 angstrom single-walled carbon nanotubes, *Science* 292 (5526) (2001) 2462–2465.
- [161] I. Takesue, J. Haruyama, N. Kobayashi, S. Chiashi, S. Maruyama, T. Sugai, H. Shinohara, Superconductivity in entirely end-bonded multiwalled carbon nanotubes, *Phys. Rev. Lett.* 96 (2006) 057001.
- [162] I. Affleck, D. Gepner, H.J. Schulz, T. Ziman, Critical behaviour of spin-S Heisenberg antiferromagnetic chains: analytic and numerical results, *J. Phys. Math. Gen.* 22 (5) (1989) 511–529.
- [163] T. Giamarchi, H.J. Schulz, Correlation functions of one-dimensional quantum systems, *Phys. Rev. B* 39 (1989) 4620–4629.
- [164] T. Giamarchi, Theoretical framework for quasi-one dimensional systems, *Chem. Rev.* 104 (2004) 5037–5055.
- [165] G. Giuliani, G. Vignale, *Quantum Theory of the Electron Liquid*, Cambridge University Press, Cambridge, 2005.
- [166] J. Voit, One-dimensional Fermi liquids, *Rep. Prog. Phys.* 58 (9) (1995) 977–1116.
- [167] W. Kohn, J.M. Luttinger, New mechanism for superconductivity, *Phys. Rev. Lett.* 15 (1965) 524–526.
- [168] D.C. Mattis, E.H. Lieb, Exact solution of a many-fermion system and its associated boson field, *J. Math. Phys.* 6 (2) (1965) 304–312.
- [169] W. Apel, T.M. Rice, Combined effect of disorder and interaction on the conductance of a one-dimensional fermion system, *Phys. Rev. B* 26 (1982) 7063–7065.
- [170] C.L. Kane, M.P.A. Fisher, Transport in a one-channel Luttinger liquid, *Phys. Rev. Lett.* 68 (1992) 1220–1223.
- [171] C.L. Kane, M.P.A. Fisher, Transmission through barriers and resonant tunneling in an interacting one-dimensional electron gas, *Phys. Rev. B* 46 (1992) 15233–15262.
- [172] E. Jeckelmann, Local density of states of the one-dimensional spinless fermion model, *J. Phys. Condens. Matter* 25 (1) (2013) 014002.
- [173] J.-M. Bischoff, E. Jeckelmann, Density-matrix renormalization group method for the conductance of one-dimensional correlated systems using the Kubo formula, *Phys. Rev. B* 96 (2017) 195111.
- [174] Y. Ohtsubo, J.-i. Kishi, K. Hagiwara, P. Le Fèvre, F. Bertran, A. Taleb-Ibrahimi, H. Yamane, S.-i. Ideta, M. Matsunami, K. Tanaka, S.-i. Kimura, Surface Tomonaga-Luttinger-liquid state on Bi/InSb(001), *Phys. Rev. Lett.* 115 (2015) 256404.
- [175] K. Yaji, S. Kim, I. Mochizuki, Y. Takeichi, Y. Ohtsubo, P.L. Fèvre, F. Bertran, A. Taleb-Ibrahimi, S. Shin, F. Komori, One-dimensional metallic surface states of Pt-induced atomic nanowires on Ge(001), *J. Phys. Condens. Matter* 28 (28) (2016) 284001.
- [176] B. Yang, Y.-Y. Chen, Y.-G. Zheng, H. Sun, H.-N. Dai, X.-W. Guan, Z.-S. Yuan, J.-W. Pan, Quantum criticality and the Tomonaga-Luttinger liquid in one-dimensional Bose gases, *Phys. Rev. Lett.* 119 (2017) 165701.
- [177] V. Meden, K. Schönhammer, Spectral functions for the Tomonaga-Luttinger model, *Phys. Rev. B* 46 (1992) 15753–15760.
- [178] V. Meden, W. Metzner, U. Schollwöck, O. Schneider, T. Stauber, K. Schönhammer, Luttinger liquids with boundaries: power-laws and energy scales, *Eur. Phys. J. B* 16 (4) (2000) 631–646.
- [179] S. Andergassen, T. Enss, V. Meden, W. Metzner, U. Schollwöck, K. Schönhammer, Renormalization-group analysis of the one-dimensional extended Hubbard model with a single impurity, *Phys. Rev. B* 73 (2006) 045125.
- [180] S.A. Söfving, I. Schneider, S. Eggert, Low-energy local density of states of the 1D Hubbard model, *Europhys. Lett.* 101 (5) (2013) 56006.
- [181] J.-M. Bischoff, E. Jeckelmann, Density-matrix renormalization group study of the linear conductance in quantum wires coupled to interacting leads or phonons, *Phys. Rev. B* 100 (2019) 075151.
- [182] V. Vescoli, F. Zwick, W. Henderson, L. Degiorgi, M. Grioni, G. Gruner, L. K. Montgomery, Optical and photoemission evidence for a Tomonaga-Luttinger liquid in the Bechgaard salts, *Eur. Phys. J. B* 13 (3) (2000) 503–511.

- [183] J. Hager, R. Matzdorf, J. He, R. Jin, D. Mandrus, M.A. Cazalilla, E.W. Plummer, Non-Fermi-liquid behavior in quasi-one-dimensional $\text{Li}_{0.9}\text{Mo}_6\text{O}_{17}$, *Phys. Rev. Lett.* 95 (2005) 186402.
- [184] F. Wang, S.-K. Mo, J.W. Allen, H.-D. Kim, J. He, R. Jin, D. Mandrus, A. Sekiyama, M. Tsunekawa, S. Suga, Case for bulk nature of spectroscopic Luttinger liquid signatures observed in angle-resolved photoemission spectra of $\text{Li}_{0.9}\text{Mo}_6\text{O}_{17}$, *Phys. Rev. B* 74 (2006) 113107.
- [185] H. Ishii, H. Kataura, H. Shiozawa, H. Yoshioka, H. Otsubo, Y. Takayama, T. Miyahara, S. Suzuki, Y. Achiba, M. Nakatake, T. Narimura, M. Higashiguchi, K. Shimada, H. Namatame, M. Taniguchi, Direct observation of Tomonaga-Luttinger-liquid state in carbon nanotubes at low temperatures, *Nature* 426 (6966) (2003) 540–544.
- [186] I. Safi, H.J. Schulz, Transport in an inhomogeneous interacting one-dimensional system, *Phys. Rev. B* 52 (1995) R17040–R17043.
- [187] D.L. Maslov, M. Stone, Landauer conductance of Luttinger liquids with leads, *Phys. Rev. B* 52 (1995) R5539–R5542.
- [188] V.V. Ponomarenko, Renormalization of the one-dimensional conductance in the Luttinger-liquid model, *Phys. Rev. B* 52 (1995) R8666–R8667.
- [189] J. Voit, Charge-spin separation and the spectral properties of Luttinger liquids, *Phys. Rev. B* 47 (1993) 6740–6743.
- [190] H. Benthien, F. Gebhard, E. Jeckelmann, Spectral function of the one-dimensional Hubbard model away from half filling, *Phys. Rev. Lett.* 92 (25) (2004) 256401.
- [191] E. Jeckelmann, Density-matrix renormalization group methods for momentum- and frequency-resolved dynamical correlation functions, *Prog. Theor. Phys. Suppl.* 176 (2008) 143–164.
- [192] B. Bertini, F. Heidrich-Meisner, C. Karrasch, T. Prosen, R. Steinigeweg, M. Žnidarič, Finite-temperature transport in one-dimensional quantum lattice models, *Rev. Mod. Phys.* 93 (2021) 025003.
- [193] A.J. Daley, M. Rigol, D.S. Weiss, Focus on out-of-equilibrium dynamics in strongly interacting one-dimensional systems, *New J. Phys.* 16 (9) (2014) 095006.
- [194] T. Kinoshita, T. Wenger, D.S. Weiss, A quantum Newton's cradle, *Nature* 440 (7086) (2006) 900–903.
- [195] S. Hofferberth, I. Lesanovsky, B. Fischer, T. Schumm, J. Schmiedmayer, Non-equilibrium coherence dynamics in one-dimensional Bose gases, *Nature* 449 (7160) (2007) 324–327.
- [196] B. Horovitz, H. Gutfreund, M. Weger, Interchain coupling and the Peierls transition in linear-chain systems, *Phys. Rev. B* 12 (1975) 3174–3185.
- [197] B.A. Bernevig, J. Orenstein, S.-C. Zhang, Exact $\text{SU}(2)$ symmetry and persistent spin helix in a spin-orbit coupled system, *Phys. Rev. Lett.* 97 (2006) 236601.
- [198] T. Das, Interaction induced staggered spin-orbit order in two-dimensional electron gas, *Phys. Rev. Lett.* 109 (2012) 246406.
- [199] J.M. Kosterlitz, D.J. Thouless, Ordering, metastability and phase transitions in two-dimensional systems, *J. Phys. C Solid State Phys.* 6 (7) (1973) 1181–1203.
- [200] H.J. Schulz, Correlated fermions in one dimension, *Int. J. Mod. Phys. B* 5 (1991) 57–74.
- [201] C. Castellani, C. Di Castro, W. Metzner, Instabilities of anisotropic interacting Fermi systems, *Phys. Rev. Lett.* 69 (1992) 1703–1706.
- [202] P. Kopietz, V. Meden, K. Schönhammer, Anomalous scaling and spin-charge separation in coupled chains, *Phys. Rev. Lett.* 74 (1995) 2997–3000.
- [203] P. Kopietz, V. Meden, K. Schönhammer, Crossover between Luttinger and Fermi-liquid behavior in weakly coupled metallic chains, *Phys. Rev. B* 56 (1997) 7232–7244.
- [204] H.J. Schulz, Long-range Coulomb interactions in quasi-one-dimensional conductors, *J. Phys. C Solid State Phys.* 16 (35) (1983) 6769.
- [205] E. Jeckelmann, Dimensionality of metallic atomic wires on surfaces, *Phys. Rev. B* 101 (2020) 245153.
- [206] G.R. Stewart, Non-Fermi-liquid behavior in d - and f -electron metals, *Rev. Mod. Phys.* 73 (2001) 797–855.
- [207] S.-S. Lee, Recent developments in non-Fermi liquid theory, *Annu. Rev. Condens. Matter Phys.* 9 (1) (2018) 227–244.
- [208] M. Dressel, Electrodynamics of Bechgaard salts: optical properties of one-dimensional metals, *ISRN Condensed Matter Physics* 2012 (2012) 732973.
- [209] A. Sekiyama, A. Fujimori, S. Aonuma, H. Sawa, R. Kato, Fermi-liquid versus Luttinger-liquid behavior and metal-insulator transition in $\text{N,N}'$ -dicyanoquinonediimine-Cu salt studied by photoemission, *Phys. Rev. B* 51 (1995) 13899–13902.
- [210] L.K. Dash, A.J. Fisher, Does Luttinger liquid behaviour survive in an atomic wire on a surface? *J. Phys. Condens. Matter* 13 (22) (2001) 5035–5046.
- [211] D.F. Urban, C.A. Stafford, H. Grabert, Scaling theory of the Peierls charge density wave in metal nanowires, *Phys. Rev. B* 75 (2007) 205428.
- [212] T. Kwapiński, S. Kohler, P. Hänggi, Electron transport across a quantum wire in the presence of electron leakage to a substrate, *Eur. Phys. J. B* 78 (1) (2010) 75–81.
- [213] H.M. Lefcochilos-Fogelquist, O.R. Albertini, A.Y. Liu, Substrate-induced suppression of charge density wave phase in monolayer 1H-TaS_2 on $\text{Au}(111)$, *Phys. Rev. B* 99 (2019) 174113.
- [214] A. Abdelwahab, E. Jeckelmann, M. Hohenadler, Ground-state and spectral properties of an asymmetric Hubbard ladder, *Phys. Rev. B* 91 (2015) 155119.
- [215] A. Abdelwahab, E. Jeckelmann, Correlations and confinement of excitations in an asymmetric Hubbard ladder, *Eur. Phys. J. B* 91 (9) (2018) 207.
- [216] A. Abdelwahab, E. Jeckelmann, M. Hohenadler, Correlated atomic wires on substrates. I. Mapping to quasi-one-dimensional models, *Phys. Rev. B* 96 (2017) 035445.
- [217] T. Shirakawa, S. Yunoki, Block Lanczos density-matrix renormalization group method for general Anderson impurity models: application to magnetic impurity problems in graphene, *Phys. Rev. B* 90 (2014) 195109.
- [218] A. Allerdt, C.A. Büsser, G.B. Martins, A.E. Feiguin, Kondo versus indirect exchange: role of lattice and actual range of RKKY interactions in real materials, *Phys. Rev. B* 91 (2015) 085101.
- [219] K.G. Wilson, The renormalization group: critical phenomena and the Kondo problem, *Rev. Mod. Phys.* 47 (4) (1975) 773–840.
- [220] A. Abdelwahab, E. Jeckelmann, Effective narrow ladder model for two quantum wires on a semiconducting substrate, *Phys. Rev. B* 103 (2021) 245405.
- [221] A. Abdelwahab, E. Jeckelmann, M. Hohenadler, Correlated atomic wires on substrates. II. Application to Hubbard wires, *Phys. Rev. B* 96 (2017) 035446.
- [222] A. Abdelwahab, E. Jeckelmann, Luttinger liquid and charge density wave phases in a spinless fermion wire on a semiconducting substrate, *Phys. Rev. B* 98 (2018) 235138.
- [223] M. Gaudin, *The Bethe Wavefunction*, Cambridge University Press, 2014.
- [224] J. Des Cloizeaux, M. Gaudin, Anisotropic linear magnetic chain, *J. Math. Phys.* 7 (8) (1966) 1384–1400.
- [225] P. Donohue, M. Tsuchiizu, T. Giamarchi, Y. Suzumura, Spinless fermion ladders at half filling, *Phys. Rev. B* 63 (2001) 045121.
- [226] M. Fabrizio, Role of transverse hopping in a two-coupled-chains model, *Phys. Rev. B* 48 (1993) 15838–15860.
- [227] H. Yoshioka, Y. Suzumura, Roles of interchain hopping in two coupled chains of Tomonaga model, *J. Phys. Soc. Jpn.* 64 (10) (1995) 3811–3825.
- [228] D.J. Scalapino, Y. Imry, P. Pincus, Generalized Ginzburg-Landau theory of pseudo-one-dimensional systems, *Phys. Rev. B* 11 (1975) 2042–2048.
- [229] H. Shim, S.-Y. Yu, W. Lee, J.-Y. Koo, G. Lee, Control of phase transition in quasi-one-dimensional atomic wires by electron doping, *Appl. Phys. Lett.* 94 (23) (2009) 231901.
- [230] H. Morikawa, C.C. Hwang, H.W. Yeom, Controlled electron doping into metallic atomic wires: $\text{Si}(111) 4 \times 1$ -In, *Phys. Rev. B* 81 (2010) 075401.
- [231] W.G. Schmidt, M. Babilon, C. Thierfelder, S. Sanna, S. Wippermann, Influence of Na adsorption on the quantum conductance and metal-insulator transition of the In-Si(111)(4×1)-(8×2) nanowire array, *Phys. Rev. B* 84 (2011) 115416.
- [232] Y. Ergün, E. Jeckelmann, Grand-canonical Peierls theory for atomic wires on substrates, *Phys. Rev. B* 101 (2020) 085403.
- [233] E. Speiser, N. Esser, B. Halbig, J. Geurts, W.G. Schmidt, S. Sanna, Vibrational Raman spectroscopy on adsorbate-induced low-dimensional surface structures, *Surf. Sci. Rep.* 75 (1) (2020) 100480.
- [234] K. Yonemitsu, K. Nasu, Theory of photoinduced phase transitions in itinerant electron systems, *Phys. Rep.* 465 (1) (2008) 1.
- [235] B. Stoeckly, D.J. Scalapino, Statistical mechanics of Ginzburg-Landau fields for weakly coupled chains, *Phys. Rev. B* 11 (1975) 205–210.
- [236] V. Bärns, Ginzburg-Landau theory beyond the linear-chain approximation: the 2D case, *J. Phys. Condens. Matter* 18 (40) (2006) 9273–9286.
- [237] H. Risken, *The Fokker-Planck Equation Methods of Solution and Applications*, second ed., Springer, Berlin, Heidelberg, 1996.
- [238] H. Fujisaka, H. Tutu, P.A. Rikvold, Dynamic phase transition in a time-dependent Ginzburg-Landau model in an oscillating field, *Phys. Rev. E* 63 (2001) 036109.
- [239] D.J. Scalapino, M. Sears, R.A. Ferrell, Statistical mechanics of one-dimensional Ginzburg-Landau fields, *Phys. Rev. B* 6 (1972) 3409–3416.
- [240] T. Frigge, B. Hafke, T. Witte, B. Krenzer, C. Streubühr, A. Samad Syed, V. Mikšić Trontl, I. Avigo, P. Zhou, M. Ligges, D. von der Linde, U. Bovensiepen, M. Horn-von Hoegen, S. Wippermann, A. Lücke, S. Sanna, U. Gerstmann, W.G. Schmidt, Optically excited structural transition in atomic wires on surfaces at the quantum limit, *Nature* 544 (7649) (2017) 207–211.
- [241] M. Chávez-Cervantes, R. Krause, S. Aeschlimann, I. Gierz, Band structure dynamics in indium wires, *Phys. Rev. B* 97 (2018) 201401.
- [242] C.W. Nicholson, A. Lücke, W.G. Schmidt, M. Puppig, L. Rettig, R. Ernstorfer, M. Wolf, Beyond the molecular movie: dynamics of bands and bonds during a photoinduced phase transition, *Science* 362 (6416) (2018) 821–825.
- [243] M. Chávez-Cervantes, G.E. Topp, S. Aeschlimann, R. Krause, S.A. Sato, M. A. Sentef, I. Gierz, Charge density wave melting in one-dimensional wires with femtosecond subgap excitation, *Phys. Rev. Lett.* 123 (2019) 036405.
- [244] C.W. Nicholson, M. Puppig, A. Lücke, U. Gerstmann, M. Krenz, W.G. Schmidt, L. Rettig, R. Ernstorfer, M. Wolf, Excited-state band mapping and momentum-resolved ultrafast population dynamics in In/Si(111) nanowires investigated with XUV-based time- and angle-resolved photoemission spectroscopy, *Phys. Rev. B* 99 (2019) 155107.
- [245] J.G. Horstmann, H. Böckmann, B. Wit, F. Kurtz, G. Storeck, C. Ropers, Coherent control of a surface structural phase transition, *Nature* 583 (7815) (2020) 232–236.
- [246] R.N. Bhatt, W.L. McMillan, Theory of phonon dynamics near a charge-density-wave instability, *Phys. Rev. B* 12 (1975) 2042–2044.
- [247] H. Schäfer, V.V. Kabanov, M. Beyer, K. Biljakovic, J. Demsar, Disentanglement of the electronic and lattice parts of the order parameter in a 1D charge density wave system probed by femtosecond spectroscopy, *Phys. Rev. Lett.* 105 (2010) 066402.
- [248] H. Schaefer, V.V. Kabanov, J. Demsar, Collective modes in quasi-one-dimensional charge-density wave systems probed by femtosecond time-resolved optical studies, *Phys. Rev. B* 89 (2014) 045106.
- [249] W.L. McMillan, Theory of discommensurations and the commensurate-incommensurate charge-density-wave phase transition, *Phys. Rev. B* 14 (1976) 1496–1502.
- [250] S.A. Jackson, P.A. Lee, T.M. Rice, Triple point of the lock-in and onset transitions of charge-density waves, *Phys. Rev. B* 17 (1978) 3611–3615.
- [251] G. Travaglini, I. Mörke, P. Wachter, CDW evidence in one-dimensional $\text{K}_{0.3}\text{MoO}_3$ by means of Raman scattering, *Solid State Commun.* 45 (3) (1983) 289–292.
- [252] H. Kuzmany, Resonance Raman scattering from neutral and doped polyacetylene, *Phys. Status Solidi B* 97 (2) (1980) 521–531.

- [253] B. Horowitz, Infrared activity of Peierls systems and application to polyacetylene, *Solid State Commun.* 41 (10) (1982) 729–734.
- [254] J.P. Pouget, B. Hennion, C. Escribe-Filippini, M. Sato, Neutron-scattering investigations of the Kohn anomaly and of the phase and amplitude charge-density-wave excitations of the blue bronze $K_0.3\text{MoO}_3$, *Phys. Rev. B* 43 (1991) 8421–8430.
- [255] T. Lichtenstein, Z. Mamiyev, E. Jeckelmann, C. Tegenkamp, H. Pfnür, Anisotropic 2D metallicity: plasmons in Ge(100)-Au, *J. Phys. Condens. Matter* 31 (17) (2019) 175001.
- [256] F. Stern, Polarizability of a two-dimensional electron gas, *Phys. Rev. Lett.* 18 (1967) 546–548.
- [257] P.F. Williams, A.N. Bloch, Self-consistent dielectric response of a quasi-one-dimensional metal at high frequencies, *Phys. Rev. B* 10 (1974) 1097–1108.
- [258] A. Gold, Elementary excitations in multiple quantum wire structures, *Z. Phys. B Condens. Matter* 89 (2) (1992) 213–230.
- [259] T. Nagao, S. Yaginuma, T. Inaoka, T. Sakurai, One-dimensional plasmon in an atomic-scale metal wire, *Phys. Rev. Lett.* 97 (11) (2006) 116802.
- [260] R.K. Moudgil, V. Garg, K.N. Pathak, Confinement and correlation effects on plasmons in an atom-scale metallic wire, *J. Phys. Condens. Matter* 22 (13) (2010) 135003.
- [261] C.G. Hwang, N.D. Kim, S.Y. Shin, J.W. Chung, Possible evidence of non-Fermi liquid behaviour from quasi-one-dimensional indium nanowires, *New J. Phys.* 9 (8) (2007) 249, 249.
- [262] C. Liu, T. Inaoka, S. Yaginuma, T. Nakayama, M. Aono, T. Nagao, Disappearance of the quasi-one-dimensional plasmon at the metal-insulator phase transition of indium atomic wires, *Phys. Rev. B* 77 (20) (2008) 205415.
- [263] T. Block, C. Tegenkamp, J. Baringhaus, H. Pfnür, T. Inaoka, Plasmons in Pb nanowire arrays on Si(557): between one and two dimensions, *Phys. Rev. B* 84 (2011) 205402.
- [264] U. Krieg, C. Brand, C. Tegenkamp, H. Pfnür, One-dimensional collective excitations in Ag atomic wires grown on Si(557), *J. Phys. Condens. Matter* 25 (2013) 014013.
- [265] T. Lichtenstein, C. Tegenkamp, H. Pfnür, Lateral electronic screening in quasi-one-dimensional plasmons, *J. Phys. Condens. Matter* 28 (35) (2016) 354001.
- [266] S. Sanna, T. Lichtenstein, Z. Mamiyev, C. Tegenkamp, H. Pfnür, How one-dimensional are atomic gold chains on a substrate? *J. Phys. Chem. C* 122 (44) (2018) 25580–25588.
- [267] E.P. Rugeramigabo, C. Tegenkamp, H. Pfnür, T. Inaoka, T. Nagao, One-dimensional plasmons in ultrathin metallic silicide wires of finite width, *Phys. Rev. B* 81 (2010) 165407.
- [268] Q.P. Li, S. Das Sarma, R. Joynt, Elementary excitations in one-dimensional quantum wires: exact equivalence between the random-phase approximation and the Tomonaga-Luttinger model, *Phys. Rev. B* 45 (1992) 13713–13716.
- [269] G. Zhang, M. Takiguchi, K. Tateno, T. Tawara, M. Notomi, H. Gotoh, Telecom-band lasing in single InP/InAs heterostructure nanowires at room temperature, *Sci. Adv.* 5 (2) (2019) eaat8896.
- [270] J. Hicks, A. Tejada, A. Taleb-Ibrahimi, M. Nevius, F. Wang, K. Shepperd, J. Palmer, F. Bertran, P. Le Fevre, J. Kunc, et al., A wide-bandgap metal-semiconductor-metal nanostructure made entirely from graphene, *Nat. Phys.* 9 (1) (2013) 49–54.
- [271] J.N. Crain, A. Kirakosian, K.N. Altmann, C. Bromberger, S.C. Erwin, J. L. McChesney, J.-L. Lin, F.J. Himpsel, Fractional band filling in an atomic chain structure, *Phys. Rev. Lett.* 90 (17) (2003) 176805.
- [272] I. Song, D.-H. Oh, H.-C. Shin, S.-J. Ahn, Y. Moon, S.-H. Woo, H.J. Choi, C.-Y. Park, J.R. Ahn, Direct momentum-resolved observation of one-dimensional confinement of externally doped electrons within a single subnanometer-scale wire, *Nano Lett.* 15 (1) (2015) 281–288.
- [273] Z. Mamiyev, C. Fink, K. Holtgrewe, H. Pfnür, S. Sanna, Enforced long-range order in 1D wires by coupling to higher dimensions, *Phys. Rev. Lett.* 126 (2021) 106101.
- [274] R. Rechciński, M. Galicka, M. Simma, V.V. Volobuev, O. Caha, J. Sánchez-Barriga, P.S. Mandal, E. Golias, A. Varykhalov, O. Rader, G. Bauer, P. Kacman, R. Buczko, G. Springholz, Structure inversion asymmetry and Rashba effect in quantum confined topological crystalline insulator heterostructures, *Adv. Funct. Mater.* 31 (23) (2021) 2008885.
- [275] H. Okino, I. Matsuda, S. Yamazaki, R. Hobarra, S. Hasegawa, Transport in defective quasi-one-dimensional arrays of chains of gold atoms on a vicinal silicon surface, *Phys. Rev. B* 76 (2007) 035424.
- [276] S. Wippermann, W.G. Schmidt, Entropy explains metal-insulator transition of the Si(111)-In nanowire array, *Phys. Rev. Lett.* 105 (2010) 126102.
- [277] C. González, P. Snijders, J. Ortega, R. Pérez, F. Flores, S. Rogge, H. Weitering, Formation of atom wires on vicinal silicon, *Phys. Rev. Lett.* 93 (12) (2004) 126106.
- [278] T. Sekiguchi, S. Yoshida, K.M. Itoh, Self-assembly of parallel atomic wires and periodic clusters of silicon on a vicinal Si(111) surface, *Phys. Rev. Lett.* 95 (10) (2005) 106101.
- [279] M. Czubanowski, A. Schuster, S. Akbari, H. Pfnür, C. Tegenkamp, Adsorbate induced refacetting: Pb chains on Si(557), *New J. Phys.* 9 (11) (2007).
- [280] B. Hafke, T. Frigge, T. Witte, B. Krenzer, J. Aulbach, J. Schäfer, R. Claessen, S. C. Erwin, M. Horn-von Hoegen, Two-dimensional interaction of spin chains in the Si(553)-Au nanowire system, *Phys. Rev. B* 94 (16) (2016) 161403.
- [281] F. Edler, I. Miccoli, H. Pfnür, C. Tegenkamp, Charge-transfer transition in Au-induced quantum wires on Si(553), *Phys. Rev. B* 100 (2019) 045419.
- [282] C. Braun, S. Neufeld, U. Gerstmann, S. Sanna, J. Plaickner, E. Speiser, N. Esser, W. G. Schmidt, Vibration-driven self-doping of dangling-bond wires on Si(553)-Au surfaces, *Phys. Rev. Lett.* 124 (2020) 146802.
- [283] J.N. Crain, J.L. McChesney, F. Zheng, M.C. Gallagher, P.C. Snijders, M. Bissen, C. Gundelach, S.C. Erwin, F.J. Himpsel, Chains of gold atoms with tailored electronic states, *Phys. Rev. B* 69 (12) (2004) 125401.
- [284] J. Aulbach, S.C. Erwin, R. Claessen, J. Schäfer, Spin chains and electron transfer at stepped silicon surfaces, *Nano Lett.* 16 (4) (2016) 2698.
- [285] P. Segovia, D. Purdie, M. Hengsberger, Y. Baer, Observation of spin and charge collective modes in one-dimensional metallic chains, *Nature* 402 (1999) 504.
- [286] R. Losio, K.N. Altmann, A. Kirakosian, J.L. Lin, D.Y. Petrovykh, F.J. Himpsel, Band splitting for Si(557)-Au: is it spin-charge separation? *Phys. Rev. Lett.* 86 (20) (2001) 4632–4635.
- [287] T. Oguchi, Quasi-one-dimensional nature of the Rashba states of Au wires on Si(557) surface, *J. Electron. Spectrosc. Relat. Phenom.* 201 (2015) 18–22.
- [288] M. Krawiec, Spin-orbit splitting in the Si(335)-Au surface, *Surf. Sci.* 609 (C) (2013) 44–47.
- [289] H.W. Yeom, S.W. Jung, J.S. Shin, J. Kim, K.S. Kim, K. Miyamoto, T. Okuda, H. Namatame, A. Kimura, M. Taniguchi, Direct observation of the spin polarization in Au atomic wires on Si(553), *New J. Phys.* 16 (9) (2014) 093030.
- [290] M. Krawiec, M. Kopciuszynski, R. Zdyb, Different spin textures in one-dimensional electronic bands on Si(553)-Au surface, *Appl. Surf. Sci.* 373 (2016) 26–31.
- [291] S.C. Erwin, P.C. Snijders, Silicon spin chains at finite temperature: dynamics of Si(553)-Au, *Phys. Rev. B* 87 (23) (2013) 235316.
- [292] S. Polei, P.C. Snijders, S.C. Erwin, F.J. Himpsel, K.H. Meiwes-Broer, I. Barke, Structural transition in atomic chains driven by transient doping, *Phys. Rev. Lett.* 111 (2013) 156801.
- [293] S. Polei, P.C. Snijders, K.H. Meiwes-Broer, I. Barke, Current-dependent periodicities of Si(553)-Au, *Phys. Rev. B* 89 (20) (2014) 205420.
- [294] C. Braun, C. Hogan, S. Chandola, N. Esser, S. Sanna, W.G. Schmidt, Si(775)-Au atomic chains: geometry, optical properties, and spin order, *Phys. Rev. Mater.* 1 (2017) 055002.
- [295] C. Hogan, E. Speiser, S. Chandola, S. Suchkova, J. Aulbach, J. Schäfer, S. Meyer, R. Claessen, N. Esser, Controlling the local electronic properties of Si(553)-Au through hydrogen doping, *Phys. Rev. Lett.* 120 (2018) 166801.
- [296] Z. Mamiyev, S. Sanna, T. Lichtenstein, C. Tegenkamp, H. Pfnür, Extrinsic doping on the atomic scale: tuning metallicity in atomic Au chains, *Phys. Rev. B* 98 (2018) 245414.
- [297] J.N. Crain, D.T. Pierce, End states in one-dimensional atom chains, *Science* 307 (2005) 703.
- [298] J.R. Ahn, P.G. Kang, K.D. Ryang, H.W. Yeom, Coexistence of two different Peierls distortions within an atomic scale wire: Si(553)-Au, *Phys. Rev. Lett.* 95 (2005) 196402.
- [299] P.C. Snijders, S. Rogge, H.H. Weitering, Competing periodicities in fractionally filled one-dimensional bands, *Phys. Rev. Lett.* 96 (2006) 076801.
- [300] J.N. Crain, M.D. Stiles, J.A. Stroscio, D.T. Pierce, Electronic effects in the length distribution of atom chains, *Phys. Rev. Lett.* 96 (2006) 156801.
- [301] K.-D. Ryang, P.G. Kang, H.W. Yeom, S. Jeong, Structures and defects of atomic wires on Si(553)-Au: an STM and theoretical study, *Phys. Rev. B* 76 (2007) 205325.
- [302] J. Aulbach, S.C. Erwin, J. Kemmer, M. Bode, J. Schäfer, R. Claessen, Parity breaking in a double atomic chain system, *Phys. Rev. B* 96 (2017) 081406.
- [303] S. Ghose, I. Robinson, P. Bennett, F. Himpsel, Structure of double row quantum wires in Au/Si(553), *Surf. Sci.* 581 (2) (2005) 199.
- [304] S. Riikonen, D. Sanchez-Portal, Systematic investigation of the structure of the Si(553)-Au surface from first principles, *Phys. Rev. B* 77 (2008) 165418.
- [305] M. Krawiec, Structural model of the Au-induced Si(553) surface: double Au rows, *Phys. Rev. B* 81 (11) (2010) 115436.
- [306] C. Braun, U. Gerstmann, S. Wg, Spin pairing versus spin chains at Si(553)-Au surfaces, *Phys. Rev. B* 98 (2018) 121402.
- [307] I. Barke, F. Zheng, T.K. Rügheimer, F.J. Himpsel, Experimental evidence for spin-split bands in a one-dimensional chain structure, *Phys. Rev. Lett.* 97 (2006) 226405.
- [308] M.D. Pashley, Electron counting model and its application to island structures on molecular-beam epitaxy grown GaAs(001) and ZnSe(001), *Phys. Rev. B* 40 (1989) 10481.
- [309] D.J. Chadi, Stabilities of single-layer and bilayer steps on Si(001) surfaces, *Phys. Rev. Lett.* 59 (1987) 1691–1694.
- [310] P. Krüger, J. Pollmann, Dimer reconstruction of Diamond, Si, and Ge(001) surfaces, *Phys. Rev. Lett.* 74 (1995) 1155–1158.
- [311] G.-X. Qian, R.M. Martin, D.J. Chadi, Stoichiometry and surface reconstruction: an ab initio study of GaAs(100) surfaces, *Phys. Rev. Lett.* 60 (1988) 1962–1965.
- [312] W. Mönch, *Semiconductor Surfaces and Interfaces*, Springer-Verlag, 1995.
- [313] V. Derycke, P.G. Soukiasian, F. Amy, Y.J. Chabal, M.D. D'angelo, H.B. Enriquez, M.G. Silly, Nanochemistry at the atomic scale revealed in hydrogen-induced semiconductor surface metallization, *Nat. Mater.* 2 (4) (2003) 253–258.
- [314] J. Xiao, A. Kuc, T. Frauenheim, T. Heine, Stabilization mechanism of ZnO nanoparticles by Fe doping, *Phys. Rev. Lett.* 112 (2014) 106102.
- [315] J.P. Perdew, K. Burke, M. Ernzerhof, Generalized gradient approximation made simple, *Phys. Rev. Lett.* 77 (1996) 3865.
- [316] J.P. Perdew, A. Ruzsinszky, G.I. Csonka, O.A. Vydrov, G.E. Scuseria, L. A. Constantin, X. Zhou, K. Burke, Restoring the density-gradient expansion for exchange in solids and surfaces, *Phys. Rev. Lett.* 100 (2008) 136406.
- [317] J.P. Perdew, A. Zunger, Self-interaction correction to density-functional approximation for many-electron systems, *Phys. Rev. B* 23 (1981) 5048.
- [318] P.V.C. Medeiros, S. Stafström, J. Björk, Effects of extrinsic and intrinsic perturbations on the electronic structure of graphene: retaining an effective primitive cell band structure by band unfolding, *Phys. Rev. B* 89 (2014) 041407.

- [319] K. Biedermann, S. Regensburger, T. Fauster, F.J. Himpsel, S.C. Erwin, Spin-split silicon states at step edges of Si(553)-Au, *Phys. Rev. B* 85 (24) (2012) 245413.
- [320] W.H. Choi, P.G. Kang, K.D. Ryang, H.W. Yeom, Bandstructure engineering of gold atomic wires on silicon by controlled doping, *Phys. Rev. Lett.* 100 (2008) 126801.
- [321] J.R. Ahn, H.W. Yeom, H.S. Yoon, I.-W. Lyo, Metal-insulator transition in Au atomic chains on Si with two proximal bands, *Phys. Rev. Lett.* 91 (2003) 196403.
- [322] H.W. Yeom, J.R. Ahn, H.S. Yoon, I.-W. Lyo, H. Jeong, S. Jeong, Real-space investigation of the metal-insulator transition of Si(557)-Au, *Phys. Rev. B* 72 (2005) 035323.
- [323] S. Riikonen, D. Sánchez-Portal, Interplay between electronic and atomic structures in the Si(557)-Au reconstruction from first principles, *Phys. Rev. B* 76 (2007) 035410.
- [324] B. Hafke, C. Brand, T. Witte, B. Sothmann, M. Horn-von Hoegen, S.C. Erwin, Thermally induced crossover from 2D to 1D behavior in an array of atomic wires: silicon dangling-bond solitons in Si(553)-Au, *Phys. Rev. Lett.* 124 (2010) 016102.
- [325] E. Speiser, J. Plaickner, S. Chandola, N. Esser, B. Halbig, J. Geurts, Raman spectroscopy on surface phonons of Si(hhk) surfaces modified by Au submonolayers, *Phys. Status Solidi* 256 (2) (2019) 1800341.
- [326] J. Plaickner, E. Speiser, C. Braun, W.G. Schmidt, N. Esser, S. Sanna, Surface localized phonon modes at the Si(553)-Au nanowire system, *Phys. Rev. B* 103 (2021) 115441.
- [327] C. Tegenkamp, T. Ohta, J.L. McChesney, H. Dil, E. Rotenberg, H. Pfnür, K. Horn, Coupled Pb chains on Si(557): origin of one-dimensional conductance, *Phys. Rev. Lett.* 100 (7) (2008) 076802.
- [328] S. Wippermann, N. Koch, W.G. Schmidt, Adatom-induced conductance modification of in nanowires: potential-well scattering and structural effects, *Phys. Rev. Lett.* 100 (2008) 106802.
- [329] C. Tegenkamp, D. Lükermann, S. Akbari, M. Czubanowski, A. Schuster, H. Pfnür, Pb nanowires on vicinal Si(111) surfaces: effects of refacetting on transport, *Phys. Rev. B* 82 (20) (2010) 205413.
- [330] U. Krieg, T. Lichtenstein, C. Brand, C. Tegenkamp, H. Pfnür, Origin of metallicity in atomic Ag wires on Si(557), *New J. Phys.* 17 (4) (2015) 043062.
- [331] F. Edler, I. Miccoli, J.P. Stöckmann, H. Pfnür, C. Braun, S. Neufeld, S. Sanna, W. G. Schmidt, C. Tegenkamp, Tuning the conductivity along atomic chains by selective chemisorption, *Phys. Rev. B* 95 (2017) 125409.
- [332] T. Lichtenstein, Z. Mamiyev, C. Braun, S. Sanna, W.G. Schmidt, C. Tegenkamp, H. Pfnür, Probing quasi-one-dimensional band structures by plasmon spectroscopy, *Phys. Rev. B* 97 (2018) 165421.
- [333] P. Yogi, J. Koch, S. Sanna, H. Pfnür, Electronic phase transitions in quasi-one-dimensional atomic chains: Au wires on Si(553), *Phys. Rev. B* 105 (2022) 235407.
- [334] F. Edler, I. Miccoli, H. Pfnür, C. Tegenkamp, Space charge layer effects in silicon studied by in situ surface transport, *J. Phys. Condens. Matter* 31 (2019) 214001.
- [335] J.W. Park, J.S. Shin, S.K. Song, H.W. Yeom, Discovering fractional mobile solitons along trimer atomic chains, *Nat. Nanotechnol.* 17 (2022) 244.
- [336] J. Kraft, M.G. Ramsey, F.P. Netzer, Surface reconstructions of In on Si(111), *Phys. Rev. B* 55 (1997) 5384–5393.
- [337] F.J. Himpsel, K.N. Altmann, R. Bennewitz, J.N. Crain, A. Kirakosian, J.-L. Lin, J. L. McChesney, One-dimensional electronic states at surfaces, *J. Phys. Condens. Matter* 13 (49) (2001) 11097–11113.
- [338] J.J. Lander, J. Morrison, Surface reactions of silicon(111) with aluminum and indium, *J. Appl. Phys.* 36 (5) (1965) 1706–1713.
- [339] O. Bunk, G. Falkenberg, J.H. Zeysing, L. Lottermoser, R.L. Johnson, M. Nielsen, F. Berg-Rasmussen, J. Baker, R. Feidenhans'l, Structure determination of the indium-induced Si(111) – (4 × 1) reconstruction by surface x-ray diffraction, *Phys. Rev. B* 59 (1999) 12228–12231.
- [340] K. Sakamoto, H. Ashima, H.W. Yeom, W. Uchida, Angle-resolved high-resolution electron-energy-loss study of In-adsorbed Si(111)-(4 × 1) and -(8 × 2) surfaces, *Phys. Rev. B* 62 (2000) 9923.
- [341] T. Uchihashi, U. Ramsperger, Electron conduction through quasi-one-dimensional indium wires on silicon, *Appl. Phys. Lett.* 80 (2002) 4169–4171.
- [342] T. Tanikawa, I. Matsuda, T. Kanagawa, S. Hasegawa, Surface-state electrical conductivity at a metal-insulator transition on silicon, *Phys. Rev. Lett.* 93 (2004) 016801.
- [343] S.J. Park, H.-W. Yeom, S.-H. Min, D.-H. Park, I.-W. Lyo, Direct evidence of the charge ordered phase transition of indium nanowires on Si(111), *Phys. Rev. Lett.* 93 (2004) 106402.
- [344] T. Shibusaki, N. Nagamura, T. Hirahara, H. Okino, Phase transition temperatures determined by different experimental methods: Si(111) 4x1-In surface with defects, *Phys. Rev. B* 81 (2010) 035314.
- [345] A. Lücke, U. Gerstmann, T.D. Kühne, W.G. Schmidt, Efficient PAW-based bond strength analysis for understanding the In/Si(111)(8 × 2) – (4 × 1) phase transition, *J. Comput. Chem.* 38 (26) (2017) 2276–2282.
- [346] Y. Terada, S. Yoshida, A. Okubo, K. Kanazawa, M. Xu, O. Takeuchi, H. Shigekawa, Optical doping: active control of metal-insulator transition in nanowire, *Nano Lett.* 8 (11) (2008) 3577–3581.
- [347] K. Fleischer, S. Chandola, N. Esser, W. Richter, J.F. McGilp, Phonon and polarized reflectance spectra from Si(111)-(4 × 1)In: evidence for a charge-density-wave driven phase transition, *Phys. Rev. B* 67 (2003) 235318.
- [348] I. Gregora, J. Hlinka, B. Brezina, Amplitudon mode in deuterated thiourea by Raman scattering, *Ferroelectrics* 302 (1) (2004) 155–157.
- [349] D.H. Torchinsky, F. Mahmood, A.T. Bollinger, I. Božović, N. Gedik, Fluctuating charge-density waves in a cuprate superconductor, *Nat. Matters* 12 (2013) 387–391.
- [350] Y.K. Kato, R.C. Myers, A.C. Gossard, D.D. Awschalom, Observation of the spin Hall effect in semiconductors, *Science* 306 (5703) (2004) 1910.
- [351] M. König, S. Wiedmann, C. Brüne, A. Roth, H. Buhmann, L.W. Molenkamp, X.-L. Qi, S.-C. Zhang, Quantum spin Hall insulator state in HgTe quantum wells, *Science* 318 (5851) (2007) 766.
- [352] D. Hsieh, D. Qian, L. Wray, Y. Xia, Y.S. Hor, R.J. Cava, M.Z. Hasan, A topological Dirac insulator in a quantum spin Hall phase, *Nature* 452 (7190) (2008) 970–974.
- [353] J.C.R. Sánchez, L. Vila, G. Desfonds, S. Gambarelli, J.P. Attané, J.M. De Teresa, C. Magén, A. Fert, Spin-to-charge conversion using Rashba coupling at the interface between non-magnetic materials, *Nat. Commun.* 4 (1) (2013) 2944.
- [354] A.F. Santander-Syro, F. Fortuna, C. Baille, T.C. Rödel, G. Landolt, N.C. Plumb, J. H. Dil, M. Radović, Giant spin splitting of the two-dimensional electron gas at the surface of SrTiO₃, *Nat. Mater.* 13 (12) (2014) 1085–1090.
- [355] J. Sinova, I. Žutić, New moves of the spintronics tango, *Nat. Mater.* 11 (5) (2012) 368–371.
- [356] P. Larson, I.I. Mazin, D.A. Papaconstantopoulos, Calculation of magnetic anisotropy energy in SmCo₅, *Phys. Rev. B* 67 (2003) 214405.
- [357] B.J. Kim, H. Jin, S.J. Moon, J.-Y. Kim, B.-G. Park, C.S. Leem, J. Yu, T.W. Noh, C. Kim, S.-J. Oh, J.-H. Park, V. Durairaj, G. Cao, E. Rotenberg, Novel $J_{\text{eff}} = 1/2$ Mott state induced by relativistic spin-orbit coupling in Sr₂IrO₄, *Phys. Rev. Lett.* 101 (2008) 076402.
- [358] J.J. Yang, Y.J. Choi, Y.S. Oh, A. Hogan, Y. Horibe, K. Kim, B.I. Min, S.-W. Cheong, Charge-orbital density wave and superconductivity in the strong spin-orbit coupled IrTe₂: Pd, *Phys. Rev. Lett.* 108 (2012) 116402.
- [359] T. Das, Spin-orbit density wave induced hidden topological order in URu₂Si₂, *Sci. Rep.* 2 (1) (2012) 596.
- [360] M. Hupalo, T.L. Chan, C.Z. Wang, K.M. Ho, M.C. Tringides, Atomic models, domain-wall arrangement, and electronic structure of the dense Pb/Si(111) – $\sqrt{3} \times \sqrt{3}$ phase, *Phys. Rev. B* 66 (2002) 161410.
- [361] M. Hupalo, J. Schmalian, M.C. Tringides, “Devil’s Staircase” in Pb/Si(111) ordered phases, *Phys. Rev. Lett.* 90 (21) (2003) 216106.
- [362] T. Zhang, P. Cheng, W.-J. Li, Y.-J. Sun, G. Wang, X.-G. Zhu, K. He, L. Wang, X. Ma, X. Chen, Y. Wang, Y. Liu, H.-Q. Lin, J.-F. Jia, Q.-K. Xue, Superconductivity in one-atomic-layer metal films grown on Si(111), *Nat. Phys.* 6 (2010) 104.
- [363] M. Kopciuszynski, P. Dymiec, M. Krawiec, P. Łukasik, M. Jałochowski, R. Zdyb, Pb nanoribbons on the Si(553) surface, *Phys. Rev. B* 88 (15) (2013) 155431.
- [364] M. Kopciuszynski, P. Łukasik, R. Zdyb, M. Jałochowski, Ordering of the Si(553) surface with Pb atoms, *Appl. Surf. Sci.* 305 (2014) 139–142.
- [365] M. Kopciuszynski, M. Krawiec, R. Zdyb, M. Jałochowski, Purely one-dimensional bands with a giant spin-orbit splitting: Pb nanoribbons on Si(553) surface, *Sci. Rep.* 7 (2017) 46215.
- [366] L. Żurawek, M. Kopciuszynski, M. Dachniewicz, M. Stróżak, M. Krawiec, M. Jałochowski, R. Zdyb, Partially embedded Pb chains on a vicinal Si(113) surface, *Phys. Rev. B* 101 (May 2020) 195434.
- [367] C. Brand, S. Muff, M. Fanciulli, H. Pfnür, M.C. Tringides, J.H. Dil, C. Tegenkamp, Spin-resolved band structure of a densely packed Pb monolayer on Si(111), *Phys. Rev. B* 96 (3) (2017) 035432.
- [368] H. Morikawa, K.S. Kim, D.Y. Jung, H.W. Yeom, Scanning tunneling microscopy observation of Pb-induced superstructures on Si(557), *Phys. Rev. B* 76 (16) (2007) 165406.
- [369] C. Tegenkamp, H. Pfnür, Switching between one- and two-dimensional conductance: coupled chains in the monolayer of Pb on Si(557), *Surf. Sci.* 601 (13) (2007) 2641–2646.
- [370] M. Quentin, T.T.N. Nguyen, H. Pfnür, C. Tegenkamp, Electronic correlation effects in Pb quantum wires on Si(557), *Phys. Rev. B* 102 (2020) 035438.
- [371] C. Tegenkamp, Z. Kallassy, H. Pfnür, H.-L. Günter, V. Zielasek, M. Henzler, Switching between one and two dimensions: conductivity of Pb-induced chain structures on Si(557), *Phys. Rev. Lett.* 95 (2005) 176804.
- [372] H. Pfnür, C. Tegenkamp, M. Czubanowski, D. Lükermann, J. Rönspies, S. Wießell, Correlation of geometrical and electronic properties in metallic nanowires, *Phys. Status Solidi B* 247 (10) (2010) 2509–2521.
- [373] M. Yakes, V. Yeh, M. Hupalo, M.C. Tringides, Self-organization at finite temperatures of the devil’s staircase in Pb/Si(111), *Phys. Rev. B* 69 (2004) 224103.
- [374] M. Czubanowski, H. Pfnür, C. Tegenkamp, Atomic chain ordering with ultra-long periods: Pb/Si(557), *Surf. Sci.* 603 (19) (2009) L121–L124.
- [375] M. Ligges, M. Sandhofer, I. Sklyadneva, R. Heid, K.-P. Bohnen, S. Freutel, L. Rettig, P. Zhou, P.M. Echenique, E.V. Chulkov, U. Bovensiepen, Electron-phonon coupling in quantum-well states of the Pb/Si(111) system, *J. Phys. Condens. Matter* 26 (35) (2014) 352001.
- [376] A.S. Syed, V. Mikšić Trontl, M. Ligges, S. Sakong, P. Kratzer, D. Lükermann, P. Zhou, I. Avigo, H. Pfnür, C. Tegenkamp, U. Bovensiepen, Unoccupied electronic structure and momentum-dependent scattering dynamics in Pb/Si(557) nanowire arrays, *Phys. Rev. B* 92 (2015) 134301.
- [377] M.H. Upton, C.M. Wei, M.Y. Chou, T. Miller, T.-C. Chiang, Thermal stability and electronic structure of atomically uniform pb films on Si(111), *Phys. Rev. Lett.* 93 (2004) 026802.
- [378] P.S. Kirchmann, L. Rettig, X. Zubizarreta, V.M. Silkin, E.V. Chulkov, U. Bovensiepen, Quasiparticle lifetimes in metallic quantum-well nanostructures, *Nat. Phys.* 6 (2010) 782–785.
- [379] T. Valla, A.V. Fedorov, P.D. Johnson, S.L. Hulbert, Many-body effects in angle-resolved photoemission: quasiparticle energy and lifetime of a Mo(110) surface state, *Phys. Rev. Lett.* 83 (1999) 2085–2088.
- [380] P.S. Kirchmann, L. Rettig, D. Nandi, U. Lipowski, M. Wolf, U. Bovensiepen, A time-of-flight spectrometer for angle-resolved detection of low energy electrons in two dimensions, *Appl. Phys. A* 91 (2) (2008) 211–217.

- [381] U. Bovensiepen, P.S. Kirchmann, Elementary relaxation processes investigated by femtosecond photoelectron spectroscopy of two-dimensional materials, *Laser Photon. Rev.* 6 (5) (2012) 589–606.
- [382] M. Sandhofer, I.Y. Sklyadneva, V. Sharma, V.M. Trontl, P. Zhou, M. Ligges, R. Heid, K.-P. Bohnen, E.V. Chulkov, U. Bovensiepen, Unoccupied electronic structure and relaxation dynamics of Pb/Si(111), *J. Electron. Spectrosc. Relat. Phenom.* 195 (2014) 278–284.
- [383] M. Roth, M. Pickel, W. Jinxiong, M. Weinelt, T. Fauster, Electron scattering at steps: image-potential states on Cu(119), *Phys. Rev. Lett.* 88 (2002) 096802.
- [384] A. Mugarza, J.E. Ortega, Electronic states at vicinal surfaces, *J. Phys. Condens. Matter* 15 (47) (2003) S3281–S3310.
- [385] J.E. Ortega, M. Ruiz-Osés, J. Cordón, A. Mugarza, J. Kuntze, F. Schiller, One-dimensional versus two-dimensional electronic states in vicinal surfaces, *New J. Phys.* 7 (2005) 101, 101.
- [386] R.C. Dynes, V. Narayanamurti, J.P. Garno, Direct measurement of quasiparticle-lifetime broadening in a strong-coupled superconductor, *Phys. Rev. Lett.* 41 (1978) 1509–1512.
- [387] F.c. v. Herman, R. Hlubina, Microscopic interpretation of the Dynes formula for the tunneling density of states, *Phys. Rev. B* 94 (2016) 144508.
- [388] F. Ming, T.S. Smith, S. Johnston, P.C. Snijders, H.H. Weitering, Zero-bias anomaly in nanoscale hole-doped mott insulators on a triangular silicon surface, *Phys. Rev. B* 97 (2018) 075403.
- [389] G. Li, B. Movaghar, A. Nitzan, M.A. Ratner, Polaron formation: Ehrenfest dynamics vs. exact results, *J. Chem. Phys.* 138 (4) (2013).
- [390] M. Czubanowski, A. Schuster, H. Pfnür, C. Tegenkamp, Temperature-driven refacetting phase transition in Pb chains on Si(557), *Phys. Rev. B* 77 (2008) 174108.
- [391] U. Fano, Effects of configuration interaction on intensities and phase shifts, *Phys. Rev.* 124 (1961) 1866–1878.
- [392] D. Lükermann, M. Gauch, M. Czubanowski, H. Pfnür, C. Tegenkamp, Magnetotransport in anisotropic Pb films and monolayers, *Phys. Rev. B* 81 (2010) 125429.
- [393] P. Kröger, D. Abdelbarey, M. Siemens, D. Lükermann, S. Sologub, H. Pfnür, C. Tegenkamp, Controlling conductivity by quantum well states in ultrathin Bi (111) films, *Phys. Rev. B* 97 (2018) 045403.
- [394] D. Abdelbarey, J. Koch, Z. Mamiyev, C. Tegenkamp, H. Pfnür, Thickness-dependent electronic transport through epitaxial nontrivial Bi quantum films, *Phys. Rev. B* 102 (2020) 115409.
- [395] O. Pfennigstorf, A. Petkova, H.L. Guenter, M. Henzler, Conduction mechanism in ultrathin metallic films, *Phys. Rev. B* 65 (2002) 045412.
- [396] O. Pfennigstorf, A. Petkova, Z. Kallassy, M. Henzler, Conductivity of ultrathin Pb films during growth on Si(111) at low temperatures, *Eur. Phys. J. B* 30 (1) (2002) 111–115.
- [397] T.T.N. Nguyen, N. de Vries, H. Karakachian, M. Gruschwitz, J. Aproz, A. A. Zakharov, C. Polley, T. Balasubramanian, U. Starke, C.F.J. Flipse, C. Tegenkamp, Topological surface state in epitaxial zigzag graphene nanoribbons, *Nano Lett.* 21 (7) (2021) 2876–2882.
- [398] J.H. Dil, Spin and angle resolved photoemission on non-magnetic low-dimensional systems, *J. Phys. Condens. Matter* 21 (40) (2009) 403001.
- [399] S.A. Tarasenko, Scattering induced spin orientation and spin currents in gyrotropic structures, *JETP Lett.* 84 (4) (2006) 199–203.
- [400] D. Pines, D. Bohm, A collective description of electron interactions: II. Collective vs. individual particle aspects of the interactions, *Phys. Rev.* 85 (1952) 338–353.
- [401] D. Pines, Collective energy losses in solids, *Rev. Mod. Phys.* 28 (1952) 184–198.
- [402] T. Nagao, S. Yaginuma, T. Inaoka, T. Sakurai, D. Jeon, Sound-wave-like collective electronic excitations in Au atom chains, *J. Phys. Soc. Japan* 76 (2007) 114714.
- [403] J.M. Pitarke, V.M. Silkin, E.V. Chulkov, P.M. Echenique, Theory of surface plasmons and surface-plasmon polaritons, *Rep. Prog. Phys.* 70 (2007) 1–87.
- [404] V.M. Silkin, A. Garcia-Lekue, J.M. Pitarke, E.V. Chulkov, E. Zaremba, P. M. Echenique, Novel low-energy collective excitation at metal surfaces, *Europhys. Lett.* 66 (2004) 260.
- [405] J. Chen, M. Badioli, P. Alonso-González, S. Thongrattanasiri, F. Huth, J. Osmond, M. Spasenovic, A. Centeno, A. Pesquera, P. Godignon, A.Z. Elorza, N. Camara, F. J. Garcia de Abajo, R. Hillenbrand, F.H.L. Koppens, Optical nano-imaging of gate-tunable graphene plasmons, *Nature* 487 (2012) 77.
- [406] Z. Fei, A.S. Rodin, G.O. Andreev, W. Bao, A.S. McLeod, M. Wagner, L.M. Zhang, Z. Zhao, M. Thieme, G. Dominguez, M.M. Fogler, A.H. Castro Neto, C.N. Lau, F. Keilmann, D.N. Basov, Gate-tuning of graphene plasmons revealed by infrared nano-imaging, *Nature* 487 (2012) 82.
- [407] S. Law, L. Yu, A. Rosenberg, D. Wasserman, All-semiconductor plasmonic nanoantennas for infrared sensing, *Nano Lett.* 13 (2013) 4569.
- [408] H. Ibach, D.L. Mills, *Electron Energy Loss Spectroscopy and Surface Vibrations*, Academic Press, 1982.
- [409] A. Bill, H. Morawitz, V.Z. Kresin, Electronic collective modes and superconductivity in layered conductors, *Phys. Rev. B* 68 (2003) 144519.
- [410] B. Diaconescu, K. Pohl, L. Vattuone, L. Savio, P. Hofmann, V.M. Silkin, J. M. Pitarke, E.V. Chulkov, P.M. Echenique, D. Farias, et al., Low-energy acoustic plasmons at metal surfaces, *Nature* 448 (7149) (2007) 57–59.
- [411] S. Park, R. Palmer, Acoustic plasmon on the Au(111) surface, *Phys. Rev. Lett.* 105 (2010) 016801.
- [412] K. Pohl, B. Diaconescu, G. Vercelli, L. Vattuone, V.M. Silkin, E.V. Chulkov, P. M. Echenique, M. Rocca, Acoustic surface plasmon on Cu(111), *Europhys. Lett.* 90 (2010) 57006.
- [413] M. Jahn, M. Müller, M. Endlich, N. Neel, J. Kröger, V. Chis, B. Hellsing, Oxygen vibrations and acoustic surface plasmon on Be(0001), *Phys. Rev. B* 86 (2012) 085453.
- [414] L. Vattuone, M. Smerieri, T. Langer, C. Tegenkamp, H. Pfnür, V.M. Silkin, E. V. Chulkov, P.M. Echenique, M. Rocca, Correlated motion of electrons on the Au (111) surface: anomalous acoustic surface plasmon dispersion and single-particle excitations, *Phys. Rev. Lett.* 110 (2013) 127405.
- [415] M. Smerieri, L. Vattuone, L. Savio, T. Langer, C. Tegenkamp, H. Pfnür, V. M. Silkin, M. Rocca, Anisotropic dispersion and partial localization of acoustic surface plasmons on an atomically stepped surface: Au(788), *Phys. Rev. Lett.* 113 (18) (2014) 186804.
- [416] T. Langer, J. Baringhaus, H. Pfnür, H.W. Schumacher, C. Tegenkamp, Plasmon damping below the Landau regime: the role of defects in epitaxial graphene, *New J. Phys.* 12 (2010) 033017.
- [417] A. Politano, A.R. Marino, V. Formoso, D. Farias, R. Miranda, G. Chiarello, Evidence for acoustic-like plasmons on epitaxial graphene on Pt(111), *Phys. Rev. B* 84 (2011) 033401.
- [418] S. Das Sarma, E.H. Hwang, L. Zheng, Plasmon-pole approximation for semiconductor quantum-wire electrons, *Phys. Rev. B* 54 (1996) 8057–8063.
- [419] T. Nagao, Characterization of atomic-level plasmonic structures by low-energy EELS, *Surf. Interface Anal.* 40 (2008) 1764–1767.
- [420] T. Inaoka, Predicted energy-loss spectrum of low-dimensional plasmons in a metallic strip monolayer on a semiconductor surface, *Phys. Rev. B* 71 (2005) 115305.
- [421] T. Lichtenstein, J. Aulbach, J. Schäfer, R. Claessen, C. Tegenkamp, H. Pfnür, Two-dimensional crossover and strong coupling of plasmon excitations in arrays of one-dimensional atomic wires, *Phys. Rev. B* 93 (16) (2016) 161408.
- [422] H. Claus, A. Büssenschütt, M. Henzler, Low-energy electron diffraction with energy resolution, *Rev. Sci. Instrum.* 63 (1992) 2195.
- [423] T. Nagao, T. Hildebrandt, M. Henzler, S. Hasegawa, Dispersion and damping of a two-dimensional plasmon in a metallic surface-state band, *Phys. Rev. Lett.* 86 (2001) 5747–5750.
- [424] Z. Mamiyev, C. Tegenkamp, H. Pfnür, Plasmon localization by adatoms in gold atomic wires on Si(775), *J. Phys. Condens. Matter* 33 (20) (2021) 205001.
- [425] U. Krieg, Y. Zhang, C. Tegenkamp, H. Pfnür, Tuning of one-dimensional plasmons by Ag-doping in Ag-ordered atomic wires, *New J. Phys.* 16 (4) (2014) 043007.
- [426] C.W. Nicholson, C. Monney, U. Krieg, C. Tegenkamp, H. Pfnür, K. Horn, M. Wolf, Electronic structure of self-assembled Ag nanowires on Si(557): spectroscopic evidence for dimensionality, *New J. Phys.* 17 (2015) 093025.
- [427] C. González, F. Flores, J. Ortega, Soft phonon, dynamical fluctuations, and a reversible phase transition: indium chains on silicon, *Phys. Rev. Lett.* 96 (2006) 136101.
- [428] C. Blumenstein, S. Meyer, A. Ruff, B. Schmid, J. Schäfer, R. Claessen, High purity chemical etching and thermal passivation process for Ge(001) as nanostructure template, *J. Chem. Phys.* 135 (2011) 64201.
- [429] T. Lichtenstein, H. Teiken, H. Pfnür, J. Wollschläger, C. Tegenkamp, Au-chains grown on Ge(100): a detailed SPA-LEED study, *Surf. Sci.* 632 (2015) 64–70.
- [430] J. Wang, M. Li, E.I. Altman, Scanning tunneling microscopy study of self-organized Au atomic chain growth on Ge(001), *Phys. Rev. B* 70 (2004) 233312.
- [431] J. Wang, M. Li, E. Altman, Scanning tunneling microscopy study of Au growth on Ge(001): bulk migration, self-organization, and clustering, *Surf. Sci.* 596 (2005) 126–143.
- [432] J. Schäfer, C. Blumenstein, S. Meyer, M. Wisniewski, R. Claessen, New model system for a one-dimensional electron liquid: self-organized atomic gold chains on Ge(001), *Phys. Rev. Lett.* 101 (2008) 236802.
- [433] A. van Houselt, M. Fischer, B. Poelsema, H.J.W. Zandvliet, Giant missing row reconstruction of Au on Ge(001), *Phys. Rev. B* 78 (23) (2008) 233410.
- [434] M.C. Gallagher, S. Melnik, D. Mahler, Temperature- and exposure-dependent study of the Ge(001)c(8 × 2)-Au surface, *Phys. Rev. B* 83 (2011) 033302.
- [435] R. Niikura, K. Nakatsuji, F. Komori, Local atomic and electronic structure of Au-adsorbed Ge(001) surfaces: scanning tunneling microscopy and x-ray photoemission spectroscopy, *Phys. Rev. B* 83 (2011) 1–6.
- [436] C. Blumenstein, S. Meyer, S. Mietke, J. Schäfer, A. Bostwick, E. Rotenberg, R. Matzdorf, R. Claessen, Au-induced quantum chains on Ge(001)-symmetries, long-range order and the conduction path, *J. Phys. Condens. Matter* 25 (2013) 014015.
- [437] A. Safaei, A. van Houselt, B. Poelsema, H.J.W. Zandvliet, R. van Gastel, Dynamics of the wetting-induced nanowire reconstruction of Au/Ge(001), *Phys. Rev. B* 88 (2013) 085415.
- [438] S. Sauer, F. Fuchs, F. Bechstedt, C. Blumenstein, J. Schäfer, First-principles studies of Au-induced nanowires on Ge(001), *Phys. Rev. B* 81 (2010) 075412.
- [439] K. Seino, S. Sanna, W. Gero Schmidt, Temperature stabilizes rough Au/Ge(001) surface reconstructions, *Surf. Sci.* 667 (2018) 101–104.
- [440] S.-F. Tsay, Au-induced deep groove nanowire structure on the Ge(001) surface: DFT calculations, *Surf. Sci.* 651 (2016) 164–174.
- [441] K. Yaji, R. Yukawa, S. Kim, Y. Ohtsubo, P.L. Fèvre, F. Bertran, A. Taleb-Ibrahimi, I. Matsuda, K. Nakatsuji, S. Shin, F. Komori, Surface electronic states of Au-induced nanowires on Ge(001), *J. Phys. Condens. Matter* 30 (7) (2018) 075001.
- [442] S. Das Sarma, W.-y. Lai, Screening and elementary excitations in narrow-channel semiconductor microstructures, *Phys. Rev. B* 32 (2) (1985) 1401–1404.
- [443] Q. Li, S. Das Sarma, Plasmon excitations in one-dimensional lateral-quantum-wire superlattices, *Phys. Rev. B* 41 (1990) 10268–10271.
- [444] S. Das Sarma, E.H. Hwang, Dynamical response of a one-dimensional quantum-wire electron system, *Phys. Rev. B* 54 (3) (1996) 1936–1946.
- [445] W. Swiech, E. Bauer, M. Mundschau, A low-energy electron microscopy study of the system Si(111)-Au, *Surf. Sci.* 253 (1–3) (1991) 283–296.
- [446] L.D. Marks, R. Plass, Atomic structure of Si(111)-(5 × 2)-Au from high resolution electron microscopy and heavy-atom holography, *Phys. Rev. Lett.* 75 (1995) 2172–2175.

- [447] Y. Nakajima, C. Voges, T. Nagao, S. Hasegawa, G. Klos, H. Pfnür, Critical scattering at the order-disorder phase transition of Si(111)- $\sqrt{3}\sqrt{3}R30^\circ$ -Au surface: a phase transition with particle exchange, *Phys. Rev. B* 55 (1997) 8129–8135.
- [448] D. Grozea, E. Bengu, L. Marks, Surface phase diagrams for the Ag-Ge(111) and Au-Si(111) systems, *Surf. Sci.* 461 (1) (2000) 23–30.
- [449] I. Barke, F. Zheng, S. Bockenhauer, K. Sell, V.V. Oeynhausen, K.H. Meiwes-Broer, S.C. Erwin, F.J. Himpsel, Coverage-dependent faceting of Au chains on Si(557), *Phys. Rev. B* 79 (2009) 155301.
- [450] S.C. Erwin, I. Barke, F.J. Himpsel, Structure and energetics of Si(111)-(5 × 2)-Au, *Phys. Rev. B* 80 (2009) 155409.
- [451] C. Hogan, E. Ferraro, N. McAlinden, J.F. McGilp, Optical fingerprints of Si honeycomb chains and atomic gold wires on the Si(111)-(5×2)-Au surface, *Phys. Rev. Lett.* 111 (8) (2013) 087401.
- [452] T. Abukawa, Y. Nishigaya, Structure of the Si(111)-(5 × 2)-Au surface, *Phys. Rev. Lett.* 110 (2013) 036102.
- [453] S.G. Kwon, M.H. Kang, Identification of the Au coverage and structure of the Au/Si(111)-(5 × 2) surface, *Phys. Rev. Lett.* 113 (2014) 086101.
- [454] F. Hötzel, K. Seino, C. Huck, O. Skibbe, F. Bechstedt, A. Pucci, Metallic properties of the Si(111) - 5 × 2 - Au surface from infrared plasmon polaritons and ab initio theory, *Nano Lett.* 15 (2015) 4155–4160.
- [455] J. Kautz, M.W. Copel, M.S. Gordon, R.M. Tromp, S.J. van der Molen, Titration of submonolayer Au growth on Si(111), *Phys. Rev. B* 89 (2014) 035416.
- [456] Z. Mamiyev, H. Pfnür, View on Si(111)-(5 × 2)-Au with plasmon spectroscopy, *Phys. Rev. B* 102 (2020) 075438.
- [457] A. Stepniak, P. Nita, M. Krawiec, M. Jalochowski, In and Si adatoms on Si(111)5 × 2-Au: scanning tunneling microscopy and first-principles density functional calculations, *Phys. Rev. B* 80 (2009) 125430.
- [458] A. Stepniak, M. Krawiec, G. Zawadzki, M. Jalochowski, Electronic stabilization of the Si(111)5 × 2-Au surface: Pb and Si adatoms, *J. Phys. Condens. Matter* 24 (2012) 095002.
- [459] I. Song, J.S. Goh, S.-h. Lee, S.W. Jung, J.S. Shin, H. Yamane, N. Kosugi, H. W. Yeom, Realization of a strained atomic wire superlattice, *ACS Nano* 9 (2015) 10621–10627.
- [460] Z. Mamiyev, S. Sanna, F. Ziese, C. Dues, C. Tegenkamp, H. Pfnür, Plasmon localization by H-induced band switching, *J. Phys. Chem. C* 124 (2020) 958–967.
- [461] H. Pfnür, C. Tegenkamp, L. Vattuone, Plasmons in one and two dimensions, ch. 19. *Springer Handbook of Surface Science*, Springer, Heidelberg, 2021, pp. 557–584.
- [462] Z. Mamiyev, M. Tzschoppe, C. Huck, A. Pucci, H. Pfnür, Plasmon standing waves by oxidation of Si(553)-Au, *J. Phys. Chem. C* 123 (14) (2019) 9400–9406.
- [463] M. Krawiec, M. Jalochowski, Doping of the step-edge Si chain: Ag on a Si(557)-Au surface, *Phys. Rev. B* 82 (2010) 195443.
- [464] T. Nagao, G. Han, C. Hoang, J.-S. Wi, A. Pucci, D. Weber, F. Neubrech, V. M. Silkin, D. Enders, O. Saito, M. Rana, Plasmons in nanoscale and atomic-scale systems, *Sci. Technol. Adv. Mater.* 11 (2010) 054506.
- [465] F. Hötzel, N. Galden, S. Baur, A. Pucci, One-dimensional plasmonic excitations in gold-induced superstructures on Si(553): impact of gold coverage and silicon step edge polarization, *J. Phys. Chem. C* 121 (553) (2017) 8120.
- [466] M. Tzschoppe, C. Huck, F. Hötzel, A. Butkevich, Z. Mamiyev, C. Ulrich, B. Günther, L. Gade, A. Pucci, How adsorbates alter the metallic behavior of quasi-one-dimensional electron systems of the Si(553)-Au surface, *J. Phys. Condens. Matter* 31 (2018) 195001.
- [467] C. Preinesberger, T. Kalka, S. Vandrè, M. Dähne, Formation of dysprosium silicide wires on Si(001), *J. Phys. D Appl. Phys.* 31 (1998) L43.
- [468] Y. Chen, D.A.A. Ohlberg, G. Medeiros-Ribeiro, Y.A. Chang, R.S. Williams, Self-assembled growth of epitaxial erbium disilicide nanowires on silicon (001), *Appl. Phys. Lett.* 76 (2000) 4004.
- [469] J. Nogami, B.Z. Liu, M.V. Katkov, C. Ohbuchi, N.O. Birge, Self-assembled rare-earth silicide nanowires on Si(001), *Phys. Rev. B* 63 (2001) 233305.
- [470] C. Preinesberger, S.K. Becker, S. Vandrè, T. Kalka, M. Dähne, Structure of DySi₂ nanowires on Si(001), *J. Appl. Phys.* 91 (2002) 1695.
- [471] Y. Chen, D.A.A. Ohlberg, R.S. Williams, Nanowires of four epitaxial hexagonal silicides grown on Si(001), *J. Appl. Phys.* 91 (2002) 3213.
- [472] B.Z. Liu, J. Nogami, A scanning tunneling microscopy study of dysprosium silicide nanowire growth on Si(001), *J. Appl. Phys.* 93 (2003) 593.
- [473] C. Preinesberger, G. Pruskil, S.K. Becker, M. Dähne, D.V. Vyalikh, S.L. Molodtsov, C. Laubschat, F. Schiller, Structure and electronic properties of dysprosium silicide nanowires on vicinal Si(001), *Appl. Phys. Lett.* 87 (2005) 083107.
- [474] H.W. Yeom, Y.K. Kim, E.Y. Lee, K.-D. Ryang, P.G. Kang, Robust one-dimensional metallic band structure of silicide nanowires, *Phys. Rev. Lett.* 95 (2005) 205504.
- [475] V. Iancu, P.R.C. Kent, C.G. Zeng, H.H. Weitering, Structure of YSi₂ nanowires from scanning tunneling spectroscopy and first principles, *Appl. Phys. Lett.* 95 (2009) 123107.
- [476] C. Eames, M.L.J. Probert, S.P. Tear, The structure and growth direction of rare earth silicide nanowires on Si(100), *Appl. Phys. Lett.* 96 (2010) 241903.
- [477] M. Wanke, K. Löser, G. Pruskil, D.V. Vyalikh, S.L. Molodtsov, S. Danzenbacher, C. Laubschat, M. Dähne, Electronic properties of self-assembled rare-earth silicide nanowires on Si(001), *Phys. Rev. B* 83 (2011) 205417.
- [478] V. Iancu, P.R.C. Kent, C. Hus, H. Hu, C.G. Zeng, H.H. Weitering, Structure and growth of quasi-one-dimensional YSi₂ nanophases on Si(100), *J. Phys. Condens. Matter* 25 (2013) 014011.
- [479] M. Dähne, M. Wanke, Metallic rare-earth silicide nanowires on silicon surfaces, *J. Phys. Condens. Matter* 25 (2013) 014012.
- [480] S. Appelfeller, S. Kuls, M. Dähne, Tb silicide nanowire growth on planar and vicinal Si(001) surfaces, *Surf. Sci.* 641 (2015) 180.
- [481] I. Miccoli, F. Edler, H. Pfnür, S. Appelfeller, M. Dähne, K. Holtgrewe, S. Sanna, W. G. Schmidt, C. Tegenkamp, Atomic size effects studied by transport in single silicide nanowires, *Phys. Rev. B* 93 (2016) 125412.
- [482] S. Appelfeller, M. Franz, M. Kubicki, P. Reiß, T. Niermann, M.A. Schubert, M. Lehmann, M. Dähne, Capping of rare earth silicide nanowires on Si(001), *Appl. Phys. Lett.* 108 (2016) 013109.
- [483] S. Appelfeller, M. Franz, H.-F. Jirschik, J. Große, M. Dähne, The electronic structure of Tb silicide nanowires on Si(001), *New J. Phys.* 18 (2016) 113005.
- [484] F. Timmer, J. Bahlmann, J. Wollschläger, On the diffraction pattern of bundled rare-earth silicide nanowires on Si(001), *J. Phys. Condens. Matter* 29 (2017) 435304.
- [485] S. Chandola, E. Speiser, N. Esser, S. Appelfeller, M. Franz, M. Dähne, Optical anisotropy of quasi-1D rare-earth silicide nanostructures on Si(001), *Appl. Surf. Sci.* 399 (2017) 648.
- [486] S. Appelfeller, Atomic Structure and Electronic Properties of Tb Silicide Nanowire, PhD thesis, Technische Universität Berlin, 2018, <https://depositonce.tu-berlin.de/handle/11303/8534>.
- [487] S. Appelfeller, J. Heggemann, T. Niermann, M. Lehmann, M. Dähne, Refined structure model of rare earth silicide nanowires on Si(001), *Appl. Phys. Lett.* 114 (2019) 093104.
- [488] K. Holtgrewe, S. Appelfeller, M. Franz, M. Dähne, S. Sanna, Structure and one-dimensional metallicity of rare-earth silicide nanowires on Si(001), *Phys. Rev. B* 99 (2019) 214104.
- [489] J. Heggemann, S. Appelfeller, T. Niermann, M. Lehmann, M. Dähne, Internal atomic structure of terbium silicide nanowires on Si(001) capped by silicon, *Surf. Sci.* 696 (2020) 121563.
- [490] Z. He, M. Stevens, D.J. Smith, P.A. Bennett, Dysprosium silicide nanowires on Si(110), *Appl. Phys. Lett.* 83 (2003) 5292.
- [491] M. Wanke, K. Löser, G. Pruskil, M. Dähne, Structural and electronic properties of rare earth silicide nanowires on Si(557), *Phys. Rev. B* 79 (2009) 155428.
- [492] M. Wanke, M. Franz, M. Vetterlein, G. Pruskil, C. Prohl, B. Höpfner, P. Stojanov, E. Huwald, J.D. Riley, M. Dähne, Electronic properties of dysprosium silicide nanowires on Si(557), *J. Appl. Phys.* 108 (6) (2010) 064304.
- [493] I.-H. Hong, Y.-F. Tsai, Y.-F. Chen, Self-organization of mesoscopically ordered parallel Gd-silicide nanowire arrays on a Si(110)-16 × 2 surface: a massively parallel active architecture, *Appl. Phys. Lett.* 98 (2011) 193118.
- [494] S.M. Hus, H.H. Weitering, Formation of uni-directional ultrathin metallic YSi₂ nanowires on Si(110), *Appl. Phys. Lett.* 103 (2013) 073101.
- [495] M. Franz, J. Große, R. Kohlhaas, M. Dähne, Terbium induced nanostructures on Si(111), *Surf. Sci.* 637–638 (2015) 149.
- [496] F. Timmer, R. Oelke, C. Dues, S. Sanna, W.G. Schmidt, M. Franz, S. Appelfeller, M. Dähne, J. Wollschläger, Strain-induced quasi-one-dimensional rare-earth silicide structures on Si(111), *Phys. Rev. B* 94 (2016) 205431.
- [497] F. Timmer, J. Wollschläger, Effects of domain boundaries on the diffraction patterns of one-dimensional structures, *Condens. Matter* 2 (2017) 7.
- [498] S. Appelfeller, M. Franz, L. Freter, C. Hassenstein, H.F. Jirschik, M. Dähne, Growth and characterization of Tb silicide nanostructures on Si(hhk) substrates, *Phys. Rev. Mater.* 3 (2019) 126002.
- [499] S. Appelfeller, K. Holtgrewe, M. Franz, L. Freter, C. Hassenstein, H.F. Jirschik, S. Sanna, M. Dähne, Continuous crossover from two-dimensional to one-dimensional electronic properties for metallic silicide nanowires, *Phys. Rev. B* 102 (2020) 115433.
- [500] S. Appelfeller, M. Franz, M. Karadag, M. Kubicki, R. Zielinski, M. Krivenkov, A. Varykhalov, A. Preobrajenski, M. Dähne, Self-organized formation of unidirectional and quasi one-dimensional metallic Tb silicide nanowires on Si(110), *Appl. Surf. Sci.* 607 (2023) 154875.
- [501] L. Stauffer, A. Mharchi, C. Pirri, P. Wetzel, D. Bolmont, G. Gewinner, C. Minot, Electronic structure and interfacial geometry of epitaxial two-dimensional Er silicide on Si(111), *Phys. Rev. B* 47 (1993) 10555.
- [502] S. Vandrè, T. Kalka, C. Preinesberger, M. Dähne-Prietsch, Flatband conditions observed for lanthanide silicide monolayers on n-type Si(111), *Phys. Rev. Lett.* 82 (1999) 1927.
- [503] C. Rogero, C. Koitzsch, M.E. González, P. Aebi, J. Cerdá, J.A. Martín-Gago, Electronic structure and Fermi surface of two-dimensional rare-earth silicides epitaxially grown on Si(111), *Phys. Rev. B* 69 (2004) 045312.
- [504] I. Engelhardt, C. Preinesberger, S.K. Becker, H. Eisele, M. Dähne, Atomic structure of thin dysprosium-silicide layers on Si(111), *Surf. Sci.* 600 (2006) 755.
- [505] M. Wanke, M. Franz, M. Vetterlein, G. Pruskil, B. Höpfner, C. Prohl, I. Engelhardt, P. Stojanov, E. Huwald, J.D. Riley, M. Dähne, Energy surfaces of rare-earth silicide films on Si(111), *Surf. Sci.* 603 (2009) 2808.
- [506] M. Franz, S. Appelfeller, C. Prohl, J. Große, H.-F. Jirschik, V. Füllert, C. Hassenstein, Z. Diemer, M. Dähne, Growth and electronic properties of Tb silicide layers on Si(111), *J. Vac. Sci. Technol. A* 34 (2016) 061503.
- [507] S. Sanna, C. Dues, W.G. Schmidt, F. Timmer, J. Wollschläger, M. Franz, S. Appelfeller, M. Dähne, Rare-earth silicide thin films on the Si(111) surface, *Phys. Rev. B* 93 (2016) 159407.
- [508] J. Bahlmann, F. Timmer, and J. Wollschläger, “Diffraction Study of the Development of the Dy Induced Wetting Layer on Si(001).” (unpublished).
- [509] H. Okino, I. Matsuda, R. Hobara, Y. Hosomura, S. Hasegawa, P.A. Bennett, In situ resistance measurements of epitaxial cobalt silicide nanowires on Si(110), *Appl. Phys. Lett.* 86 (2005) 233108.
- [510] P. Weightman, D.S. Martin, R.J. Cole, T. Farrell, Reflection anisotropy spectroscopy, *Rep. Prog. Phys.* 68 (2005) 1251.
- [511] W.G. Schmidt, F. Bechstedt, J. Bernholz, Terrace and step contributions to theoretical anisotropy of Si(001) surfaces, *Phys. Rev. B* 63 (2001) 045322.

- [512] N. Witkowski, R. Coustel, O. Pluchery, Y. Borensztein, RAS: an efficient probe to characterize Si(001)-(2 × 1) surfaces, *Surf. Sci.* 600 (2006) 5142.
- [513] K. Fleischer, S. Chandola, T. Herrmann, N. Esser, W. Richter, J. McGilp, Free-electron response in reflectance anisotropy spectra, *Phys. Rev. B* 74 (2006) 195432.
- [514] P. Puschnig, S. Berkebile, A.J. Fleming, G. Koller, K. Emtsev, T. Seyller, J.D. Riley, C. Ambrosch-Draxl, F.P. Netzer, M.G. Ramsey, Reconstruction of molecular orbital densities from photoemission data, *Science* 326 (2009) 702.
- [515] M. Wießner, D. Hauschild, A. Schöll, F. Reinert, V. Feyer, K. Winkler, B. Krömker, Electronic and geometric structure of the PTCDA/Ag(110) interface probed by angle-resolved photoemission, *Phys. Rev. B* 86 (2012) 045417.
- [516] C. Kumpf, O. Bunk, J. Zeysing, Y. Su, M. Nielsen, R. Johnson, R. Feidenhans, K. Bechgaard, Low-temperature structure of indium quantum chains on silicon, *Phys. Rev. Lett.* 85 (2000) 4916.
- [517] H. Yeom, K. Horikoshi, H. Zhang, K. Ono, R. Uhrberg, Nature of the broken-symmetry phase of the one-dimensional metallic In/Si (111) surface, *Phys. Rev. B* 65 (2002) 241307.
- [518] J.R. Ahn, J.H. Byun, H. Koh, E. Rotenberg, S.D. Kevan, H.W. Yeom, Mechanism of gap opening in a triple-band Peierls system: in atomic wires on Si, *Phys. Rev. Lett.* 93 (2004) 106401.
- [519] J. Guo, G. Lee, E.W. Plummer, Intertwined electronic and structural phase transitions in the In/Si (111) interface, *Phys. Rev. Lett.* 95 (2005) 046102.
- [520] C. González, J. Ortega, F. Flores, Metal-insulator transition in one-dimensional In-chains on Si(111): combination of a soft shear distortion and a double-band Peierls instability, *New J. Phys.* 7 (2005) 100, 100.
- [521] S. Riikonen, A. Ayuela, D. Sánchez-Portal, Metal-insulator transition in the In/Si (1 1 1) surface, *Surf. Sci.* 600 (2006) 3821–3824.
- [522] S. Hellmann, T. Rohwer, M. Kalläne, K. Hanff, C. Sohr, A. Stange, A. Carr, M. Murnane, H. Kapteyn, L. Kipp, et al., Time-domain classification of charge-density-wave insulators, *Nat. Commun.* 3 (2012) 1–8.
- [523] R. Dronskowski, P. Blöchl, Crystal orbital Hamilton populations (COHP): energy-resolved visualization of chemical bonding in solids based on density-functional calculations, *J. Phys. Chem.* 97 (1993) 8617–8624.
- [524] G. Lee, S.-Y. Yu, H. Kim, J.-Y. Koo, Defect-induced perturbation on Si (111) 4 × 1-In: period-doubling modulation and its origin, *Phys. Rev. B* 70 (2004) 121304.
- [525] C.-Y. Ruan, F. Vigliotti, V.A. Lobastov, S. Chen, A.H. Zewail, *Ultrafast Electron Crystallography: Transient Structures of Molecules, Surfaces, and Phase Transitions*, vol. 101, Proceedings of the National Academy of Sciences, 2004, pp. 1123–1128.
- [526] A. Ichimiya, P.I. Cohen, P.I. Cohen, *Reflection High-Energy Electron Diffraction*, Cambridge University Press, 2004.
- [527] C.W. Nicholson, C. Berthod, M. Puppini, H. Berger, M. Wolf, M. Hoesch, C. Monney, Dimensional crossover in a charge density wave material probed by angle-resolved photoemission spectroscopy, *Phys. Rev. Lett.* 118 (2017) 206401.
- [528] Y. Sun, S. Agario, S. Souma, K. Sugawara, Y. Tago, T. Sato, T. Takahashi, Cooperative structural and Peierls transition of indium chains on Si (111), *Phys. Rev. B* 77 (2008) 125115.
- [529] S. Lee, J. Ahn, N. Kim, J. Min, C. Hwang, J. Chung, H. Yeom, S.V. Ryjkov, S. Hasegawa, Adsorbate-induced pinning of a charge-density wave in a quasi-1d metallic chains: Na on the In/Si (111)-(4 × 1) surface, *Phys. Rev. Lett.* 88 (2002) 196401.
- [530] G. Lee, J. Guo, E.W. Plummer, Real-space observation of nanoscale inhomogeneities and fluctuations in a phase transition of a surface quasi-one-dimensional system: in/Si (111), *Phys. Rev. Lett.* 95 (2005) 116103.
- [531] H. Morikawa, K.S. Kim, Y. Kitaoka, T. Hirahara, S. Hasegawa, H.W. Yeom, Conductance transition and interwire ordering of Pb nanowires on Si (557), *Phys. Rev. B* 82 (2010) 045423.
- [532] H.-J. Kim, J.-H. Cho, Driving force of phase transition in indium nanowires on Si (111), *Phys. Rev. Lett.* 110 (2013) 116801.
- [533] G. Lee, S.-Y. Yu, H. Shim, W. Lee, J.-Y. Koo, Roles of defects induced by hydrogen and oxygen on the structural phase transition of Si(111)4 × 1-In, *Phys. Rev. B* 80 (2009) 075411.
- [534] B. Hafke, T. Witte, D. Janoschka, P. Dreher, F.-J. Meyer to Heringdorf, M. Horn-von Hoegen, Condensation of ground state from a supercooled phase in the Si (111)-(4 × 1) → (8 × 2)-indium atomic wire system, *Structural Dynamics* 6 (2019) 045101.
- [535] G. Kresse, J. Furthmüller, Efficiency of ab-initio total energy calculations for metals and semiconductors using a plane-wave basis set, *Comput. Mater. Sci.* 6 (1996) 15.
- [536] L. Perfetti, P. Loukakos, M. Lisowski, U. Bovensiepen, H. Berger, S. Biermann, P. Cornaglia, A. Georges, M. Wolf, Time evolution of the electronic structure of 1T-TaS₂ through the insulator-metal transition, *Phys. Rev. Lett.* 97 (2006) 067402.
- [537] L. Rettig, R. Cortés, J.-H. Chu, I. Fisher, F. Schmitt, R. Moore, Z.-X. Shen, P. Kirchmann, M. Wolf, U. Bovensiepen, Persistent order due to transiently enhanced nesting in an electronically excited charge density wave, *Nat. Commun.* 7 (2016) 1–6.
- [538] I. Waller, Zur Frage der Einwirkung der Wärmebewegung auf die Interferenz von Röntgenstrahlen, *Z. Phys.* 17 (1923) 398–408.
- [539] P. Zhou, C. Streubühr, A. Kalus, T. Frigge, S. Wall, A. Hanisch-Blicharski, M. Kammler, M. Ligges, U. Bovensiepen, D. von der Linde, et al., Ultrafast time resolved reflection high energy electron diffraction with tilted pump pulse fronts, in: EPJ Web of Conferences, vol. 41, EDP Sciences, 2013 10016.
- [540] Y.-X. Gu, W.-H. Liu, Z. Wang, S.-S. Li, L.-W. Wang, J.-W. Luo, Origin of immediate damping of coherent oscillations in photoinduced charge density wave transition, *Phys. Rev. Lett.* accepted (2023), 0000-9999.
- [541] C. Sohr, A. Stange, M. Bauer, K. Rossnagel, How fast can a Peierls–Mott insulator be melted? *Faraday Discuss* 171 (2014) 243–257.
- [542] G.R. Fleming, M.A. Ratner, Grand challenges in basic energy sciences, *Phys. Today* 61 (2008) 28.